Light Hadron Spectroscopy in Lattice QCD

Joyce Garden

Doctor of Philosophy
The University of Edinburgh
2000

Abstract

This thesis presents the results of a numerical calculation of the light hadron spectrum in the lattice formulation of Quantum Chromodynamics. Results were obtained in both the quenched approximation, where the effects of quark loops in the QCD vacuum were neglected, and in "full" QCD, where two degenerate flavours of dynamical fermions were included in the simulation. All numerical simulations employed the standard Wilson gauge action with an $O(a)$ improved Wilson fermion action. This study confirms that the quenched light hadron mass spectrum agrees with experiment at the 10% level. Finite size effects at one value of the coupling were investigated and an improved scaling behaviour arising from the implementation of the $O(a)$ improvement programme was observed for the quenched simulations.

With the aim of observing effects in the spectrum due to the inclusion of fermion loops in the QCD vacuum, simulations in "full" QCD forming a matched ensemble were compared with a quenched simulation at the same lattice spacing. Each simulation in the matched ensemble was selected to have approximately the same lattice spacing as defined with respect to a physical observable in order to investigate chiral extrapolations independently from continuum extrapolations. A further simulation with a lighter sea quark mass at a smaller lattice spacing was included in the analysis for comparison. Evidence for small yet significant dynamical effects arising from the comparison with the quenched data were observed in the hyperfine splitting and partially quenched chiral extrapolations. Results obtained from the matched ensemble displayed a reduced residual dependence upon lattice artifacts.

Declaration

This thesis has been written and composed by me and contains the results of my work as part of the UKQCD Collaboration. The analysis was performed using code developed from the existing analysis code written by members of the Collaboration. The quenched correlators and gauge configurations were generated by Collaboration members. The correlators analysed in chapter 4 were generated by me upon gauge configurations generated by Bálint Joó with code written by other members of UKQCD. The data in chapter 4 was analysed by me and the quenched analysis in chapter 3 was analysed by me, in collaboration with Hartmut Wittig for the purposes of publication. The results from chapter 3 and 4 appear in:

- (UKQCD Collaboration), K. C. Bowler et al., hep-lat/9910022, to be published in Phys. Rev. D.
- (UKQCD Collaboration), J. Garden, hep-lat/9909066, to be published in Nuc. Phys. B. (Proc. Suppl.)
- (UKQCD Collaboration), C. R. Allton et al., in preparation.

Other publications to which I have contributed:

- (ALPHA and UKQCD Collaborations), J. Garden, J. Heitger, R. Sommer and H. Wittig, hep-lat/9906013, to be published in Nuc. Phys. B.
- (ALPHA and UKQCD Collaborations), J. Garden, M. Guagnelli, J. Heitger, R. Sommer and H. Wittig, hep-lat/9909098
- (UKQCD Collaboration), C. R. Allton et al., Phys. Rev. D **60**, 034507, (1999)
- (UKQCD Collaboration), A. C. Irving et al., Phys. Rev. D **58**, 114504, (1998)

Joyce Garden

Acknowledgements

Firstly, I would like to thank my family for all their love and support throughout my years at University, especially my mum, Elizabeth and my sister Katherine. Cheers.

I gratefully acknowledge the financial support of the Carnegie Trust for the Universities of Scotland and latterly the President's Fund - The Edinburgh Association of University Women. I would like to thank my supervisors Richard Kenway and Ken Bowler for their help and advice over the years, and for a careful reading of this thesis. Thanks also to Brian for a thorough scrutiny of chapters one and two, and for illuminating lunchtime discussions.

I would like to say thanks to all the members of the UKQCD Collaboration I have had the pleasure of working with. In particular, I want to thank Hartmut Wittig for making sure the quenched paper was finally published, and Alan Irving, Chris Allton and Bálint Joó for their input in the dynamical fermion project.

The past few years would not have been the same without the smiling, happy faces of the PPT group. Thanks everyone. Special thanks go to Gary for making life at the office fun, and to Harry, Zbigniew and Doug for guiding me towards the pub and being great to have a laugh with.

I would also like to say thanks to Alison for being a great flatmate, and to Douglas my best friend for always being there for me.

Contents

Chapter 1

Introduction

The success of perturbative methods in describing the short distance (large momentum transfer) behaviour of quarks and gluons has meant that Quantum Chromodynamics (QCD) has become well established as the theory of strong interactions. Confirmation of this requires that QCD also explains the experimentally observed phenomenon of quark confinement, whereby quarks are bound in colour singlet states known as hadrons. Consequently, a complete understanding of the strong interaction requires a theoretical explanation for the experimentally observed hadron mass spectrum. Unfortunately at the low energies, $\mu \lesssim 1$ GeV, associated with the characteristic length scale of a hadron of approximately 1 fm, the asymptotic freedom property of QCD means that the strong coupling is of $O(1)$, and thus perturbative methods fail. Instead a non-perturbative approach, such as Lattice QCD, is required.

Lattice QCD was formulated by K. G. Wilson [1] in 1974 in order to provide a non-perturbative mechanism for confinement in the strong coupling limit and to enable a numerical study of the low energy behaviour of QCD. In particular, it allows a first principles determination of the mass spectrum of the lightest hadrons, the first numerical results of which were reported in [2, 3]. Reproducing the experimentally observed spectrum serves as a test of QCD and provides an important check on the validity of the lattice approach. Confidence in the spectrum results obtained from the lattice mean that the technique may be used as a predictive tool for other phenomenologically interesting quantities which cannot be measured directly by experiment. The cost of the considerable computational effort required to numerically determine these quantities has meant that the quenched approximation, where quark loops in the vacuum are neglected, is still widely used. How closely this approximation describes the real world can be assessed through a comparison of the numerical results for the quenched light hadron spectrum with experiment. In order to achieve the precision measurements required for such a comparison it is necessary to have control over systematic effects such as lattice artifacts. In chapter 3, residual lattice artifacts in the quenched spectrum results are reduced by using an improved action. The results confirm the recent findings from unimproved simulations performed by the CP-PACS Collaboration [4] which showed that the quenched light hadron spectrum agrees with experiment at the 10% level.

New theoretical developments and more powerful computational resources have meant that recently progress towards simulations of full QCD has been made. In particular, larger simulations with two degenerate flavours of light dynamical quarks have become possible. A review of the results obtained from the most recent simulations from around the world can be found in [5]. So far, full QCD simulations have not reached the stage where precision measurements of the spectrum can be made. However, it is still possible to investigate the evidence for quark loop effects in spectral quantities by comparing full QCD simulations with simulations performed in the quenched approximation. In chapter 4, "matched" simulations (where the lattice spacing was measured to be the same) were selected for comparison in order to separate the effects due to lattice artifacts from genuine dynamical effects.

1.1 Lattice QCD

The formulation of lattice gauge theories, first proposed in [1], is now the subject of textbooks [6, 7] and introductory lecture courses (see for example [8, 9]). A brief outline of the key elements of the theory required for the study of the light hadron spectrum is presented in the following sections.

1.2 Path integral formulation of QCD

The information concerning physical observables in a quantum field theory is contained within an infinite number of vacuum expectation values of time ordered products of quantum field operators, known as Green's functions. These quantum probability amplitudes can be related to probability distributions of classical fields via the path integral formalism [10]. For a gauge theory such as QCD this means that the Green's functions can be expressed in terms of the functional integral over all field configurations

$$\langle 0|\,\hat{\mathcal{T}}\{\hat{\mathcal{O}}[\bar{\psi},\psi,A_\mu]\}\,|0\rangle = \frac{1}{Z}\int \mathcal{D}\bar{\psi}\mathcal{D}\psi\mathcal{D}A_\mu \mathcal{O}[\bar{\psi},\psi,A_\mu]e^{iS[\bar{\psi},\psi,A_\mu]} \tag{1.1}$$

where the partition function is defined by

$$Z = \int \mathcal{D}\bar{\psi}\mathcal{D}\psi\mathcal{D}A_\mu e^{iS[\bar{\psi},\psi,A_\mu]} \tag{1.2}$$

The function $\hat{\mathcal{O}}[\bar{\psi},\psi,A_\mu]$ on the left hand side of equation 1.1 corresponds to a product of quantum operators and on the right hand side $\mathcal{O}[\bar{\psi},\psi,A_\mu]$ corresponds to a product of the anti-fermion, fermion and gauge fields. Here $\hat{\mathcal{T}}$ denotes that the operators are time ordered and S is the classical action. Note that natural units where $\hbar = c = 1$ are used throughout this thesis.

The functional integral in equation 1.1 is complex and strongly oscillating. This is hard to evaluate numerically. The standard method for dealing with this is to analytically continue from Minkowski to Euclidean spacetime via the Wick rotation, $x_0 \to -ix_4$. This corresponds to making the replacement, $iS \to -S_{\mathrm{E}}$, in the partition function [6]

$$Z = \int \mathcal{D}\bar{\psi}\mathcal{D}\psi\mathcal{D}A_\mu e^{-S_{\mathrm{E}}[\bar{\psi},\psi,A_\mu]} \tag{1.3}$$

where the Euclidean action, S_{E}, is defined later in section 1.3. The Green's functions defined in equation 1.1 are replaced by the corresponding Euclidean correlation functions. The partition function, now weighted by $e^{-S_{\mathrm{E}}}$, is amenable to the numerical techniques used to study statistical mechanics provided S_{E} is a real valued function of the field variables and is bounded from below.

In practice, the theory is formulated in Euclidean spacetime and must satisfy certain conditions which ensure that it provides information regarding the Minkowski theory [11]. The main condition is that of reflection positivity, a full description of which can be found in [7]. The proof that these conditions are satisfied for the lattice action considered here is beyond the scope of this thesis (see [12] for further details). For quantities which are not time dependent, such as the mass spectrum, it is not necessary to perform the continuation back to Minkowski spacetime, as will be seen in chapter 2.

1.3 The continuum QCD action

The QCD action is invariant under $SU(3)$ local gauge transformations, $G(x)$, where the fermion and gauge fields transform as

$$\begin{aligned} \psi(x) &\rightarrow G(x)\psi(x) && (1.4)\\ \bar{\psi}(x) &\rightarrow \bar{\psi}(x)G^{-1}(x) && (1.5)\\ A_\mu(x) &\rightarrow G(x)A_\mu(x)G^{-1}(x) - (\partial_\mu G(x))G^{-1}(x) && (1.6) \end{aligned}$$

The continuum action in four dimensional Euclidean spacetime is then given by

$$S_{\mathrm{E}}(x) = \int d^4x \, \frac{-1}{2g_0^2}\mathrm{Tr}\left(F_{\mu\nu}(x)F_{\mu\nu}(x)\right) + \sum_{f=1}^{N_{\mathrm{f}}} \bar{\psi}_f(x)\left(\not{D} + m_f\right)\psi_f(x) \tag{1.7}$$

where N_f is the number of quark flavours and $\mu, \nu = 1, \ldots, 4$. The first term is the Yang-Mills term describing the dynamics of the gluon gauge fields, A_μ, where the gauge field strength tensor, $F_{\mu\nu}(x)$, is defined in terms of the commutator of the covariant derivative, $D_\mu = \partial_\mu + A_\mu(x)$, by

$$F_{\mu\nu}(x) = [D_\mu, D_\nu] = \partial_\mu A_\nu(x) - \partial_\nu A_\mu(x) + [A_\mu(x), A_\nu(x)] \tag{1.8}$$

The gluon gauge fields are defined in terms of the generators of the $SU(3)$ group

$$A_\mu^\dagger(x) = -A_\mu(x), \qquad A_\mu(x) = -ig_0 A_\mu^a(x) T^a, \qquad a = 1, \ldots, 8 \tag{1.9}$$

where the eight $A_\mu^a(x)$ are real fields and g_0 is the bare strong coupling constant. The generators satisfy the commutation relations and normalisation condition

$$[T^a, T^b] = i f_{abc} T^c, \qquad \mathrm{Tr}[T^a T^b] = \tfrac{1}{2}\delta_{a,b} \tag{1.10}$$

where f_{abc} are the anti-symmetric structure constants and the generators are represented in the standard way by the eight Gell-Mann matrices, $T^a = \lambda^a/2$ [7]. The second term in equation 1.7 is the Euclidean Dirac action, describing the interaction of the fermion fields, $\bar{\psi}_f(x)$ and $\psi_f(x)$, where m_f is the mass of the fermion with flavour f and the Dirac spinor and colour indices have been suppressed. The explicit sum over flavours is omitted from now on. Note that $\not{D} \equiv \gamma_\mu D_\mu$. The Euclidean Dirac γ matrices are related to the Minkowski matrices, γ^{M}, by

$$\gamma_4 = \gamma_0^{\mathrm{M}}, \qquad \gamma_j = -i\gamma_j^{\mathrm{M}}, \quad j = 1, \ldots, 3 \tag{1.11}$$

and satisfy the Hermiticity condition and commutation relations [7]

$$\gamma_\mu^\dagger = \gamma_\mu, \qquad \{\gamma_\mu, \gamma_\nu\} = 2\delta_{\mu,\nu} \tag{1.12}$$

The QCD action defined in equation 1.7 can now be substituted into the path integral formalism, where the subscript E is now dropped. However, the path integral is not well defined due to the gauge invariance of the action. This means that the integration is performed over an infinite number of physically equivalent gauge field configurations. One approach which resolves this problem is to discretise spacetime by a four dimensional lattice.

1.4 The lattice approach

The original formulation of lattice gauge theory was proposed in [1]. To transcribe the continuum theory into the lattice description there are several key steps, each of which will be discussed briefly below. Further details can be found in [6, 7]. First, spacetime is discretised and the representations of the fermion and gauge fields on the lattice are discussed. The construction of the lattice action is presented after the integration measure of the path integral is defined and the numerical evaluation of observables is outlined.

1.4.1 Discretisation of spacetime

Spacetime is discretised by the introduction of a four dimensional isotropic hypercubic lattice, Λ_{E}, with lattice spacing a, where

$$\Lambda_{\mathrm{E}} = \{x \in \mathbb{R}^4 |\ x_\mu/a \in \mathbf{Z},\ \mu = 1, \ldots, 4\} \tag{1.13}$$

The integration over Euclidean spacetime in the action is then replaced by the sum over all sites on the lattice, x,

$$\int d^4x \rightarrow a^4 \sum_x \tag{1.14}$$

and dimensionful quantities are rescaled by the lattice spacing to yield dimensionless variables. For example, the fermion mass is replaced by $m \rightarrow am$ since in natural units mass has the dimensions of inverse length.

1.4.2 Lattice representations of the fermion and gauge fields

The fermion fields are represented on the lattice by anti-commuting Grassmann variables situated at the sites of the lattice. The Grassmann nature of the fields means that it is difficult to simulate the path integral numerically. Fortunately, the action is bilinear in the quark fields and the integration over the fermion variables can be performed analytically, avoiding the problem.

The representation of the gauge fields on the lattice is not so straightforward due to the requirements of gauge invariance. If the gauge fields are represented by field variables situated at each site, the gauge invariance of the action is spoiled due to the discretisation of the derivative by a finite difference. An alternative transcription of the gauge fields [1] which maintains gauge invariance is outlined below. In the presence of a gauge field in the continuum, a quark field transported from x to y accrues a phase factor

$$\psi(y) = \mathcal{P} \exp \left\{ - \int_x^y A_\mu(z) dz_\mu \right\} \psi(x) \equiv U(y,x)\psi(x) \tag{1.15}$$

where $\mathcal{P}$ denotes the path ordered product, required due to the non-abelian nature of the gauge fields. Under a local $SU(3)$ gauge transformation, the parallel transporter, $U(y,x)$, transforms as

$$U(y,x) \to G(y)U(y,x)G^{-1}(x) \tag{1.16}$$

and hence

$$\bar{\psi}(y)U(y,x)\psi(x) \tag{1.17}$$

is gauge invariant. On the lattice the parallel transporter is represented by a link variable, $U_\mu(x)$, associated with the link originating at site x oriented in the direction μ

$$U_\mu(x) = e^{-aA_\mu(x+\frac{a\hat{\mu}}{2})} \tag{1.18}$$

where the average gauge field over the link is conventionally defined to be at the midpoint. Here $\hat{\mu}$ is a unit vector in the lattice direction μ. These directed gauge links are represented by 3×3 unitary matrices with unit determinant belonging to the fundamental representation of $SU(3)$. The property that $U_\mu(x) = U^\dagger_{-\mu}(x+a\hat{\mu})$ follows from the path ordering condition. The gauge links transform under $SU(3)$ as

$$U_\mu(x) \to G(x)U_\mu(x)G^{-1}(x+a\hat{\mu}) \tag{1.19}$$

provided $G(x)$ belongs to the same representation of the group as the gauge links. From this equation and the transformation equations for the fermion fields given by equations 1.4 and 1.5, two types of gauge invariant object can be formed on the lattice. The first of these is a string

$$\bar{\psi}(y)U_\mu(y)\ldots U_\nu(x-a\hat{\nu})\psi(x) \tag{1.20}$$

where the gauge links are path ordered and the trace over the colour indices is implicit. The second gauge invariant object is formed by taking the trace of a product of gauge links forming a closed loop, referred to as a Wilson loop. The simplest example of which is the plaquette, $\mathrm{Tr}U_\Box$, where

$$U_\Box \equiv U_\mu(x)U_\nu(x+a\hat{\mu})U_\mu^\dagger(x+a\hat{\nu})U_\nu^\dagger(x) \tag{1.21}$$

is the product of gauge links around an elementary square of the lattice.

1.4.3 The lattice action

The QCD action can be discretised in many ways. The choice of discretised action is governed primarily by the requirement that the action must reproduce the continuum action in the limit where the lattice spacing tends to zero. This allows higher order terms in the lattice spacing which vanish in the continuum limit to be added to the action.

The lattice action is constructed from appropriate combinations of the gauge invariant objects defined in section 1.4.2, and is written in terms of a pure gauge action and a term dependent on the fermion fields

$$S[\bar{\psi},\psi,U] = S_{\mathrm{G}}[U] + S_{\mathrm{F}}[\bar{\psi},\psi,U] \tag{1.22}$$

The fermion action for a single quark flavour can be written in the general form

$$S_{\mathrm{F}}[\bar{\psi},\psi,U] = \sum_{x,y} \bar{\psi}(x)M_{x,y}[U]\psi(y) \tag{1.23}$$

where M is the fermion matrix. The particular form used for each term in the action is discussed later in sections 1.7 and 1.8.

1.4.4 The integration measure

Once the fermion and gauge fields have been represented on the lattice and the action constructed, the partition function can now be expressed in terms of the lattice variables

$$Z = \int \mathcal{D}\bar{\psi}\mathcal{D}\psi\mathcal{D}U e^{-S_G[U]-\sum\limits_{x,y}\bar{\psi}(x)M_{x,y}[U]\psi(y)} \tag{1.24}$$

where

$$\mathcal{D}\bar{\psi}\mathcal{D}\psi \equiv \prod_x d\bar{\psi}(x)d\psi(x), \qquad \mathcal{D}U \equiv \prod_{x,\mu} dU_\mu(x) \tag{1.25}$$

Performing the integration over the Grassmann valued fermion fields, the partition function becomes

$$Z = \int \prod_{x,\mu} dU_\mu(x) \det M[U] e^{-S_G[U]} \tag{1.26}$$

where dU is the gauge invariant or Haar measure defined by the condition

$$\int_G dU f(U) = \int_G dU f(UV) = \int_G dU f(VU) \tag{1.27}$$

where $V \in SU(3)$ and $f(U)$ is an arbitrary function over the group. Since the gauge links are elements of a compact group the normalisation condition

$$\int_G dU = 1 \tag{1.28}$$

can be imposed. This condition reduces the path integral to a large but finite number of integrations and removes the need for gauge fixing. The precise form of the Haar measure can be found in [6]. The remaining integration over the gauge links is performed numerically.

1.4.5 Numerical simulation

In section 1.2, the expectation values of quantum field operators corresponding to physical observables were expressed in the path integral formalism. In terms of the lattice variables, this statement becomes

$$\langle 0|\,\mathcal{T}\{\hat{\mathcal{O}}(\bar{\psi},\psi,U)\}\,|0\rangle = \frac{1}{Z}\int \mathcal{D}\bar{\psi}\mathcal{D}\psi\mathcal{D}U\mathcal{O}(\bar{\psi},\psi,U)e^{-S[\bar{\psi},\psi,U]} \tag{1.29}$$

Since the fermion term in the action is bilinear in the quark fields, the path integral over the Grassmann valued variables can be performed analytically. By considering the integration rules for Grassmann integrals [6], the observable, $\mathcal{O}(\bar{\psi},\psi,U)$, must contain equal numbers of fermion and anti-fermion fields otherwise the integral will vanish. This means that the integral over the fermion fields for a general operator will consist of integrals of the type

$$\int \mathcal{D}\bar{\psi}\mathcal{D}\psi\; e^{-\sum\limits_{x,y}\bar{\psi}(x)M_{x,y}[U]\psi(y)} = \det M[U] \tag{1.30}$$

and

$$\int \mathcal{D}\bar{\psi}\mathcal{D}\psi\;\psi(x')\bar{\psi}(y')e^{-\sum\limits_{x,y}\bar{\psi}(x)M_{x,y}[U]\psi(y)} = M^{-1}_{x',y'}[U]\det M[U] \tag{1.31}$$

Dividing equation 1.31 by equation 1.30 yields the quark propagator in a background gauge field, $G^{\alpha,\beta}_{a,b}(x,y;U)$, in terms of the inverse of the fermion matrix

$$G^{\alpha,\beta}_{a,b}(x,y;U) = M^{-1}_{\alpha,a,x;\beta,b,y}[U] \tag{1.32}$$

where the colour indices (a,b) and the Dirac spinor indices (α,β) are now indicated. The quark propagator is the basic building block from which correlation functions, and in particular, hadron correlators, are constructed on the lattice. The determination of the masses from hadron correlators is the subject of chapter 2.

Once the integration over the fermion fields has been performed analytically, the expectation value of the general operator, $\hat{\mathcal{O}}(\bar{\psi},\psi,U)$, is given by the path integral over the gauge fields

$$\begin{aligned}\langle 0|\,\hat{\mathcal{T}}\{\hat{\mathcal{O}}(\bar{\psi},\psi,U)\}\,|0\rangle &= \frac{1}{Z}\int \mathcal{D}U\mathcal{O}(U,M^{-1}[U])e^{-S_{\rm eff}[U]} && (1.33)\\ &\equiv \left\langle \mathcal{O}(U,M^{-1}[U])\right\rangle_U && (1.34)\end{aligned}$$

where the action has been replaced by the effective action

$$S_{\rm eff}[U] = S_{\rm G}[U] - \ln\det M[U] \qquad (1.35)$$

The notation $<>_U$ has been introduced to denote the path integral over the gauge field configurations. Provided $S_{\rm eff}$ is real valued, the remaining integration over the gauge links can be performed numerically using the technique of Monte Carlo integration with importance sampling [13]. This integration method generates gauge field configurations, labelled by $\{U\}_i$, where $\{U\}_i$ represents the assignment of a link variable to every link on the lattice, with a probability proportional to $e^{-S_{\rm eff}[U]}$. Successive configurations are obtained via an algorithmic update, where the specific algorithms used to generate the configurations analysed in this thesis are referenced later at the appropriate points. The data sets referred to throughout this thesis, are composed from an ensemble of N of these configurations, $\{U\}_i$, $i = 1,\ldots,N$. Neighbouring configurations in the ensemble are separated by several algorithmic updates (known as sweeps or trajectories depending on the type of algorithm) since successive updates of the configurations are in general highly correlated with each other. The expectation value of an observable is approximated by the ensemble average of the observable measured on each configuration

$$\langle 0|\,\hat{\mathcal{T}}\{\hat{\mathcal{O}}(\bar{\psi},\psi,U)\}\,|0\rangle \approx \frac{1}{N}\sum_{i=1}^{N}\mathcal{O}(\{U\}_i, M^{-1}[\{U\}_i]) \qquad (1.36)$$

where the statistical error in the average is $1/\sqrt{N}$ for independent configurations. Correlations in the ensemble mean that this error is increased.

1.5 Simulating QCD

The numerical simulation of QCD requires considerable computational effort in order to generate sufficient statistics to achieve reliable results with acceptable statistical errors. This section discusses the approximation which was made for the data sets analysed in chapter 3 in order to achieve this goal (the quenched approximation) and the subsequent process towards simulating full QCD, the $N_\mathrm{f} = 2$ dynamical fermion simulations investigated in chapter 4.

1.5.1 The quenched approximation

The most computationally intensive part of the configuration generation procedure concerns the need to take into account the determinant of the fermion matrix which appears in the effective action, defined in equation 1.35. This is due to the non-local nature of the inverse of the fermion matrix, which is required in the algorithmic update of the configurations, and the fact that the matrix consists of a large number $(4_{\mathrm{spins}} \times 3_{\mathrm{colours}} \times N_{\mathrm{lattice\ sites}})^2$ of elements which increase with the lattice volume. The computational overhead can be significantly reduced if the approximation

$$\det M[U] = \text{constant} \tag{1.37}$$

is made. The constant was set equal to one in this case. This approximation is known as the *quenched approximation* and corresponds to neglecting quark anti-quark loops in the QCD vacuum (effectively these quarks are made infinitely heavy and thus they decouple from the theory). The quarks and anti-quarks in these loops are commonly referred to as dynamical fermions. The only reason for making this approximation is to significantly simplify the configuration generation procedure. Some motivation for the use of the quenched approximation comes from phenomenological evidence, for example Zweig's rule, which suggests that the effects in the observed spectrum and decay modes due to quark loops are small. This rule is used to explain the dominant decay of the ϕ meson to $\mathrm{K}^-\mathrm{K}^+$ observed experimentally, even though the phase space available for the decay to 3π's is significantly more favourable. The presence of quark loops in the latter decay is used to explain the suppression of the decay mode. Both decay modes are depicted by quark line diagrams in Figure 1.1.

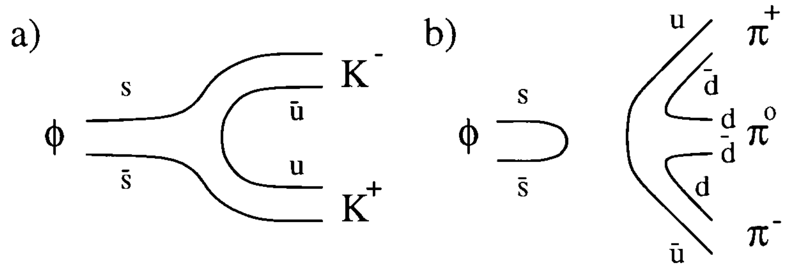

Figure 1.1: Quark line diagrams of two possible decay modes of the ϕ meson. The decay represented by diagram b) $\phi \rightarrow \pi^+\pi^0\pi^-$ is suppressed relative to the decay represented by diagram a) $\phi \rightarrow \mathrm{K}^-\mathrm{K}^+$ even though the available phase space for decay mode b) is much larger [14].

Fortunately quenched QCD retains most of the important features of full QCD such as confinement and chiral symmetry breaking, and in essence, the spectrum calculation proceeds in a similar manner to the full QCD case. One of the main effects of quenching is to shift the value of the coupling. This means that quenched and dynamical simulations should be compared at the same value of the lattice spacing instead of at the same value of the coupling. Simulations with the same value of the lattice spacing defined with reference to a particular observable but with different lattice parameters are referred to as a "matched" ensemble of data sets. The method by which this was achieved for the data sets examined in this thesis is discussed in chapter 4.

Neglecting the quark anti-quark loops in the vacuum has several important consequences. For example, resonances such as the ρ meson are stable in the quenched approximation (in full QCD the ρ mass receives a contribution from intermediate states composed from two π's) and this implies that the masses will be shifted. In the case of the ρ, the broad resonance of 150 MeV [14] measured experimentally suggests that the coupling to the π's is relatively large and thus may have a significant impact on the ρ mass [15]. As a further consequence of the quenched approximation, the static quark potential between a quark anti-quark pair is expected to rise linearly with distance. In full QCD the potential should level off due to the effects of string breaking, where quark anti-quark pairs are created from the vacuum as the separation is increased. In addition, the force between the quarks at small distances is expected to be larger in the dynamical case due to screening effects. The evidence for these effects in the potential is reviewed in chapter 4. One place where the inclusion of quark loops in the vacuum is expected to have a large effect is in the determination of the mass of the η' meson. The axial $U(1)$ flavour symmetry is spontaneously broken in the limit of massless quarks. However, the only candidate for the associated Goldstone boson, the η', has a large mass of 958 MeV [14]. This is known as the $U(1)$ problem. To solve this problem it has been proposed that the η' acquires its large mass through contributions arising from the QCD vacuum, for example from quark loop effects (a discussion of this can be found in [16]). As a consequence, the η' is degenerate with the π in the quenched approximation.

Although the quenched approximation has successfully demonstrated that the non-singlet light hadron spectrum can be determined to within 10% of the experimental results, as confirmed by this thesis in chapter 3, it still represents an uncontrolled error in the simulation. Within recent years, the advent of more powerful computers and efficient configuration generation algorithms, has meant that it is now feasible to simulate two light degenerate flavours of dynamical quarks, denoted by $N_{\mathrm{f}} = 2$. It is straightforward to show the primary reason why the dynamical simulation has been limited to two degenerate quarks and not three quarks of different flavours, which would be required in order to simulate the three lightest quarks, the up, down and strange quarks (u, d, s).

1.5.2 $N_{\mathrm{f}} = 2$ dynamical fermions

Considerable simplifications in the numerical simulation of full QCD arise from considering pairs of degenerate quark flavours. In section 1.4.5, the numerical simulation required that the effective action, defined in equation 1.35, be real valued in order that importance sampling can be implemented easily. This requirement means that $\det M[U]$ is real and positive. That the determinant of the fermion matrix is real follows from the lattice Hermiticity relation

$$M[U] = \gamma_5 M^\dagger[U]\gamma_5 \tag{1.38}$$

which holds in the case of the improved Wilson fermion matrix, defined later in section 1.8. However, equation 1.38 does not guarantee the positivity of $\det M[U]$. Consider an action with two fermion terms, one describing the interaction of the u flavoured quarks and the other the d flavoured quarks. Performing the integration over the fermion fields results in the following determinant

$$\det M[U] \rightarrow \det M_{\mathrm{u}}[U] \det M_{\mathrm{d}}[U] = (\det M_{\mathrm{u}}[U])^2 \geq 0 \tag{1.39}$$

provided $M_{\mathrm{u}} = M_{\mathrm{d}}$. Thus positivity is satisfied in the case of pairs of degenerate fermion flavours.

In both the quenched approximation and the dynamical simulations, the inversion of the fermion matrix must be performed in order to calculate the quark propagators corresponding to the valence quarks. This can be a computationally intensive process, particularly if simulations are performed at the physical masses of the light quarks. For this reason, quark propagators are generated at unphysically heavy quark masses and the lattice masses extracted from the data are extrapolated to the physical light quark masses. These *chiral extrapolations* are discussed later in section 1.11, but first the form of the lattice action constructed within the $O(a)$ improvement programme is discussed.

1.6 $O(a)$ improvement

One of the major sources of error in the lattice simulation arises from the discrete nature of the lattice. The computational cost of simulating at arbitrarily small lattice spacings means that practical simulations must be performed at small yet finite lattice spacings. This is particularly applicable for simulations with two flavours of dynamical fermions which require significant computational resources and necessitate that simulations be carried out at relatively coarse lattice spacings, $a \approx 0.1$ fm. As a consequence, the discretisation errors in spectral quantities become larger. One way to reduce the problem is to consider improved actions. Although the pure gauge action, defined later in section 1.7, can be improved, this thesis investigates the effect of improving the fermion action. The improved fermion action considered here is based on the ideas of the Symanzik improvement programme [17] which aims to construct a lattice realisation of the theory with an improved approach to the continuum limit. This is achieved by the addition of appropriately chosen higher order terms in the lattice spacing to the lattice action and operators, selected to cancel the discretisation errors of a particular order of the lattice spacing in on-shell physical quantities, such as hadron masses. Spectral quantities should then show an improved approach to the continuum limit at the expense of only a relatively small rise in the computational cost of the simulation. With this in mind, the choice of lattice action used in this thesis is now discussed.

1.7 The gauge action

The pure gauge part of the action, $S_{\mathrm{G}}[U]$, is defined to be the standard Wilson gauge action [1]

$$S_{\mathrm{G}}[U] = \beta \sum_{\Box} \left(1 - \frac{1}{3}\Re\mathrm{e}\mathrm{Tr}U_{\Box}\right), \qquad \beta = \frac{6}{g_0^2} \tag{1.40}$$

where β parametrises the dependence on the strong coupling constant. The sum is over all the positively oriented plaquettes originating from every lattice site, where $U_{\Box}$ was defined in equation 1.21 and $\Re\mathrm{e}$ denotes that the real part of the trace is taken. Upon substituting equation 1.18 into the gauge action, $S_{\mathrm{G}}[U]$, the Yang-Mills term in the continuum action is obtained up to discretisation errors of $O(a^2)$. However, this is only the simplest choice for the gauge action which can be made. Improved gauge actions, which aim to reduce the discretisation errors further, can be formed by adding a contribution from Wilson loops created from six (or more) gauge links. In "full" QCD simulations, the CP-PACS Collaboration [18] use the improved gauge action obtained from an approximate renormalisation group analysis [19]

$$S_{\mathrm{G}}^{\mathrm{I}}[U]=\beta\left(\sum_{1\times1}W_{1\times1}-0.0907\sum_{1\times2}W_{1\times2}\right),\qquad W_{1\times1}=\Re\mathrm{eTr}U_{\Box}\tag{1.41}$$

where $W_{1\times2}$ denotes the real part of the trace over a 1×2 rectangular Wilson loop in the μ,ν plane. The sums are over all the positively oriented Wilson loops. The motivation and method used to obtain this action are not discussed further and can be found in [19]. This choice of action is expected to eliminate the $O(a^2)$ discretisation errors.

1.8 The fermion action

The fermion action used in this thesis is the $O(a)$ improved Wilson fermion action

$$S_{\mathrm{F}}[\bar\psi,\psi,U]=S_{\mathrm{F}}^{\mathrm{Wilson}}[\bar\psi,\psi,U]+S_{\mathrm{F}}^{\mathrm{SW}}[\bar\psi,\psi,U]\tag{1.42}$$

The first term is the Wilson fermion action [20] and the second is the counterterm known as the Sheikholeslami-Wohlert or Clover term [21], which can be tuned in order to cancel the $O(a)$ discretisation errors arising from the Wilson fermion action. The lattice fermion action is obtained through the discretisation of the continuum fermion action

$$S_{\mathrm{F}}^{\mathrm{cont}}[\bar\psi,\psi,A_\mu]=\int d^4x\ \bar\psi(x)(\not{D}+m)\psi(x)\tag{1.43}$$

where $\not{D}=\gamma_\mu D_\mu$. In the discretisation known as the naïve discretisation the covariant derivative, D_μ, is replaced by the symmetrised lattice derivative, $\tilde\nabla_\mu=\frac{1}{2}(\nabla_\mu+\nabla_\mu^*)$, where the forward and backward lattice derivatives are given by the finite differences

$$\begin{aligned}\nabla_\mu\psi(x)&=\frac{1}{a}\{U_\mu(x)\psi(x+a\hat\mu)-\psi(x)\}\\ \nabla_\mu^*\psi(x)&=\frac{1}{a}\{\psi(x)-U_\mu^\dagger(x-a\hat\mu)\psi(x-a\hat\mu)\}\end{aligned}\tag{1.44}$$

The symmetrised form is taken to ensure that the action is Hermitian. The naïve fermion action is then

$$S_{\mathrm{F}}^{\mathrm{N}}[\bar{\psi},\psi,U] = \sum_{x,y} \bar{\psi}(x) M^{\mathrm{N}}_{x,y}[U]\psi(y) \tag{1.45}$$

where

$$M^{\mathrm{N}}_{x,y}[U] = m\delta_{x,y} + \frac{1}{2}\sum_{\mu} \gamma_\mu [\delta_{x+\hat{\mu},y} U_\mu(x) - \delta_{x-\hat{\mu},y} U^\dagger_\mu(y)] \tag{1.46}$$

and the lattice spacing has been set equal to unity. Taylor expanding the lattice fermion fields and the gauge links in equation 1.45 appears to give the correct classical continuum limit up to discretisation errors of $O(a^2)$. Unfortunately it gives rise to $2^d = 16$ quark flavours instead of one, where $d = 4$ is the dimension of spacetime. This is most easily seen by examining the quark propagator in the free field case. Setting the gauge fields to the identity matrix, the quark propagator for a free fermion field is given by the inverse of the fermion matrix, as in equation 1.32. Inverting the naïve fermion matrix defined in equation 1.46 by taking the momentum space Fourier transform, the quark propagator is

$$G_{\mathrm{N}}(x,y) = \frac{1}{V}\sum_{p} \frac{e^{ip(x-y)}}{m + i\sum_\mu \gamma_\mu \sin(p_\mu)} \tag{1.47}$$

where the lattice delta function used in the Fourier transform is defined as

$$\delta_{x,y} = \frac{1}{V}\sum_{p} e^{ip(x-y)} \tag{1.48}$$

and V is the lattice volume. The momentum p is periodic with period $2\pi/a$ and is restricted to values in the Brillouin zone defined by

$$\left\{ p \in \mathcal{B} \middle| -\frac{\pi}{a} < p_\mu \leq \frac{\pi}{a} \right\} \tag{1.49}$$

Taking the continuum limit ($a \to 0$) of the propagator in equation 1.47 is equivalent to taking the limits, $m \to 0$ and $p_\mu \to 0$. The resulting pole in the propagator corresponds to an on-shell fermion. However, additional poles in the propagator occur when $p_\mu = \pm\pi$ (where $a = 1$), giving rise to 15 extra fermions - the fermion doubling problem. The doubling problem is not solved by including the gauge fields.

To alleviate this problem, Wilson added a higher order term to the action which gives the fermion doublers a mass proportional to the inverse lattice spacing. This is achieved by adding an additional term corresponding to the lattice discretisation of the second derivative to the discretisation of the covariant derivative

$$\not{D} \rightarrow D_{\mathrm{w}} \equiv \gamma_\mu \tilde{\nabla}_\mu - \frac{ar}{2}\nabla^*_\mu \nabla_\mu, \qquad r = 1 \tag{1.50}$$

which preserves the Hermiticity of the action. The parameter r is usually chosen to be one. The Wilson action is then written as

$$S_{\mathrm{F}}^{\mathrm{Wilson}}[\bar{\psi}, \psi, U] = \sum_{x,y} \bar{\psi}(x) M^{\mathrm{W}}_{x,y}[U] \psi(y) \tag{1.51}$$

where the Wilson fermion matrix is given by

$$M^{\mathrm{W}}_{x,y}[U] = \delta_{x,y} - \kappa \sum_{\mu} \left[\delta_{x+\hat{\mu},y}(1-\gamma_\mu)U_\mu(x) + \delta_{x-\hat{\mu},y}(1+\gamma_\mu)U^\dagger_\mu(y) \right] \tag{1.52}$$

and the fermion fields in the action have been rescaled by making the replacements, $\psi(x) \rightarrow \psi(x)\sqrt{2\kappa}$ and $\bar{\psi}(x) \rightarrow \bar{\psi}(x)\sqrt{2\kappa}$. The hopping parameter, κ, is related to the fermion mass via

$$\kappa = \frac{1}{2m + 8} \tag{1.53}$$

Note that additional flavours of quarks can be simulated by including terms with different hopping parameters in the action. In the continuum limit, the higher order term in the action vanishes and the masses of the fermion doublers become infinite, decoupling from the theory. This can be seen by considering the quark propagator in the free field case for the Wilson fermion action

$$G_{\mathrm{W}}(x,y) = \frac{1}{V}\sum_{p} \frac{e^{ip(x-y)}}{m + \sum_\mu r(1-\cos(p_\mu)) + i\gamma_\mu \sin(p_\mu)} \tag{1.54}$$

where there are no longer poles arising from momenta at the edges of the Brillouin zone in the continuum limit. Unfortunately solving the fermion doubling problem is achieved at the expense of the global chiral symmetry of the action at zero quark mass, (where the fermion fields transform as $\psi(x) = e^{i\alpha\gamma_5}\psi(x)$ and $\bar{\psi}(x) = \bar{\psi}(x)e^{i\alpha\gamma_5}$). Although this is not considered to be a fundamental problem, since in the continuum limit it is expected that chiral symmetry will be restored, it is a big practical problem. Some of the consequences of sacrificing chiral symmetry are discussed in section 1.11. In fact it is not possible to define a Hermitian lattice action which is ultra-local, translationally invariant, preserves chiral symmetry and presents no fermion doublers. This is the statement of the "no-go" theorem by Nielsen and Ninomiya [22]. However, recent developments have meant that it is now possible to preserve chiral symmetry on the lattice at the expense of relaxing the criterion of ultra-locality, by requiring that the lattice discretisation of the Dirac operator, D, satisfies the Ginsparg-Wilson relation [23],

$$\gamma_5 D + D\gamma_5 = aD\gamma_5 D \tag{1.55}$$

The condition of ultra-locality, where the Dirac operator only depends upon the gauge field variables in a finite neighbourhood, is relaxed in order to allow the spatial dependence of the operator to decay exponentially, provided the rate of decay is proportional to the lattice cutoff [24]. If this condition is satisfied, this definition of locality can be considered to be as good as ultra-locality. The major difficulty of simulating fermion actions which satisfy equation 1.55 is the need for further algorithmic developments in order to make numerical simulations feasible.

The Wilson fermion action introduces discretisation errors of $O(a)$. For simulations at relatively coarse lattice spacings, such as the dynamical fermion simulations considered in this thesis, this introduces a potentially unacceptable discretisation error. One way to reduce this error is to add $O(a)$ counter-terms to the action, which can be tuned to reduce the discretisation errors in on-shell quantities. By considering all terms of $O(a)$ which are gauge invariant and respect the discrete symmetries of the lattice, it can be shown [25] that the counter-term can be written in the continuum as a linear combination of five terms which satisfy these requirements. Two of the terms can be eliminated by applying the field equations and a further two amount to a rescaling of the bare parameters of the theory, the strong force coupling and the fermion mass, by a factor proportional to $(1+O(am_{\mathrm{q}}))$, where m_{q} is the quark mass defined in section 1.11. The discretised form of the remaining term is referred to as the Sheikholeslami-Wohlert or Clover term [21]

$$S_{\mathrm{F}}^{\mathrm{SW}}[\bar{\psi},\psi,U] = -c_{\mathrm{sw}}\frac{i\kappa}{2}\sum_{x,\mu,\nu}\bar{\psi}(x)\sigma_{\mu\nu}F_{\mu\nu}(x)\psi(x) \tag{1.56}$$

where $\sigma_{\mu\nu} = \frac{i}{2}[\gamma_\mu,\gamma_\nu]$ and a symmetric definition of the lattice field strength tensor, $F_{\mu\nu}(x)$, is defined by

$$F_{\mu\nu}(x) = \frac{1}{8}(Q_{\mu\nu}(x) - Q^\dagger_{\mu\nu}(x)) \tag{1.57}$$

where $Q_{\mu\nu}(x)$ is the sum of the four plaquettes situated around a lattice site, x, in the plane defined by the lattice directions, μ and ν

$$\begin{aligned} Q_{\mu\nu}(x) &= U_\mu(x)U_\nu(x+\hat{\mu})U^\dagger_\mu(x+\hat{\nu})U^\dagger_\nu(x) \\ &+ U_\nu(x)U^\dagger_\mu(x-\hat{\mu}+\hat{\nu})U^\dagger_\nu(x-\hat{\mu})U_\mu(x-\hat{\mu}) \\ &+ U^\dagger_\mu(x-\hat{\mu})U^\dagger_\nu(x-\hat{\mu}-\hat{\nu})U_\mu(x-\hat{\mu}-\hat{\nu})U_\nu(x-\hat{\nu}) \\ &+ U^\dagger_\nu(x-\hat{\nu})U_\mu(x-\hat{\nu})U_\nu(x+\hat{\mu}-\hat{\nu})U^\dagger_\mu(x) \quad . \end{aligned} \tag{1.58}$$

Pictorially, the field strength tensor resembles a four-leaf clover. The $O(a)$ improved fermion action is then given by

$$S_{\mathrm{F}}[\bar{\psi},\psi,U] = \sum_{x,y}\bar{\psi}(x)M_{x,y}[U]\psi(y) \tag{1.59}$$

where the fermion matrix is defined as

$$\begin{aligned} M_{x,y}[U] &= \delta_{x,y}\left(1 - c_{\text{sw}}\frac{i\kappa}{2}\sum_{\mu,\nu}\sigma_{\mu\nu}F_{\mu\nu}(x)\right) \\ &- \kappa\sum_{\mu}\left[\delta_{x+\hat{\mu},y}(1-\gamma_\mu)U_\mu(x) + \delta_{x-\hat{\mu},y}(1+\gamma_\mu)U_\mu^\dagger(y)\right] \end{aligned} \tag{1.60}$$

The clover coefficient, c_{sw} in the Sheikholeslami-Wohlert term is a function of the bare coupling, g_0, and can be tuned in order to remove the $O(a)$ discretisation errors in on-shell quantities. Two possible choices for c_{sw} obtained from the *tadpole* and *non-perturbative* improvement schemes are discussed below.

1.9 Tadpole improvement

The gauge links, defined by equation 1.18, can be Taylor expanded in terms of the continuum gauge fields for small a to yield

$$U_\mu(x) \to 1 - aA_\mu(x) + \ldots = 1 + iag_0A_\mu^a(x)T^a + \ldots \tag{1.61}$$

where corrections to this relation would appear to vanish as powers of a. Unfortunately, this is not the case in the quantum theory [26]. Instead, when pairs of gauge fields present in higher order terms in the expansion are contracted together they generate tadpole contributions which exactly cancel the powers of a. These ultraviolet divergences, arising from momenta of the order of the lattice cutoff, mean that higher order terms in the expansion of equation 1.18 are only suppressed by powers of g_0^2. The large contribution from the tadpoles has the effect of renormalising the gauge links. In order to take account of this, the tadpole improvement scheme described in [26] advocates replacing the gauge links that appear in the lattice action and operators with

$$U_\mu(x) \to U_\mu(x)/u_0, \qquad u_0 < 1 \tag{1.62}$$

where u_0 is the mean field parameter representing the mean value of the gauge link. The mean value of a gauge link cannot be measured directly since the expectation value of the gauge dependent link variables vanishes. Instead, a gauge invariant choice for u_0 can be obtained by considering the expectation value of the plaquette

$$u_0 \equiv \left\langle \frac{1}{3}\Re\mathrm{eTr}U_\Box \right\rangle_U^{1/4} \tag{1.63}$$

Other choices for u_0, such as the expectation value of a gauge link measured in a gauge fixed lattice simulation where the (continuum) Landau gauge fixing condition, $\partial_\mu A_\mu = 0$, transcribed on the lattice has been used [27], have not been considered in this thesis. Replacing the gauge links by the tadpole improved links amounts to rescaling the free parameters in the lattice action

$$g_0 \to g_0/u_0^2 \equiv g, \qquad \kappa \to \kappa u_0 \tag{1.64}$$

where g is the "boosted" coupling. From these replacements, the clover coefficient is redefined as

$$c_{\mathrm{sw}} \to c_{\mathrm{sw}}/u_0^3 = 1/u_0^3 \tag{1.65}$$

where the original value of c_{sw} is taken to be the tree-level value of unity [21]. The tadpole improvement procedure is expected to reduce the $O(ag_0^2)$ discretisation errors present in the tree-level improved fermion action.

1.10 Non-perturbative improvement

The non-perturbative improvement scheme, discussed in [9, 25, 28, 29, 30], aims to completely eliminate the discretisation errors of $O(a)$ in on-shell quantities through improving the action and the operators non-perturbatively. Full $O(a)$ improvement of the action is achieved by choosing the clover coefficient appropriately. The clover coefficient is determined by requiring that the measured violation of chiral symmetry resulting from the Wilson fermion action is of $O(a^2)$.

In the limit of degenerate, massless quarks, chiral flavour symmetry in the continuum is spontaneously broken. As a consequence of the breaking of the $SU(2)$ axial isospin symmetry for the u and d quarks, the π's are identified as the three massless Goldstone bosons of the theory. However, physical quarks have a small mass and thus the π's are no longer true Goldstone bosons but "pseudo-Goldstone bosons". This explicit breaking of the symmetry means that the associated conserved current in the massless case is replaced by the partially conserved axial current (PCAC) relation

$$\partial_\mu A^i_\mu(x) = 2m_{\mathrm{PCAC}} P^i(x) \tag{1.66}$$

defined in the continuum, where m_{PCAC} is the unrenormalised current quark mass (the determination of which is described later in section 3.3). The isovector axial current and pseudoscalar density are given by

$$A^i_\mu(x) = \bar{\psi}(x)\gamma_\mu\gamma_5\frac{\tau^i}{2}\psi(x), \qquad P^i(x) = \bar{\psi}(x)\gamma_5\frac{\tau^i}{2}\psi(x) \tag{1.67}$$

where the Pauli matrices, τ^i, act on the flavour indices of the fermion fields. The index $i = 1, 2, 3$ is referred to as the isospin index. In the Wilson fermion formulation, correction terms of $O(a)$ arise in the lattice discretisation of equation 1.66, where the details of the discretisation are given later in section 3.3. The improvement scheme then requires that these lattice artifacts in the discretisation of the PCAC relation are reduced to $O(a^2)$. This can be achieved by eliminating the errors of $O(a)$ present in the determination of m_{PCAC} by tuning the improvement coefficients in the Clover term of the action and in the lattice axial current operator. The strategy used to determine the improvement coefficients is outlined in [25, 30]. In this case, the PCAC mass was measured in the Schrödinger functional scheme in which Dirichlet boundary conditions are imposed in the time direction of the lattice. The improvement coefficients were determined by requiring that the PCAC mass was independent of the kinematical parameters (such as the temporal insertion point of the axial current, x_4, and the external fields employed in the Dirichlet boundary conditions) up to terms of $O(a^2)$. This is equivalent to minimising the difference in the results obtained for the PCAC mass for two sets of kinematical parameters, A and B

$$m^A_{\mathrm{PCAC}} - m^B_{\mathrm{PCAC}} = O(a) \tag{1.68}$$

by tuning the improvement coefficients. In practice, a third value of m_{PCAC} was considered as two improvement coefficients were determined.

In section 1.8, it was noted that the full $O(a)$ improvement of the fermion action required the rescaling of the strong coupling constant and bare quark mass by a factor proportional to $(1+O(am_{\mathrm{q}}))$. This rescaling of the bare parameters is required in order that a mass independent renormalisation scheme which is consistent with $O(a)$ improvement can be defined [25], and hence spectral quantities approach the continuum limit with a rate proportional to $O(a^2)$. The improved coupling constant and bare quark mass are defined by

$$\widetilde{m}_{\mathrm{q}} = m_{\mathrm{q}}(1 + b_{\mathrm{m}}(g_0^2)m_{\mathrm{q}}), \qquad \widetilde{g}_0^2 = g_0^2(1 + b_{\mathrm{g}}(g_0^2)m_{\mathrm{q}}) \tag{1.69}$$

where b_{m} and b_{g} are improvement coefficients which can be tuned in order to cancel the residual lattice artifacts of $O(am_{\mathrm{q}})$. Note that in the quenched approximation, $b_{\mathrm{g}} = 0$, (since in the quenched case observables composed entirely from gluon fields which are improved at zero quark mass are also improved at non-zero quark mass [25]) where to one-loop in perturbation theory [31, 32]

$$b_{\mathrm{g}} = 0.012N_{\mathrm{f}}g_0^2 + O(g_0^4) \tag{1.70}$$

where N_{f} is the number of dynamical quark flavours. For the $N_{\mathrm{f}} = 2$ dynamical fermion simulations the improvement of the coupling was neglected. The statistical accuracy of the dynamical fermion data considered here is not sufficient to observe any noticeable effects arising from the very small improvement in the bare coupling. The values for all the improvement coefficients used in this thesis are specified in the following chapters as required.

1.11 Chiral limit

In section 1.8, it was noted that chiral symmetry is explicitly broken by the Wilson fermion action when $a \neq 0$, even in the limit of vanishing quark mass. In addition to the $O(a)$ correction terms appearing in the PCAC relation for the unimproved action, as discussed in section 1.10, this means that the fermion mass, m, is additively (as well as multiplicatively) renormalised. The bare quark mass is then defined by

$$m_{\mathrm{q}} = m - m_{\mathrm{c}} \tag{1.71}$$

where m_{c} is a constant which must be determined from the simulation. In terms of the hopping parameter, defined in equation 1.53, the bare quark mass is defined as

$$m_{\mathrm{q}} = \frac{1}{2}\left(\frac{1}{\kappa} - \frac{1}{\kappa_{\mathrm{crit}}}\right) \tag{1.72}$$

where κ_{crit}, the critical value of the hopping parameter, depends on the lattice spacing. The value of κ_{crit} for each lattice simulation was determined in two ways by extrapolating two different quantities, the pseudoscalar meson mass and the PCAC mass, measured at several unphysical values of the quark mass. In each case an extrapolation to the chiral limit at zero quark mass was performed. The form of the extrapolations are given later in section 3.9.

The critical value of the hopping parameter is measured through a statistical average over an ensemble of configurations. This means that the value of κ_{crit} for individual configurations will be distributed about the mean value. As a consequence, it is possible that $\kappa \simeq \kappa_{\mathrm{crit}}$ for some configurations in the ensemble, particularly if small quark masses are considered. These configurations, where the fermion matrix has a zero mode, are referred to as exceptional configurations. (Other factors which contribute to the incidence of exceptional configurations are discussed later in section 3.1). In dynamical fermion simulations the occurrence of exceptional configurations in the configuration generation procedure is suppressed by the factor $\det M$. However, this is not the case in the quenched approximation. Exceptional configurations in the quenched simulations considered here are discussed further in section 3.1.

Once the bare quark mass has been defined in terms of κ_{crit}, the quark masses measured at the physical masses of the light mesons can be determined, as discussed later in section 3.10, and the physical masses of the lightest hadrons in lattice units can be calculated. The final stage in the lattice calculation is then to determine the hadron masses in physical units by taking the *continuum limit.*

1.12 Continuum limit

In section 1.4.3, the addition of higher order terms in the lattice spacing to the action was permitted provided the continuum action was reached in the limit $a \to 0$, known as the classical continuum limit. This section contains a brief discussion of the main conditions required in order that the lattice theory can be used to extract continuum physics at finite values of the lattice spacing. Further details can be found in [6].

Observables measured on the lattice (such as the hadron masses) are expressed in terms of the lattice spacing. Since the only free parameters in the theory are the strong coupling and the quark masses, the lattice spacing is not known *a priori.* This means that physical predictions from the lattice are made by considering dimensionless ratios of observables. For the correct continuum limit to be reached these dimensionless ratios of observables should be independent of the lattice spacing and, in particular, the lattice masses should vanish in such a way that the corresponding mass in physical units remains finite as the lattice spacing is taken to zero. This occurs for simulations near criticality, where the lattice correlation length, ξ (which is inversely related to the mass of a typical hadron in the simulation), diverges. At this point, where $\xi \gg a$, the theory no longer "sees" the underlying structure of the lattice as required in the continuum limit. In the case of massless quarks, the critical point is reached by tuning the strong coupling, g_0 (or equivalently β), to the critical value, $g_0^{\rm crit}$, defined at the point where the correlation length diverges. This means that the coupling can be expressed as a function of the lattice spacing. (When massive quarks are considered there is an additional dependence upon the κ values).

In the case of massless quarks, a generic hadron mass in lattice units, $m_{\rm H}$, at the physical quark masses measured on a particular lattice simulation, depends on β and hence g_0. The physical value of the hadron mass, $M_{\rm H}$, obtained by setting the lattice scale, is defined by

$$M_{\mathrm{H}}(g_0, a) = m_{\mathrm{H}}(g_0)/a \tag{1.73}$$

where M depends on both the coupling and the lattice spacing. The physical mass in the continuum limit, $M_{\mathrm{H}}^{\mathrm{phys}}$, can be reached in the limit $a \to 0$

$$\lim_{a \to 0} M_{\mathrm{H}}(g_0, a) = M_{\mathrm{H}}^{\mathrm{phys}} \tag{1.74}$$

provided $g_0(a)$ is a well defined function of a which tends to the critical value of the coupling, g_0^{crit} in the limit. For QCD the critical value of the coupling occurs at $g_0^{\mathrm{crit}} = 0$ due to asymptotic freedom, or in terms of the lattice parameters, as $\beta \to \infty$. From the discussion above, the functional dependence of the coupling on the lattice spacing depends on the choice of observable. However, if the lattice spacing is sufficiently small a region of parameter space exists where a universal function can be defined for $g_0(a)$. This region of parameter space is known as the *scaling region.*

Lattice simulations are said to be in the scaling region, $\mathcal{S}$, if dimensionless mass ratios measured on lattices with different lattice spacings give the same result

$$\frac{m_1(g_0)}{m_2(g_0)} = \frac{m_1(g_0')}{m_2(g_0')} = \text{constant}, \qquad g_0,\ g_0' \in \mathcal{S} \tag{1.75}$$

where g_0 and g_0' label two simulations in the scaling region. In practice, residual lattice artifacts will result in scaling violations. The improvement programme, discussed in section 1.6, aims to reduce the scaling violations in order that simulations from a wider range of β values can be considered to lie in the scaling region. In the scaling region, lattice hadron masses can be parametrised in terms of a dimensionless constant c and their functional dependence on the strong coupling. If the functional dependence on the coupling, $f(g_0)$, is the same for two different lattice masses, denoted by m_1 and m_2

$$m_i(g_0) = c_i f(g_0) \equiv c_i \Lambda_{\mathrm{Lat}} a, \qquad i = 1, 2 \tag{1.76}$$

then the simulation is said to be in the scaling region of parameter space. As a consequence of requiring that the observables are independent of the lattice cutoff, π/a, a mass scale, Λ_{Lat}, is introduced through a process known as dimensional transmutation.

The introduction of a mass scale is not unique to the lattice formulation, but parametrises the asymptotic freedom property of QCD. In order that the QCD Lagrangian simultaneously explains the high energy and the low energy behaviour, the functional dependence on the coupling in the lattice theory is defined from the renormalisation group equation

$$\left[a\frac{\partial}{\partial a} - \beta_{\mathrm{Lat}}(g_0)\frac{\partial}{\partial g_0} - \gamma_{\mathrm{Lat}}(g_0, m_{\mathrm{q}})\frac{\partial}{\partial m_{\mathrm{q}}}\right] \mathcal{O}(a, g_0, m_{\mathrm{q}}) = 0 \tag{1.77}$$

where $\mathcal{O}(a, g_0, m_{\mathrm{q}})$ is an observable measured in physical units. Note that the dependence on the bare mass of one flavour of quark has now been included. The lattice β-function and γ-function are defined by,

$$\beta_{\mathrm{Lat}}(g_0) = -a\frac{\partial g_0}{\partial a} = -\beta_0 g_0^3 - \beta_1 g_0^5 + \ldots \tag{1.78}$$

$$\gamma_{\mathrm{Lat}}(g_0) = -a\frac{\partial m_{\mathrm{q}}}{\partial a} = -d_0 g_0^2 m_{\mathrm{q}} + \ldots \tag{1.79}$$

where the coefficients of the β-function and γ-function have been determined in perturbation theory [33, 34, 35, 36, 37]. In the quenched approximation, where the number of dynamical quark flavours is assumed to be zero ($N_{\mathrm{f}} = 0$), they are given by

$$\beta_0 = 11/16\pi^2, \qquad \beta_1 = 102/(16\pi^2)^2, \qquad d_0 = 8/16\pi^2 \tag{1.80}$$

The β-function in equation 1.78 can be integrated to yield the following expression for Λ_{Lat} which parametrises the dependence of the coupling on the lattice spacing

$$\Lambda_{\mathrm{Lat}} = \frac{1}{a}\exp\left(-\frac{1}{2\beta_0 g_0^2}\right)(\beta_0 g_0^2)^{-\beta_1/(2\beta_0^2)}[1 + O(g_0^2)] \tag{1.81}$$

where Λ_{Lat} arises as an integration constant. Lattice simulations where Λ_{Lat} is given by equation 1.81 are said to be in the *asymptotic scaling* region. This is the region in parameter space where lattice simulations should ideally be performed. Equation 1.81 is related to the phenomenon of asymptotic freedom and describes how the coupling runs as the energy scale (defined by the lattice spacing) is varied. Note that the strong coupling is usually expressed in terms of $\alpha_{\rm s}$, where $\alpha_{\rm s} \equiv g_0^2/4\pi$. In theory, $\Lambda_{\rm Lat}$, can be measured on the lattice and compared with the perturbative expression in equation 1.81 in order to assess the scaling violations and ensure that a reliable extrapolation to the continuum limit can be performed. In practice, several lattice simulations are performed for different lattice spacings in the scaling region and dimensionless mass ratios are then extrapolated to the limit $a \to 0$ where the scale is set by comparing one of the hadron masses with its experimentally measured value. The details of the continuum extrapolations performed with the data from the quenched simulations are discussed in section 3.12.

The γ-function defined in equation 1.79 can be integrated to yield the renormalisation group invariant quark mass, M

$$M = m_{\rm q}(2\beta_0 g_0^2)^{-d_0/(2\beta_0)}[1 + O(g_0^2)] \tag{1.82}$$

which describes how the current quark masses run with the coupling. This expression is used in section 3.10.1 where the determination of the renormalised current quark masses from the quenched simulations is discussed.

1.13 Overview of thesis

In chapter 2, the construction of hadron correlators on the lattice is discussed, and the fit procedures used in this thesis to determine the light hadron masses from the hadron correlators are described. Chapter 3 presents the results of the light hadron spectrum determined from simulations employing the quenched approximation. The physical masses of the pseudoscalar and vector mesons, and the octet and decuplet baryons, are determined in the continuum limit from data sets at three values of the lattice spacing. The effect of the $O(a)$ improvement of the fermion action on the scaling behaviour of ratios of lattice masses at different lattice spacings is investigated. A comparison of the scaling behaviour was made between simulations using the two improvement schemes described in sections 1.9 and 1.10. The error due to finite size effects is examined for one value of β. Results for the ratio of the strange and "normal" current quark masses are presented, where the normal quark mass is defined as the average of the up and down quark masses.

Chapter 4 presents the first results for the light hadron spectrum obtained from a matched ensemble of data sets with $N_\mathrm{f} = 2$ dynamical fermions. The results are compared with a data set in the quenched approximation at the same lattice spacing. Comparisons were made with a simulation with a lighter dynamical fermion mass at a slightly smaller lattice spacing. The evidence for quark loops effects in the light hadron spectrum is examined. Evidence of dynamical effects observed in other quantities measured on the matched ensemble, such as the static quark potential, is reviewed. The final chapter summarises the conclusions obtained from the results presented in the previous chapters.

Chapter 2

Hadron masses from correlation functions

This chapter discusses the methods used in this thesis to extract the lattice values of the hadron masses from Euclidean *correlation functions.* First, the construction of the correlators from interpolating quantum field operators is described, and the generation of the correlators on the lattice is discussed. The *smearing* and *fuzzing* techniques, used to improve the overlap with the ground state with respect to the excited states, are introduced. The relationship between the hadron masses and the behaviour of the correlators at large times is presented. The types of fit investigated are then described and finally the general fit procedure and selection criteria for the best fit are outlined.

2.1 Correlation functions

Euclidean correlation functions, or correlators, are defined in terms of vacuum expectation values of time ordered products of quantum field operators. Hadron masses are determined from examining the large time behaviour at zero three-momentum of the particular type of correlators known as *two-point functions.* A two-point function (which shall be considered to be the correlator which is referred to throughout this thesis), $C(\boldsymbol{x}, t)$, is defined to be the vacuum expectation value of the time ordered product of the interpolating quantum field operators

$$C(\boldsymbol{x}, t) = \langle 0| \hat{\mathcal{T}} \left\{ \mathcal{O}(x) \mathcal{O}^\dagger(0) \right\} |0\rangle \tag{2.1}$$

The interpolating operators represent the hadron under study, created at the origin by the source operator, $\mathcal{O}^\dagger(0)$, and annihilated at some other point in spacetime by the sink operator, $\mathcal{O}(x)$. Each operator is chosen to have the same colour, spin, valence quark content and parity as the hadron it represents. The source operator acting on the vacuum creates a state which is a linear combination of all the eigenstates of the Hamiltonian with the same quantum numbers, including excited states of the hadron state in question. Many such operators can be formed and the local operators used in this thesis are detailed in section 2.2 (operators which include a dependence on the spatial distribution of the hadron wavefunction are considered later in section 2.4). The main selection criterion for the interpolating operators is that they should have a non-zero overlap with the hadron state

$$\langle 0| \mathcal{O}(x) |n, \boldsymbol{p}\rangle \neq 0 \tag{2.2}$$

while minimising the overlap with the excited states.

2.2 Interpolating operators for mesons and baryons

Interpolating operators must possess the same quantum numbers as the hadron under study. Meson operators with the correct colour, spin and parity can be written generically in a form bilinear in the quark field operators [38]

$$\mathcal{O}_{\mathrm{M}}(x) = \bar{\psi}_a(x)\Gamma\psi_a(x) \tag{2.3}$$

where Γ represents one of the 16 possible Dirac gamma matrix combinations which lead to a operator invariant under the residual hypercubic symmetry of the lattice and a labels the colour index. The Dirac spinor and flavour indices have been suppressed for clarity. Table 2.1 shows the local operators corresponding to the pseudoscalar and vector mesons used in this thesis. (The axial pseudoscalar operator is required for later use in the determination of the partially conserved axial current mass). Considering only the lightest flavours of quark, up, down and strange (u, d and s), correlators constructed from these operators can be used to determine the masses of the pseudoscalar mesons (π and K) and the vector mesons (ρ, K* and ϕ). Note that electromagnetic effects are neglected. Baryon

Lightest meson	J^{PC}	Operator	Channel
$\pi^0(135)$	0^{-+}	$P(x) = \bar{\psi}_a(x)\gamma_5\psi_a(x)$ $A_4(x) = \bar{\psi}_a(x)\gamma_4\gamma_5\psi_a(x)$	Pseudoscalar Axial pseudoscalar
$\rho(770)$	1^{--}	$V_i(x) = \bar{\psi}_a(x)\gamma_i\psi_a(x)$	Vector
Lightest baryon	$I(J^P)$	Operator	Channel
$N(940)$	$\frac{1}{2}(\frac{1}{2}^+)$	$(\psi_a^T(x)C\gamma_5\psi_b(x))\psi_c^\alpha(x)\varepsilon_{abc}$ $(\psi_a^T(x)C\gamma_4\gamma_5\psi_b(x))\psi_c^\alpha(x)\varepsilon_{abc}$	Nucleon
$\Delta(1232)$	$\frac{3}{2}(\frac{3}{2}^+)$	$(\psi_a^T(x)C\gamma_\mu\psi_b(x))\psi_c^\alpha(x)\varepsilon_{abc}$	Delta

Table 2.1: Interpolating operators used in this thesis and the corresponding lightest hadron state. The spin, parity and charge conjugation properties of the operator are shown. The index i runs from 1 to 3 and μ from 1 to 4. Note that charge conjugation is only defined for neutral mesons.

operators are formed from three quark fields and take the general form

$$\mathcal{O}_{\mathrm{B}}^\alpha(x) = (\psi_a^T(x)C\Gamma\psi_b(x))\psi_c^\alpha(x)\varepsilon_{abc} \tag{2.4}$$

where a, b, c are colour indices, α is the free spinor index and the flavour indices have been suppressed. Note that ε_{abc} is the totally anti-symmetric colour tensor. The charge conjugation matrix, $C = \gamma_4\gamma_2$, transforms a quark field to an anti-quark field while retaining the same spin orientation. This baryon operator does not have a well defined parity and in fact couples to both parity states. The operator can be modified by multiplication with the Dirac projection operator, $\frac{1}{2}(1+\gamma_4)$, which projects out the positive parity state studied here. The negative parity state is similarly obtained by multiplication with the operator, $\frac{1}{2}(1-\gamma_4)$. In practice the positive parity correlator (denoted by C_{B}^+) is obtained from the baryon correlator by averaging over the (11) and (22) free spinor indices. Similarly the correlator corresponding to the negative parity state, C_{B}^-, can be obtained by averaging the (33) and (44) indices.

Table 2.1 shows the baryon operators examined in this thesis. The delta baryon operator contains both a spin-$\frac{3}{2}$ and a spin-$\frac{1}{2}$ state [38]. In order for this operator to represent the spin-$\frac{3}{2}$ decuplet baryons, the spin-$\frac{3}{2}$ component is projected out by noting that the delta correlator created by the operator with $\gamma_\mu = \gamma_4$ is a pure spin-$\frac{1}{2}$ state. The spin-$\frac{3}{2}$ part of the delta correlator is then obtained by averaging over the correlators constructed from the three spatial gamma matrices, γ_i, and subtracting the delta spin-$\frac{1}{2}$ correlator. This is performed after the projection onto definite parity states described above. Note that the delta operator is flavour symmetric under the interchange of any two quarks. If non-degenerate combinations of quark flavours are considered, this operator can be used to study the Δ, Σ^*, Ξ^* and Ω decuplet baryons.

The nucleon baryon operators in Table 2.1 are used to construct correlators corresponding to the spin-$\frac{1}{2}$ octet baryons. The octet correlators are harder to construct due to flavour symmetry considerations in the first two quarks, the full details of which can be found in [39, 40, 41]. Basically, the octet baryon operators are composed from a linear combination of the general operator, chosen to have the appropriate flavours of quarks which make the flavour symmetry of the baryon explicit. Examples of the octet baryon operators, taken from [40], are shown below

$$\begin{aligned}
\mathcal{O}^{\alpha}_{\mathrm{N}}(x) &= \sqrt{2}\{(d^{\mathrm{T}}_a(x)C\gamma_5 u_b(x))d^{\alpha}_c(x) + (d^{\mathrm{T}}_a(x)C\gamma_5 d_b(x))u^{\alpha}_c(x)\}\varepsilon_{abc} && (2.5)\\
\mathcal{O}^{\alpha}_{\Sigma^0}(x) &= -\{(s^{\mathrm{T}}_a(x)C\gamma_5 u_b(x))d^{\alpha}_c(x) + (s^{\mathrm{T}}_a(x)C\gamma_5 d_b(x))u^{\alpha}_c(x)\}\varepsilon_{abc} && (2.6)\\
\mathcal{O}^{\alpha}_{\Lambda^0}(x) &= \frac{1}{\sqrt{3}}\{(u^{\mathrm{T}}_a(x)C\gamma_5 d_b(x))s^{\alpha}_c(x) + (u^{\mathrm{T}}_a(x)C\gamma_5 s_b(x))d^{\alpha}_c(x) \\
&- (d^{\mathrm{T}}_a(x)C\gamma_5 s_b(x))u^{\alpha}_c(x) - (d^{\mathrm{T}}_a(x)C\gamma_5 u_b(x))s^{\alpha}_c(x)\}\,\varepsilon_{abc} && (2.7)
\end{aligned}$$

These symmetrised forms have been used in order to project against the flavour singlet state and the relative normalisation is governed by the $SU(3)$ flavour symmetry. Note that the sign of each term flips under the interchange of the quark fields in parentheses. The spin-$\frac{1}{2}$ octet correlators are split into two main types, "sigma-like" (used to study the N, Σ and Ξ baryons) and "lambda-like"(used to study the Λ baryon), referred to by the labels sigma and lambda respectively. The operators used to construct the sigma/lambda correlators are flavour symmetric/anti-symmetric under the interchange of the first two quarks. Although created from linear combinations of the same basic operator, the symmetry conditions enforce different contractions between the quark fields which result in the appropriate correlator. This can be seen more clearly in the next section which describes the construction of correlators from hadron operators.

2.3 Hadron correlators from quark propagators

Once a choice of hadron operator has been made, the corresponding correlator can then be constructed. This section describes how this is achieved, by using the generic meson operator as an example. The correlator is obtained by substituting the meson operator defined in equation 2.3 into equation 2.1

$$C_{\mathrm{M}}(\boldsymbol{x},t) = \langle 0|\,\hat{\mathcal{T}}\left\{\bar{\psi}^{\alpha}_{a}(x)\Gamma^{\alpha\beta}\psi^{\beta}_{a}(x)\bar{\psi}^{\delta}_{b}(0)(\gamma_4\Gamma^{\dagger}\gamma_4)^{\delta\gamma}\psi^{\gamma}_{b}(0)\right\}|0\rangle \tag{2.8}$$

where the spinor (Greek) and colour (Latin) indices have been shown. Integrating out the fermions gives the following trace over the spin and colour indices

$$C_{\mathrm{M}}(\boldsymbol{x},t) = \left\langle -\mathrm{Tr}_{\mathrm{sc}}\left\{G^{\gamma\alpha}_{ba}(0,x;U)\Gamma^{\alpha\beta}G^{\beta\delta}_{ab}(x,0;U)(\gamma_4\Gamma^{\dagger}\gamma_4)^{\delta\gamma}\right\}\right\rangle_U \tag{2.9}$$

where the minus sign arises from the anti-commuting nature of the fermion fields and $\langle\rangle_U$ denotes the average over the gauge field configurations. Here $G^{\alpha\beta}_{ab}(x,0;U)$ is the quark propagator evaluated on each gauge configuration. If the quark fields in equation 2.8 all have the same flavour an additional contraction of the fermion fields is possible

$$\left\langle \mathrm{Tr}_{\mathrm{sc}}\left\{G^{\beta\alpha}_{aa}(x,x;U)\Gamma^{\alpha\beta}\right\}\mathrm{Tr}_{\mathrm{sc}}\left\{G^{\gamma\delta}_{bb}(0,0;U)(\gamma_4\Gamma^{\dagger}\gamma_4)^{\delta\gamma}\right\}\right\rangle_U \tag{2.10}$$

For the flavour non-singlet mesons considered here (e.g. $\pi^0 = \bar{u}u - \bar{d}d$) these disconnected terms will largely cancel, assuming the approximate flavour symmetry of the vacuum [16]. (Indeed, these terms exactly cancel in this example since $m_{\mathrm{u}} = m_{\mathrm{d}}$ in the lattice simulation). For this reason, terms of this type have been neglected. Expression 2.9 can then be simplified by using the Hermiticity relation for quark propagators

$$G^{\gamma\alpha}_{ba}(0,x;U) = \gamma_5^{\gamma\epsilon} G^{\dagger\epsilon\zeta}_{ba}(x,0;U)\gamma_5^{\zeta\alpha} \tag{2.11}$$

where the adjoint (†) is defined with respect to the spinor and colour indices, to yield the final expression for the meson correlator

$$C_{\mathrm{M}}(\boldsymbol{x},t) = \left\langle -\mathrm{Tr}_{\mathrm{sc}}\left\{\gamma_5 G^{\dagger}(x,0;U)\gamma_5 \Gamma G(x,0;U)(\gamma_4\Gamma^{\dagger}\gamma_4)\right\}\right\rangle_U \tag{2.12}$$

The indices have now been suppressed for clarity. The correlator is then evaluated by performing the trace over the quark propagators and appropriate Γ matrices. A schematic diagram of the trace is shown in the meson contraction diagram in Figure 2.1.

Baryon correlators are similarly constructed from quark propagators, summed with the relevant spin and colour contractions. As an example, consider the nucleon correlator

$$C_{\mathrm{N}}(\boldsymbol{x},t) = \left\langle \mathrm{Tr}_{\mathrm{s}}\left[\mathcal{F}(G_d, G_u, C\gamma_5 G_d (C\gamma_5)^{\dagger})\right] + \ldots\right\rangle_U \tag{2.13}$$

where only the contribution from the first term in the operator defined in equation 2.5 has been written explicitly. The function, $\mathcal{F}$, is defined following the notation of [42, 43] by

$$\begin{aligned}\mathcal{F}(G_{f_1}, G_{f_2}, G_{f_3}) &= \varepsilon_{abc}\varepsilon_{a'b'c'}\Big\{G^{aa'}_{f_1}(x,0;U)\mathrm{Tr}_{\mathrm{s}}\left[G^{bb'}_{f_2}(x,0;U)G^{cc'\mathrm{T}}_{f_3}(x,0;U)\right] \\ &+ G^{aa'}_{f_1}(x,0;U)G^{cc'\mathrm{T}}_{f_3}(x,0;U)G^{bb'}_{f_2}(x,0;U)\Big\}\end{aligned} \tag{2.14}$$

where the colour quantum numbers are labelled by the Latin indices and f_i, $i = 1, 2, 3$ labels the flavour of the quark propagator. Diagrams a) and b) in Figure 2.1 show schematic depictions of each term in equation 2.14. Note that the trace over the spin and colour indices, as defined in 2.13, has still to be taken in order to obtain the baryon correlator. This would correspond to contracting the filled circles in the diagram together at both the source and the sink in order to form a two-point function. The other baryons are constructed similarly.

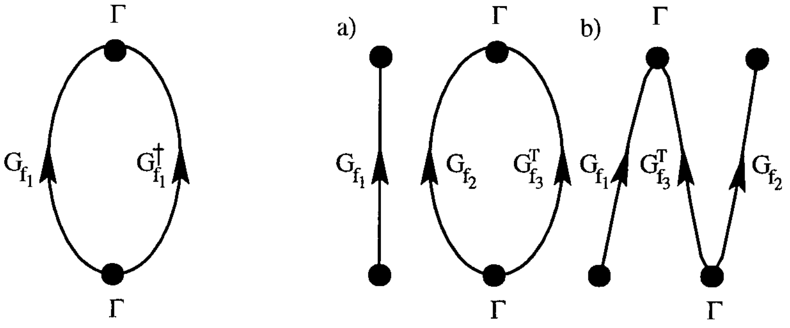

Meson Contraction

Baryon contractions

Figure 2.1: Schematic diagrams of meson and baryon contractions formed by taking the trace over the spin and colour indices. Each line represents a quark propagator, $G(x, 0; U)$, where the flavour is labelled by f_i. The Γ's denote the insertion points for the Dirac γ matrices. Note that figures a) and b) correspond to each term in the intermediate stage, defined in equation 2.14, of the contraction to form the baryon correlator. The trace over the spin and colour indices must be performed in order to obtain the baryon correlator defined in equation 2.13.

On the lattice, the correlator (as defined in equation 2.12 for a meson) is measured on each gauge configuration in the statistical ensemble, where the quark propagators are computed by inverting the fermion matrix. In order to obtain a Monte Carlo estimate, defined in equation 1.36, of the true hadron correlator, correlators evaluated on each gauge configuration are averaged. In practice, the discrete momentum space Fourier transform of the correlator on each gauge configuration is taken (known as time slicing) and then the correlators are averaged over all configurations.

2.4 Smearing

The previous section has shown how local hadron operators can be used to create correlators composed from quark propagators. However, in section 2.1 it was suggested that hadron operators should ideally be selected in order to maximise the overlap with the hadron state under examination. This can be achieved by modifying some or all of the fermion fields in the operator by making the appropriate replacements

$$\psi(\boldsymbol{x},t) \to \sum_{\boldsymbol{y}} S'(\boldsymbol{x},\boldsymbol{y})\psi(\boldsymbol{y},t), \qquad \bar{\psi}(\boldsymbol{x},t) \to \sum_{\boldsymbol{y}} \bar{\psi}(\boldsymbol{y},t)S(\boldsymbol{y},\boldsymbol{x}) \tag{2.15}$$

where the smearing functions, S or S' model the spatial distribution of the hadron wavefunction. Note that S and S' can be different. The *smeared* fermion fields result in a modification of the quark propagator in the background gauge field, $G(x,0;U)$. In order to show the explicit time dependence of the propagator, the notation $G_U(\boldsymbol{x},t;0) \equiv G(x,0;U)$ in used in this section, where the subscript U indicates that the propagator is evaluated on each gauge configuration. The smeared propagator is then

$$G_U^{\mathrm{SS}}(\boldsymbol{x},t;0) = \frac{1}{Z}\int \mathcal{D}\bar{\psi}\mathcal{D}\psi S'(\boldsymbol{x},\boldsymbol{y})\psi(\boldsymbol{y},t)\bar{\psi}(\boldsymbol{z},0)S(\boldsymbol{z},0)e^{-S_{\mathrm{F}}[\bar{\psi},\psi,U]} \tag{2.16}$$

where Z is given by the integral in equation 1.30. The label SS denotes that both the source and the sink of the propagator are smeared. Note that the dependence of the smearing functions on the gauge configurations is implicit. Equation 2.16 can be written as

$$G_U^{\mathrm{SS}}(\boldsymbol{x},t;0) = \sum_{\boldsymbol{y}} S'(\boldsymbol{x},\boldsymbol{y})G_U^{\mathrm{SL}}(\boldsymbol{y},t;0) \tag{2.17}$$

where the source smeared propagator, $G_U^{\mathrm{SL}}(\boldsymbol{y},t;0)$, is expressed in terms of the local propagator, $G_U(\boldsymbol{y},t;\boldsymbol{z},0)$, by

$$G_U^{\mathrm{SL}}(\boldsymbol{y},t;0) = \sum_{\boldsymbol{z}} G_U(\boldsymbol{y},t;\boldsymbol{z},0)S(\boldsymbol{z},0) \tag{2.18}$$

Since the local propagator is derived from the inverse of the fermion matrix, the source smeared correlator on each configuration is then obtained by solving the matrix equation

$$\sum_{\boldsymbol{y}} M_U(\boldsymbol{z},t';\boldsymbol{y},t)G_U^{\mathrm{SL}}(\boldsymbol{y},t;0) = S(\boldsymbol{z},0)\delta_{t',0} \tag{2.19}$$

where $M(z,y;U)$ is the fermion matrix defined in equation 1.60. (Note that this equation is used to obtain the local propagator if the smearing function, S, is replaced by $\delta_{\mathbf{z},0}$). Correlators constructed from propagators which are smeared are found to be statistically noisier than local correlators, thus propagators smeared at only the source or only the sink have been included in the analysis. All that is needed now is an appropriate smearing function. One choice of function can be obtained via the *Jacobi smearing* procedure.

2.5 Jacobi smearing

Jacobi smearing [44] is used to obtain a smearing function which approximates the spherically symmetric ground state wavefunction of the hadron. The procedure is a variant of the Wuppertal iterative scheme applied to Wuppertal scalar propagator smearing [45]. One advantage of this smearing method is that it creates a gauge invariant smearing function and hence there is no need to fix the gauge. In the Wuppertal scalar propagator scheme, the quark propagators are smeared by choosing S in equation 2.19 to be the three dimensional scalar propagator. For free scalar field theory in the continuum, the scalar propagator takes the form of an exponential

$$\langle 0|\,\Phi(\boldsymbol{x})\Phi(\mathbf{0})\,|0\rangle \propto \frac{1}{|\boldsymbol{x}|}e^{-m|\boldsymbol{x}|} \tag{2.20}$$

where m is the mass of the scalar field. Since this form is spherically symmetric and vanishes as $|\boldsymbol{x}| \to \infty$, it is then expected that the lattice scalar propagator can be used to approximate the ground state wavefunction. On the lattice the scalar propagator, S, is determined by solving the matrix equation

$$\sum_{\boldsymbol{y}} K(\boldsymbol{x},\boldsymbol{y})S(\boldsymbol{y},\mathbf{0}) = \delta_{x,0} \tag{2.21}$$

where K is the three dimensional lattice Klein-Gordon operator

$$K(\boldsymbol{x}, \boldsymbol{y}) = \delta_{\boldsymbol{x},\boldsymbol{y}} - \kappa_S J(\boldsymbol{x}, \boldsymbol{y}) \tag{2.22}$$

where

$$J(\boldsymbol{x}, \boldsymbol{y}) = \sum_{\mu=1}^{3} \left[\delta_{\boldsymbol{y},\boldsymbol{x}-\hat{\boldsymbol{\mu}}} U_\mu^\dagger(\boldsymbol{x} - \hat{\boldsymbol{\mu}}) + \delta_{\boldsymbol{y},\boldsymbol{x}+\hat{\boldsymbol{\mu}}} U_\mu(\boldsymbol{x}) \right] \tag{2.23}$$

and the scalar hopping parameter, κ_S, is directly related to the mass and hence the radius of the wavefunction. The lattice spacing has been set equal to unity. A similar matrix equation can be solved for every time slice in order to obtain the sink smearing function. However this introduces a significant computational overhead. In order to reduce the computational effort, an alternative smearing function can be obtained by iteratively solving equation 2.21 as a power series in κ_S. In this case, Jacobi iteration [7] given by

$$S^{(n)}(\boldsymbol{x}, \boldsymbol{0}) = \delta_{\boldsymbol{x},0} + \kappa_S \sum_{\boldsymbol{y}} J(\boldsymbol{x}, \boldsymbol{y}) S^{(n-1)}(\boldsymbol{y}, \boldsymbol{0}), \qquad S^0(\boldsymbol{x}, \boldsymbol{0}) = \delta_{\boldsymbol{x},0} \tag{2.24}$$

and applied N_{jac} times, was used to obtain the source smearing function. The sink smearing function can be obtained in a similar manner. Note that if κ_S is less than some critical value then the power series converges to the scalar propagator. However, larger values of κ_S which result in a divergent series still provide a valid smearing function. The two parameters in the smearing procedure, N_{jac} and κ_S were tuned to find the optimum radius of the wavefunction, where the radius is defined by

$$r^2 = \sum_{\boldsymbol{x}} |\boldsymbol{x}|^2 |S(\boldsymbol{x}, \boldsymbol{0})|^2 / \sum_{\boldsymbol{x}} |S(\boldsymbol{x}, \boldsymbol{0})|^2 \tag{2.25}$$

The number of iterations, N_{jac}, was selected to be the minimum number required to obtain a value of the radius which maximises the overlap with the ground state while keeping the statistical noise in the signal to a minimum. An investigation to determine the optimum smearing parameters used in this thesis was carried out in [39]. For the quenched simulations using the Jacobi smearing procedure, which are indicated by the label jac in Table 3.1, the values $N_{\text{jac}} = 16, 30$ were used for the data sets at $\beta = 5.7, 6.0$ respectively. A value of $\kappa_S = 0.25$ was used throughout.

Although there is no direct physical motivation for modelling the smearing function by the scalar propagator, the Jacobi smearing technique does indeed increase the overlap with the ground state, as can be seen later in chapter 3. An alternative prescription used to obtain a smearing function is *fuzzing.* Fuzzing aims to reduce the contamination of the ground state due to excited state contributions, and has the benefit that it is computationally less intensive than Jacobi smearing.

2.6 Fuzzing

Mesons composed from heavy quarks (for example $c\bar{c}$ and $b\bar{b}$) are approximately non-relativistic. Assuming that the characteristic time scale associated with the movement of the heavy quarks is significantly larger than that of the gluons and light quark loops in the vacuum, the adiabatic approximation can be made. This approximation means that the effect of the gluons and quark loops can be modelled by an interaction potential between the heavy quarks. From these assumptions it is then expected that the spectra of these states can be approximately described by heavy point particles bound by a non-relativistic central potential, $V(r)$. The potential $V(r)$ can be characterised by the energy of static colour sources separated by a distance r, where the static colour sources are connected by a colour flux tube or string. Although there is no corresponding physical interpretation for light quark hadrons, the fuzzing prescription described in [46] can be used to construct hadron operators which create such a colour flux tube connecting the quark fields. The implementation of the fuzzing procedure in this context was motivated by the consideration of the smeared meson operator defined by

$$\mathcal{O}_{\mathrm{M}}^{S}(x) = \sum_{\boldsymbol{y}} \bar{\psi}(\boldsymbol{y}, t) S(\boldsymbol{y}, \boldsymbol{x}) \Gamma \psi(\boldsymbol{x}, t) \tag{2.26}$$

where the smeared anti-quark field defined in 2.15 has been substituted into equation 2.3. The smearing function can be defined to be the path ordered product of the spatial gauge links along the shortest path between the quark and anti-quark. In order to maintain the correct J^{PC}, the resulting operator is symmetrised by averaging over the six spatial directions. This operator is interpreted as a gluon flux tube between the fermion fields and has the advantage that this choice of operator leads to a gauge invariant correlator. However the operator has a poor overlap with the hadron state due to the fact that the probability that the gluon field is so localised is small [47]. The overlap can be improved by considering the contribution from non-local gluon fields. This is achieved through fuzzing the gauge links.

Fuzzed gauge links were formed by iteratively updating each of the gauge field links in the spatial directions, $U_\mu(x)$, $\mu = 1, \ldots, 3$, by adding a weighted sum of the four spatial staples associated with each link

$$U_\mu^{(n)}(x) = \mathcal{P}_{SU(3)}\left[cU_\mu^{(n-1)}(x) + \sum_{\substack{\pm\nu=1\\ \nu\neq\mu}}^{3} U_\nu^{(n-1)}(x)U_\mu^{(n-1)}(x+\hat\nu)U_\nu^{\dagger(n-1)}(x+\hat\nu)\right] \quad (2.27)$$

where c is the link-staple mixing ratio and $\mathcal{P}_{SU(3)}$ denotes that the updated link must be projected back onto the $SU(3)$ group manifold, since the $SU(3)$ group is not closed under addition. This process was iterated N_{fuzz} times to obtain the fuzzed gauge link, $U_\mu^{\mathrm{F}}(x)$, used to create the smearing function. The smearing function is then given by

$$S(\boldsymbol{y}, \boldsymbol{x}) = \sum_{\mu=1}^{3} \left\{ \delta_{\boldsymbol{y},\boldsymbol{x}-R\hat\mu} \prod_{i=1}^{R} U_\mu^{\mathrm{F}\dagger}(\boldsymbol{x} - i\hat{\boldsymbol{\mu}}) + \delta_{\boldsymbol{y},\boldsymbol{x}+R\hat\mu} \prod_{i=1}^{R} U_\mu^{\mathrm{F}}(\boldsymbol{x} + (i-1)\hat{\boldsymbol{\mu}}) \right\} \quad (2.28)$$

where the fuzzing radius, R, indicates the spatial extent of the function in lattice units. This smearing function can then be used to generate source and/or sink fuzzed propagators as described in section 2.4.

For the quenched simulations where fuzzed correlators were generated, denoted by the label fuzz in Table 3.1, an investigation into the optimum fuzzing radius was performed in [39]. The fuzzing radius R was tuned to minimise the overlap with the first excited state by examining the relative amplitudes of the ground and first excited states obtained through the fit procedure as described in [39]. This study indicated that the optimum radius was $R = 6(8)$ for the $\beta = 6.0(6.2)$ data sets respectively. In both cases the fuzzing parameters $N_{\mathrm{fuzz}} = 5$ and $c = 2$ were used. For all simulations examined in chapter 4 the values $N_{\mathrm{fuzz}} = 5$, $c = 2.5$ and $R = 2$ were used. A larger link-staple mixing ratio and a reduced fuzzing radius were selected based on a study of the quenched data at $\beta = 5.7$ and the fact that in this case the lattice spacing was coarser than for the quenched simulations in chapter 3.

2.7 Notation conventions for correlators

This section sets out the correlator notation used throughout this thesis. As described in section 2.3, hadron correlators are constructed from tying together the appropriate number of quark propagators. Each quark propagator in a correlator can either be Jacobi smeared, fuzzed or local at the source and/or sink. Although in principle any combination can be formed, the Jacobi smeared hadron correlators analysed in this thesis were created from quark propagators which all had the same smearing at the source and/or sink. It was observed [46] that correlators composed entirely from fuzzed propagators with the same fuzzing radius lead to a partial cancellation of the fuzzed gauge links between them, creating a component which is essentially unfuzzed. Thus the fuzzed correlators were created by combining either one or two fuzzed quark propagators with a local propagator to form meson and baryon correlators respectively. For baryons where two fuzzed propagators were combined with a local propagator the source and/or sink fuzzing were the same. Taking this into consideration means that the smearing status of a correlator can be labelled by just two letters, one for the source and one for the sink. The types of smearing are denoted by; L for local or point operators, S for Jacobi smearing and F for fuzzed. For example, the label FL denotes a correlator which has been fuzzed at the source but not at the sink.

Once the hadron correlators have been generated on the lattice, the next stage is to determine the ground state mass of the hadron in question. The next section shows how the mass is obtained from the exponential decay of Euclidean correlation functions at large times.

2.8 Hadron masses from correlation functions

The functional dependence of the hadron correlator, defined in equation 2.1, on the mass can be seen by taking the discrete Fourier transform, a process referred to as time slicing

$$C(\boldsymbol{p},t) = \sum_{\boldsymbol{x}} C(\boldsymbol{x},t) e^{-i\boldsymbol{p}\cdot\boldsymbol{x}} \tag{2.29}$$

where the lattice spacing has been set equal to unity. The values of the momenta in each spatial direction are restricted to the values $p_i = 2\pi n_i/L$, $i = 1,\ldots,3$, where $n_i = 0,\ldots,L-1$ is an integer and L is the spatial extent of the lattice. Substituting equation 2.1 into equation 2.29 and inserting a complete set of discrete states defined by

$$\mathbb{1} = \frac{1}{L^3} \sum_{\mathrm{n},\boldsymbol{q}} \frac{1}{2E_{\mathrm{n}}(\boldsymbol{q})} \left|n,\boldsymbol{q}\right\rangle \left\langle n,\boldsymbol{q}\right| \tag{2.30}$$

gives the momentum space correlator

$$C(\boldsymbol{p},t) = \frac{1}{L^3} \sum_{\boldsymbol{x},\mathrm{n},\boldsymbol{q}} \frac{1}{2E_{\mathrm{n}}(\boldsymbol{q})} \left\langle 0\right| \mathcal{O}(x) \left|n,\boldsymbol{q}\right\rangle \left\langle n,\boldsymbol{q}\right| \mathcal{O}^{\dagger}(0) \left|0\right\rangle e^{-i\boldsymbol{p}\cdot\boldsymbol{x}} \tag{2.31}$$

where $E_{\mathrm{n}}(\boldsymbol{q})$ is the energy of the state with momentum $\boldsymbol{q}$. The operators are assumed to be time ordered. Using the Euclidean translational invariance relation for operators

$$\mathcal{O}(x) = e^{Ht - i\boldsymbol{Q}\cdot\boldsymbol{x}} \mathcal{O}(0) e^{-Ht + i\boldsymbol{Q}\cdot\boldsymbol{x}} \tag{2.32}$$

(where H and $\boldsymbol{Q}$ are the Hamiltonian and three momentum operators respectively), and the lattice delta function defined as

$$\delta_{\boldsymbol{q},\boldsymbol{p}} = \frac{1}{L^3} \sum_{\boldsymbol{x}} e^{i(\boldsymbol{q}-\boldsymbol{p})\cdot\boldsymbol{x}} \tag{2.33}$$

equation 2.31 can be written as

$$C(\boldsymbol{p},t)=\sum_{\mathrm{n}}\frac{1}{2E_{\mathrm{n}}(\boldsymbol{p})}|\langle 0|\,\mathcal{O}(0)\,|n,\boldsymbol{p}\rangle|^2e^{-E_{\mathrm{n}}(\boldsymbol{p})t} \tag{2.34}$$

The masses of each state can be obtained by considering equation 2.34 at zero three momentum, $\boldsymbol{p}=\mathbf{0}$. This results in the general form for the correlator

$$C(\mathbf{0},t)=\sum_{\mathrm{n}}A_{\mathrm{n}}e^{-m_{\mathrm{n}}t} \tag{2.35}$$

where the amplitude is defined as $A_{\mathrm{n}}=|\langle 0|\,\mathcal{O}(0)\,|n,\mathbf{0}\rangle|^2/2m_{\mathrm{n}}$. The behaviour of this equation at large times is dominated by the ground state mass

$$\lim_{t\to\infty}C(\mathbf{0},t)\to A_0e^{-m_0t} \tag{2.36}$$

This relation shows that the ground state masses of the hadrons can be extracted from the exponential decay of time sliced correlators at large Euclidean times.

2.9 The effect of periodic boundary conditions

The discussion on obtaining masses from correlators in the previous section assumed an infinite time direction. However for a lattice simulation on a finite lattice of spatial length L and temporal extent T, it is necessary to introduce boundary conditions. The choice of boundary conditions made for the simulations studied here imposed anti-periodic boundary conditions on quark propagators in the time direction (and periodic in the spatial directions). The anti-periodicity in the time direction allows the hadron to propagate both forwards and backwards in time. This means that the behaviour of the backward propagating hadron must be taken into account. The general form that the correlators can be fitted to is then

$$C(\mathbf{0},t)=\sum_{\mathrm{n}}A_{\mathrm{n}}e^{-m_{\mathrm{n}}t}+\eta B_{\mathrm{n}}e^{-m_{\mathrm{n}}^*(T-t)} \tag{2.37}$$

where the second term corresponds to the backward propagating hadron. The parameter η can be either ±1 depending upon how the hadron operators transform under the time reversal operator defined by $\hat{\mathrm{T}} = \gamma_4\gamma_5$. For mesons, the backward propagating state has the same mass as the forward propagating state ($m_{\mathrm{n}} = m^*_{\mathrm{n}}$) and in the limit of infinite statistics the correlator is symmetric (or anti-symmetric depending on the sign of η) about the mid time slice, $T/2$. Assuming sufficient statistics so that this is nearly the case, the meson correlator is *folded* about the midpoint and averaged in order to increase the amount of information used in the fits. The ground state mass of the mesons can then be fitted to a cosh function

$$\begin{aligned} C_{\mathrm{M}}(\mathbf{0},t) &= A_0(e^{-m_0 t} + e^{-m_0(T-t)}) \\ &= 2A_0 e^{-\frac{m_0 T}{2}} \cosh\left[m_0\left(\frac{T}{2} - t\right)\right] \end{aligned} \tag{2.38}$$

For baryon correlators the backward propagating state corresponds to the parity partner of the baryon, which has a different mass in general. In this case, the positive parity correlator, C^+_{B}, from the first half of the lattice is averaged with negative parity correlator, C^-_{B}, from the second half of the lattice

$$C_{\mathrm{B}}(\mathbf{0},t) = [C^+_{\mathrm{B}}(\mathbf{0},t) + C^-_{\mathrm{B}}(\mathbf{0},T-t)]/2 \tag{2.39}$$

The ground state of the baryon is then extracted by fitting the averaged baryon correlator to the form

$$C_{\mathrm{B}}(\mathbf{0},t) = A_0 e^{-m_0 t} \tag{2.40}$$

Fits to extract the ground state mass can then be performed following the general procedure outlined later in section 2.12. However, fits to the ground state mass have to be carried out at sufficiently large times to ensure that the contamination from the excited states has died away. This means that the fits are performed over a small set of the available data points and, in particular, in a region where the statistical errors in the signal are becoming larger. In order to determine the ground state more accurately it is better to have an estimate of the first excited state. Fitting to both the ground and first excited states enables earlier time slices to be included in the fit. In practice, performing fits to both the ground state and one (or more) excited states using a single correlator type are usually unstable. To achieve a more stable fitting procedure a variational basis of correlators with different smearing combinations can be used, provided that each correlator type has different overlaps with the ground and first excited states. This type of fit is referred to as *simultaneous fitting.*

2.10 Simultaneous fitting

The simultaneous fitting procedure described in this section is based on the technique detailed in [48]. The idea is that each correlator used in the simultaneous fit should have a significant overlap with one of the energy states to be determined. The simplest case is to consider a simultaneous fit to a pair of correlators to extract the ground and first excited states. The pairs of correlators used in this thesis consist of one local correlator, LL, and one correlator which has been either Jacobi smeared or fuzzed at the source and/or sink. In this case the Jacobi smeared correlator was selected because it has a large overlap with the ground state. Similarly fuzzed correlators have a good overlap with the ground state as the fuzzing procedure minimises the contamination from excited states. The local correlator included in the fit has a significant overlap with the first excited state and was used to provide an estimate of the excited state mass. Fits to more than one excited state were not considered further, as no correlators with a good overlap with the second excited state were generated.

For a general simultaneous fit, several meson correlators, denoted by $C_{\mathrm{M}}^{s_{\mathrm{c}}s_{\mathrm{k}}}(\mathbf{0},t)$ where s_{c} and s_{k} label the type of smearing (L, S or F) used at the source and sink respectively, are simultaneously fitted to the equation

$$C_{\mathrm{M}}^{s_{\mathrm{c}}s_{\mathrm{k}}}(\mathbf{0},t) = \sum_{\mathrm{n}=0}^{N_{\mathrm{ex}}} A_{\mathrm{n}}^{s_{\mathrm{c}}s_{\mathrm{k}}} \left(e^{-m_{\mathrm{n}}t} + e^{-m_{\mathrm{n}}(T-t)}\right) \tag{2.41}$$

where N_{ex} is equal to the number of excited states included in the fit. In order to increase the stability of the fit, the number of fit parameters is reduced by constraining the masses extracted from each correlator type to be the same, $m_{\mathrm{n}}^{s_{\mathrm{c}}s_{\mathrm{k}}} \equiv m_{\mathrm{n}}$. Baryon correlators are fitted in a similar manner to just the first exponential in equation 2.41. In all the simultaneous fits considered here, two correlators were fitted simultaneously to the ground and first excited states, resulting in a six parameter fit. For simulations containing a limited number of statistics (such as the dynamical simulations considered in this thesis), a further type of fit known as a *factorising fit* was considered.

2.11 Factorising fits

Factorising fits [48] are a generalisation of the simultaneous fits considered above which impose further constraints on the fit parameters. This is achieved by factorising the amplitudes of each state

$$A_{\mathrm{n}}^{s_{\mathrm{c}}s_{\mathrm{k}}} = B_{\mathrm{n}}^{s_{\mathrm{k}}} B_{\mathrm{n}}^{s_{\mathrm{c}}} \tag{2.42}$$

where the matrix elements given by

$$B_{\mathrm{n}}^{s_{\mathrm{k}}} = \langle 0 | \, \mathcal{O}_{s_{\mathrm{k}}}(0) \, | n, \mathbf{0} \rangle \, / \sqrt{2m_{\mathrm{n}}}, \qquad B_{\mathrm{n}}^{s_{\mathrm{c}}} = \langle n, \mathbf{0} | \, \mathcal{O}_{s_{\mathrm{c}}}^{\dagger}(0) \, | 0 \rangle \, / \sqrt{2m_{\mathrm{n}}} \tag{2.43}$$

are in general complex. The form of the factorising fit to the meson correlators is written as

$$C_{\mathrm{M}}^{s_{\mathrm{c}}s_{\mathrm{k}}}(\mathbf{0}, t) = \sum_{\mathrm{n}=0}^{N_{\mathrm{ex}}} B_{\mathrm{n}}^{s_{\mathrm{k}}} B_{\mathrm{n}}^{s_{\mathrm{c}}} \left(e^{-m_{\mathrm{n}} t} + e^{-m_{\mathrm{n}}(T-t)} \right) \tag{2.44}$$

This equation is fitted simultaneously to several different correlator types. The factorised amplitudes, $B_{\mathrm{n}}^{s_{\mathrm{c}}}$ and $B_{\mathrm{n}}^{s_{\mathrm{k}}}$, can be defined to be real since the hadron operators under consideration obey charge conjugation symmetry in the case of equal mass quarks [48]. Baryon correlators are fitted similarly to the first exponential term in equation 2.44. In practice, the factorising fits to the ground and first excited states performed with the data sets discussed in chapter 4 used three correlator types, LL, FL and FF, resulting in a six parameter fit.

2.12 General fit procedure to extract lattice masses

In this section the fit procedure used to determine the lattice values of the light hadron masses is described. The same general method was used for both the quenched data and the dynamical data. A discussion of the χ^2 fitting procedure is outlined, first defining the χ^2 merit function and then the method used to find the minimum value of the χ^2 and hence obtain the best fit parameters. There follows a brief discussion of the *smoothing* technique implemented to improve the general stability of the fit and the method used to obtain an estimate of the errors on the fitted masses. Finally the selection criteria used to determine the best fit interval are set out.

2.12.1 Effective mass plots

In the initial stages of the analysis it is often useful to consider *effective mass* plots. In order to extract the ground state mass the correlator data must be fitted over a time interval where the minimum time slice, t_{min}, is large enough that the excited states excluded in the fit can be considered to have decayed. One way to decide when this occurs is to examine the effective mass plot.

On the lattice the correlators are measured on a data set of N gauge configurations. The average time sliced correlator over these configurations is defined by

$$C(t) = \frac{1}{N}\sum_{i=1}^{N} C_i(\mathbf{0},t) \tag{2.45}$$

The effective masses for mesons and baryons are then defined in terms of the averaged time sliced correlator by

$$m_{\mathrm{eff}}^{\mathrm{meson}}(t) = \cosh^{-1}\left[\frac{C(t-1)+C(t+1)}{2C(t)}\right], \quad m_{\mathrm{eff}}^{\mathrm{baryon}}(t) = \ln\left[\frac{C(t+1)}{C(t)}\right] \tag{2.46}$$

As time increases, the value of the effective mass will level off (*i.e.* begin to plateau), which indicates that all the excited states have decayed. The height of the plateau can be used to provide an estimate of the ground state mass. The time slice which marks the onset of the plateau can be used as a rough guide to select the appropriate fit interval over which to extract the ground state mass (a longer fit range can be selected when the first excited state is included in the fit). The final values for the lattice masses are then fitted over this interval by minimising the χ^2 *merit function.*

2.12.2 χ^2 fitting

Minimising the χ^2 merit function is a standard procedure for fitting data to a model function [49]. The description below uses notation specific to fitting the correlator data considered here. The averaged correlator, $C(t)$, defined in equation 2.45, is fitted to the model function, $f(\boldsymbol{a}, t)$, where $\boldsymbol{a} = (a_1, \ldots, a_{\mathrm{m}})$ represents the fit parameters to be determined. For example, in the case of a meson correlator the simplest $f(\boldsymbol{a}, t)$ is the function defined in equation 2.38. The data is fitted to the model function by minimising the χ^2 statistic

$$\chi^2 = \sum_{t_{\mathrm{i}}, t_{\mathrm{j}}} [f(\boldsymbol{a}, t_{\mathrm{i}}) - C(t_{\mathrm{i}})] \mathrm{Cov}^{-1}(t_{\mathrm{i}}, t_{\mathrm{j}}) [f(\boldsymbol{a}, t_{\mathrm{j}}) - C(t_{\mathrm{j}})] \tag{2.47}$$

This form for the χ^2 takes into account the correlations in the data between different time slices via the covariance matrix. The covariance matrix, $\mathrm{Cov}(t_{\mathrm{i}}, t_{\mathrm{j}})$, is computed using

$$\mathrm{Cov}(t_{\mathrm{i}}, t_{\mathrm{j}}) = \frac{1}{N(N-1)} \sum_{k=1}^{N} [C_k(t_{\mathrm{i}}) - C(t_{\mathrm{i}})][C_k(t_{\mathrm{j}}) - C(t_{\mathrm{j}})] \tag{2.48}$$

where $C_k(t)$ is the k'th time sliced correlator in the ensemble and $C(t)$ has been defined in equation 2.45. When the data to be fitted to the model function is some function of several correlator types, *i.e.* $C(t)$ in equation 2.47 is replaced by $D(t) = f(C^A(t), C^B(t), \ldots)$, the covariance matrix is instead computed using the Jackknife sampling technique

$$\mathrm{Cov}(t_{\mathrm{i}}, t_{\mathrm{j}}) = \frac{N-1}{N} \sum_{k=1}^{N} [D_k(t_{\mathrm{i}}) - \overline{D(t_{\mathrm{i}})}][D_k(t_{\mathrm{j}}) - \overline{D(t_{\mathrm{j}})}] \tag{2.49}$$

where $D_k(t)$ is the time sliced data function determined on the k'th jackknife sample obtained by removing the k'th configuration from the ensemble. In other words, $D_k(t)$, is evaluated in terms of the appropriate averaged time sliced correlators, defined by equation 2.45, where the correlators determined on the $i = k$

configuration have been removed from the average. The jackknife sampling technique repeats this for each configuration in the data set. The average data function $D_k(t)$ is compared with $\overline{D(t)}$, the average of $D_k(t)$ over all the jackknife samples, for each jackknife sample. In both cases the diagonal entries are just the variance of the data points. It is easier to see the correlations in the data by looking at the correlation matrix defined by

$$\mathrm{Corr}(t_\mathrm{i}, t_\mathrm{j}) = \frac{\mathrm{Cov}(t_\mathrm{i}, t_\mathrm{j})}{\sqrt{\mathrm{Cov}(t_\mathrm{i}, t_\mathrm{i})\mathrm{Cov}(t_\mathrm{j}, t_\mathrm{j})}} \tag{2.50}$$

The entries of the correlation matrix are in the range $[-1, 1]$, where 1 means the data are strongly correlated and -1 means that the data points are anti-correlated. Once the χ^2 has been defined, the next stage is to determine the fit parameters, at which the minimum value of the χ^2 occurs.

2.12.3 Minimising the χ^2

The χ^2 is minimised using the Marquardt-Levenberg method [49] which combines the method of steepest descent with the inverse Hessian technique. The Hessian matrix or curvature matrix α is constructed from the second derivatives of the χ^2 with respect to the fit parameters. It is inverted using the SVD, singular value decomposition algorithm, to obtain the next guess for the fit parameters. The χ^2 is then re-evaluated using the new fit parameters. The algorithm is repeated until the minimum of the χ^2 is found and the best fit parameters are obtained at this point.

2.12.4 Eigenvalue smoothing

When performing simultaneous fits, the minimisation algorithm was found to be sensitive to the initial guesses for the excited state fit parameters. Varying the initial guesses for these parameters, even slightly, affected the ability of the algorithm to converge to the minimum of the χ^2 as a result of the curvature matrix, α, becoming close to singular. This indicates that it is difficult to fit the excited state. The method used to stabilise the fit was derived from the eigenvalue smoothing technique for the correlation matrix described in reference [50]. In this thesis, the smoothing technique is applied to the eigenvalues calculated in the SVD process used to invert the α matrix. The three lowest eigenvalues, corresponding to the parameters associated with the excited state, were smoothed. This was achieved by comparing these eigenvalues with the average of the three eigenvalues. If a given eigenvalue was lower than the average then the eigenvalue was replaced by the average value. This procedure does not effect the position of the minimum of the χ^2 only the route taken through parameter space to reach it. It was found that with this technique the fitted parameter values were independent of the initial guess and resulted in a more stable fitting procedure. This technique was implemented for both the simultaneous and factorising fits.

2.12.5 Bootstrap re-sampling

In order to obtain an estimate of the error on the fitted parameters the technique of bootstrap re-sampling [51] was used. A bootstrap sample is created by selecting N correlators from the data set at random and with replacement. The χ^2 fit procedure described above is then repeated. This is repeated 1000 times for the quenched data sets and 500 times for the data sets in chapter 4, due to the fact that there are less statistics available for the dynamical data sets. The error is then calculated by taking the 68% confidence limits. This occurs when 68% of the results obtained from the bootstrap analysis are within σ of the average value. Asymmetric errors are calculated by determining the difference between the parameter values obtained from the best fit (determined from the original ordering of the data set) and the upper and lower confidence limits.

2.12.6 Goodness of fit

One indication of the goodness of the fit can be obtained by considering the minimum value of the χ^2. An acceptable χ^2 value should be close to the number of degrees of freedom (d.o.f) in the fit. The d.o.f in this case is equal to the number of time slices in the fit interval minus the number of fit parameters, $\mathrm{d.o.f} = \mathrm{t} - \mathrm{m} \equiv \nu$. In addition to the χ^2, the quality of the fit can be assessed by computing the incomplete gamma function

$$Q\left(\frac{\nu}{2},\frac{\chi^2}{2}\right)=\frac{1}{\Gamma(\frac{\nu}{2})}\int_{\chi^2/2}^{\infty}e^{-t}t^{(\frac{\nu}{2}-1)}dt \tag{2.51}$$

The Q value is the probability that the χ^2 (assuming that the errors on the data are normally distributed) should exceed the particular value of the χ^2 obtained, by chance. A value for $Q < 0.001$ means that either the model function does not describe the data or the size of the errors are too small or are not normally distributed. Values for Q close to 1 indicate too good a fit and usually means that the errors on the data points have been overestimated. Ideally the Q value should be around 0.5.

2.12.7 Sliding window analysis

To determine the optimum fit range over which the lattice masses are extracted, a *sliding window analysis* was performed. This was achieved by first selecting the maximum time slice, t_{max}, included in the fit and gradually pushing the minimum time slice, t_{min}, closer towards the origin. Fits were then performed for each interval and compared. Unless otherwise stated in the text, the maximum time slice was selected to be half the temporal extent of the lattice, provided an acceptable χ^2/d.o.f. was obtained from the fit. Where this was not the case, t_{max} was reduced. The final fit range was determined by considering the following criteria,

- The value of the fitted mass should be consistent within errors when t_{min} is changed by one time slice.
- The fit should have χ^2/d.o.f. of around 1.
- The Q value should ideally be approximately 0.5.

A further consideration is that the fit interval should be as long as possible while satisfying the points above. This includes as much of the available information in the fit in order to reduce the bias of the fit due to the correlated fluctuations present in the data.

2.13 Application of the fitting procedure

The determination of the best fits for the ground state masses for all the mesons and baryons considered in this thesis implemented the general fit procedure outlined above. The selection of the type of fit (ground state only, simultaneous or factorising) is discussed for each simulation in the following chapters. Fits to secondary quantities determined from the masses were also determined using the χ^2 minimisation technique. The next two chapters present the results obtained for the light hadron spectrum in the quenched approximation and for the dynamical simulations respectively.

Chapter 3

Quenched spectrum results

In this chapter the results obtained from the analysis of the data sets generated in the quenched approximation are presented. The results for the lattice values of the hadron masses obtained by implementing the general fit procedure described in section 2.12 in the previous chapter are discussed in detail for each data set. All the final values for the lattice masses can be found in appendix A. In addition, the Partially Conserved Axial Current (PCAC) mass is determined for each data set. Then results which can be obtained without requiring any extrapolations, such as the hyperfine mass splitting and the J parameter are discussed. Chiral extrapolations are then performed followed by continuum extrapolations which are compared with experiment. Some of the quenched data has been analysed independently by other members of the UKQCD Collaboration. Results obtained from the tadpole improved data sets have been published in [52, 53, 54, 55] and results for both the tadpole and non-perturbatively improved data sets were presented in [39]. The results presented here represent the final results for the quenched light hadron mass spectrum to be published in [56].

3.1 Simulation parameters

This section outlines the simulation parameters used in the quenched light hadron spectrum analysis. Data sets at three values of the lattice parameter β were generated in order to explore the continuum limit. The hybrid over-relaxed algorithm described in [57] was employed in the production of the gauge configurations, which use the standard Wilson plaquette action. The quark propagators were generated using $O(a)$ improved Wilson fermions.

Tadpole improved data sets

β	c_{sw}	$L^3 \cdot T$	L[fm]	κ	# conf.	smearing
5.7	1.5678	$16^3 \cdot 32$	2.7	0.13843, 0.14077	147	jac
6.0	1.4785	$16^3 \cdot 48$	1.5	0.13856, 0.13810, 0.13700	499	fuzz
6.2	1.4424	$24^3 \cdot 48$	1.6	0.13745, 0.13710, 0.13640	218	fuzz

Non-perturbatively improved data sets

β	c_{sw}	$L^3 \cdot T$	L[fm]	κ	# conf.	smearing
6.0	1.7692	$16^3 \cdot 48$	1.5	0.13455, 0.13417, 0.13344	496(3)	fuzz
6.0	1.7692	$32^3 \cdot 64$	3.0	0.13455, 0.13417, 0.13344	70(2)	jac
6.2	1.6138	$24^3 \cdot 48$	1.6	0.13530, 0.13510, 0.13460	216	fuzz

Table 3.1: Simulation parameters for the quenched data sets. The parentheses show the number of exceptional configurations removed from the ensemble. The lattice size in physical units has been estimated using r_0 (defined later in section 3.7) to set the scale.

Table 3.1 summarises the simulation parameters for the quenched data sets. The κ values have been chosen to lie in the region of the strange quark mass in order to study the strange sector of the spectrum. Meson and baryon correlators have been computed using non-degenerate combinations of quark masses for all data sets except for the $\beta = 5.7$ data set where non-degenerate baryons were not generated. Some quark mass combinations of baryon correlators from the $\beta = 6.2$ tadpole improved data set were generated on only 200 configurations. For the non-perturbatively improved data sets the number of exceptional configurations which have been removed from the ensemble are noted in the parentheses. The exceptional configurations present in the original ensemble were identified by the inability of the numerical inversion of the fermion matrix to converge for some components of the quark propagator. This is due to the occurrence of near zero eigenvalues of the fermion matrix, known as zero modes, the presence of which has been verified for the exceptional configurations encountered here [58, 59]. Note that in simulations with dynamical fermions the incidence of exceptional configurations is suppressed due to the inclusion of the fermion determinant in the gauge generation procedure, where the presence of zero modes means that $\det M[U]$ is very small.

The fraction of exceptional configurations within a particular ensemble is expected to increase for smaller quark masses and/or larger values of g_0^2, c_{sw} and L/a [30]. This was investigated in [56] by comparing the LL correlator at $T/2$ for the smallest quark mass from both the tadpole and non-perturbatively improved data sets at $\beta = 6.0$. The width of each distribution of the correlator data was defined by

$$\Delta x_{\mathrm{u}}/x_{\mathrm{m}}, \qquad \Delta x_{\mathrm{u}} = x_{\mathrm{u}} - x_{\mathrm{m}} \tag{3.1}$$

where x_{m} is the median and x_{u} is the upper value of the 68% confidence limit. In both cases the width was approximately the same, $\Delta x_{\mathrm{u}}/x_{\mathrm{m}} \approx 0.65$ and the distribution was found to extend smoothly out to $x_{\mathrm{m}}+9\Delta x_{\mathrm{u}}$. The main difference occurred in the number of points lying far beyond this region. In the tadpole data set only one such point at approximately $37\Delta x_{\mathrm{u}}$ above the median was encountered as opposed to three points at $44\Delta x_{\mathrm{u}}$, $65\Delta x_{\mathrm{u}}$ and $360\Delta x_{\mathrm{u}}$ above the median for the non-perturbatively improved data set. This indicates that although the level of statistical fluctuations is approximately the same, the incidence of exceptional configurations is indeed observed to be higher for larger values of the clover coefficient. A third exceptional configuration was found in the process of fuzzing the propagators in the non-perturbative data set. Attempts to treat the exceptional configurations using techniques such as the Modified Quenched Approximation described in [60, 61, 62] have not been implemented here. In the case of the small volume at $\beta = 6.0$, these exceptional configurations account for less than 1% (3% for the large volume) of the total number of configurations. Thus their removal should not seriously distort the results.

3.2 Fitting the lattice hadron masses

The detailed mass results obtained from the fitting procedure are explained in the following sections for all the quenched data sets. The analysis of the data sets with fuzzed correlators proceeded in a similar manner and are thus discussed together. The $\beta = 5.7$ and large volume $\beta = 6.0$ data sets, which implement the Jacobi smearing technique described in section 2.5, are discussed separately.

3.2.1 Fits to the fuzzed data sets

Fuzzed correlators have been generated for both the tadpole and non-perturbatively improved data sets at $\beta = 6.0$ and $\beta = 6.2$. The details of the fuzzing technique and the particular parameters used for each data set were described in section 2.6. Correlators with the fuzzing combinations LL, FL, LF and FF, have been constructed where the notation used has been defined in section 2.7.

Meson correlators were fitted by simultaneously fitting a pair of correlators to the ground and first excited states using the function

$$C_{\mathrm{M}}(\mathbf{0},t) = A_0\left(e^{-m_0 t} + e^{-m_0(T-t)}\right) + A_1\left(e^{-m_1 t} + e^{-m_1(T-t)}\right) \tag{3.2}$$

as described in section 2.10. Both the correlator combinations LL,FL and LL,FF, were considered for the fits to the pseudoscalar and vector channels. Combinations involving the sink fuzzed correlator LF were not considered because this correlator behaves in a similar manner to the source fuzzed correlator FL but has a lower signal to noise ratio. The degenerate nucleon and delta baryons were analysed in the same way, to a double exponential form

$$C_{\mathrm{B}}(\mathbf{0},t) = A_0 e^{-m_0 t} + A_1 e^{-m_1 t} \tag{3.3}$$

For the delta, sigma and lambda non-degenerate baryons it was only possible to consider simultaneous fits to the LL,FL combination of correlators, as these were the only correlators generated due to limits imposed upon the computing resources.

The optimum fit range for each correlator combination considered was selected by performing a sliding window analysis as described in section 2.12.7. As an illustration of the information obtained from this type of analysis, the $\beta = 6.0$ non-perturbatively improved data set has been chosen as an example. Figure 3.1

shows the values obtained from the sliding window fits to the correlators with the heaviest quark mass, $\kappa = 0.13344$, for the pseudoscalar and vector mesons. The top row of plots show the fitted value of the mass obtained as t_{min} is varied. The maximum time slice was held fixed at $t_{\text{max}} = 23$. The plots directly below show the χ^2/d.o.f. and the Q values for each fit. Using the criteria that the fit range should be as long as possible while observing an acceptable χ^2/d.o.f. and Q value, the fit range was selected to be [6-23]. The final t_{min} selected is indicated on the plots by the arrow. In general fits to the pseudoscalar were found to be very stable under small variations of the fitting range. For the vector channel, systematic effects in the value of the fitted mass were observed by varying the fit interval. The variation was around one σ for the worst case. The sliding window plots for the vector show an example of an unstable fit for the fit range [7-23]. For this point the fitting routine failed to find the minimum of the χ^2 as occasionally happens for the vector channel. The fit range of [6-23] has been chosen for the best fit as the effect of decreasing t_{min} by two time slices gives a result for the mass which is consistent within errors.

Figure 3.2 shows an example of the sliding window plots obtained for the degenerate nucleon and delta for the heaviest quark mass correlator. The final fit range selected was [9-23] as this gives the longest possible fit range with an acceptable χ^2/d.o.f. and Q value. Plots for correlators with lighter quark masses show the same general trend but the errors are larger due to increased noise in the signal. For the other data sets considered here, a similar sliding window analysis for all the baryon data was performed.

Figures 3.3 to 3.6 show example effective mass plots, as described in section 2.12.1, for all four data sets for the pseudoscalar, vector, nucleon and delta channels for the heaviest quark mass. Plots for correlators composed from lighter quark masses show a similar picture but with noisier signals. Effective mass plots for the non-degenerate baryons show the same qualitative features as the degenerate delta and nucleon and hence have not been shown. The data points show the effective mass determined from each of the correlators used in the final fit. The effective masses obtained from the fuzzed correlators for the non-perturbative

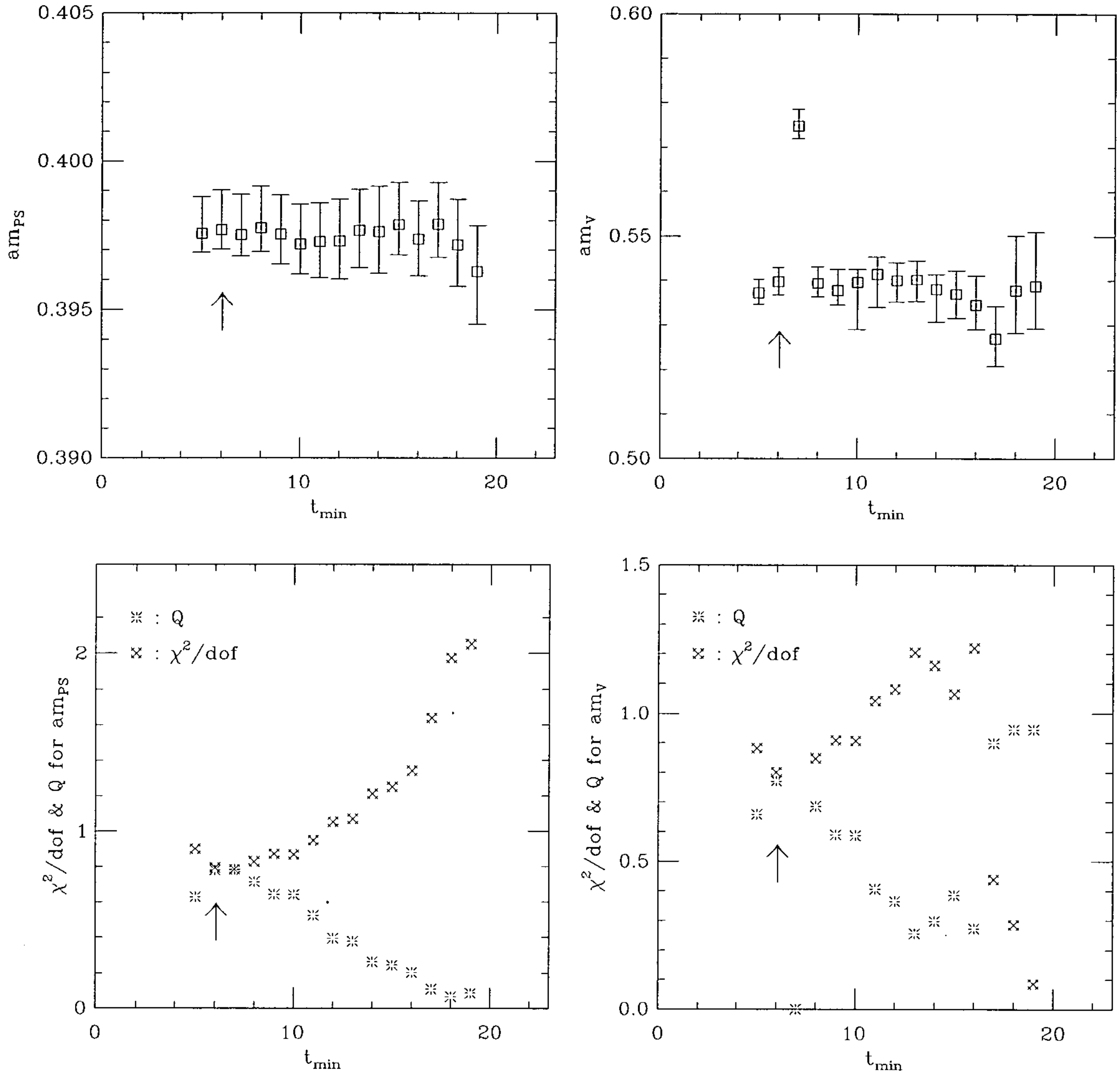

Figure 3.1: Sliding window plots from the $\beta = 6.0$ non-perturbatively improved data set for the degenerate pseudoscalar and vector at $\kappa = 0.13344$. The top plots show the values obtained for the fitted mass when $t_{\text{max}} = 23$ and t_{min} has been varied. The plots beneath show the resulting χ^2/d.o.f. and Q for each fit. An arrow marks the value of t_{min} selected for the final fit. In this case a correlated double cosh form has been fitted simultaneously to the LL,FF combination of correlators.

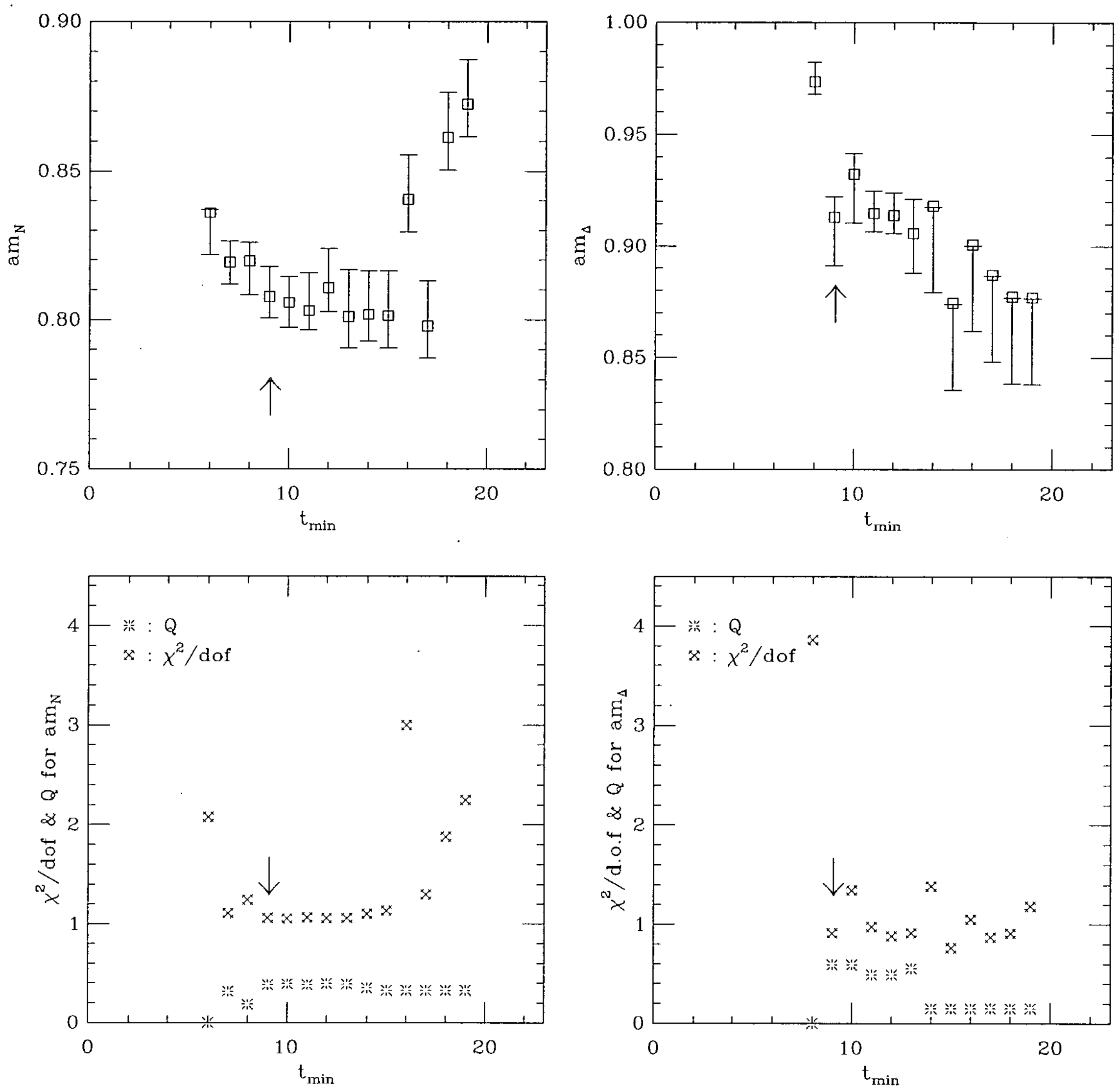

Figure 3.2: As for figure 3.1 for the nucleon and delta. In this case a correlated double exponential form has been fitted simultaneously to the LL,FF combination of correlators.

data sets are in general noisier than the tadpole improved data, however this difference did not have a significant effect on the relative ease of fitting the data. Superimposed on the graphs is the actual fitted value obtained for the mass, the horizontal length of which corresponds to the fit range. This straight line is not a fit to the data points shown on the graph. The χ^2/d.o.f. indicated on each graph was obtained in the best fit for the mass. The graphs show that the fuzzed correlator isolates the ground state before the local correlator, but the signal is noisier. Where the source fuzzed correlator has been used to fit the vector for the $\beta = 6.2$ data sets, the plots show that the effective mass approaches the plateau from below. This is because the matrix element is not constrained to be positive definite.

Data set	Pseudoscalar	Vector	Nucleon	Delta
$\beta = 6.0$ TAD	LL,FF	LL,FF	LL,FL	LL,FL
$\beta = 6.2$ TAD	LL,FF	LL,FL	LL,FF	LL,FF
$\beta = 6.0$ N-P	LL,FF	LL,FF	LL,FF	LL,FF
$\beta = 6.2$ N-P	LL,FF	LL,FL	LL,FF	LL,FF

Table 3.2: Correlator combinations selected for the final fit for the $\beta = 6.0, 6.2$ data sets. Note that TAD indicates tadpole improvement and N-P indicates non-perturbative improvement. All fits are simultaneous fits to the ground and first excited states.

The results for all the hadron masses obtained from simultaneous fits to both correlator combinations were found to be in agreement with each other within errors and with fits performed to the ground state of a single correlator type. The correlator combination chosen for the final fit was selected on the basis that the best fit gave a lower χ^2/d.o.f. and better overall stability of the fitted mass as $t_{\rm min}$ was varied. Table 3.2 shows the correlator combinations selected for the final fit for the mesons and degenerate baryons. For the non-degenerate baryons, double exponential fits to the LL,FL correlator combination were chosen.

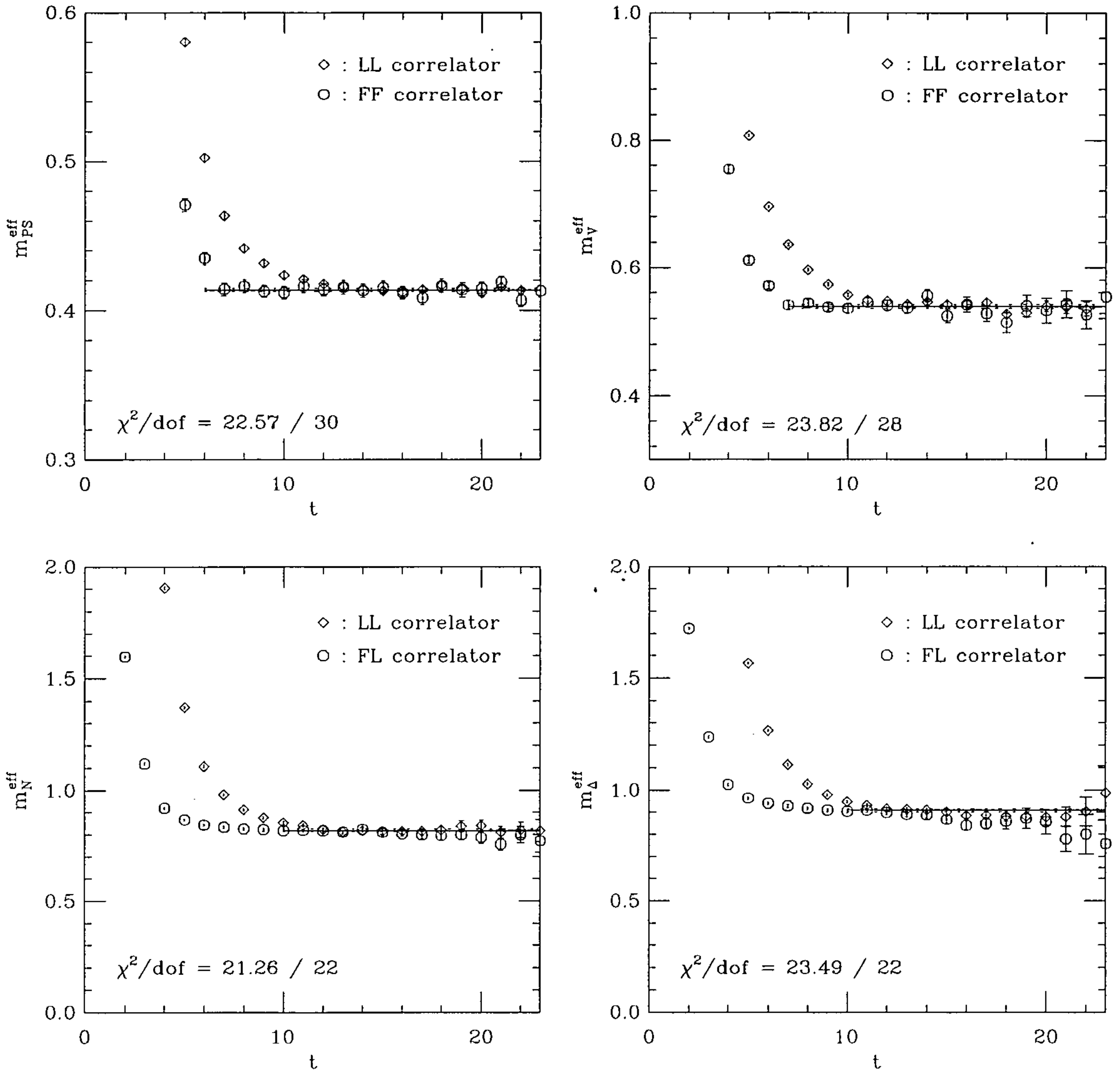

Figure 3.3: Effective mass plots from the $\beta = 6.0$ tadpole improved data set for the degenerate pseudoscalar, vector, nucleon and delta channels. The plots show the correlator combinations used in the final fit for $\kappa = 0.13700$. Superimposed on the graphs is the fit range selected and the value of the fitted mass obtained from a fit to the ground and first excited states.

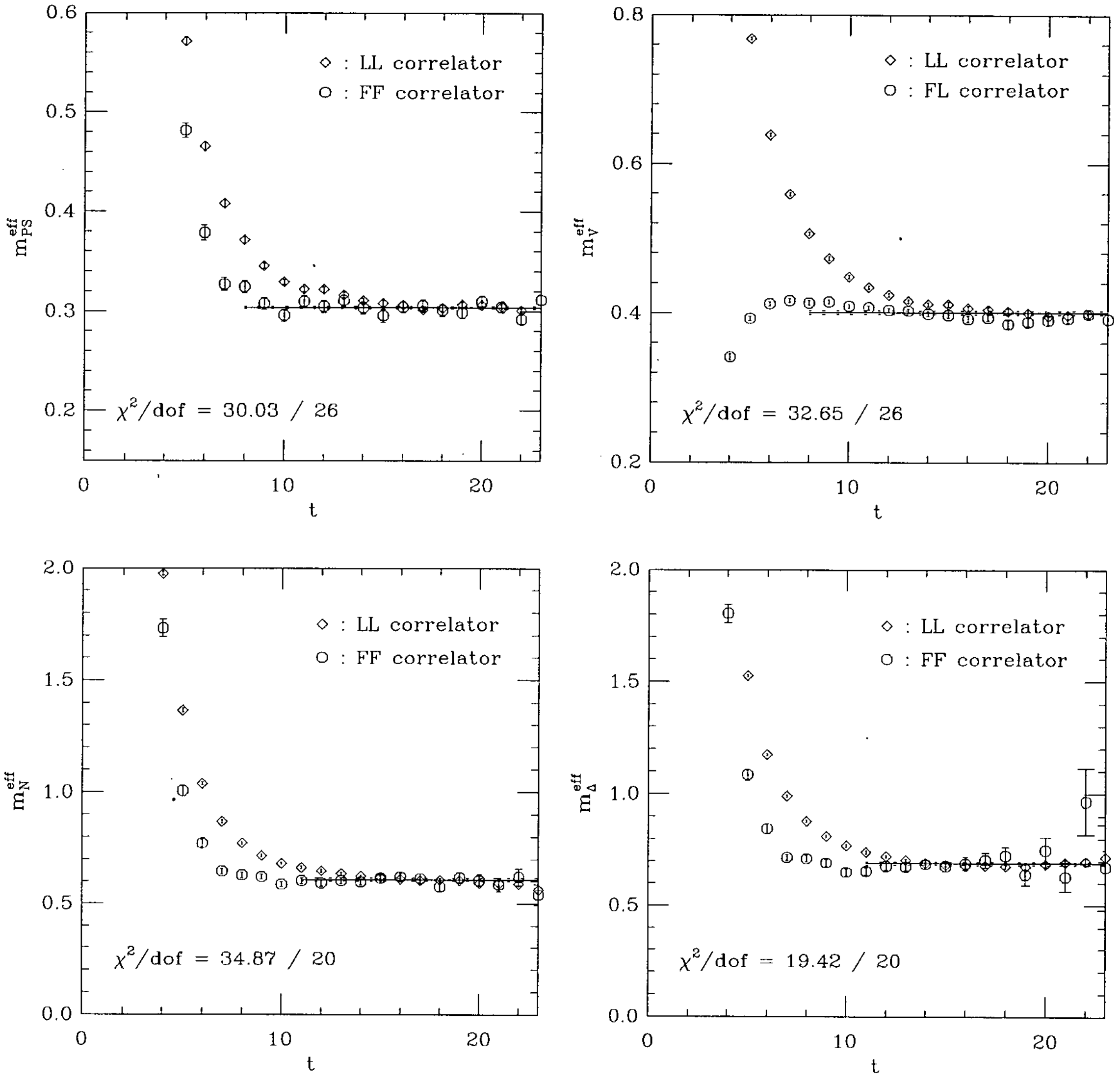

Figure 3.4: As for Figure 3.3 for the $\beta = 6.2$ tadpole improved data set for $\kappa = 0.13640$.

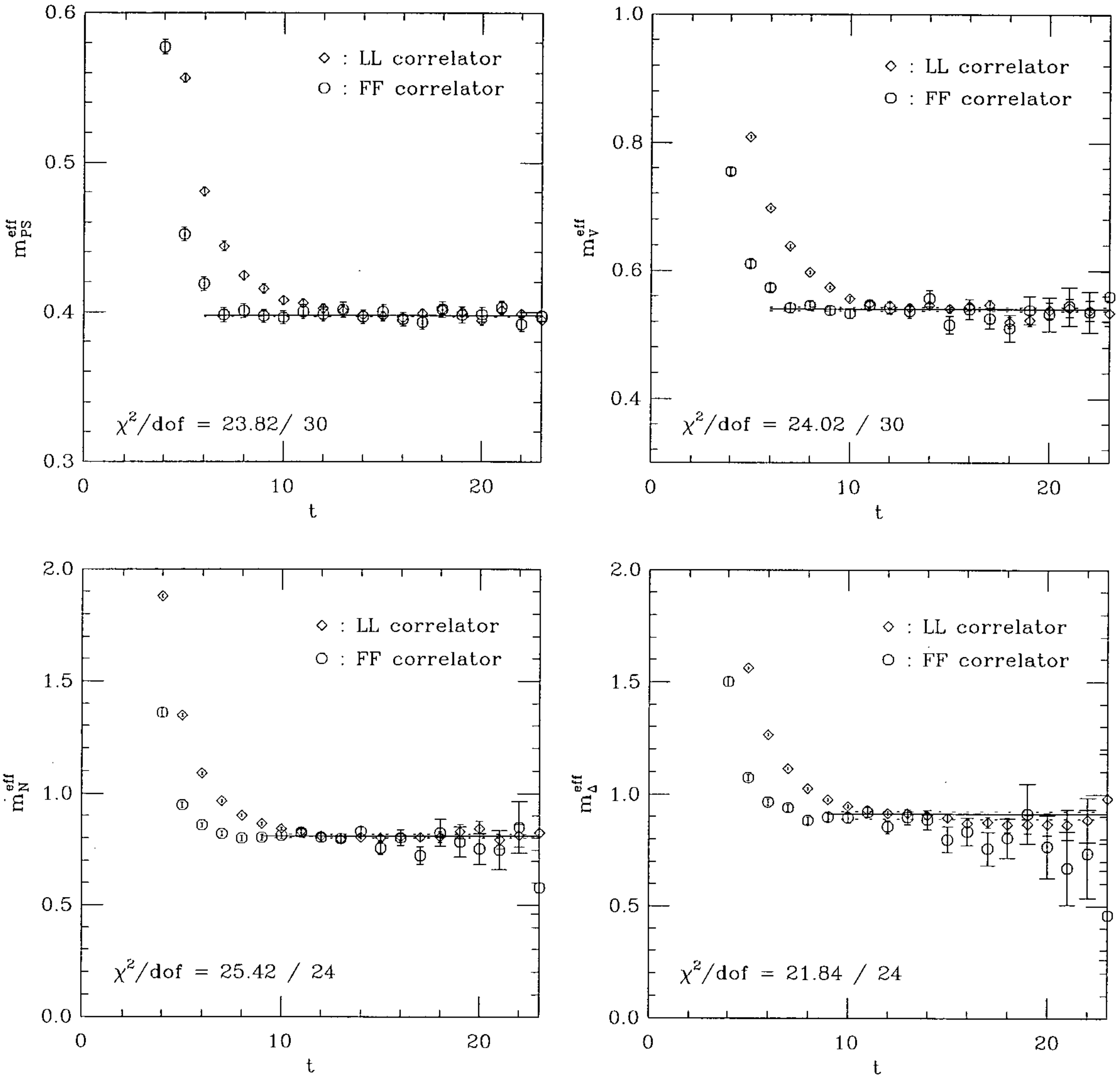

Figure 3.5: As for Figure 3.3 for the $\beta = 6.0$ non-perturbatively improved data set for $\kappa = 0.13344$.

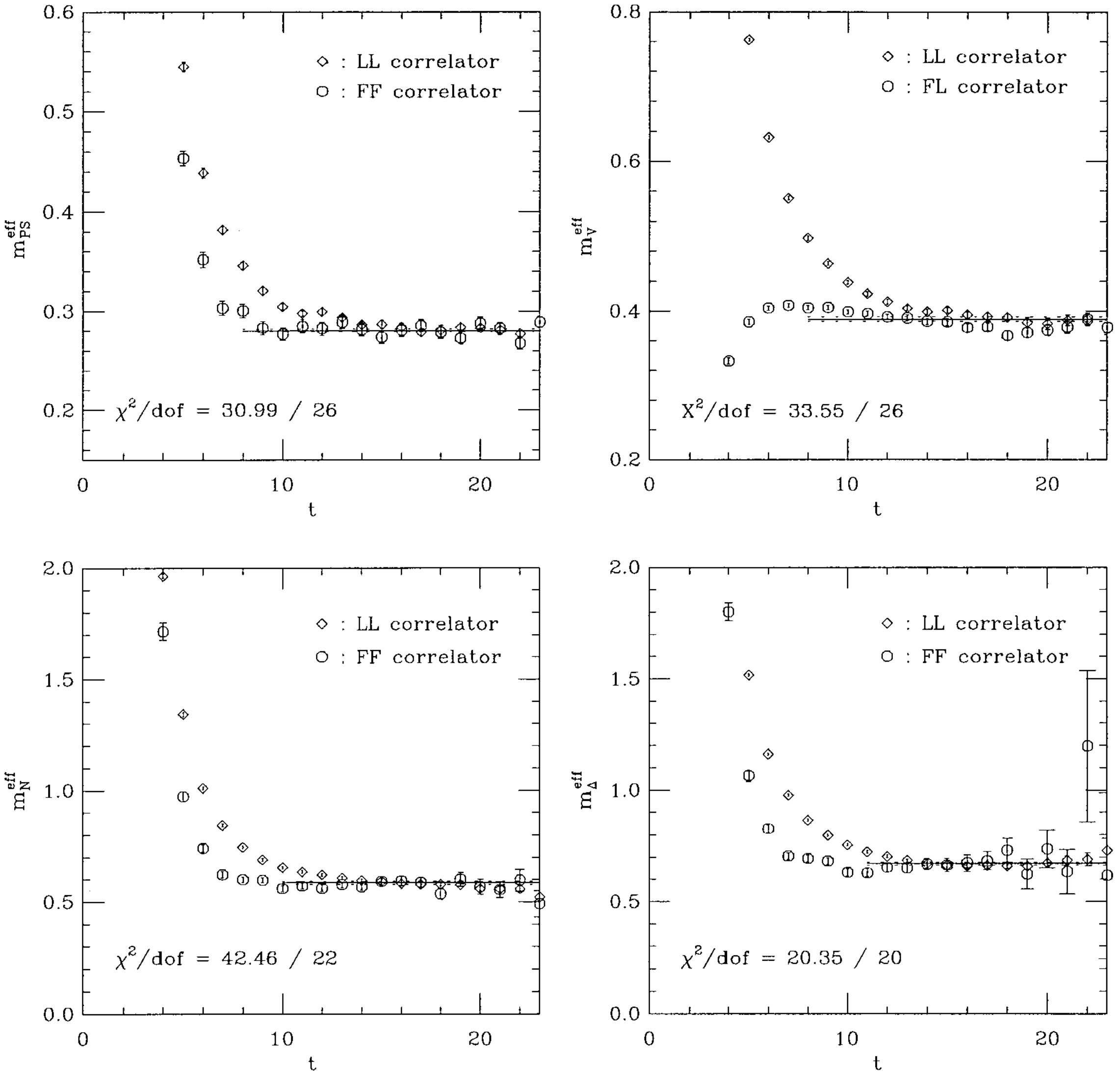

Figure 3.6: As for Figure 3.3 for the $\beta = 6.2$ non-perturbatively improved data set for $\kappa = 0.13460$.

3.2.2 Fitting the $\beta = 5.7$ tadpole improved data set

The correlators from the $\beta = 5.7$ tadpole improved data set were generated using the Jacobi smearing technique detailed in section 2.5. Both local correlators, LL, and source smeared correlators, SL, were used in the analysis. Simultaneous fits were performed using the double cosh form of equation 3.2 to the LL,SL pair of correlators. Figure 3.7 shows the effective mass plots for the LL and SL correlators for the heaviest quark mass. The final mass values are superimposed on the graph, showing the fit ranges selected. Following a sliding window analysis and a consistency check with the results obtained from a single cosh fit to the SL correlator, a fit range of [6-15] or [5-15] was selected for the pseudoscalar as this gave the best χ^2/d.o.f. The vector was fitted similarly in the range [7-15]. For this data set only degenerate correlators were generated for the baryons. Fits were performed using a double exponential fit to the LL,SL combination of correlators. A fit range of either [6-15] or [7-15] was selected for the delta and nucleon.

3.2.3 Fitting the $\beta = 6.0$ large volume data set

The large volume non-perturbatively improved correlators at $\beta = 6.0$ were generated using Jacobi smearing. Correlator combinations smeared at the source, SL, or at the source and sink, SS, were simulated. For this data set purely local correlators were not created. This means that it was no longer possible to perform simultaneous fits to pairs of correlators to extract the ground and excited state. The final fits for the mesons were selected from a single cosh fit to the SL correlator. The SS correlator was examined using a similar fit but the signal was much noisier and a better χ^2/d.o.f. was not obtained. It was possible to fit the pseudoscalar all the way out to $t_{\mathrm{max}} = 31$, since the signal to noise ratio does not increase with time for the pseudoscalar meson. This can be seen by examining the variance of a general hadron correlator

$$\sigma^2 = \left\langle \{\mathcal{O}_{\mathrm{H}}(x)\}^2 \{\mathcal{O}_{\mathrm{H}}^{\dagger}(0)\}^2 \right\rangle - \left\langle \mathcal{O}_{\mathrm{H}}(x) \mathcal{O}_{\mathrm{H}}^{\dagger}(0) \right\rangle^2 \tag{3.4}$$

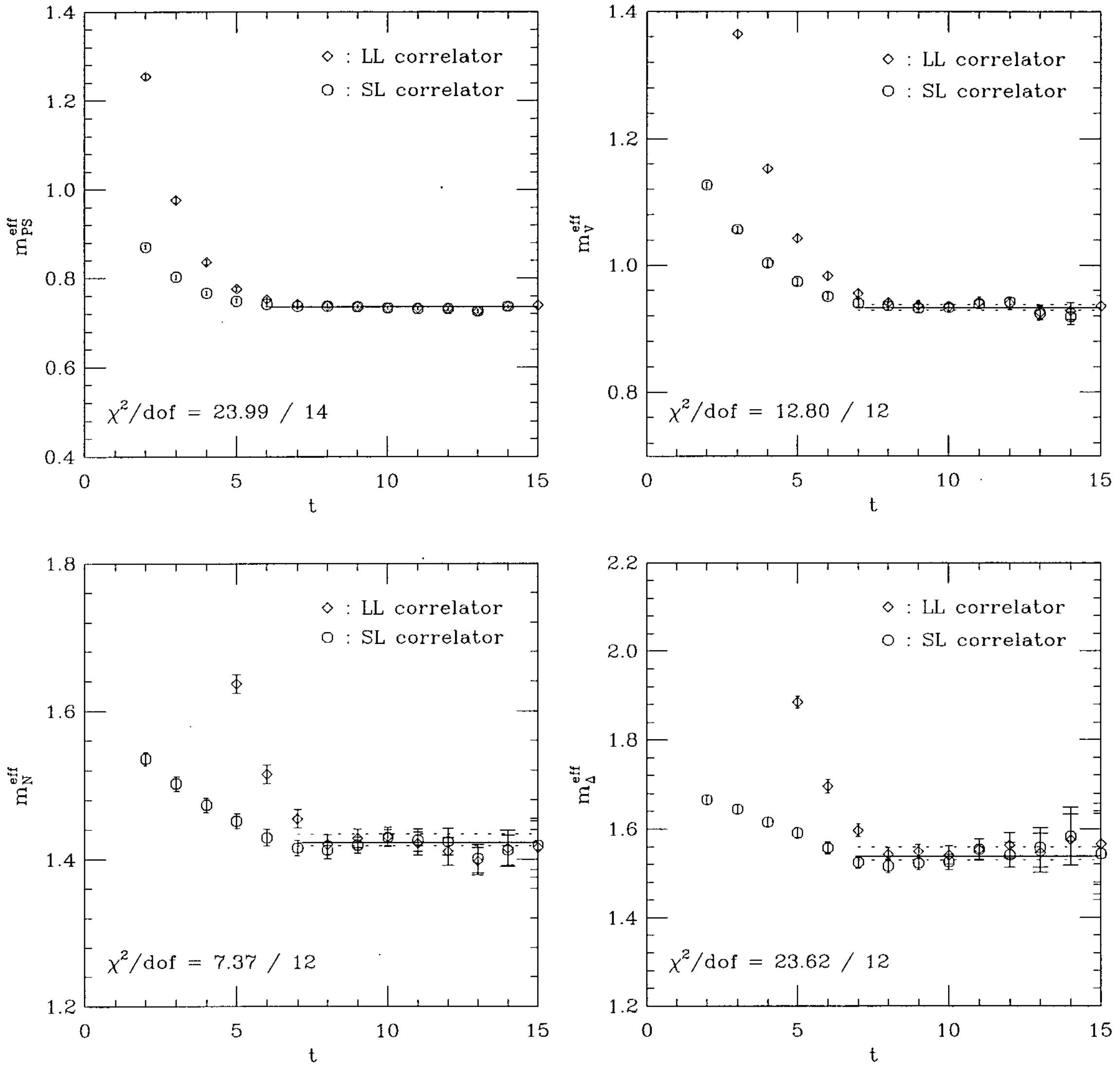

Figure 3.7: As for Figure 3.3 for the $\beta = 5.7$ tadpole improved data set for $\kappa = 0.13843$.

The error in the signal is dominated by the exponential decay of the lightest state which is created by the first term in this equation [63]. Through the squaring of the hadron operators, the first term has positive charge conjugation and parity quantum numbers which means that the lightest state is given by 2 π's for mesons and 3 π's for baryons. Thus the variance is approximately

$$\sigma^2 \propto e^{(nm_\pi - 2m_{\mathrm{H}})t}, \qquad n = 2, 3 \tag{3.5}$$

where $n = 2$ for meson correlators and $n = 3$ for baryons. This shows that the error in the mass grows exponentially with time except for the pseudoscalar correlator where $\sigma^2 \propto$ constant, since $m_{\mathrm{H}} = m_\pi$ and $n = 2$ in this case.

For the vector channel, t_{max} was reduced to 20. After this point the signal became too noisy and the fits were unstable. Figure 3.8 shows the effective mass plots for the SL correlator for the heaviest quark mass, for the pseudoscalar, vector, nucleon and delta. The final fitted results for the masses, and the χ^2/d.o.f., are superimposed on the plots. For the baryons it was possible to perform a double exponential fit to both the ground state and first excited state using the SL correlator. At large times the signal becomes noisy and t_{max} was reduced to 18 for the nucleon and 16 for the delta. The minimum time slice selected was $t_{\mathrm{min}} = 2$ or $t_{\mathrm{min}} = 3$, where t_{min} was able to be reduced much further due to the fact that the first excited state was included in the fit.

3.3 Computation of the PCAC mass

This section discusses the determination of the partially conserved axial current (PCAC) mass for all the quenched data sets. The method described below can be used to directly extract lattice estimates of the bare unrenormalised quark mass from the correlator data.

In the continuum, using Euclidean spacetime co-ordinates, the isovector axial current, $A_\mu(x)$, satisfies the PCAC relation (previously defined in equation 1.66)

$$\partial_\mu A_\mu(x) = 2m_{\mathrm{PCAC}} P(x) \tag{3.6}$$

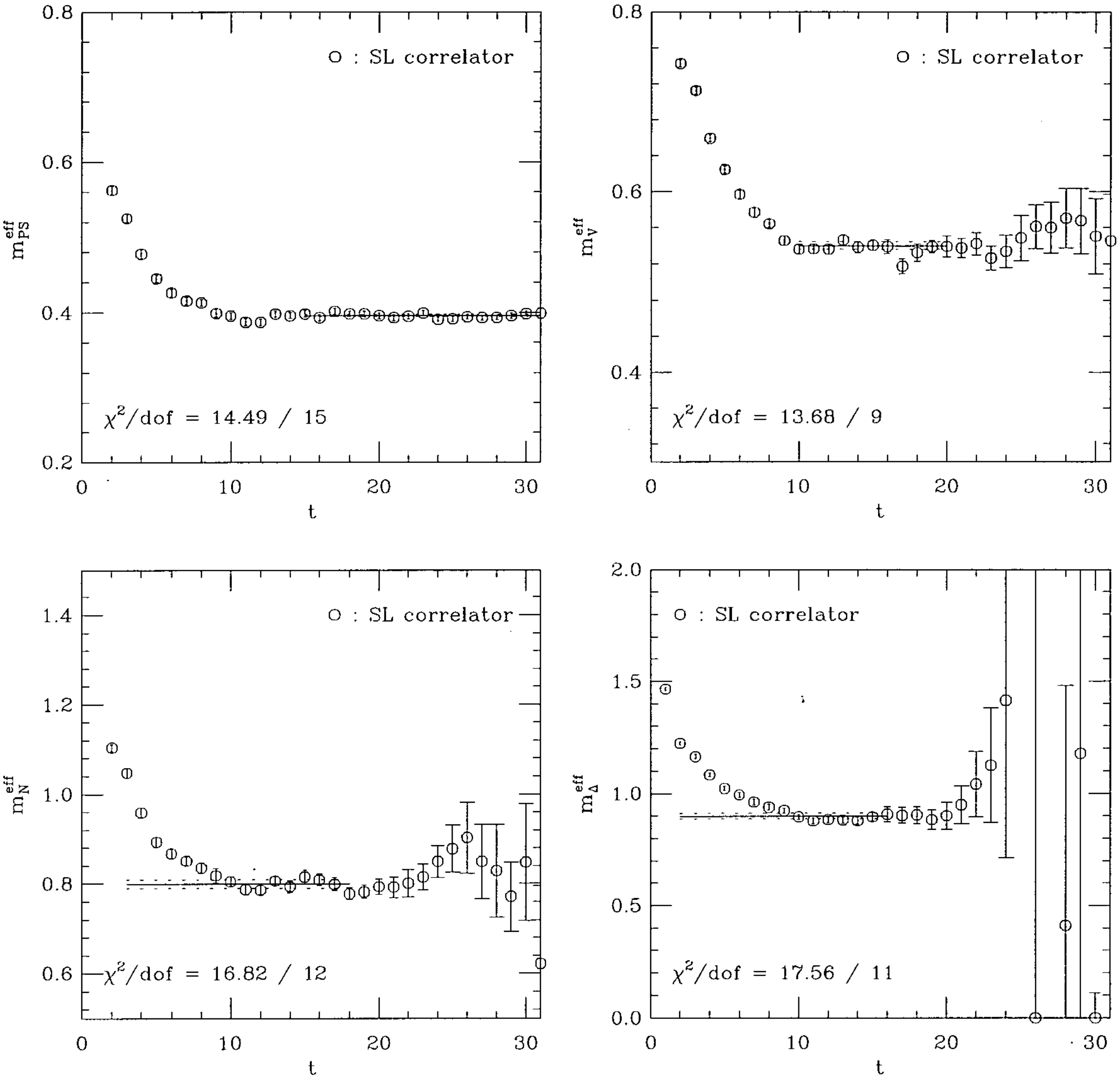

Figure 3.8: As for Figure 3.3 for the large volume $\beta = 6.0$ non-perturbatively improved data set. The plots show the SL correlator used in the final fit for $\kappa = 0.13344$. Superimposed on the graphs is the fit range selected and the value of the fitted mass obtained from a fit to the ground state for the mesons and to the ground and first excited state for the baryons.

where $P(x)$ is the pseudoscalar density and m_{PCAC} is the current quark mass. The isospin indices have been suppressed for clarity. On the lattice this relation can be expressed as [25]

$$\tilde{\partial}_\mu \left\langle A_\mu(x)\mathcal{O}^\dagger(0)\right\rangle = 2m_{\mathrm{PCAC}} \left\langle P(x)\mathcal{O}^\dagger(0)\right\rangle + O(a) \tag{3.7}$$

where $\tilde{\partial}_\mu$ denotes the average of the forward, ∂_μ, and backwards, ∂^*_μ, lattice derivatives and $\mathcal{O}$ is any operator. This holds everywhere except when $x = 0$. In the scheme of $O(a)$ improvement, the axial vector operator is replaced by the improved operator

$$A_\mu(x) \to A_\mu(x) + ac_{\mathrm{A}}\tilde{\partial}_\mu P(x) \tag{3.8}$$

where the improvement coefficient, c_{A} has been determined in one-loop perturbation theory using the bare coupling [29]

$$c_{\mathrm{A}} = -0.00756\ g_0^2 + O(g_0^4) \tag{3.9}$$

and more recently non-perturbatively [30]

$$c_{\mathrm{A}} = -0.00756\ g_0^2 \times \frac{1 - 0.748\ g_0^2}{1 - 0.977\ g_0^2} + O(g_0^6), \qquad 0 \le g_0^2 \le 1 \tag{3.10}$$

Choosing the operator $\mathcal{O}$ to be the pseudoscalar operator defined in Table 2.1, the $O(a)$ improved identity is

$$\tilde{\partial}_\mu \left\langle A_\mu(x)P^\dagger(0)\right\rangle + ac_{\mathrm{A}}\partial_\mu\partial^*_\mu \left\langle P(x)P^\dagger(0)\right\rangle = 2m_{\mathrm{PCAC}} \left\langle P(x)P^\dagger(0)\right\rangle + O(a^2) \tag{3.11}$$

Note that trace over the isospin indices in the operators as defined in equation 1.67 has been taken, where the normalisation condition for the Pauli matrices results in an overall constant which can be divided out. Taking the Fourier transform and writing equation 3.11 in terms of momentum space correlation functions with zero three-momentum, the PCAC mass can be determined from

$$m_{\mathrm{PCAC}} = \frac{\tilde{\partial}_4 C_{\mathrm{A_4P^\dagger}}(\mathbf{0},t) + ac_{\mathrm{A}}\partial^*_4\partial_4 C_{\mathrm{PP^\dagger}}(\mathbf{0},t)}{2C_{\mathrm{PP^\dagger}}(\mathbf{0},t)} \tag{3.12}$$

where ∂_4 is the temporal lattice derivative and the lower indices on each correlator indicate the operators (defined in Table 2.1) from which they are composed. A fit to this ratio of correlators was performed using a correlated least-χ^2 fit to a plateau function to determine the PCAC mass. For the tadpole data sets the one-loop value for c_A was used. The non-perturbative value was used for the other data sets. Local sink and source fuzzed or smeared correlators were used in the analysis. Figure 3.9 shows an example effective mass plot and sliding window analysis plots for the $\beta = 6.0$ non-perturbatively improved data set for $\kappa = 0.13344$. The effective mass was evaluated by performing the ratio of the relevant time sliced correlators. The graphs show that the plateau is very stable over a large range of time slices and that the mass determined from a sliding window analysis has very small errors. The fit range selected was [12-22]. Note that the errors on the PCAC mass are in general very small. Heavier quark masses show a similar picture, but with a slightly noisier signal. The final results for m_{PCAC} can be found in appendix A.

3.4 Finite volume effects

The finite size of the lattice simulation is a potential source of large errors in the spectrum calculation if the lattice dimensions are too small. Finite volume effects can originate from several sources. The volume can be too small to contain the wavefunction of the bound state as discussed in [64, 65], or errors can arise from the squeezing of the cloud of virtual particles which surround point-like hadrons [66]. Both of these effects occur as a result of virtual particle propagation across the lattice boundary due to the imposition of periodic boundary conditions. In a hadron state consisting of loosely bound constituents, the particle which propagates across the boundary can be one of the constituents. Multiple copies of the hadron can also interact directly across the boundary [67]. Finite size effects can be reduced by simulating at large enough lattice volumes. To compensate for the finite size of the lattice, simulations should ideally be performed at several different volumes to enable an extrapolation to the infinite volume limit. However, in this case, an estimate of the finite volume effects present in the quenched

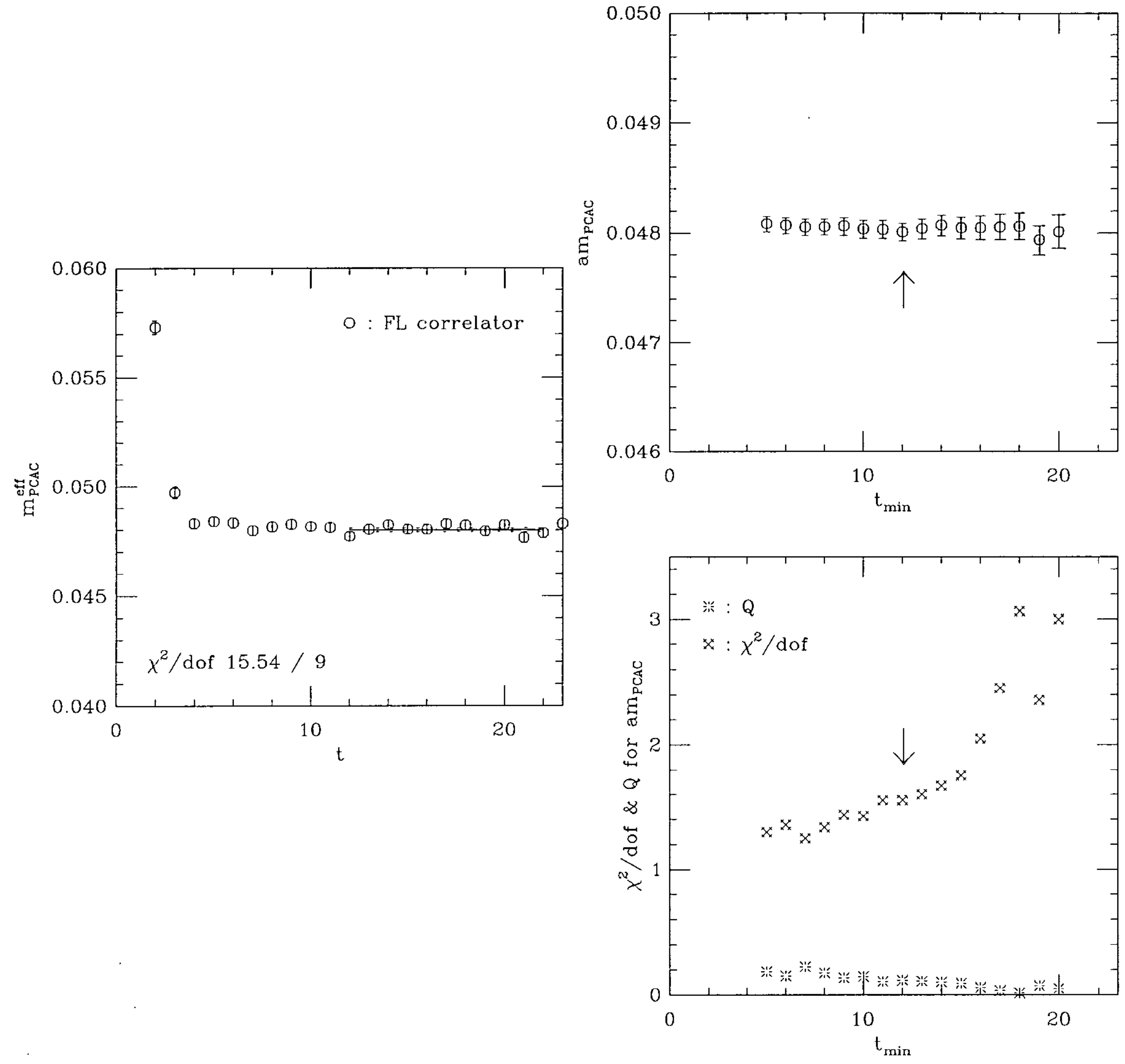

Figure 3.9: The left-hand plot shows the effective mass for the PCAC mass for the non-perturbatively improved $\beta = 6.0$ data set at $\kappa = 0.13344$. Superimposed on the graph is the final value and fit ranged selected from the sliding window analysis shown in the right-hand plots. The arrow indicates the minimum time slice selected and the value of the mass, χ^2/d.o.f. and Q values obtained by varying t_{min}.

calculation was investigated for two different volumes (1.5 and 3.0 fm) at $\beta = 6.0$ for the non-perturbatively improved fermion action.

For the pseudoscalar, the percentage difference for the masses determined on the two different volumes was approximately 0.6% for the heaviest quark mass, rising to 1.5% for the lightest. In all cases the difference was a 2σ effect. The pseudoscalar masses, shown in Table A.2, are smaller for the larger volume and the difference between the two results tends to increase with decreasing quark mass. This is in line with expectations that lighter hadrons, having a greater Compton wavelength and thus a greater extent on the lattice, are more susceptible to finite volume effects. In the case of the vector meson a comparison of the results in Table A.4 indicated that statistically significant finite volume effects were not observed. At the lightest quark mass, the difference was just 0.7σ. In contrast to the pseudoscalar, the vector masses for the larger volume were slightly larger.

In order to investigate whether this mass difference in the pseudoscalar could be attributed to the fact that no mass estimate for the excited state was available for the large volume, single cosh fits were performed on the smaller lattice. These results were entirely consistent with those obtained from the double cosh fits. However, it was possible to choose small fitting intervals close to $t_{\max}$ for the single cosh fits which yielded mass results compatible with those obtained on the larger volume, albeit with larger errors. The conclusion is then that no finite size effects are observed for the vector, and small yet statistically significant effects appear to be present in the pseudoscalar mass. However, it cannot be ruled out that the finite size effects in the pseudoscalar mass have a statistical origin without further investigation.

Finite size effects are expected to be more pronounced in the baryons, due to the greater extent of the bound state wavefunction. Examining the masses obtained for both volumes for the octet baryons in Tables A.8, A.12 and A.15, the percentage difference in the masses ranges from 1.2% for the heaviest quark masses to 3.6% for the lightest. The deviation is around one σ, where the masses on the larger volume are smaller. For the decuplet baryons in Tables A.6

and A.10, a greater finite volume effect was observed. The mass difference ranges from 2.3% to 5.3% at the lightest quark mass. Here the deviation is around 2σ and again the masses are in general lighter for the larger volume. The effect in the octet baryons, although twice as large as the effect in the pseudoscalar, is not significant given the level of statistical accuracy of the data. However the finite size effects in the decuplet baryons have a more significant impact on the final results.

3.5 The Edinburgh plot

The Edinburgh plot [68] is a useful way of comparing results for different actions and lattice spacings without the need for any extrapolations of the data. The mass ratio of the nucleon and vector meson is plotted against the mass ratio of the pseudoscalar to vector meson for the degenerate data. Figure 3.10 shows the Edinburgh plots for the tadpole and non-perturbatively improved data sets. If the data sets exhibit scaling as described in section 1.12, then the data points should lie on the same universal curve. Shown on the graphs are the experimental ratios and the values obtained in the static quark limit, where the hadron mass is equal to the sum of the valence quark masses. The data is compared with the curve obtained from the phenomenological model for the hadron masses described in [69]. The model predicts the hadron masses from the following equations

$$M_{\text{baryon}} = M_{\text{b}} + \sum_{i=1}^{3} m_i + \xi_{\text{b}} \sum_{i>j} \frac{\boldsymbol{s}_i \cdot \boldsymbol{s}_j}{m_i m_j} \tag{3.13}$$

$$M_{\text{meson}} = M_{\text{m}} + \sum_{i=\bar{q},q} m_i + \xi_{\text{m}} \sum_{i>j} \frac{\boldsymbol{s}_{\bar{q}} \cdot \boldsymbol{s}_q}{m_{\bar{q}} m_q} \tag{3.14}$$

where the constants are taken to have the values, $M_{\text{b}} = 0.077$ GeV, $M_{\text{m}} = -0.057$ GeV, $\xi_{\text{b}} = 0.02205$ GeV^3 and $\xi_{\text{m}} = 0.0715$ GeV^3. These formulae depend on the masses, m_i, and the spin, $\boldsymbol{s}_i$, of the constituent quarks of the hadron in question. The curve is shown as a guide for the eye. The data points show good agreement with the model curve, but it is hard to draw conclusive evidence of the effect of improvement between the tadpole and the non-perturbatively improved results.

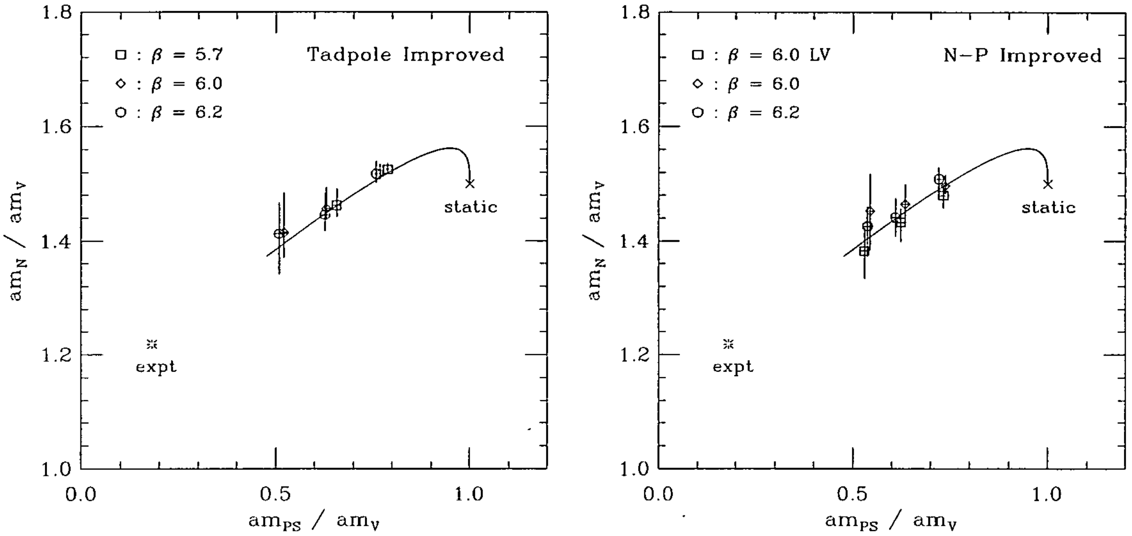

Figure 3.10: Edinburgh plots for the degenerate hadrons for the tadpole and non-perturbatively improved data sets. The phenomenological curve is shown as a guide for the eye. The graph shows both the experimental value and the static quark limit.

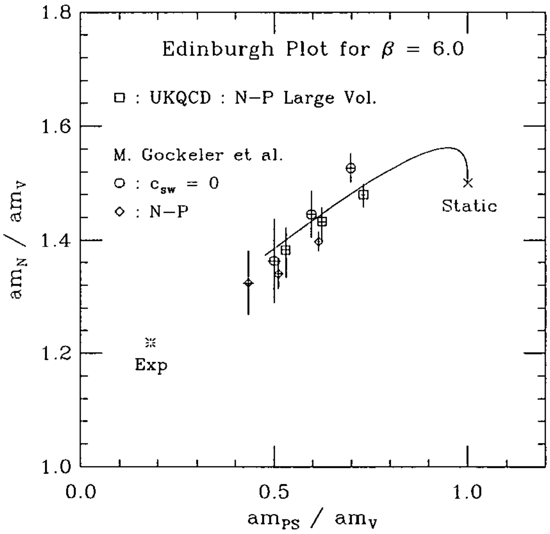

Figure 3.11: Edinburgh plot at $\beta = 6.0$. Results for the large volume data set are compared with results from [70] for data sets using both non-perturbatively improvement (◇) and no improvement (○).

To investigate the effect of improvement, the large volume data can be compared with recent results reported in [70] for $\beta = 6.0$, shown in Figure 3.11. At lighter quark masses the results are all in agreement within errors, with the unimproved results increasing more rapidly as the quark mass is increased. The data from [70] have been compared with the large volume data set rather than the small volume data. The reason for this was because of the finite volume effects present in the nucleon for the smaller volume which has the effect of increasing the nucleon mass as can be seen from Figure 3.10. To observe any deviation of the quenched spectrum results from experiment it is better to study quantities which are defined purely in terms of the meson masses, such as the J *parameter.*

3.6 The J parameter

The J parameter [71] is defined as

$$J = m_{\mathrm{V}} \frac{dm_{\mathrm{V}}}{dm_{\mathrm{PS}}^2}, \qquad \frac{m_{\mathrm{V}}}{m_{\mathrm{PS}}} = \left(\frac{M_{\mathrm{K}^*}}{M_{\mathrm{K}}}\right)_{\mathrm{phys}} \tag{3.15}$$

where J is evaluated at the experimental mass ratio of the K and K* mesons. (Throughout this thesis, lower case letters denote lattice masses while capitals denote their physical values). It enables a comparison of the meson sector of the spectrum with experiment without the need for a chiral extrapolation. As an alternative, the J parameter can instead be evaluated at the mass ratio, $M_\phi / M_{\eta_s} = 1.49$, where this value has been obtained by assuming the valence quark content of the the η_s pseudoscalar meson is purely strange, (strictly speaking the η_s meson is not detected experimentally). The J parameter is determined by performing a correlated fit to the linear relation

$$m_{\mathrm{V}} = A + B m_{\mathrm{PS}}^2 \tag{3.16}$$

to calculate the slope, B, which is then multiplied by the K* mass in lattice units, where the mass of the K* is determined from the intercept of equation 3.16 with the experimental ratio, $M_{\mathrm{K}^*}/M_{\mathrm{K}}$. Figure 3.12 shows the results of a fit to equation 3.16 for the $\beta = 6.0$ non-perturbatively improved data set. The lattice values for the meson masses at the mass ratios, $M_{\mathrm{K}^*}/M_{\mathrm{K}}$ and M_ϕ/M_{η_s} have been included in the plot. The plot shows that the data is well represented by a linear fit.

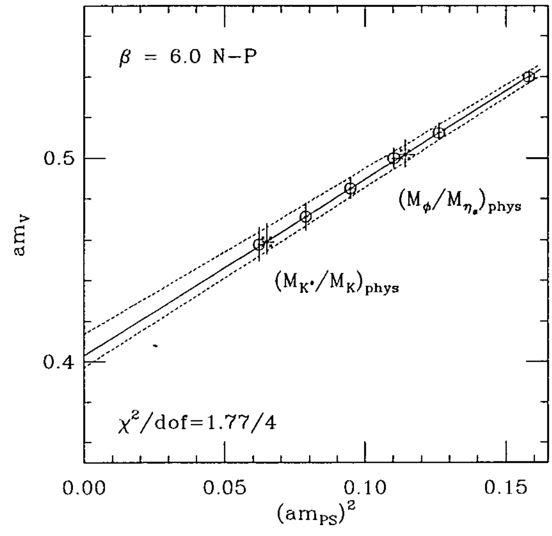

Figure 3.12: The vector meson mass plotted against the squared pseudoscalar mass for the $\beta = 6.0$ non-perturbatively improved data set. A correlated linear fit was performed to the data. The lattice masses at the $M_{\mathrm{K}^*}/M_{\mathrm{K}}$ mass ratio and the ratio M_ϕ/M_{η_s} have been shown by the crosses on the plot.

Using experimental values as input, the phenomenological value for $J = 0.48(2)$. Figure 3.13 shows the values obtained for the J parameter for all the quenched data sets, plotted against the value of the lattice spacing in units of the Sommer scale, r_0, defined later in section 3.7. The plots show that while the results for each data set are consistent with each other, showing little a dependence, they fail to reproduce the experimental value. Evaluating J at the ϕ meson mass ratio, gives an increased value, but which is still inconsistent with experiment. Since J is consistently low, this suggests that the discrepancy in the J parameter has little to do with lattice artifacts and instead appears to be an intrinsic feature of the quenched approximation. In the left-hand plot in Figure 3.13 the result for J determined by D. Becirevic et al. [72] for their $\beta = 6.2$ non-perturbatively

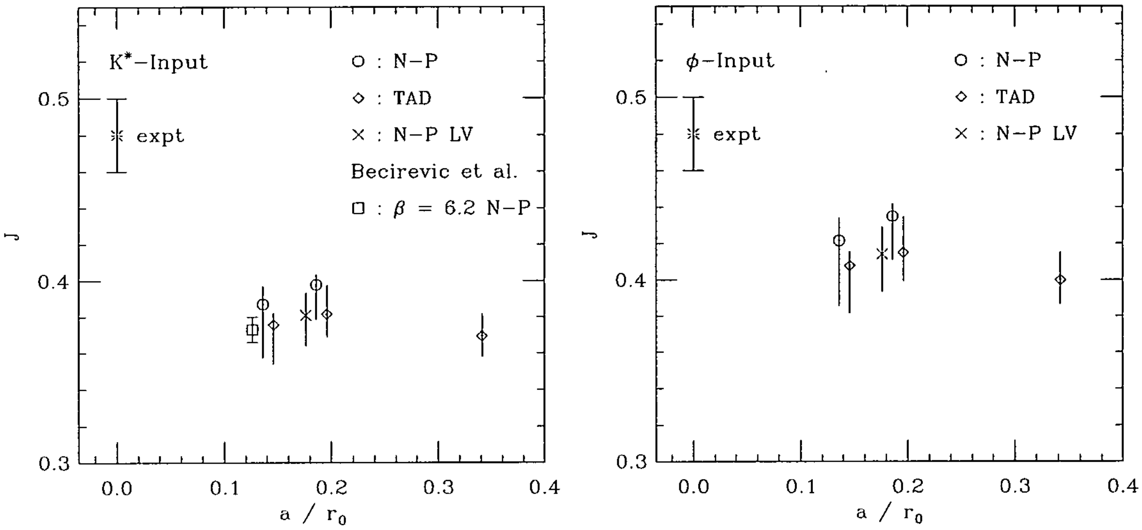

Figure 3.13: The J parameter for the quenched data sets plotted against the lattice spacing in units of r_0. The results have been offset for clarity. In the left-hand plot J has been evaluated at the M_{K^*}/M_K mass ratio and by the ratio M_ϕ/M_{η_s} in the right-hand plot. Results are compared with the $\beta = 6.2$ non-perturbatively improved data set (□) from [72].

improved data set is shown. Their result is consistent with the findings reported here.

Related to the J parameter, the *vector-pseudoscalar hyperfine splitting* is another quantity which can be compared with experimental results without requiring an extrapolation to the physical quark masses. In order to compare the results from data sets with different β's first the lattice scale must be set.

3.7 Setting the scale

The lattice spacing, a, is set by comparing a physically measured quantity with its value in lattice units. One quantity which can be used to set the scale is the Sommer scale r_0 [73], given by

$$F(r_0/a)(r_0/a)^2 = 1.65, \qquad r_0 = 0.5\text{fm} \tag{3.17}$$

where $F(r_0/a)$ is the force between a static quark anti-quark pair separated by a distance r_0/a. The value of 1.65 has been chosen such that $r_0 = 0.5$fm in physical units when compared with phenomenological effective potential models. This characteristic length scale, r_0, has been chosen to be in the region where the potential is well defined. However since the pure gauge theory is unphysical, r_0 cannot be determined directly by experiment. Choosing r_0 to set the lattice scale has the advantage that it can be calculated with good statistical precision and is defined in the same way for both quenched and dynamical gauge configurations, which means it can be used to compare results in both regimes. In contrast, selecting the string tension, K, to set the scale

$$K = \lim_{r/a \to \infty} F(r/a) \tag{3.18}$$

requires that the limit of infinite distance be taken for the potential, which becomes more difficult as the errors in the potential measurement increase with the separation. Additionally, the string is expected to break in dynamical simulations where pair production is expected to occur as the separation increases.

The ALPHA Collaboration [74] have performed an interpolation of their results for r_0 to yield the formula

$$\ln(a/r_0) = -1.6805 - 1.7139(\beta - 6) + 0.8155(\beta - 6)^2 - 0.6667(\beta - 6)^3 \quad (3.19)$$

from which r_0/a can be determined for β values in the range $6.57 \geq \beta \geq 5.7$. All the values for the Sommer scale for the quenched data sets have been computed from equation 3.19, where the relative error has been evaluated using the linear relation, described in [74]

$$e_{\text{rel}} = 10/29 \times \beta - 1.67 \quad (3.20)$$

The scale can be set using the lattice values of various hadron masses. The method used to determine the K* mass was described in section 3.6. The ρ meson mass can be determined in the same way by instead considering the physical ratio, M_ρ/M_π. Although the ρ meson is stable in the quenched approximation, it is expected to couple to two π's in dynamical fermion simulations. For this reason the ρ was only used to set the scale in order to compare the final results.

3.8 Hyperfine splitting

Experimentally the vector-pseudoscalar hyperfine mass splitting has a roughly constant value of ${m_V}^2 - {m_{PS}}^2 \approx 0.55\text{GeV}^2$ for a wide range of quark masses. Heavy quark symmetry [75] predicts that this should indeed be the case for heavy-light mesons. For mesons composed from one light quark, (u, d, s) and one heavy quark, (c, b), only the quantum numbers associated with the light degrees of freedom (the light quark and the gluons) dictate the properties of the bound state. This means that the hyperfine splitting for heavy-light mesons should be independent of the mass and spin of the heavy quark up to correction terms proportional to the inverse of the square of the heavy quark mass. This thesis only examines mesons composed from light quarks, but by studying the results as the quark mass is increased, the probable results for the splitting in the heavy-light sector can be inferred. A detailed study of heavy-light meson spectroscopy in the quenched approximation can be found in [76], which finds that the physical mass splittings are significantly greater than the values obtained from the lattice simulation.

The hyperfine splitting has been plotted against the pseudoscalar mass squared in Figure 3.14 where the scale has been set by both r_0 and the K* mass. The data sets which use tadpole and non-perturbative improvement have been shown in separate plots in order to study the effect of improvement. The results are compared with the experimental results obtained from [14]. The physical mass values used for the π and K* have been computed by taking the average mass of the charged states with the neutral particle. The η_s has been assumed to be composed purely of strange valence quarks. Comparing the tadpole and non-perturbatively improved plots, the a dependence appears reduced for the fully $O(a)$ improved case, particularly when the scale is set by r_0. (This could be confirmed by comparing the results obtained on different lattices extrapolated to the same values of the meson masses).

Setting the scale with r_0, the results obtained overshoot the experimental points for the lighter quark masses. However if the scale is set from the K* mass the splittings underestimate the experimental results, as has been observed in a previous analysis of the quenched results [77]. This is because the results are very sensitive to the lattice scale. Choosing different quantities to set the scale results in slight differences which are magnified in the hyperfine splitting. In all cases there is a small but significant negative slope in the data as the quark mass is increased. This slope is shallower than results from the unimproved case reported in [57]. However this suggests that the results obtained from the lattice simulation fail to reproduce the observed very weak dependence of the hyperfine splitting on the quark mass. The implication is that for heavy-light mesons the hyperfine splitting will not be consistent with the experimental results.

Figure 3.15 compares the non-perturbatively improved data at $\beta = 6.0$ for the hyperfine splitting with the results reported in [70]. The results obtained

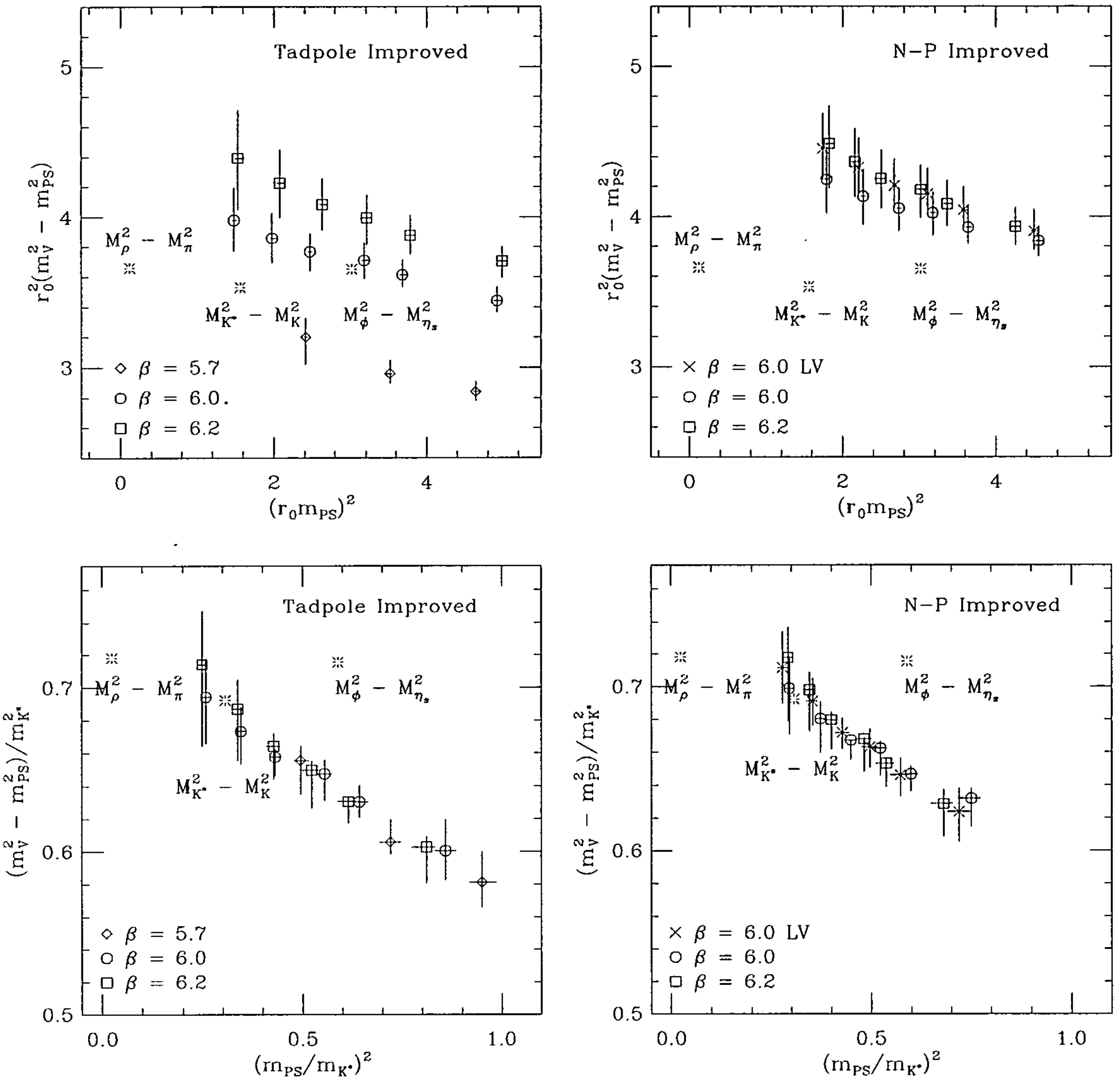

Figure 3.14: Vector-pseudoscalar hyperfine splitting for the tadpole improved and non-perturbative improved data sets. The scale has been set by the Sommer scale, r_0, and by the K* meson mass.

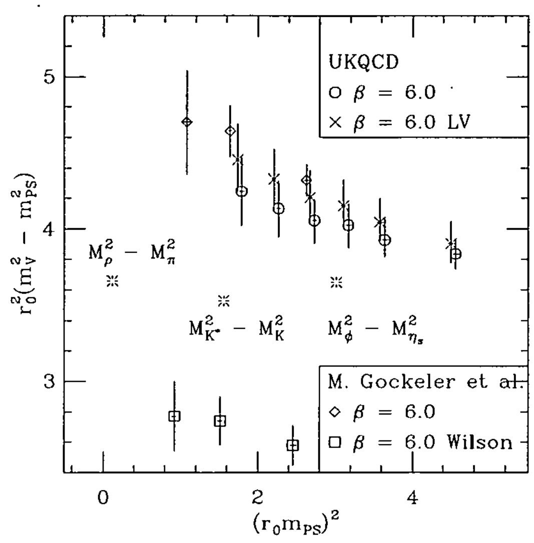

Figure 3.15: Vector-pseudoscalar hyperfine splitting at $\beta = 6.0$. Results for the non-perturbatively improved data sets are compared with results from [70] for data sets using both non-perturbatively improvement (◇) and no improvement (□).

for the non-perturbatively improved data sets are in agreement with the results from [70] within errors, with closer agreement occurring with the large volume data set. The unimproved Wilson data is much lower, showing that the effect of improvement is to increase the hyperfine splitting.

3.9 Chiral extrapolations

The hadron masses determined so far have been obtained at unphysical values of the quark masses. To determine the physical masses of the hadrons, they must first be extrapolated to the chiral limit, where the bare quark mass vanishes. This section discusses two ways of calculating the critical value of the hopping parameter, κ_{crit}, which determines the vanishing quark mass in the chiral limit.

3.9.1 Determination of κ_{crit} from the pseudoscalar mass

The Wilson fermion action explicitly breaks chiral symmetry and results in the additive renormalisation of the bare quark mass. The bare quark mass is defined as

$$m_{\mathrm{q}} = \frac{1}{2}\left(\frac{1}{\kappa} - \frac{1}{\kappa_{\mathrm{crit}}}\right) \tag{3.21}$$

The value of κ_{crit} is determined in the chiral limit when the quark mass is zero. From the partially conserved axial current (PCAC) relation this occurs when the squared mass of the pseudoscalar meson vanishes, $m_{\mathrm{PS}}^2 = 0$.

At lowest order in the chiral expansion of m_{PS}, this relationship can be expressed as

$$m_{\mathrm{PS}}^2 = B(\widetilde{m}_{\mathrm{q}_1} + \widetilde{m}_{\mathrm{q}_2}) \tag{3.22}$$

This is the simplest form consistent with $O(a)$ improvement for non-degenerate combinations of quarks, where the improved quark mass [25] is defined by

$$\widetilde{m}_{\mathrm{q}_i} = m_{\mathrm{q}_i}(1 + b_{\mathrm{m}} m_{\mathrm{q}_i}), \qquad i = 1, 2 \tag{3.23}$$

The improvement coefficient, b_{m} has been determined in one-loop perturbation theory [78] as

$$b_{\mathrm{m}} = -\tfrac{1}{2} - 0.0962 g_0^2 + O(g_0^4) \tag{3.24}$$

Recently a non-perturbative determination of b_{m} was performed at $\beta = 6.2$ as detailed in [79].

If the quark masses are very light, equation 3.22 will have additional terms from quenched chiral perturbation theory [80, 81]. The identification of the $\eta\prime$ meson as a pseudo-Goldstone boson in the quenched theory results in the addition of terms proportional to the log of the quark mass. These terms will only have an appreciable effect on the fit for small values of the quark mass. For the range of quark masses considered here the quark masses are sufficiently large that these correction terms are not representative of the data and hence they have not been taken into account. Significant contributions from quenched chiral logs have only been observed for quark masses smaller than the lightest mass used in these quenched simulations [4]. At the other end of the scale, possible contributions from higher order terms in the quark mass have to be considered. These higher order terms can occur from two possible sources. One possibility is a phenomenological effect, motivated by the Gell-Mann-Oakes-Renner formula [82]

$$m_{\rm PS}^2 = -\frac{4}{f_\pi^2}\left\langle\bar\psi\psi\right\rangle m_{\rm q} + O(m_{\rm q}^2) \qquad (3.25)$$

where f_π is the π decay constant and $\left\langle\bar\psi\psi\right\rangle$ is the chiral condensate. The other is due to lattice artifacts, which can be eliminated to $O(a)$ by using the improved quark mass. The latter is investigated using the following fit ansatz [83], constructed by inserting the improved mass into equation 3.22 and writing the resulting expression in terms of the hopping parameters

$$m_{\rm PS}^2 = \alpha + \beta\left(\frac{1}{\kappa_1}+\frac{1}{\kappa_2}\right) + \gamma\left(\frac{1}{\kappa_1^2}+\frac{1}{\kappa_2^2}\right) \qquad (3.26)$$

where the coefficients α, β and γ are related to B, $b_{\rm m}$ and $\kappa_{\rm crit}$ in the following way

$$\alpha = \frac{B}{\kappa_{\rm crit}}\left(-1+\frac{b_{\rm m}}{2\kappa_{\rm crit}}\right), \quad \beta = \frac{B}{2}\left(1-\frac{b_{\rm m}}{\kappa_{\rm crit}}\right), \quad \gamma = \frac{Bb_{\rm m}}{4} \qquad (3.27)$$

The fits were performed using an uncorrelated least-χ^2 fit to equation 3.26 for the parameters, B and $\kappa_{\rm crit}$. The value of $b_{\rm m}$ was used as input to the fit in order to constrain the fit and was thus not determined. Correlated fits were investigated, but resulted in large values for the χ^2/d.o.f. of up to 17 in the worst case. This may be due to the fact that the errors on the pseudoscalar mass squared are very small and thus the fit is tightly constrained. Large χ^2/d.o.f.'s have been observed by other collaborations [72, 84] for linear fits. Uncorrelated fits were therefore selected for the final choice of fits.

The effect on the fitted value of $\kappa_{\rm crit}$, resulting from varying the definitions of $b_{\rm m}$ used in the fit, was investigated. The tree-level (TL) value, corresponding to

$b_{\mathrm{m}}(\mathrm{TL}) = -0.5$ was compared with b_{m} as determined from equation 3.24 using both the bare coupling, $g_0^2 = 6/\beta$, and the "boosted" coupling, $g^2 = g_0^2/u_0^4$. Fits for the unimproved case, $b_{\mathrm{m}} = 0$, were investigated for completeness. The non-perturbative result for b_{m} at $\beta = 6.2$, where $b_{\mathrm{m}}(\mathrm{NP}) = -0.62(3)$, has also been included in the fits for the non-perturbative data set at $\beta = 6.2$. Table 3.3 shows the results for κ_{crit} obtained for each data set.

The results show that κ_{crit} is not very sensitive to the choice made for b_{m}. The greatest deviations occur for the $\beta = 5.7$ data set which could be due to the fact that only three points were used in the extrapolation. For the $\beta = 6.2$ non-perturbatively improved data set, the result obtained using the non-perturbative estimate for b_{m} is entirely consistent with the results obtained from the one-loop values. In order to be consistent for all the data sets, the boosted one-loop estimate for b_{m} was selected for the best fit. The final results are highlighted in bold in Table 3.3.

Comparing these results with the unimproved case yields results for κ_{crit} which are significantly higher. The χ^2/d.o.f. obtained in the fits for the unimproved case is slightly lower, suggesting that this is a better fit to the data. Other collaborations [72] have concluded that this suggests that there is an additional factor of $O(\widetilde{m}_{\mathrm{q}}^2)$ that must be included in the fit which is attributed to a real physical effect as in equation 3.25. However this may be due to the fact that they include heavier quark masses in the extrapolation. Another possibility is that the fit ansatz is too simple and a more complicated fit as described in [79] should be considered. This type of fit includes higher order terms in the improved quark mass fitted to a wide range of non-degenerate and degenerate combinations of quark masses, in order to distinguish between contributions from terms depending upon b_{m} and terms depending on the difference of further improvement coefficients (chosen to reduce the $O(am_{\mathrm{q}})$ errors) of the axial-vector and pseudoscalar operators, $b_{\mathrm{A}} - b_{\mathrm{P}}$. To examine these issues, the pseudoscalar mass squared was plotted against the averaged quark mass, $(\widetilde{m}_{\mathrm{q}_1} + \widetilde{m}_{\mathrm{q}_2})/2$ in lattice units. Figure 3.16 shows the fit to equation 3.22 for the $\beta = 6.0$ non-perturbative data set. The averaged quark mass has been determined using the value of κ_{crit} selected as the best fit. Note

Tadpole improved data sets

β	$L^3 \cdot T$	Value of $b_{\rm m}$		$\kappa_{\rm crit}$	χ^2/d.o.f.
5.7	$16^3 \cdot 32$	$b_{\rm m}$	$= 0$	$0.143408 \;^{+29}_{-45}$	0.08 / 1
		$b_{\rm m}(\textsc{tl})$	$= -0.5$	$0.143240 \;^{+26}_{-40}$	0.08 / 1
		$b_{\rm m}(g_0^2)$	$= -0.6013$	$0.143206 \;^{+26}_{-39}$	0.08 / 1
		$b_{\rm m}(g^2)$	$= -0.6844$	**0.143178** $^{+25}_{-39}$	**0.08 / 1**
6.0	$16^3 \cdot 48$	$b_{\rm m}$	$= 0$	$0.139240 \;^{+20}_{-\ 6}$	1.33 / 4
		$b_{\rm m}(\textsc{tl})$	$= -0.5$	$0.139216 \;^{+19}_{-\ 6}$	2.43 / 4
		$b_{\rm m}(g_0^2)$	$= -0.5962$	$0.139212 \;^{+19}_{-\ 6}$	2.74 / 4
		$b_{\rm m}(g^2)$	$= -0.6620$	**0.139209** $^{+19}_{-\ 6}$	**2.98 / 4**
6.2	$24^3 \cdot 48$	$b_{\rm m}$	$= 0$	$0.137912 \;^{+19}_{-13}$	1.48 / 4
		$b_{\rm m}(\textsc{tl})$	$= -0.5$	$0.137900 \;^{+18}_{-12}$	1.93 / 4
		$b_{\rm m}(g_0^2)$	$= -0.5931$	$0.137898 \;^{+18}_{-12}$	2.03 / 4
		$b_{\rm m}(g^2)$	$= -0.6517$	**0.137897** $^{+18}_{-12}$	**2.10 / 4**

Non-perturbatively improved data sets

β	$L^3 \cdot T$	Value of $b_{\rm m}$		$\kappa_{\rm crit}$	χ^2/d.o.f.
6.0	$16^3 \cdot 48$	$b_{\rm m}$	$= 0$	$0.135280 \;^{+17}_{-\ 9}$	0.14 / 4
		$b_{\rm m}(\textsc{tl})$	$= -0.5$	$0.135259 \;^{+16}_{-\ 9}$	0.42 / 4
		$b_{\rm m}(g_0^2)$	$= -0.5962$	$0.135255 \;^{+16}_{-\ 9}$	0.51 / 4
		$b_{\rm m}(g^2)$	$= -0.6620$	**0.135252** $^{+16}_{-\ 9}$	**0.58 / 4**
6.0	$32^3 \cdot 64$	$b_{\rm m}$	$= 0$	$0.135260 \;^{+\ 9}_{-11}$	0.19 / 4
		$b_{\rm m}(\textsc{tl})$	$= -0.5$	$0.135241 \;^{+\ 9}_{-10}$	0.34 / 4
		$b_{\rm m}(g_0^2)$	$= -0.5962$	$0.135237 \;^{+\ 9}_{-10}$	0.41 / 4
		$b_{\rm m}(g^2)$	$= -0.6620$	**0.135235** $^{+\ 9}_{-10}$	**0.47 / 4**
6.2	$24^3 \cdot 48$	$b_{\rm m}$	$= 0$	$0.135828 \;^{+17}_{-14}$	0.34 / 4
		$b_{\rm m}(\textsc{tl})$	$= -0.5$	$0.135818 \;^{+17}_{-14}$	0.40 / 4
		$b_{\rm m}(g_0^2)$	$= -0.5931$	$0.135816 \;^{+17}_{-14}$	0.42 / 4
		$b_{\rm m}(\textsc{np})$	$= -0.62$	$0.135816 \;^{+17}_{-14}$	0.42 / 4
		$b_{\rm m}(g^2)$	$= -0.6517$	**0.135815** $^{+17}_{-14}$	**0.43 / 4**

Table 3.3: Results for $\kappa_{\rm crit}$ obtained from an uncorrelated fit to equation 3.26 using different values for $b_{\rm m}$. Definitions of $b_{\rm m}$ used were: no improvement, tree-level and one-loop perturbation theory using both the bare and "boosted" coupling. For the non-perturbative $\beta = 6.2$ data set, the non-perturbative value for $b_{\rm m}$ has been included. The final results used in the rest of this thesis are highlighted in bold.

that in all the plots in this thesis the quark mass is always the improved quark mass.

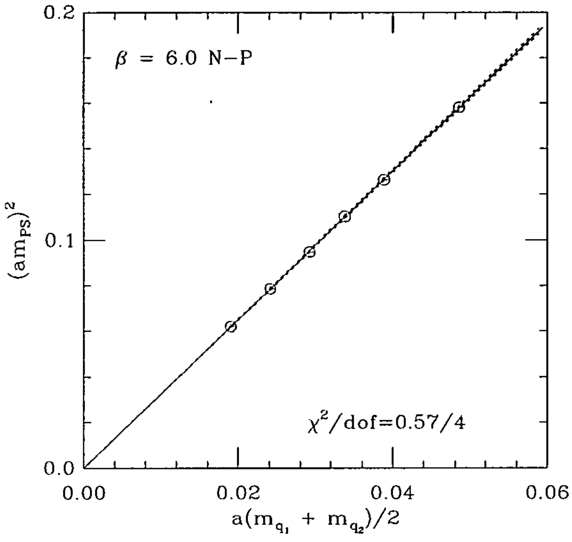

Figure 3.16: The pseudoscalar mass squared as a function of the average improved quark mass for the $\beta = 6.0$ non-perturbative data set. The data has been fitted to equation 3.22 using an uncorrelated fit.

Figure 3.17 shows fits to equation 3.22 for all data sets in units of r_0 in order to compare the tadpole improved and non-perturbatively improved data sets. The fit in units of r_0 has been performed using an uncorrelated fit using linear regression [49] to minimise the χ^2. Only the best fit has been shown. There is no evidence from the plots to suggest any deviation from the linear ansatz for the range of quark masses studied. Further analysis of the chiral behaviour of the pseudoscalar in [85] showed that the contributions of terms proportional to $(\widetilde{m}_{q1} - \widetilde{m}_{q2})^2$ constitute less than 1% of the overall error. The plots show improved scaling behaviour for the pseudoscalar meson for the non-perturbatively improved data sets relative to the tadpole data sets.

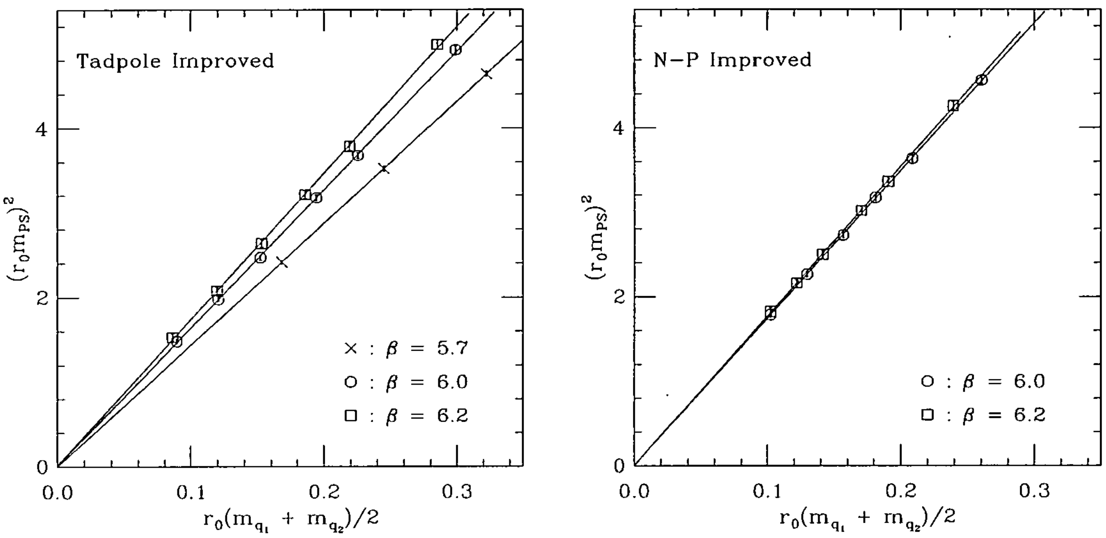

Figure 3.17: The pseudoscalar mass squared for the tadpole and non-perturbatively improved data sets plotted against the averaged improved quark mass, $(\widetilde{m}_{q_1} + \widetilde{m}_{q_2})/2$ in units of r_0. The improved quark mass has been determined using the boosted one-loop perturbative value of b_m.

3.9.2 Alternative determination of κ_{crit}

The critical value of the hopping parameter can alternatively be defined at the point where the unrenormalised PCAC mass vanishes [30]

$$m_{PCAC} = \tilde{B}(\widetilde{m}_{q_1} + \widetilde{m}_{q_2}) \tag{3.28}$$

The same fit ansatz in equation 3.26, used to extract κ_{crit} from the pseudoscalar mass squared, was used where m_{PS}^2 was replaced by m_{PCAC}. Following the same general fit procedure, the results for κ_{crit} are listed in Table 3.4. The results obtained for different definitions of b_m are again stable for $\beta \geq 6.0$, with the largest difference arising when using the unimproved value for b_m. Correlated fits were considered, but the resulting χ^2/d.o.f. was very large due to the fact that the errors on the PCAC mass are so small, thus tightly constraining the fit. The final values reported in Table 3.4 have been obtained from uncorrelated fits.

The results obtained for κ_{crit} from this method differ by terms of $O(a^2)$ from κ_{crit} determined from the pseudoscalar mass. Comparing the results for κ_{crit} from both methods shows that values determined from m_{PCAC} are in general lower with much smaller errors. At the smallest β the difference in the results for both methods is of $O(10^{-4})$. For the chiral extrapolations of all the other hadrons, the improved quark mass was determined using the one-loop boosted perturbation theory value for b_{m} and κ_{crit} from the pseudoscalar extrapolation, in preference to κ_{crit} determined from the PCAC mass. This was because the functional dependence of the baryons on the PCAC mass is more complicated.

3.9.3 Vector chiral extrapolation

Motivated by the results obtained for the quark mass dependence for the pseudoscalar meson, the lowest order chiral expansion for the vector meson was selected as the fit ansatz. Ignoring terms arising from quenched chiral perturbation theory, the fit ansatz was

$$m_{\mathrm{V}} = A + C(\widetilde{m}_{\mathrm{q}_1} + \widetilde{m}_{\mathrm{q}_2})/2 \tag{3.29}$$

In principle higher order terms in the improved quark mass can be included in the fit. Previous experience [39, 53, 86] has shown that for the range of quark masses considered here, the data shows no conclusive evidence of any deviation from the linear relation. An uncorrelated least-χ^2 fit was performed for all data sets, in order to maintain consistency with the pseudoscalar extrapolations, the results of which are displayed in Table 3.5. Figure 3.18 shows a fit to equation 3.29 for the $\beta = 6.0$ non-perturbative data set. This plot shows that the data is well described by the linear ansatz. Figure 3.19 shows the chiral extrapolations for the vector meson mass for all the quenched data sets where the scale was set by r_0. A reduced dependence on the lattice spacing for the non-perturbatively improved data sets is observed in the plots.

Tadpole improved data sets

β	$L^3 \cdot T$	Value of b_m		κ_crit	χ^2/d.o.f.
5.7	$16^3 \cdot 32$	b_m	$= 0$	$0.143149\ ^{+15}_{-13}$	4.49 / 1
		$b_\mathrm{m}(\mathrm{TL})$	$= -0.5$	$0.143005\ ^{+14}_{-12}$	4.49 / 1
		$b_\mathrm{m}(g_0^2)$	$= -0.6013$	$0.142976\ ^{+13}_{-11}$	4.49 / 1
		$b_\mathrm{m}(g^2)$	$= -0.6844$	$0.142953\ ^{+13}_{-11}$	4.49 / 1
6.0	$16^3 \cdot 48$	b_m	$= 0$	$0.139170\ ^{+7}_{-7}$	5.08 / 4
		$b_\mathrm{m}(\mathrm{TL})$	$= -0.5$	$0.139148\ ^{+6}_{-7}$	3.59 / 4
		$b_\mathrm{m}(g_0^2)$	$= -0.5962$	$0.139143\ ^{+6}_{-7}$	3.69 / 4
		$b_\mathrm{m}(g^2)$	$= -0.6620$	$0.139140\ ^{+6}_{-7}$	3.83 / 4
6.2	$24^3 \cdot 48$	b_m	$= 0$	$0.137911\ ^{+3}_{-3}$	2.96 / 4
		$b_\mathrm{m}(\mathrm{TL})$	$= -0.5$	$0.137899\ ^{+3}_{-3}$	1.67 / 4
		$b_\mathrm{m}(g_0^2)$	$= -0.5931$	$0.137897\ ^{+3}_{-3}$	1.83 / 4
		$b_\mathrm{m}(g^2)$	$= -0.6517$	$0.137896\ ^{+3}_{-3}$	1.99 / 4

Non-perturbatively improved data sets

β	$L^3 \cdot T$	Value of b_m		κ_crit	χ^2/d.o.f.
6.0	$16^3 \cdot 48$	b_m	$= 0$	$0.135209\ ^{+6}_{-5}$	3.36 / 4
		$b_\mathrm{m}(\mathrm{TL})$	$= -0.5$	$0.135190\ ^{+6}_{-5}$	1.22 / 4
		$b_\mathrm{m}(g_0^2)$	$= -0.5962$	$0.135186\ ^{+6}_{-5}$	0.99 / 4
		$b_\mathrm{m}(g^2)$	$= -0.6620$	$0.135184\ ^{+6}_{-5}$	0.86 / 4
6.0	$32^3 \cdot 64$	b_m	$= 0$	$0.135222\ ^{+6}_{-8}$	1.82 / 4
		$b_\mathrm{m}(\mathrm{TL})$	$= -0.5$	$0.135202\ ^{+6}_{-8}$	0.63 / 4
		$b_\mathrm{m}(g_0^2)$	$= -0.5962$	$0.135199\ ^{+6}_{-8}$	0.54 / 4
		$b_\mathrm{m}(g^2)$	$= -0.6620$	$0.135196\ ^{+6}_{-8}$	0.51 / 4
6.2	$24^3 \cdot 48$	b_m	$= 0$	$0.135819\ ^{+3}_{-3}$	0.86 / 4
		$b_\mathrm{m}(\mathrm{TL})$	$= -0.5$	$0.135809\ ^{+3}_{-3}$	0.32 / 4
		$b_\mathrm{m}(g_0^2)$	$= -0.5931$	$0.135807\ ^{+3}_{-3}$	0.30 / 4
		$b_\mathrm{m}(\mathrm{NP})$	$= -0.62$	$0.135807\ ^{+3}_{-3}$	0.30 / 4
		$b_\mathrm{m}(g^2)$	$= -0.6517$	$0.135806\ ^{+3}_{-3}$	0.30 / 4

Table 3.4: As for Figure 3.3 with κ_crit determined from the PCAC mass.

β	$c_{\rm sw}$	$L^3 \cdot T$	A	C	χ^2/d.o.f.
5.7	1.56	$16^3 \cdot 32$	$0.669\ ^{+13}_{-19}$	$2.40\ ^{+17}_{-\ 9}$	0.09 / 1
6.0	1.76	$16^3 \cdot 48$	$0.404\ ^{+11}_{-11}$	$2.79\ ^{+20}_{-20}$	0.08 / 4
6.0	1.76	$32^3 \cdot 64$	$0.414\ ^{+11}_{-10}$	$2.61\ ^{+19}_{-20}$	0.04 / 4
6.0	1.47	$16^3 \cdot 48$	$0.391\ ^{+\ 9}_{-\ 9}$	$2{:}65\ ^{+17}_{-16}$	0.25 / 4
6.2	1.61	$24^3 \cdot 48$	$0.304\ ^{+10}_{-11}$	$2.61\ ^{+30}_{-26}$	0.08 / 4
6.2	1.44	$24^3 \cdot 48$	$0.298\ ^{+\ 9}_{-\ 9}$	$2.64\ ^{+21}_{-22}$	0.09 / 4

Table 3.5: Fit parameters obtained for the vector from uncorrelated fits to equation 3.29 for all data sets.

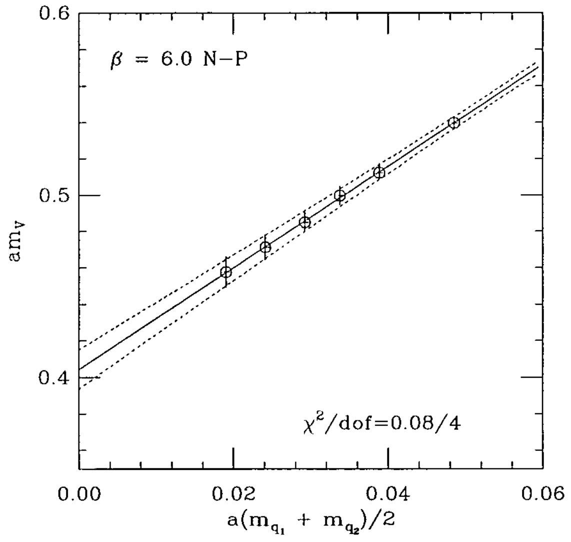

Figure 3.18: The vector mass as a function of the improved quark mass for the $\beta = 6.0$ non-perturbative data set. The data has been fitted to equation 3.29 using an uncorrelated fit.

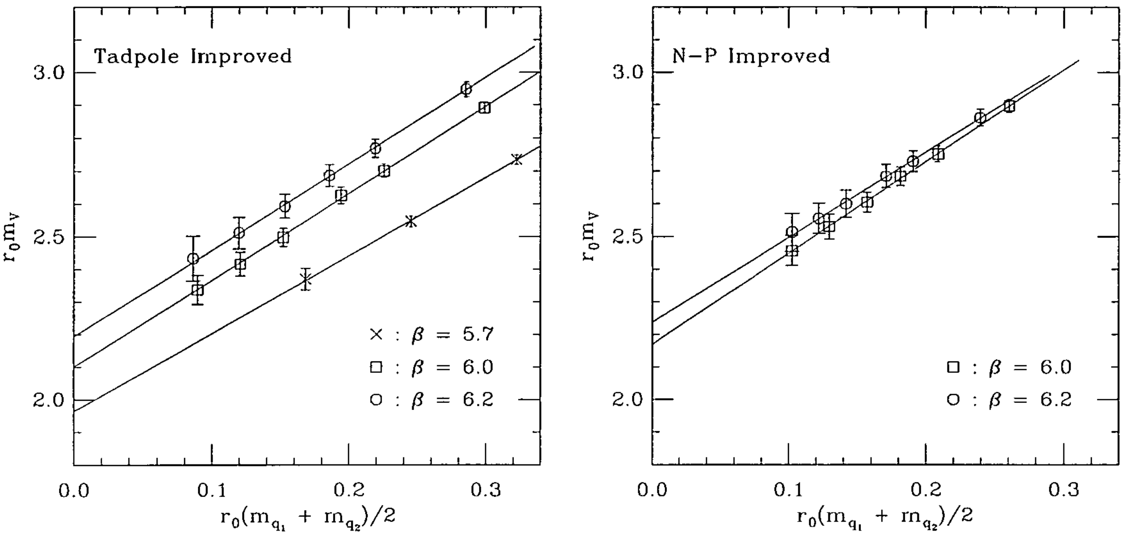

Figure 3.19: The vector mass for the tadpole and non-perturbatively improved data sets plotted against the averaged improved quark mass, $(\widetilde{m}_{\mathrm{q}_1} + \widetilde{m}_{\mathrm{q}_2})/2$ in units of r_0. The improved quark mass has been determined using the boosted one-loop perturbative value of b_{m}.

3.9.4 Baryon chiral extrapolations

Chiral extrapolations for the baryons have been performed using the simple fit ansatz

$$m_{\mathrm{B}} = A + C(\widetilde{m}_{\mathrm{q}_1} + \widetilde{m}_{\mathrm{q}_2} + \widetilde{m}_{\mathrm{q}_3})/3 \tag{3.30}$$

Terms arising from quenched chiral perturbation theory have been neglected since the simulated quark masses are too heavy to produce an observable effect. Higher order terms in the quark mass have been omitted from the fit as previous experience [39] indicates that the quality of the data is not sufficient to include them. For the spin-$\frac{1}{2}$ baryons the following fit ansatz has been motivated in [40]

$$m_{\mathrm{B}} = A + B'\widetilde{m}_{\mathrm{q}_1} + C'(\widetilde{m}_{\mathrm{q}_2} + \widetilde{m}_{\mathrm{q}_3})/2 \tag{3.31}$$

where the last term is composed from the quark masses which are symmetric/anti-symmetric under interchange of the quark flavours. In reference [39], the fit parameters obtained from fits to the degenerate spin-$\frac{1}{2}$ baryons using equation 3.30 can be compared to those obtained from fits to equation 3.31 to all the quark mass combinations. The results show that $C \approx B' + C'$ within errors. This suggests that the simple fit ansatz in equation 3.30 is sufficient to model the chiral behaviour at the current level of accuracy of the baryon data.

Uncorrelated fits were performed using equation 3.30 to the degenerate delta and nucleon baryons for all data sets (3 point fit). The $\beta = 5.7$ data set consists of only two degenerate combinations for the baryons and thus the chiral extrapolations are not well controlled. For the other data sets, a 7 point fit to the non-degenerate delta data and a 15 point fit to the non-degenerate sigma and lambda baryons were examined. Finally fits were performed to both the degenerate and non-degenerate baryon data: a 10 point fit for the delta and an 18 point fit for the sigma and lambda. The degenerate nucleon data points were included in these fits to the sigma and lambda. Table 3.6 shows the fit parameters obtained from these three different fits for the delta for the $\beta = 6.0$ and $\beta = 6.2$ non-perturbatively improved data sets. For the $\beta = 6.2$ data set the fit parameters do not depend on the choice of fit. There is a bigger variation in the $\beta = 6.0$ fit parameters, however the results are still compatible within errors. Figure 3.20 shows the fits to all the delta combinations for these two data sets.

Baryon	Data set	# points	A	C	χ^2/d.o.f.
Delta	$\beta = 6.2$ N-P	3	$0.540\ ^{+27}_{-20}$	$4.03\ ^{+52}_{-77}$	0.001 / 1
		7	$0.540\ ^{+25}_{-17}$	$4.11\ ^{+45}_{-78}$	0.034 / 5
		10	$0.542\ ^{+23}_{-17}$	$4.00\ ^{+43}_{-68}$	0.144 / 8
	$\beta = 6.0$ N-P	3	$0.728\ ^{+61}_{-42}$	$3.86\ ^{+71}_{-130}$	0.893 / 1
		7	$0.775\ ^{+45}_{-42}$	$2.87\ ^{+97}_{-99}$	0.359 / 5
		10	$0.762\ ^{+49}_{-36}$	$3.17\ ^{+72}_{-112}$	2.120 / 8

Table 3.6: Fit parameters obtained for the delta baryons from fits to equation 3.30 for the $\beta = 6.0$ and $\beta = 6.2$ non-perturbatively improved data sets. The fits corresponding to the number of points has been described in the text.

The $\beta = 6.0$ plot shows that the point corresponding to the lightest quark mass is off the best fit, explaining why, for this data set, there is a greater deviation of the fit parameters when the degenerate points are included. This problem only occurs in this data set as can be seen by examining Figure 3.21, which shows the delta extrapolations for the other data sets plotted in units of r_0. The large volume data set has been excluded from the plots for clarity. The plots show that the data is consistent with a linear fit. For the delta baryons the final fit selected was an uncorrelated linear fit to all the quark mass combinations.

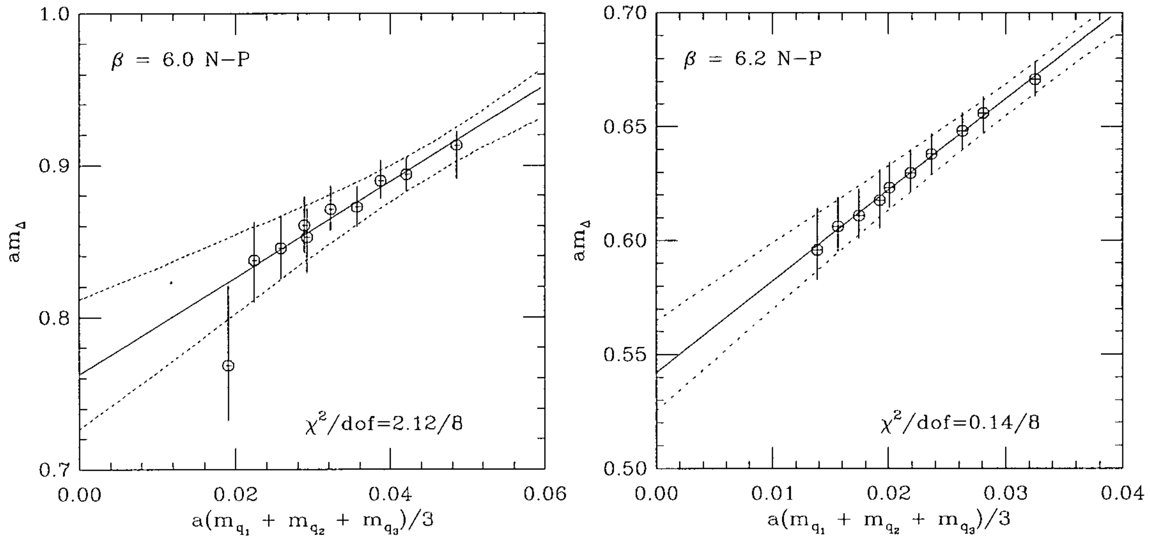

Figure 3.20: The delta mass as a function of the average improved quark mass for the $\beta = 6.0$ and $\beta = 6.2$ non-perturbative data sets. The data has been fitted to equation 3.30 using an uncorrelated fit.

Figure 3.22 shows the chiral extrapolations for the lambda and sigma baryons for the $\beta = 6.0$ non-perturbatively improved data set. These plots show that the linear ansatz is a good fit to the data and that the lambda and sigma are almost degenerate in mass. The chiral extrapolations for the spin-$\frac{1}{2}$ baryons in units of r_0 are shown in Figure 3.23. The figure shows the improved scaling behaviour for the non-perturbatively improved data sets. The $\beta = 5.7$ data set does not include non-degenerate baryons and thus does not differentiate between

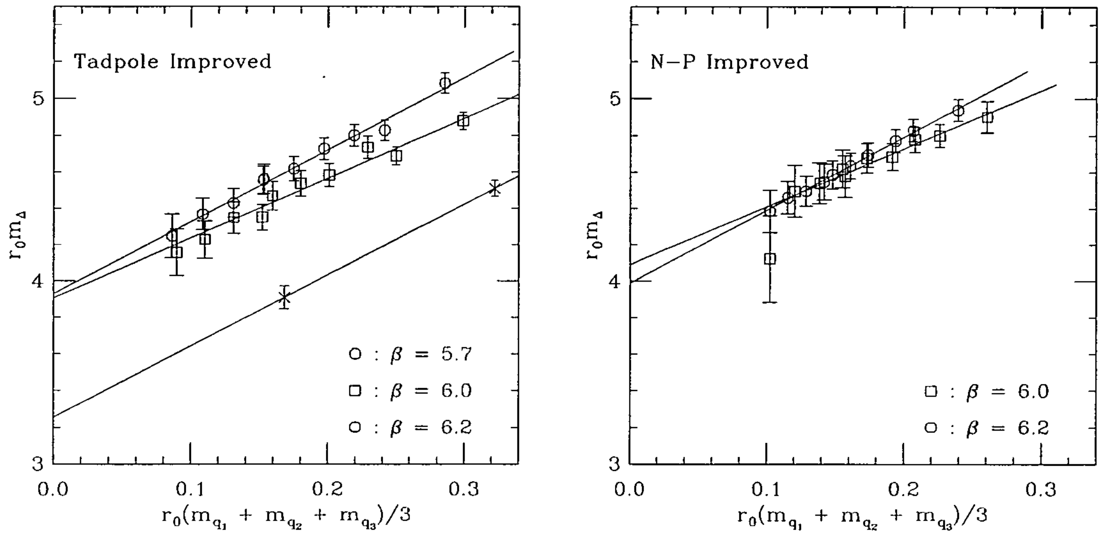

Figure 3.21: The delta mass for the tadpole and non-perturbatively improved data sets plotted against the averaged improved quark mass, $(\widetilde{m}_{q_1} + \widetilde{m}_{q_2} + \widetilde{m}_{q_3})/3$ in units of r_0. The large volume data set has been omitted for clarity.

the sigma and lambda states. For clarity, the $\beta = 5.7$ nucleon extrapolation has only been included in the plot of the lambda extrapolation. Table 3.7 gives the fit parameters obtained from linear chiral extrapolations for the $\beta = 6.0$ and $\beta = 6.2$ non-perturbatively improved data sets. The degenerate fits to the nucleon can be compared with the non-degenerate fits to the sigma and lambda baryons. From the table, the fit parameters are consistent within errors for each of the different fits. The 18 point fit was selected as the final fit for all the data sets, except at $\beta = 5.7$.

3.10 Determination of m_{n} and m_{s}

The next stage is to determine the physical quark masses in lattice units in order to extract the physical hadron masses. On the lattice the up and down quarks are degenerate in mass. The *normal* quark mass, m_{n}, is defined to be the average of the light quark masses, $m_{\mathrm{n}} = \frac{1}{2}(m_{\mathrm{u}} + m_{\mathrm{d}})$. The value of m_{n} is determined at the physical value of the π mass. This is achieved by choosing an observable

Baryon	Data set	# points	A	C	χ^2/d.o.f.
Nucleon	$\beta = 6.2$ N-P	3	0.409^{+6}_{-22}	5.44^{+66}_{-20}	0.30 / 1
	$\beta = 6.0$ N-P	3	0.567^{+31}_{-35}	4.95^{+68}_{-55}	0.02 / 1
Sigma	$\beta = 6.2$ N-P	15	0.409^{+8}_{-21}	4.99^{+73}_{-35}	7.56 / 13
		18	0.406^{+6}_{-19}	5.22^{+62}_{-23}	11.77 / 16
	$\beta = 6.0$ N-P	15	0.567^{+23}_{-28}	4.96^{+62}_{-42}	3.70 / 13
		18	0.568^{+24}_{-26}	4.95^{+56}_{-44}	3.73 / 16
Lambda	$\beta = 6.2$ N-P	15	0.410^{+4}_{-29}	4.89^{+107}_{-12}	4.20 / 13
		18	0.404^{+4}_{-23}	5.23^{+76}_{-10}	9.88 / 16
	$\beta = 6.0$ N-P	15	0.560^{+23}_{-28}	5.18^{+65}_{-41}	2.43 / 13
		18	0.563^{+24}_{-27}	5.08^{+57}_{-44}	2.58 / 16

Table 3.7: Fit parameters obtained for the spin-$\frac{1}{2}$ baryons from fits to equation 3.30 for the $\beta = 6.0$ and $\beta = 6.2$ non-perturbatively improved data sets. The fits corresponding to the number of points included in the fit is described in the text.

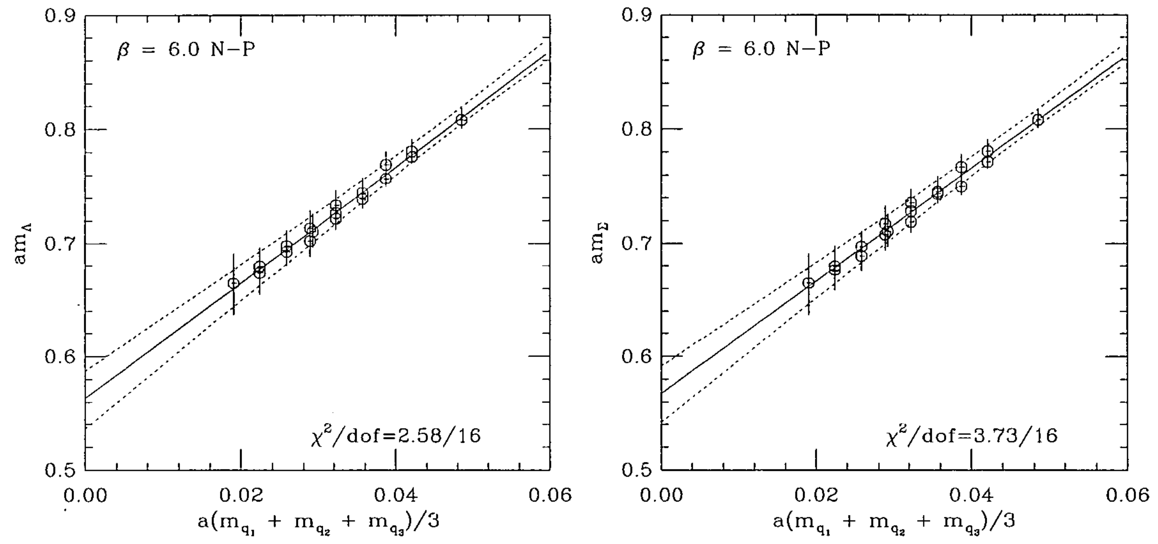

Figure 3.22: The lambda and sigma masses for the $\beta = 6.0$ non-perturbative data set plotted against the averaged improved quark mass, $(\widetilde{m}_{q_1} + \widetilde{m}_{q_2} + \widetilde{m}_{q_3})/3$. The data has been fitted to equation 3.30 using an uncorrelated fit.

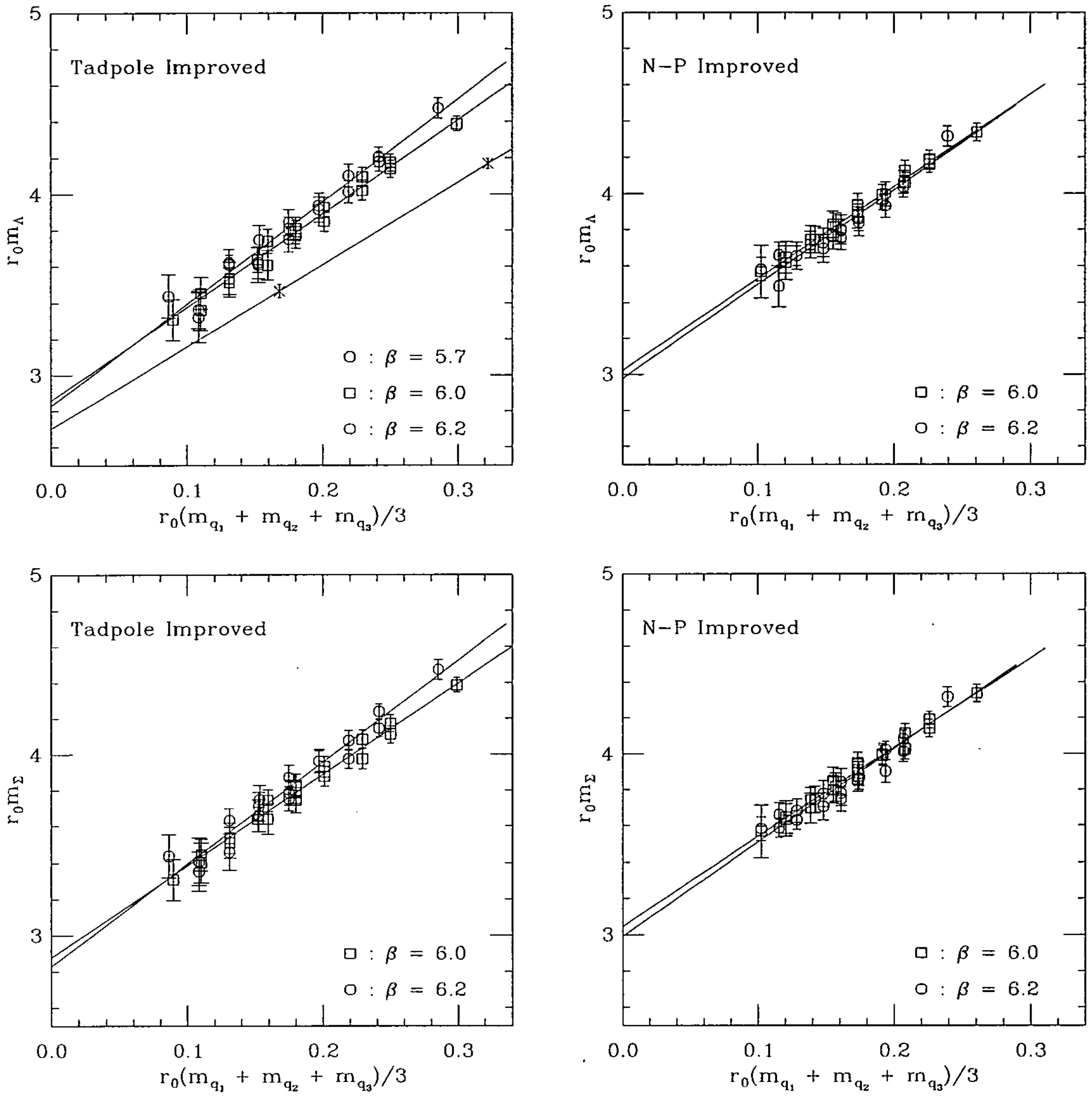

Figure 3.23: The lambda and sigma mass for the tadpole and non-perturbatively improved data sets plotted against the averaged improved quark mass, $(\widetilde{m}_{q1} + \widetilde{m}_{q2} + \widetilde{m}_{q3})/3$ in units of r_0. The large volume data set has been omitted for clarity.

quantity, Q to set the lattice scale. Rearranging equation 3.22, the improved normal quark mass is determined by

$$\widetilde{m}_{\mathrm{n}} = \frac{Q^2 \left(M_\pi/Q\right)^2_{\mathrm{phys}}}{2B} \tag{3.32}$$

where $\left(M_\pi/Q\right)^2_{\mathrm{phys}}$ is the physical ratio of the π mass over Q. In the quenched approximation the lattice scale, a, depends on the choice of Q. This scale ambiguity arises because the neglected fermion loops affect each observable differently. Different choices for Q were used to set the scale: the ρ mass, the K* mass, the nucleon mass and the Sommer scale r_0^{-1}. This was done to estimate the systematic error resulting from different determinations of the lattice spacing.

Tadpole improved data sets

		1/a [GeV]			
β	$L^3 \cdot T$	$Q = m_\rho$	$Q = m_{\mathrm{K}^*}$	$Q = m_{\mathrm{N}}$	$Q = r_0^{-1}$
5.7	$16^3 \cdot 32$	$1.140\ ^{+25}_{-23}$	$1.185\ ^{+22}_{-20}$	$0.998\ ^{+25}_{-23}$	$1.156\ ^{+\ 4}_{-\ 4}$
6.0	$16^3 \cdot 48$	$1.935\ ^{+36}_{-39}$	$2.005\ ^{+28}_{-34}$	$1.715\ ^{+51}_{-81}$	$2.119\ ^{+\ 8}_{-\ 8}$
6.2	$24^3 \cdot 48$	$2.556\ ^{+35}_{-74}$	$2.653\ ^{+35}_{-60}$	$2.392\ ^{+101}_{-\ 49}$	$2.905\ ^{+13}_{-13}$

Non-perturbatively improved data sets

		1/a [GeV]			
β	$L^3 \cdot T$	$Q = m_\rho$	$Q = m_{\mathrm{K}^*}$	$Q = m_{\mathrm{N}}$	$Q = r_0^{-1}$
6.0	$16^3 \cdot 48$	$1.890\ ^{+27}_{-49}$	$1.947\ ^{+27}_{-38}$	$1.622\ ^{+71}_{-67}$	$2.119\ ^{+\ 8}_{-\ 8}$
6.0	$32^3 \cdot 64$	$1.851\ ^{+36}_{-47}$	$1.918\ ^{+32}_{-39}$	$1.667\ ^{+82}_{-58}$	$2.119\ ^{+\ 8}_{-\ 8}$
6.2	$24^3 \cdot 48$	$2.544\ ^{+46}_{-87}$	$2.631\ ^{+43}_{-65}$	$2.266\ ^{+109}_{-\ 32}$	$2.905\ ^{+13}_{-13}$

Table 3.8: Inverse lattice spacing $1/a$ measured in GeV from four different quantities.

Table 3.8 shows the values obtained for the inverse lattice spacing in GeV when different quantities set the scale. The smallest spacing in fm occurs when r_0 sets the scale and the largest when the nucleon sets the scale. The percentage difference between the lowest and highest values is up to 30%. The method for determining the lattice value for Q has been described in section 3.7 for the Sommer scale and the mesons. The lattice value for the nucleon mass at the physical value is determined by combining the chiral extrapolations for the pseudoscalar mesons (equation 3.22) and the sigma baryons (equation 3.30). Making the assumption that the average quark mass for the pseudoscalar is equal to the average quark mass for the nucleon

$$(\widetilde{m}_{\mathrm{q}_1} + \widetilde{m}_{\mathrm{q}_2})/2 = (\widetilde{m}_{\mathrm{q}_1} + \widetilde{m}_{\mathrm{q}_2} + \widetilde{m}_{\mathrm{q}_3})/3 \tag{3.33}$$

which is valid since linearity is observed in the chiral extrapolations, the nucleon mass can be constructed from the relationship

$$m_{\mathrm{N}} = A + \frac{C}{2B} m_{\mathrm{PS}}^2, \qquad m_{\mathrm{PS}} = m_{\mathrm{N}} \left(\frac{M_\pi}{M_{\mathrm{N}}} \right)_{\mathbf{phys}} \tag{3.34}$$

Inserting the physical ratio of the π to the nucleon mass determines the lattice nucleon mass.

Setting the scale with these four different quantities, the normal quark mass is determined from equation 3.32. The normal quark mass is then used to determine the corresponding value of the hopping parameter, κ_{n},

$$\widetilde{m}_{\mathrm{n}} = m_{\mathrm{n}}(1 + b_{\mathrm{m}} m_{\mathrm{n}}), \qquad m_{\mathrm{n}} = \frac{1}{2}\left(\frac{1}{\kappa_{\mathrm{n}}} - \frac{1}{\kappa_{\mathrm{crit}}} \right) \tag{3.35}$$

the results of which are presented in Table B.1 in appendix B. The errors from the lattice determination of r_0 used to set the scale have not been taken into account at this stage. The results for the normal quark mass obtained using different quantities to set the scale, were found to be consistent within errors at $O(10^{-3})$. The largest error (discounting the uncertainty arising from quenching) in the normal quark mass arises from setting the scale from the nucleon mass.

The strange quark mass can be determined by considering the physical ratio of the K meson mass with Q

$$\widetilde{m}_{\mathrm{s}} = \frac{Q^2 \left(M_{\mathrm{K}}/Q\right)^2_{\mathrm{phys}}}{B} - \widetilde{m}_{\mathrm{n}} \tag{3.36}$$

subtracting the normal quark mass calculated previously. This method to determine the unrenormalised strange quark mass is referred to as "K - input". Alternatively the strange quark mass can be determined by considering the vector masses. Rearranging the chiral extrapolation for the vector meson mass in equation 3.29, the strange quark mass can be determined from

$$\widetilde{m}_{\mathrm{s}} = \frac{Q \left(M_{\phi}/Q\right)_{\mathrm{phys}} - A}{C} \tag{3.37}$$

using the ϕ meson as input ("ϕ - input"). The normal quark mass can also in principle be determined from the vector masses, using the physical ρ mass as input. In practice the larger statistical errors in the vector data meant that a precise determination of the normal quark mass was not possible. The results for the strange quark mass and corresponding κ_{s} value obtained from both methods are listed in Table B.2 in appendix B. Comparing results when the scale is set by the same quantity, the "ϕ - input" strange quark masses are significantly different from the "K - input" masses. This effect has also been observed in [40] and has been attributed to quenching errors. The statistical errors resulting from the "ϕ - input" method are much larger in comparison, due to the difficulty in fitting the vector meson masses. In addition, the physical ϕ meson is a mixed singlet and octet state unlike the pure octet K meson. On the lattice the ϕ meson can be assumed to be predominately $s\bar{s}$. In practice, this assumption does not matter, but is a potential source of error. Results from "ϕ - input" were thus not considered further. Comparing the results from "K - input" when the scale was set by different physical quantities Q, shows that the effect of small differences in the lattice spacing results in quark masses consistent within the statistical errors.

3.10.1 Renormalised quark masses

Quark masses in the continuum depend on the running of the strong coupling. Their values are thus dependent on the energy scale, μ. In addition the masses are dependent on the renormalisation scheme used. One choice is to renormalise the quark masses, $\widetilde{m}_{\mathrm{q}}$, in the modified minimal subtraction scheme, ($\overline{\mathrm{MS}}$),

$$m_{\mathrm{q}}^{\overline{\mathrm{MS}}}(\mu) = Z_{\mathrm{m}}^{\overline{\mathrm{MS}}}(a\mu)\, \widetilde{m}_{\mathrm{q}} \tag{3.38}$$

where $Z_{\mathrm{m}}^{\overline{\mathrm{MS}}}$ is the renormalisation constant. The renormalisation constant, Z_{m}, relating current quark masses to the renormalisation group invariant quark mass has recently been determined non-perturbatively in the region $6.0 \geq \beta \geq 6.5$ in the Schrödinger functional scheme, as described in [87]. This determination of Z_{m} can then be converted into the $\overline{\mathrm{MS}}$ scheme. However, in order to treat all the quenched data sets on an equal footing, the perturbative definition for $Z_{\mathrm{m}}^{\overline{\mathrm{MS}}}$ [70] to one-loop in perturbation theory was used. Choosing the scale, $\mu = 1/a$, in order to avoid problems arising from terms logarithmic in μ, the perturbative expression is

$$Z_{\mathrm{m}}^{\overline{\mathrm{MS}}}(1) = \left[1 - \frac{\alpha_{\mathrm{s}}^{\overline{\mathrm{MS}}}(\frac{1}{a})}{4\pi}\left(-4.11 - 10.317 c_{\mathrm{sw}} u_0^3 + 1.84 (c_{\mathrm{sw}} u_0^3)^2\right)\right] / u_0 \tag{3.39}$$

where this equation has been tadpole improved. The values for the strong coupling, $\alpha_{\mathrm{s}}^{\overline{\mathrm{MS}}}(1/a)$, for each β value were taken from [26]. They are: $\alpha_{\mathrm{s}}^{\overline{\mathrm{MS}}}(1/a) =$ 0.2579, 0.1981, 0.1774 at $\beta = 5.7,\ 6.0,\ 6.2$ respectively.

The renormalised masses, $m_{\mathrm{q}}^{\overline{\mathrm{MS}}}(1/a)$, for the normal and strange quark masses have been converted into MeV using the value of the lattice spacing obtained from the quantity that was used to set the scale. The results can be found in appendix B in Tables B.1 and B.3. It is usual to quote the final quark masses at the energy scale $\mu' = 2$ GeV. The transformation of the masses to any other energy scale is achieved by application of the renormalisation group formula (defined in equation 1.82) at lowest order

$$m_{\mathrm{q}}^{\overline{\mathrm{MS}}}(\mu') = \left(\frac{\alpha_{\mathrm{s}}^{\overline{\mathrm{MS}}}(\mu')}{\alpha_{\mathrm{s}}^{\overline{\mathrm{MS}}}(\mu)} \right)^{d_0/2\beta_0} m_{\mathrm{q}}^{\overline{\mathrm{MS}}}(\mu) \tag{3.40}$$

where

$$\beta_0 = 11/16\pi^2, \qquad d_0 = 8/16\pi^2 \tag{3.41}$$

The strong coupling at $\mu' = 2$ GeV was evaluated from the lowest order expression for the running coupling

$$\alpha_{\mathrm{s}}^{\overline{\mathrm{MS}}}(\mu) = -\frac{1}{8\pi\beta_0 \ln\left(\Lambda_{\overline{\mathrm{MS}}}/\mu\right)} \tag{3.42}$$

after first using the value of $\alpha_{\mathrm{s}}^{\overline{\mathrm{MS}}}(1/a)$ to set $\Lambda_{\overline{\mathrm{MS}}}$. A continuum extrapolation as described in detail later on in section 3.12 of the quark masses at $\mu' = 2$ GeV was performed for all the different quantities, Q, chosen to set the scale. Table 3.9 shows the continuum values for the normal and strange quark mass in the $\overline{\mathrm{MS}}$ scheme at $\mu' = 2$ GeV in MeV. There is a marked variation in the quark masses resulting from the choice of scale of approximately 2σ. The mass ratio $m_{\mathrm{s}}^{\overline{\mathrm{MS}}}/m_{\mathrm{n}}^{\overline{\mathrm{MS}}}$ is consistent for each choice, which should be expected as the mass ratio is independent of the lattice spacing. The result can be compared with the theoretical prediction made in quenched chiral perturbation theory [88], which

Q	$m_{\mathrm{n}}^{\overline{\mathrm{MS}}}$ [MeV]	$m_{\mathrm{s}}^{\overline{\mathrm{MS}}}$ [MeV]	$m_{\mathrm{s}}^{\overline{\mathrm{MS}}}/m_{\mathrm{n}}^{\overline{\mathrm{MS}}}$
m_ρ	$4.28\ ^{+33}_{-18}$	$107\ ^{+\ 8}_{-\ 5}$	$25\ ^{+\ 3}_{-\ 2}$
m_{K^*}	$4.14\ ^{+25}_{-16}$	$103\ ^{+\ 6}_{-\ 4}$	$25\ ^{+\ 2}_{-\ 1}$
m_{N}	$4.51\ ^{+16}_{-38}$	$113\ ^{+\ 4}_{-13}$	$25\ ^{+\ 1}_{-\ 3}$
r_0^{-1}	$3.71\ ^{+11}_{-11}$	$93\ ^{+\ 3}_{-\ 3}$	$25\ ^{+\ 1}_{-\ 1}$

Table 3.9: Continuum extrapolated values for the normal and strange quark masses in the $\overline{\mathrm{MS}}$ scheme at $\mu' = 2$ GeV in MeV. The lattice spacing has been set by the quantity Q in each case. The dimensionless ratio of the quark masses has been quoted for comparison.

finds the mass ratio to be, $M_s/M_n = 24.3 \pm 1.0$. A similar analysis carried out in [70] found a mass ratio of $M_s/M_n = 22 \pm 3$.

3.11 Physical hadron masses in lattice units

Interpolating the chiral extrapolations for the hadron masses to the values obtained for the unrenormalised improved normal and strange quark masses, the physical hadron masses in lattice units can be determined. Table 3.10 shows the results obtained for the meson masses at the physical quark masses for all the data sets when the K* meson sets the scale. In this case only the ρ and ϕ mesons can be determined from the simulation, the other mesons have been used to set the quark masses and the lattice spacing. The meson masses obtained for each quantity which sets the scale are listed in Table B.4 in appendix B.

β	c_{sw}	$L^3 \cdot T$	m_ρ	m_ϕ	m_{K^*}
5.7	1.56	$16^3 \cdot 32$	$0.676\,^{+13}_{-19}$	$0.833\,^{+12}_{-15}$	$0.754\,^{+13}_{-14}$
6.0	1.76	$16^3 \cdot 48$	$0.408\,^{+11}_{-10}$	$0.511\,^{+8}_{-7}$	$0.459\,^{+9}_{-6}$
6.0	1.76	$32^3 \cdot 64$	$0.419\,^{+11}_{-9}$	$0.518\,^{+9}_{-7}$	$0.466\,^{+10}_{-8}$
6.0	1.47	$16^3 \cdot 48$	$0.396\,^{+9}_{-9}$	$0.493\,^{+7}_{-6}$	$0.446\,^{+8}_{-6}$
6.2	1.61	$24^3 \cdot 48$	$0.307\,^{+9}_{-11}$	$0.378\,^{+7}_{-6}$	$0.340\,^{+9}_{-5}$
6.2	1.44	$24^3 \cdot 48$	$0.301\,^{+9}_{-9}$	$0.373\,^{+6}_{-5}$	$0.337\,^{+8}_{-4}$

Table 3.10: Lattice values of the meson masses at the physical quark masses obtained using K* to set the scale. The results for m_{K^*} are at the physical value of the K* meson in lattice units.

The baryon masses for the quenched data sets are reported in appendix B in Tables B.5 and B.6 for all the different quantities used to set the scale. Table 3.11 shows the baryon results when the K* sets the scale. The results for all the octet baryons are obtained from the sigma chiral extrapolation, except for the Λ. Results for the $\beta = 5.7$ data set are taken from the degenerate delta and nucleon extrapolations and interpolated assuming linearity to the non-degenerate baryons. Mass results in this case for the Σ and Λ are assumed to be degenerate.

This assumption was made in order to perform continuum extrapolations for these baryons.

Decuplet baryons

β	c_{sw}	$L^3 \cdot T$	m_{Δ}	m_{Σ^*}	m_{Ξ^*}	m_{Ω}
5.7	1.56	$16^3 \cdot 32$	1.122^{+42}_{-32}	1.207^{+35}_{-28}	1.292^{+30}_{-23}	1.378^{+28}_{-20}
6.0	1.76	$16^3 \cdot 48$	0.767^{+48}_{-35}	0.806^{+34}_{-28}	0.845^{+23}_{-19}	0.884^{+13}_{-14}
6.0	1.76	$32^3 \cdot 64$	0.711^{+26}_{-18}	0.762^{+21}_{-15}	0.813^{+18}_{-14}	0.864^{+18}_{-15}
6.0	1.47	$16^3 \cdot 48$	0.733^{+20}_{-29}	0.774^{+15}_{-23}	0.814^{+12}_{-18}	0.854^{+9}_{-13}
6.2	1.61	$24^3 \cdot 48$	0.547^{+22}_{-16}	0.583^{+17}_{-12}	0.619^{+13}_{-9}	0.656^{+10}_{-8}
6.2	1.44	$24^3 \cdot 48$	0.539^{+14}_{-11}	0.574^{+12}_{-9}	0.610^{+10}_{-7}	0.646^{+9}_{-6}

Octet baryons

β	c_{sw}	$L^3 \cdot T$	m_{N}	m_{Λ}	m_{Σ}	m_{Ξ}
5.7	1.56	$16^3 \cdot 32$	0.935^{+21}_{-23}	1.035^{+19}_{-19}	1.035^{+19}_{-19}	1.134^{+17}_{-17}
6.0	1.76	$16^3 \cdot 48$	0.575^{+23}_{-25}	0.633^{+19}_{-18}	0.636^{+19}_{-18}	0.696^{+16}_{-13}
6.0	1.76	$32^3 \cdot 64$	0.560^{+19}_{-27}	0.623^{+15}_{-21}	0.626^{+15}_{-21}	0.692^{+13}_{-16}
6.0	1.47	$16^3 \cdot 48$	0.544^{+25}_{-16}	0.605^{+20}_{-13}	0.607^{+21}_{-12}	0.669^{+17}_{-9}
6.2	1.61	$24^3 \cdot 48$	0.412^{+6}_{-19}	0.458^{+5}_{-15}	0.459^{+5}_{-13}	0.506^{+7}_{-10}
6.2	1.44	$24^3 \cdot 48$	0.391^{+8}_{-16}	0.442^{+5}_{-12}	0.442^{+7}_{-12}	0.494^{+7}_{-8}

Table 3.11: Lattice values for the octet baryons using an uncorrelated linear fit to all the sigma baryons. The scale was set by K*.

3.12 Continuum extrapolations

To compare the light hadron spectrum results with experiment, an extrapolation to the continuum limit is required. Ideally, simulations would be performed at more values of the lattice spacing in order to have more control over the extrapolation, however a continuum extrapolation can be still be performed using all the quenched data sets except the large volume simulation.

Tadpole improvement aims to reduce the leading order corrections in the results for the masses, but does not completely eliminate the errors of $O(a)$. Terms of $O(a^2)$ are also included in the extrapolation as they form an important contribution to the error. Taking this into account, the following fit ansatz to the tadpole data sets was made

$$m_{\mathrm{H}}^{\mathrm{TAD}}/Q = A + BQ + CQ^2 \tag{3.43}$$

where Q is the lattice quantity used to set the lattice spacing. In this analysis, Q was selected to be the same quantity which set the scale in the determination of the quark masses.

The non-perturbative improvement of the fermion action reduces the leading order lattice spacing dependence of the masses to $O(a^2)$. Thus the fit ansatz for the non-perturbative data sets was

$$m_{\mathrm{H}}^{\mathrm{NP}}/Q = A + DQ^2 \tag{3.44}$$

Independent fits to the tadpole and non-perturbatively improved data sets using these fit ansätze are uniquely determined. In order to perform a best fit analysis, the continuum result from each fit was constrained to have the same value in a simultaneous fit to all the data points. Continuum extrapolations for the ρ and ϕ mesons using an uncorrelated simultaneous fit are shown in Figure 3.24. The scale has been set by the K* meson, *i.e.* $Q = m_{\mathrm{K}^*}$. Only the best fits have been displayed in the plots for clarity. The experimental values are indicated by the burst points. The mass ratio has been plotted as a function of Q^2 to show the linear dependence of the non-perturbatively improved data points more clearly.

When the vector mesons are used to set the scale, the improved scaling behaviour of the tadpole data over the non-perturbative data cannot be examined for the vector mesons. This is because the data points have been been determined from an analysis of the same correlator channel. When the ratio of vector meson masses are formed in order to perform the continuum extrapolation, the

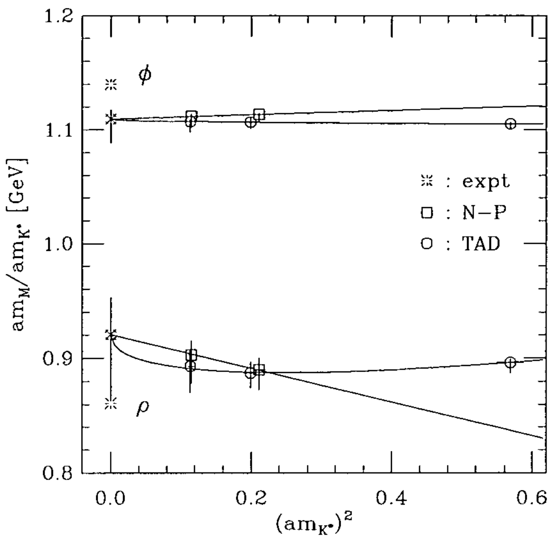

Figure 3.24: Continuum extrapolations for the mesons. The scale was set by the K* meson. The burst points indicate the experimental values.

statistical fluctuations tend to cancel out. Thus the leading order corrections in the mass ratio could be significantly reduced. One way to examine the effect of improvement is to set the scale with a quantity such as r_0 which has been determined independently. Figure 3.25 shows the continuum extrapolations for the vector mesons when the scale is set by r_0. The non-perturbative points exhibit slightly less dependence on the lattice spacing than the tadpole points. This becomes more apparent for the ϕ meson. Comparing the extrapolations for the mesons, the continuum results are significantly larger when the lattice spacing is set by the Sommer scale. Indeed this appears to be a systematic effect which affects all the hadron masses.

The continuum extrapolations for the baryons should be approached with caution as the $\beta = 5.7$ data set does not include non-degenerate baryons. However assuming linearity for the chiral extrapolations, continuum extrapolations for the baryons were investigated. For the decuplet baryons, the simultaneous fits to the lightest, Δ, and heaviest, Ω, baryons are shown in the left-hand plot in Figure 3.26, where the scale has been set by the K* meson. An improved

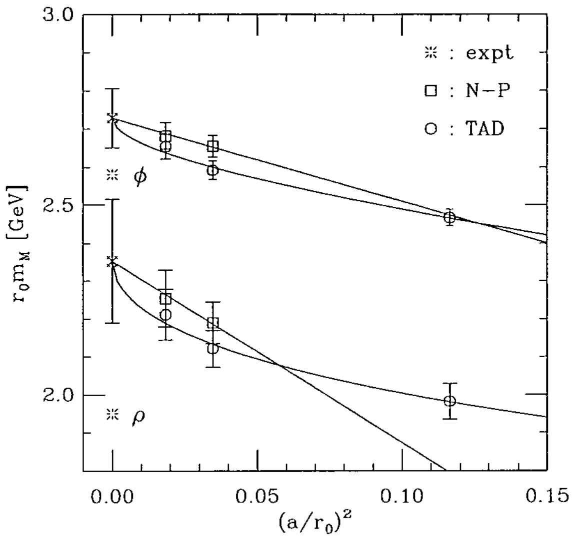

Figure 3.25: Continuum extrapolations for the mesons. The scale was set by r_0. The burst points indicate the experimental values.

scaling behaviour for the non-perturbatively improved data can be observed for the decuplet baryons, although the mass results are consistent within errors. The Σ^* and Ξ^* have not been shown in the plots for clarity. The extrapolations for these baryons are very similar to the ones shown. The Δ extrapolation was performed to masses with very large errors, resulting in a large uncertainty in the continuum value. Extrapolations for the nucleon and Ξ octet baryons are shown in the right-hand plot. The Σ and Λ extrapolations have not been shown as they are effectively degenerate. The same conclusions concerning improved scaling can be drawn as for the octet baryons.

Continuum extrapolations were performed using the ρ mass, nucleon mass and Sommer scale to set the lattice spacing, in addition to the K* mass, in order to quantify the dependence on the ambiguity of the lattice spacing. The errors in r_0 were added in quadrature and the extrapolations were performed using a standard linear regression technique. The final results for the spectrum obtained through different choices to set the scale, are shown in Figure 3.27. The results are compared with the experimental values taken from [14]. When the

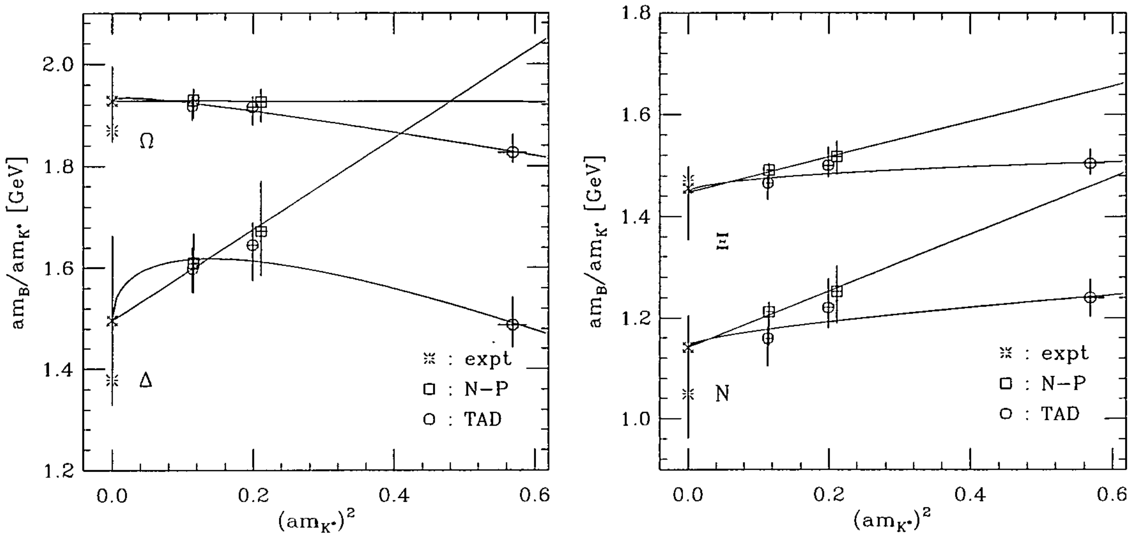

Figure 3.26: Continuum extrapolations for the baryons. The scale was set by the K^* meson. The burst points indicate the experimental values.

scale is set using a hadron mass, the results form a consistent picture for the final masses. Setting the scale with the nucleon results in very small errors for the octet baryons and even for the mesons. In the octet sector, cancellation of statistical fluctuations in the ratio of the octet baryons to the nucleon is expected as the same chiral extrapolation was used in both cases, resulting in smaller errors. The results for the decuplet baryons are comparable with the results determined when the mesons set the scale.

When the scale is set using the Sommer scale, the final results are much larger with greater errors. As stated previously, this may be an indication of a systematic effect. Comparing the results when the scale is set by the vector mesons, the continuum extrapolation results are in agreement within errors. The final results were selected when the K^* meson sets the scale. This gives smaller errors and means that a chiral extrapolation in the quantity which sets the scale was avoided. It could be argued that the scale should preferably be set by a stable particle, such as the nucleon, instead of a resonance. Comparing the spectrum results obtained from the nucleon and K^*, the maximum difference in the results

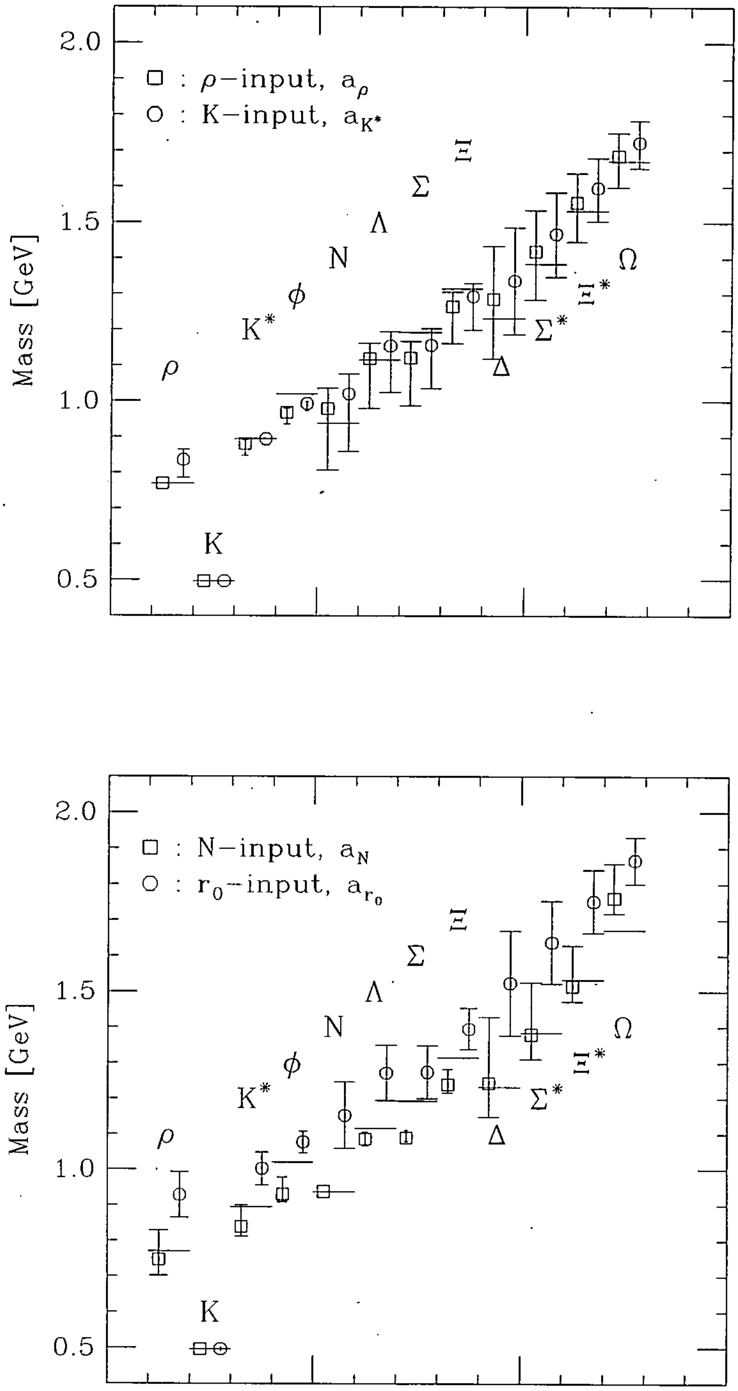

Figure 3.27: Spectrum results. The results obtained using different quantities to set the scale are compared. The horizontal lines are the experimental results [14].

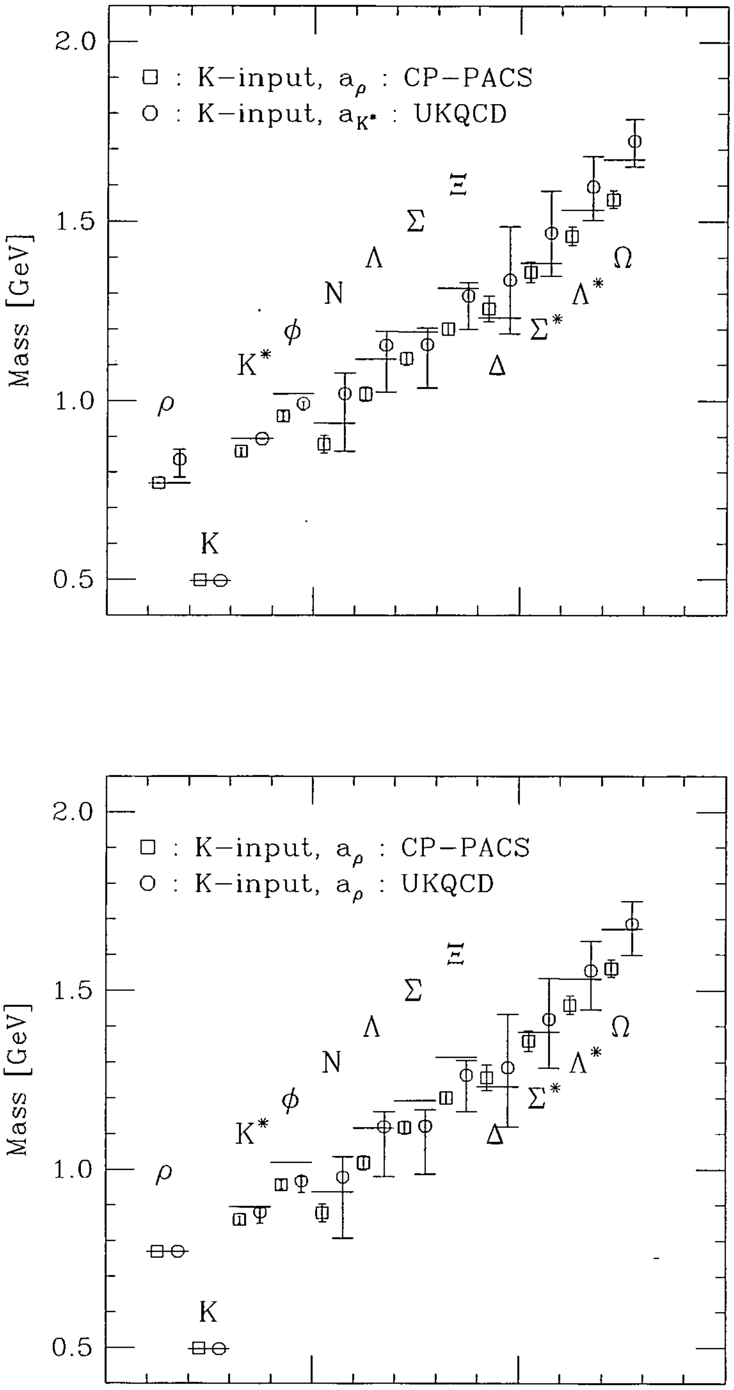

Figure 3.28: Spectrum results. In the top plot the results obtained when the K^* sets the scale are compared with results from CP-PACS [4] using "K-input". The bottom plot compares the results obtained when the scale is set from the ρ mass with the CP-PACS data. The horizontal lines are the experimental results [14].

is observed for the ρ at 10%. This is the maximum error in the spectrum results obtained by setting the scale by hadron masses.

Hadron	Experiment[GeV]	Mass[GeV]	Deviation
ρ	0.770	$0.835\ ^{+29}_{-5}$	8.4% 2.2σ
ϕ	1.019	$0.992\ ^{+7}_{-19}$	-2.6% 1.4σ
N	0.938	$1.020\ ^{+57}_{-161}$	8.7% 0.5σ
Λ	1.116	$1.155\ ^{+40}_{-130}$	3.5% 0.3σ
Σ	1.193	$1.157\ ^{+47}_{-122}$	-3.0% 0.3σ
Ξ	1.315	$1.293\ ^{+38}_{-93}$	-1.7% 0.2σ
Δ	1.232	$1.337\ ^{+149}_{-15}$	8.5% 0.7σ
Σ^*	1.384	$1.468\ ^{+116}_{-119}$	6.1% 0.7σ
Ξ^*	1.532	$1.596\ ^{+84}_{-92}$	4.2% 0.7σ
Ω	1.672	$1.723\ ^{+61}_{-72}$	3.1% 0.7σ

Table 3.12: Spectrum results. The scale has been set by the K* meson throughout. The last column shows the deviation from experiment.

The final spectrum results are compared with the results determined by the CP-PACS Collaboration. They have performed a quenched calculation of the light hadron mass spectrum using a Wilson fermion action for 4 values of β in the range $5.90 \leq \beta \leq 6.47$ on lattices with a physical extent of 3fm for five quark masses in the range $m_\pi/m_\rho \approx 0.75-0.4$. The results quoted in [4] have been compared with the results determined here when the K* meson sets the scale in the uppermost plot in Figure 3.28. CP-PACS have set the scale from the ρ mass. The bottom plot in Figure 3.28 shows the direct comparison with the CP-PACS data when the scale in both cases has been set from the ρ mass. The statistical errors on their data are much smaller due to the increased number of configurations included in their calculation. CP-PACS find that the maximum deviation of the spectrum results from the experimental values is 11%. Due to the fact that they have simulated at a lighter quark mass than the data presented here, their chiral extrapolations included terms arising from quenched chiral perturbation theory, which could explain why they observe a greater deviation from experiment, attributed to the quenched approximation.

The baryon masses are larger then the CP-PACS results. This could be due to the significant finite size effects observed in the baryon masses. However the errors on the baryon masses are large and no firm conclusions can be drawn. Table 3.12 contains the final spectrum results used in Figure 3.28. The deviation from the experimental values have been included. The greatest deviation (8.4%) occurs for the ρ meson. Increased statistics and simulations at lighter quark masses could be considered in order to obtain more precise statements concerning the effect of quenching errors in the light hadron spectrum. Another way to examine the effect of making the quenched approximation is to compare with simulations in full QCD - dynamical fermion simulations. This is the subject of the next chapter.

Chapter 4

Dynamical spectrum results

The results for the light hadron spectrum obtained from dynamical fermion simulations are presented in this chapter. An additional quenched simulation has been analysed and the results included in this chapter to facilitate a direct comparison with the dynamical results. The motivation for the study of a *matched ensemble* of data sets is discussed and a brief description of the method used to determine the matched simulation parameters is outlined. Details of all the simulation parameters are then reported. Measurements of the Sommer scale, r_0, determined by A. C. Irving [89] are included in order to set the lattice scale and estimate the accuracy of the matching technique. For each data set, the analysis of the correlator data is discussed in detail and the resulting hadron masses in lattice units are collated in appendix C. Those results which do not require a chiral extrapolation are then discussed. Chiral extrapolations in the *partially quenched* approximation are investigated, and finally the evidence for dynamical effects in the spectrum is examined. Preliminary light hadron spectrum results have been reported in [90] and the final results quoted in this thesis will be included in [91].

4.1 Motivation for the matched ensemble

First results from the initial dynamical simulations with two degenerate flavours of $O(a)$ improved Wilson fermions have been presented in [92, 93]. These simulations were performed at fixed $\beta = 5.2$ for various sea quark masses, referred to by the corresponding value of the hopping parameter, κ_{sea}. The hopping parameter associated with the hadron correlators generated on the dynamical configurations now corresponds to the valence quark mass and is referred to as κ_{val} in the following. Data sets for this first exploratory dynamical simulation were generated at three different volumes, $8^3 \cdot 24$, $12^3 \cdot 24$ and $16^3 \cdot 24$. A preliminary estimate for the non-perturbatively improved value of the clover coefficient, c_{sw}, provided by the ALPHA Collaboration, was used to reduce but not completely eliminate errors of $O(a)$ present in the action. The main focus of the analysis on these initial simulations was to study the effects of varying the sea quark mass and to investigate finite size effects. The results of this analysis were used to motivate the current choice of simulation parameters used to generate the data sets discussed in this chapter.

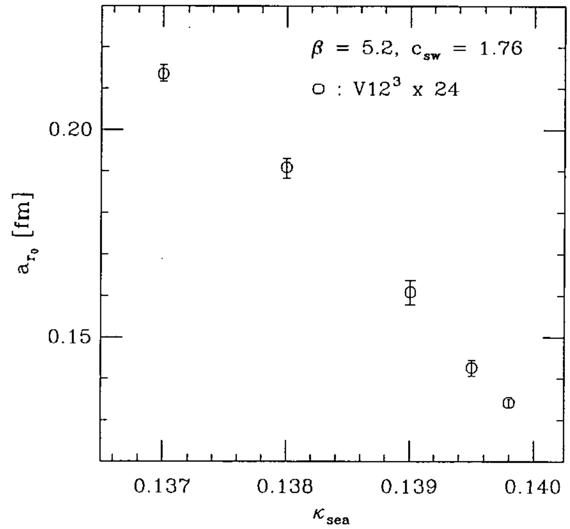

Figure 4.1: The lattice spacing determined from r_0 for the $\beta = 5.2$, $c_{sw} = 1.76$ dynamical simulations on the $12^3 \cdot 24$ volume, taken from [92]

From the investigation in [92], a significant lattice spacing dependence on the sea quark mass was observed. Figure 4.1 shows the lattice spacing as determined from r_0 for the $\beta = 5.2$, $c_{sw} = 1.76$, data set on the $12^3 \cdot 24$ volume reported in [92]. The percentage difference between the largest and smallest lattice spacings is approximately 37%. Preliminary measurements of a determined for the current dynamical simulation at $\beta = 5.2$, with the fully $O(a)$ non-perturbatively improved clover coefficient, were reported in [94]. The lattice spacings measured for simulations with different κ_{sea}, albeit with limited statistics, again show a significant dependence on the sea quark mass. A percentage difference of 24% was observed [94] when comparing a for simulations at $\kappa_{\text{sea}} = 0.1330$ and $\kappa_{\text{sea}} = 0.1350$. This means that chiral extrapolations in the sea quark mass, for hadron masses obtained from correlators with $\kappa_{\text{sea}} = \kappa_{\text{val}}$, are complicated by an additional dependence on the lattice spacing.

To investigate chiral extrapolations independently from continuum extrapolations, it was proposed that simulations with different sea quark masses should be carried out at the same lattice spacing defined with respect to a given physical quantity and hence at the same effective volume. In this way observed effects in the spectrum can be attributed to the inclusion of sea quarks rather than potentially large lattice artifacts or finite volume effects. In addition, simulating at a fixed volume facilitates direct comparisons with the quenched approximation. Three dynamical data sets with fixed a forming a matched ensemble were generated and compared with a quenched simulation at the same lattice spacing. The parameter details are described in section 4.3. In order to simulate at the same effective lattice spacing for different sea quark masses and hence form a matched ensemble of data sets, the bare lattice parameters, β and κ_{sea} must be *tuned.*

4.2 Tuning the bare parameters of the action

In [95] the method used to tune the bare lattice parameters in order to achieve the same value of the lattice spacing for different $(\beta, \kappa_{\text{sea}})$ combinations was outlined and preliminary tests of the procedure were presented. This section discusses the criteria used to match the current simulations and a brief description of the basic idea. The analysis involved to determine the matched parameters was carried out by A. C. Irving and J. C. Sexton.

One dynamical simulation $(\beta, \kappa_{\text{sea}})$, is said to be matched to another simulation $(\beta', \kappa'_{\text{sea}})$, in this particular context, when the expectation value of a lattice observable, $\mathcal{O}$, measured on each data set is equal

$$\langle\mathcal{O}\rangle_{\beta',\kappa'_{\rm sea}} = \langle\mathcal{O}\rangle_{\beta,\kappa_{\rm sea}} \tag{4.1}$$

Provided the simulations are in the scaling region this condition implies that the lattice spacing is the same to leading order for both data sets. The initial simulation is performed with the parameters $(\beta, \kappa_{\rm sea})$ and the chosen observable is measured on the gauge configurations. Since the matched simulation shares the same gauge configuration space as the original simulation the expectation values of the observable can be related by the cumulant expansion [96] to first order

$$\langle\mathcal{O}\rangle_{\beta',\kappa'_{\rm sea}} = \langle\mathcal{O}\rangle_{\beta,\kappa_{\rm sea}} + \langle\tilde{\mathcal{O}}\tilde{\Delta}\rangle_{\beta,\kappa_{\rm sea}} + \ldots \tag{4.2}$$

where

$$\tilde{\mathcal{O}} \equiv \mathcal{O} - \langle\mathcal{O}\rangle\,, \qquad \Delta \equiv S_{\beta,\kappa_{\rm sea}} - S_{\beta',\kappa'_{\rm sea}} \tag{4.3}$$

and Δ is the difference between the original action and the matched action. The action, defined in equation 1.22 can be split into a pure gauge part depending only on β and a fermion part depending on both $\kappa_{\rm sea}$ and β through the inclusion of the clover term

$$S_{\beta,\kappa_{\rm sea}} = S_{\rm G}(\beta) + S_{\rm F}(c_{\rm sw}(\beta), \kappa_{\rm sea}) \tag{4.4}$$

By requiring that the following expectation value measured on the original data set vanishes

$$\langle\tilde{\mathcal{O}}\tilde{\Delta}\rangle_{\beta,\kappa_{\rm sea}} = 0 \tag{4.5}$$

the matching condition in equation 4.1 is satisfied. This relationship can then be used to determine the parameter values $(\beta', \kappa'_{\rm sea})$ of the matched simulation. Assuming the matched parameters are related by a small shift in the original parameters, $\beta' = \beta + \delta\beta$ and $\kappa'_{\rm sea} = \kappa_{\rm sea} + \delta\kappa_{\rm sea}$, equation 4.5 can be written as

$$\frac{d\beta}{d\kappa_{\rm sea}} = -\frac{\langle\tilde{\mathcal{O}}\frac{\partial\tilde{S}_{\rm F}}{\partial\kappa_{\rm sea}}\rangle_{\beta,\kappa_{\rm sea}}}{\langle\tilde{\mathcal{O}}(\frac{d\tilde{S}_{\rm G}}{d\beta} + \frac{\partial\tilde{S}_{\rm F}}{\partial c_{\rm sw}}\frac{dc_{\rm sw}}{d\beta})\rangle_{\beta,\kappa_{\rm sea}}} \tag{4.6}$$

where the expression for $\tilde{\Delta}$ has been Taylor expanded and the limit $\delta\beta, \delta\kappa_{\rm sea} \to 0$

taken. This means that the corresponding shift in β needed to match a small change in κ_{sea} can be determined from computing the expectation values in equation 4.6. The methods used to evaluate these expectation values are described in detail in [95, 96]. The main complication arises from the fact that equation 4.6 is a non-linear function of β due to the clover coefficient in the fermion part of the action. However c_{sw} is a well known function of β and the derivative is easily determined. Evaluating equation 4.6 requires an initial estimate of the β shift, $\delta\beta$ in order to determine a first estimate of the matched value of β'. A self-consistency check can be performed by measuring the actual slope between the original and predicted parameters. In practice the expectation value of the observable is measured on the original data set for a range of β values and interpolated to perform the matching. Further details of the matching technique will be included in [91].

In general the matched parameters will depend on the choice of observable used in the tuning procedure [95]. In this case r_0 was selected. The Sommer scale has the advantage that it is independent of the valence quark mass and is defined and measured in the same way for both dynamical and quenched simulations. At this intermediate quark separation, phenomenological static quark potential models are tightly constrained by the spectrum of heavy mesons, such as $b\bar{b}$. Confidence in r_0 is gained from the fact that its physical values obtained from different models are in good agreement and that lattice calculations have a high degree of accuracy, particularly for fine lattices [73]. For these reasons it is expected that r_0 will be a good choice to highlight sea quark effects. Since r_0 is a derived quantity, the matching is actually performed with fuzzed paths of gauge links, defined later in section 4.4. These fuzzed paths are determined at the estimated values of the matched lattice parameters for a range of $\delta\beta$ shifts and r_0 is then extracted by the methods of section 4.4. A linear interpolation of the predicted r_0 values was then performed to do the matching.

The matching technique is only practicable for small changes in the bare parameters. In particular it was not suitable to directly match the dynamical simulations with the quenched approximation. The matching of the quenched simulation was instead achieved by direct investigation. This is only possible because quenched configurations can be generated comparatively quickly. An initial estimate for the matched quenched β value was obtained from the interpolating formula for r_0 as a function of the strong coupling in the quenched approximation, reported in [97]. A trial quenched run was performed at this value of β, and the Sommer scale was measured on the resulting configurations using the same method as for the dynamical simulations. This allowed a correction to the initial estimate of β to be made, which was then used for the final production run.

4.3 Simulation parameters

In addition to the three dynamical data sets forming a matched ensemble and the corresponding quenched simulation, a further dynamical data set at a lighter sea quark mass was simulated. To observe the greatest effects due to the inclusion of dynamical fermions the sea quark mass should be made as light as possible, ideally in the region of the up and down quark masses. However, simulations at light quark masses are more computationally intensive and not feasible with the current level of computing resources. The lightest sea quark mass simulated here represents the smallest quark mass at which meaningful statistics could be achieved within an acceptable time period.

Gauge configurations were generated with two degenerate flavours of $O(a)$ improved dynamical Wilson fermions using the Hybrid Monte Carlo algorithm [98] on the Cray T3E supercomputer in Edinburgh. The implementation and verification of the code was described in [93, 99]. A summary of the algorithm details was reported in [92]. For all the dynamical simulations, gauge configurations were separated by 40 trajectories. This figure was reached from a study of the autocorrelation times measured for the plaquette on every trajectory [92, 93, 100]. The matched quenched gauge configurations were generated by the hybrid over-relaxed algorithm with the compound sweep ratio of 7:1, over-relaxed to Cabbibo-Marinari sweeps [57]. Gauge configurations used for measurements were separated by 700 compound sweeps.

β	c_{sw}	κ_{sea}	κ_{val}	# conf.
5.29	1.9192	0.1340	0.1335, 0.1340, 0.1345, 0.1350	101
5.26	1.9497	0.1345	0.1335, 0.1340, 0.1345, 0.1350	101
5.2	2.0171	0.1350	0.1335, 0.1340, 0.1345, 0.1350	150
5.93	1.82	Quenched	0.1327, 0.1332, 0.1334 0.1337, 0.1339	160

Lightest κ_{sea} simulation.

5.2	2.0171	0.1355	0.1340, 0.1345, 0.1350, 0.1355	102

Table 4.1: Simulation parameters for all the dynamical simulations and matched quenched simulation.

Quark propagators were generated using $O(a)$ improved Wilson fermions. Correlators were constructed from fuzzed propagators for degenerate combinations of κ_{val} for the dynamical simulations. The range of valence quark masses was chosen to be close to the sea quark mass, and in all cases correlators were computed at $\kappa_{\mathrm{sea}} = \kappa_{\mathrm{val}}$. For the quenched simulation, degenerate and non-degenerate meson correlator combinations were generated for three values of the hopping parameter. Following the analysis of this data, a further two κ_{val} values were included in the simulation in order to achieve lower $m_{\mathrm{PS}}/m_{\mathrm{V}}$ mass ratios, comparable with the lighter dynamical simulations. The non-degenerate combination of these final two quark propagators was used in the quenched analysis. Only degenerate baryon correlators were included in the analysis.

Table 4.1 shows the simulation parameters for all the data sets. All simulations were carried out on a $16^3 \cdot 32$ lattice. The finite volume investigation in [92] suggested that this increase in lattice size would be necessary in order to keep finite size effects to a minimum as the sea quark mass was reduced (and hence the lattice spacing) for the current simulations. In particular the temporal extent of the lattice was increased to allow sufficient time for a clear plateau to be observed when considering effective mass plots for all hadron channels. In order to ensure a large enough spatial volume to accommodate hadrons ($\gtrsim$ 1.5 fm) at this lattice size, a coarse lattice spacing of $a \gtrsim 0.09$ fm is required. This means that simulations must be performed with a low value of β. The dynamical β value was selected to be as low as possible while remaining within the parameter range where a valid non-perturbative estimate of the clover coefficient had been determined.

The fully non-perturbatively $O(a)$ improved value for $c_{\rm sw}$ determined by the ALPHA Collaboration in [101] and given by

$$c_{\rm sw}^{\rm dynam} = \frac{1 - 0.454g_0^2 - 0.175g_0^4 + 0.012g_0^6 + 0.045g_0^8}{1 - 0.720g_0^2} \qquad (4.7)$$

was used for all the dynamical simulations. This interpolation formula is valid for β values as low as 5.2, the minimum β value included in the simulations. Thus residual lattice artifacts are expected to be of $O(a^2)$, which on the coarse lattices simulated here could still be significant. The clover coefficient used in the quenched simulation was determined by the SCRI Collaboration [102]

$$c_{\rm sw}^{\rm quen} = \frac{1 - 0.6084g_0^2 - 0.2015g_0^4 + 0.03075g_0^6}{1 - 0.8743g_0^2}, \qquad \beta \geq 5.7 \qquad (4.8)$$

This result extends the analysis of the ALPHA Collaboration to lower values of β. Although the interpolating formula in equation 4.7 for $c_{\rm sw}$ is only accurate to 3 decimal places, 5 significant figures were used in the generation of configurations for the purposes of reproducibility. For technical reasons, 3 significant figures for $c_{\rm sw}$ were used in the generation of quark propagators.

4.4 Determination of r_0

To determine the lattice spacing, r_0 was measured for every data set. The Sommer scale is defined in terms of the force between a static quark anti-quark pair as in equation 3.17, or in terms of the potential

$$\left.\frac{\partial V(r/a)}{\partial r}\right|_{r=r_0} (r_0/a)^2 = 1.65 \qquad (4.9)$$

In this case the physical value of r_0 was chosen to be 0.49 fm. What follows is a brief description of the method used to extract r_0, employed by A. C. Irving [89]. Further details of the method will be included in [91], which differs in part from the technique used for the previous dynamical simulation reported in [92].

The lattice static quark potential, $V(\boldsymbol{r})$, is determined from the exponential decay of Wilson loops at large times. Wilson loops, $W(\boldsymbol{r},t)$ are the product of gauge links in a closed loop, where $\boldsymbol{r}$ defines the spatial orientation of the loop and t is the temporal extent. In [92] only *on-axis* Wilson loops, where $\boldsymbol{r} = (n,0,0)$, $n = 1,2,\ldots$ were considered. Here the *off-axis* directions, $(1,1,0)$, $(2,1,0)$, $(2,2,0)$, $(3,1,0)$, $(3,2,0)$ and $(3,3,0)$, as used in [103], were included in the analysis in order to estimate the effects of lattice artifacts due to the breaking of rotational symmetry. To increase the overlap of the Wilson loops with the ground state potential the gauge links were fuzzed, as described in section 2.6. Wilson loops were then constructed by correlations of two spatial paths of fuzzed gauge links, fuzzed using two possible levels of iteration of the fuzzing algorithm [104]. Using a variational technique [105], estimates for the ground and first excited state eigenvalues from the resulting 2×2 matrix of Wilson loops can be made. The ground state eigenvector can then be used to project out a linear combination of Wilson loops with a greater overlap with the ground state, denoted by $W_{\mathrm{LC}}(\boldsymbol{r},t)$. An estimate of the ground state potential can be determined from the long time behaviour of the effective "mass" of the linear combination of Wilson loops [103]

$$V(\boldsymbol{r}) = \lim_{t\to\infty} V(\boldsymbol{r},t) \tag{4.10}$$

where

$$V(\boldsymbol{r},t) = \ln \frac{W_{\mathrm{LC}}(\boldsymbol{r},t)}{W_{\mathrm{LC}}(\boldsymbol{r},t+1)} \tag{4.11}$$

To extrapolate to the infinite time limit, corrections to the ground state potential are made by subtracting the contamination due to the contribution of the first excited state. This correction can be estimated from the ratio of the corresponding eigenvalues for both states, following the methods of [106]. The final value for the potential was determined by computing the weighted average of $V(\boldsymbol{r},t)$ in the range $t_{\text{min}} = 3$ to $t_{\text{max}} = 5$, where the relative weights were given by the inverse of the statistical errors.

Once $V(\boldsymbol{r})$ had been determined, r_0 was extracted using a similar analysis to that described in [97] and originating in [103]. The data was fitted to the ansatz

$$V(\boldsymbol{r}) = V_0 + \sigma r - eG_{\text{L}}(\boldsymbol{r}) + l\left(G_{\text{L}}(\boldsymbol{r}) - \frac{1}{r}\right) \tag{4.12}$$

where $G_{\text{L}}(\boldsymbol{r})$ is the tree-level lattice expression for the exchange of one gluon given by

$$G_{\text{L}}(\boldsymbol{r}) = 4\pi \int_{-\pi}^{\pi} \frac{d^3\boldsymbol{k}}{(2\pi)^3} \frac{\cos(\boldsymbol{k}\cdot\boldsymbol{r})}{4\sum_{i=1}^{3}\sin^2(k_i/2)} \tag{4.13}$$

The string tension, σ describes the potential at large distances, $r = |\boldsymbol{r}|$, while at short distances the potential is described by the lattice Coulomb term, $eG_{\text{L}}(\boldsymbol{r})$. The term proportional to l takes into account lattice artifacts beyond tree level. Of course, for large enough separations the string is expected to break for the dynamical simulations. Thus the fits were performed over small fit intervals chosen to straddle r_0. Systematic errors were estimated by choosing different fit ranges. The statistical errors were determined by the bootstrap method. The lattice potential can be equated with the continuum equation to within $O(a^2)$ through a subtraction of the form

$$V(r) = V_0 + \sigma r - \frac{e}{r} \approx V(\boldsymbol{r}) + (e-l)\left(G_{\text{L}}(\boldsymbol{r}) - \frac{1}{r}\right) \tag{4.14}$$

Differentiating the left hand expression for $V(r)$ with respect to r and substituting into equation 4.9, r_0 in lattice units is determined by

$$r_0 = \sqrt{\frac{1.65 - e}{\sigma}} \tag{4.15}$$

Table 4.2 displays the results for r_0 and the corresponding lattice spacing for each data set. The table shows that the $\beta = 5.2$, $\kappa_{\text{sea}} = 0.1350$ and $\beta = 5.26$, $\kappa_{\text{sea}} = 0.1345$ data sets are the most closely matched. The value of r_0 for the

β	κ_{sea}	r_0/a	a [fm]	$1/a$ [GeV]	$m_{\text{PS}}/m_{\text{V}}$
5.93	Quenched	$4.612(30)\ ^{+\ 1}_{-\ 6}$	$0.1062(7)\ ^{+14}_{-\ 3}$	1.86(1)	
5.29	0.1340	$4.450(61)\ ^{+29}_{-61}$	$0.1101(15)\ ^{+13}_{-\ 7}$	1.79(2)	$0.830\ ^{+6}_{-7}$
5.26	0.1345	$4.581(59)\ ^{+0}_{-120}$	$0.1070(14)\ ^{+30}_{-\ 0}$	1.84(2)	$0.791\ ^{+7}_{-8}$
5.2	0.1350	$4.576(80)\ ^{+14}_{-130}$	$0.1071(19)\ ^{+40}_{-\ 3}$	1.84(3)	$0.688\ ^{+12}_{-\ 8}$
5.2	0.1355	$4.914(82)\ ^{+70}_{-19}$	$0.0997(17)\ ^{+40}_{-14}$	1.98(3)	$0.584\ ^{+23}_{-19}$

Table 4.2: r_0/a and the corresponding lattice spacing. The statistical error is in parentheses and the second error is an estimate of the systematic errors. The mass ratio $m_{\text{PS}}/m_{\text{V}}$ for the dynamical data sets at $\kappa_{\text{sea}} = \kappa_{\text{val}}$ is included in the table.

heaviest sea quark mass data set differs from the other matched data sets by at most 3.5%. Of course the matching procedure is expected to be less accurate when larger shifts in the parameters are considered. The systematic errors quoted for r_0 have not been taken into account in the subsequent analysis. The effective lattice volume of the matched ensemble is 1.71 fm and for the lightest sea quark mass, slightly smaller at 1.60 fm. The mass ratio $m_{\text{PS}}/m_{\text{V}}$ at $\kappa_{\text{sea}} = \kappa_{\text{val}}$, obtained from the fitting procedure described in the following sections, is shown for the dynamical data sets. This ratio gives an indication of the value of the sea quark mass at which the simulations are performed. The lightest mass ratio is 0.584 which, at around the mass of the strange quark, is still relatively heavy.

4.5 Fitting the data

The following sections discuss the results of the analysis procedure to determine the lattice masses of the hadrons for the four dynamical data sets and the matched quenched data set. The analyses of all the simulations were carried out in the same way, as described in chapter 2. All fits used 500 bootstrap samples to estimate the errors. Fits were performed to the pseudoscalar, vector, nucleon and delta for degenerate combinations of κ_{val} for the dynamical simulations. The quenched analysis included some non-degenerate meson correlators. As in the previous chapter, effective mass plots were studied in order to determine the onset of the ground-state plateau. Fits to extract the ground state mass were then performed to the FL and FF correlators using a sliding window analysis as described in section 2.12.7. These fits are referred to by the notation FL and FF in the following. The correlator notation introduced in section 2.7 has been modified in this chapter to additionally refer to the type of fits that were performed. More complicated fits were then attempted. Simultaneous fits to the correlator combinations, LL,FL and LL,FF to the ground and first excited state using equation 3.2 for the mesons and equation 3.3 for the baryons were investigated. Finally a factorising fit to the LL,FL,FF correlator combination, as described in section 2.11, was considered. In this case the fit was performed to the ground and first excited states. The notation for the fit types is described in appendix C. In all the fits under consideration, a cosh was used to fit the mesons and the baryons were fitted by an exponential, which is implicit in the fit notation. In the sliding window analysis, the maximum time slice was able to be pushed to the latest time slice possible, $t_{\text{max}} = 15$, for all the fits. For each type of fit considered the best fit range was selected based on the selection criteria in section 2.12.7, the results of which are tabulated in appendix C. The tables in the appendix include the values of the masses in units of r_0 to facilitate comparisons between the data sets. The systematic error associated with the choice of fit type has not been included in results obtained from the subsequent analysis of the fitted masses.

The fit results for each of the dynamical and matched quenched data sets are now discussed in turn. The final choice of fit type in each case is explained and the results obtained from the analysis for correlators where $\kappa_{\text{sea}} = \kappa_{\text{val}}$ is showcased for each data set. Plots of the fitted masses for the pseudoscalar, vector, nucleon and delta resulting from a sliding window analysis are shown to illustrate the choices made for the final fit intervals. Figure 4.2 shows an example of this type of plot. The masses obtained from different fit procedures have been offset to the right for clarity. For example, points corresponding to $t_{\text{min}} = 10$ are displayed in the interval [9-10] for each type of fit. Below the main plot, is a plot of the corresponding χ^2/d.o.f. for each point, where the plotting symbols correspond to the legend in the main plot. In general the χ^2/d.o.f. is plotted in the range 0-3. For some of the fitted masses the corresponding value of the χ^2/d.o.f. is not shown in the plot. This is because the χ^2/d.o.f. is greater than the range shown. In these cases the fitted mass for the particular fit interval was not considered further in the analysis. The final fitted mass used in the subsequent analysis is marked by an arrow.

Effective mass plots of the three correlator types considered in the analysis (LL, FL and FF) are shown together with the final fitted mass superimposed on the plot as in Figure 4.4. Note that all the effective masses approach the plateau from above, with the FF correlator making the shallowest approach. If the effective mass plots are compared with the ones obtained in the previous chapter for the quenched simulation, the increase in the length of the plateau for the fuzzed correlators is less pronounced for the data sets considered here. This is probably due to differences in the choice of fuzzing radius which has not been optimised for the current simulations.

For the mesons, preference for the final fit selected was given to fits to both the ground and first excited state. The selection of the best fit type was made based on the maximal fit range possible, stability of the fitted masses with respect to small variations in the fit interval, fits with small and more symmetric errors, and a value of χ^2/d.o.f. ≈ 1. In addition, agreement with the masses obtained from fits to purely the ground state was considered important. Of course, sometimes compromises had to made between these different criteria in the final analysis. The same criteria were used to select the fits for the baryons, although in some cases the simple fits to the ground state were chosen over more complicated fits which were unstable.

4.5.1 Fitting the lightest $\kappa_{\rm sea}$ data set.

The data set at $\beta = 5.2$ and $\kappa_{\rm sea} = 0.13550$ was the lightest sea quark mass simulated. Correlators generated with $\kappa_{\rm sea} = \kappa_{\rm val}$, discussed as an example here, are thus expected to have the largest signal to noise ratio. This can be seen in

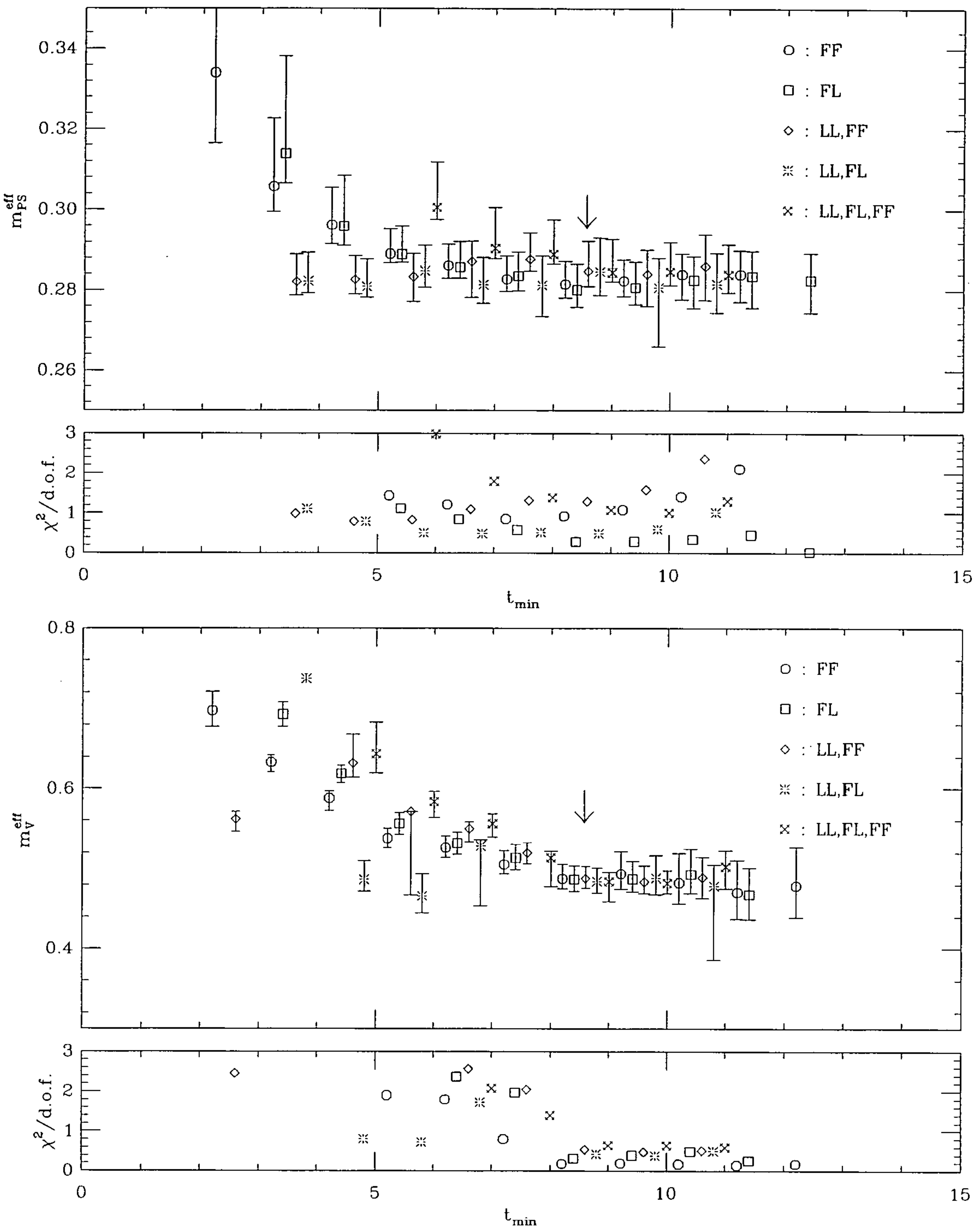

Figure 4.2: Sliding window plot for the pseudoscalar and vector masses for the $\beta = 5.2$, $\kappa_{\rm sea} = 0.13550$ data set at $\kappa_{\rm val} = 0.13550$. The fitted masses obtained for each type of fit have been offset for clarity. The arrow marks the final value selected.

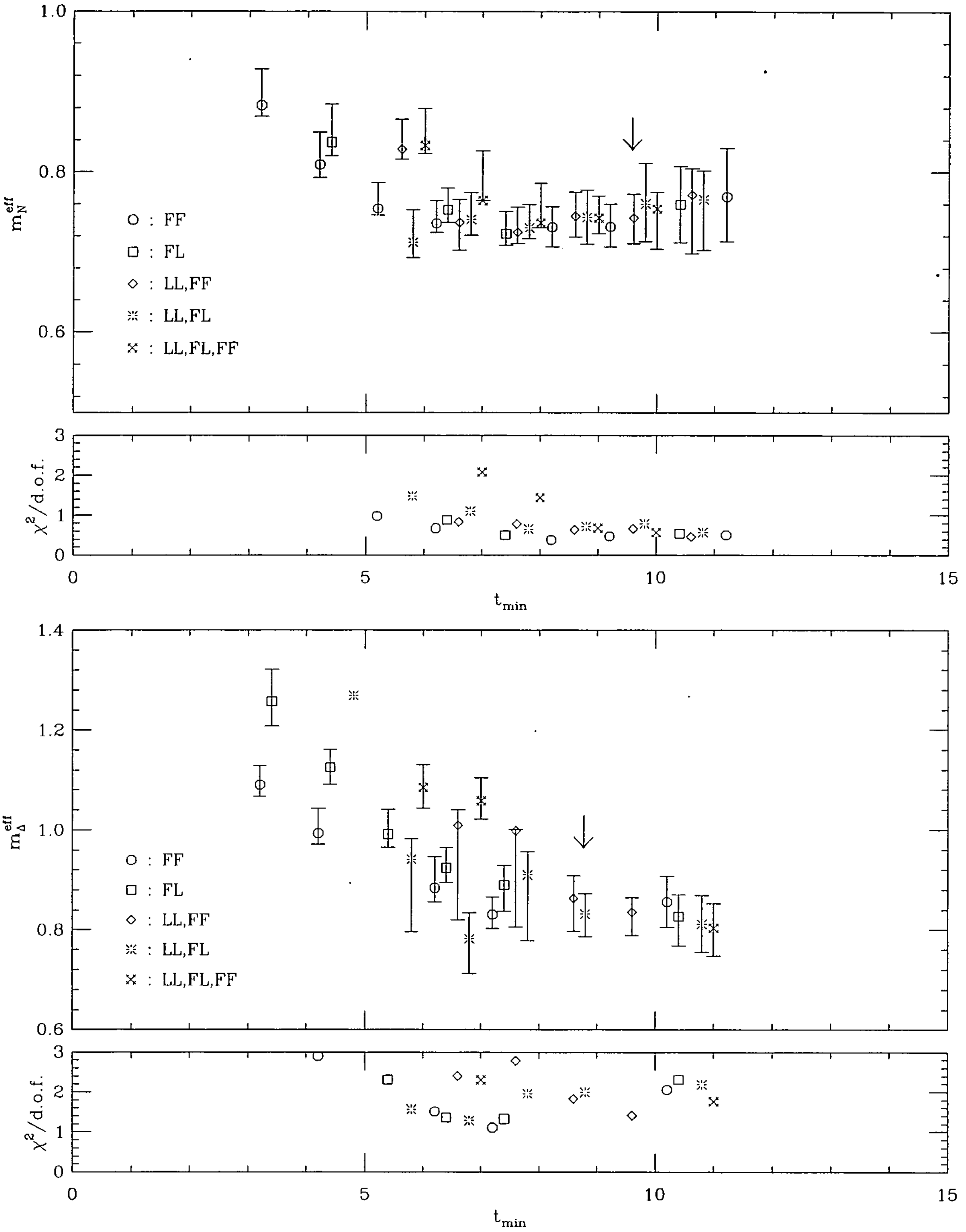

Figure 4.3: As for Figure 4.2 for the nucleon and delta for the $\beta = 5.2$, $\kappa_{\text{sea}} = 0.13550$ data set at $\kappa_{\text{val}} = 0.13550$.

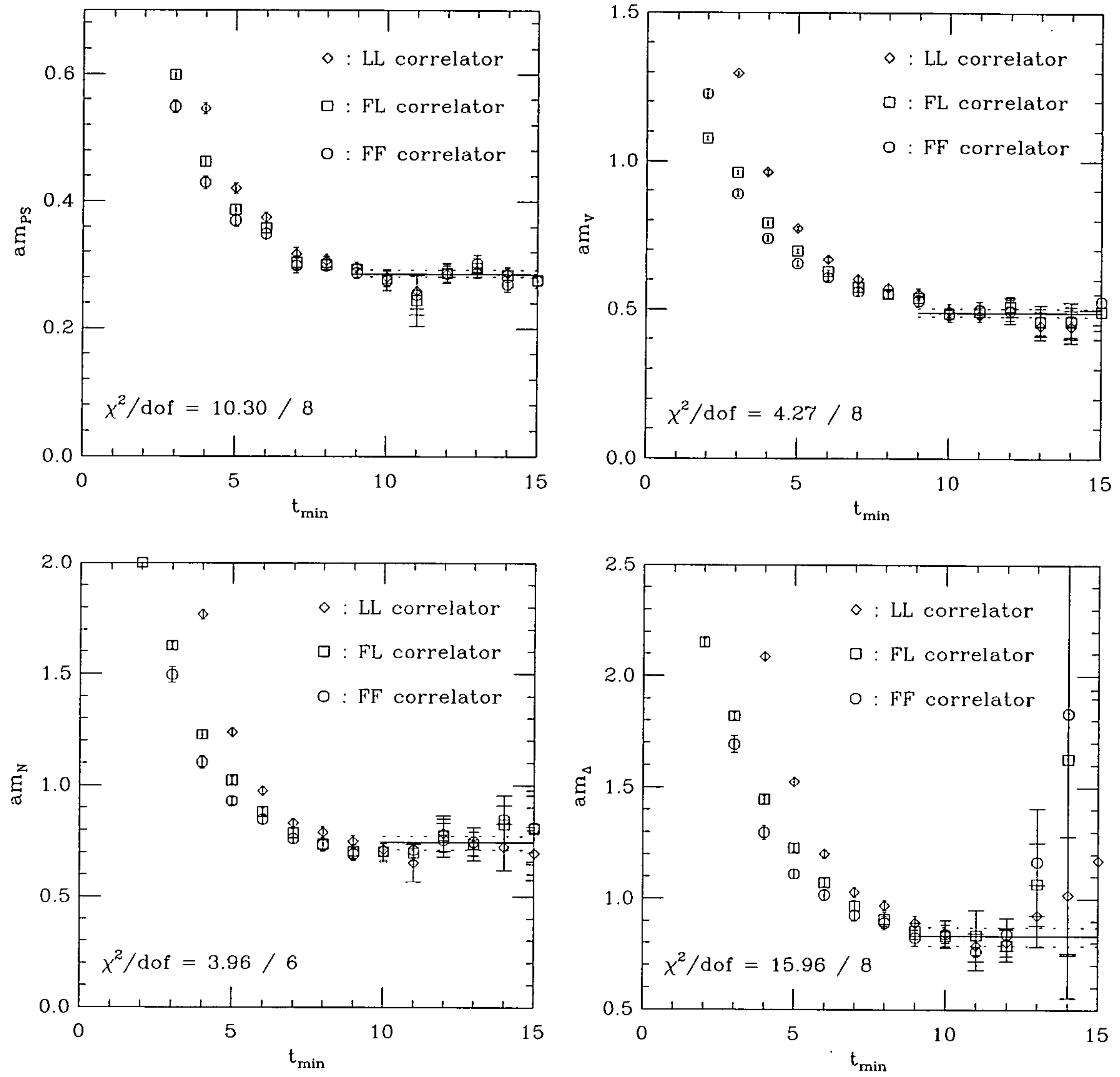

Figure 4.4: Effective mass plots for the pseudoscalar, vector, nucleon and delta for the $\beta = 5.2$, $\kappa_{sea} = 0.13550$ data set at $\kappa_{val} = 0.13550$. The pseudoscalar and vector have been fitted by a double cosh fit to the LL,FF correlator combination. The nucleon (delta) was fitted by a double exponential to the LL,FF (LL,FL) correlator combination.

the effective mass plots shown in Figure 4.4, particularly for the delta.

Figure 4.2 shows the fitted masses for the pseudoscalar and vector obtained from a sliding window analysis for each type of fit attempted. For the pseudoscalar, the mass results from all the fits start to agree from the fit range [9-15]. The LL,FL and LL,FF fits are in close agreement from $t_{\text{min}} = 5$ onwards. However the mass starts to rise slightly as t_{min} is pushed further out and it is only at $t_{\text{min}} = 9$ that the mass becomes stable as t_{min} is varied by one. Fits to the heavier κ_{val} correlators show the same general trend, the mass becoming stable at around $t_{\text{min}} = 9$. From this point, the errors on the fitted masses from the LL,FL fit are larger than those obtained from the LL,FF fit and thus the LL,FF fit was selected in preference. Comparing these results with those obtained from the single cosh fits, the results are in agreement within statistical error. The factorising fit gave results consistent and a reasonable χ^2/d.o.f. for $t_{\text{min}} \geq 10$ but was not selected for the final fit as the errors tended to be less symmetric. The percentage difference in the fitted masses rises from 0.6% to 1.4% as the valence quark mass becomes lighter. The deviation in the mass is less than one σ in all cases. In general the choice of fit does not have a significant impact on the final results. The effective mass plot in Figure 4.4 shows the final mass selected from the LL,FF fit.

The sliding window plot for the vector in Figure 4.2 shows that the fitted masses from each fit type start to agree from $t_{\text{min}} = 9$. Simultaneous fits to the LL,FL correlator combination resulted in larger errors than both the LL,FF and LL,FL,FF fits, either of which could have been selected for the final results. However the factorising fits were not as stable as the LL,FF fits with respect to small variations in t_{min}. The maximum deviation in the fitted masses from each type of fit amounts to less than one σ with the greatest percentage difference of 2.3% at the lightest valence quark mass. The effective mass plot in Figure 4.4 shows the final fitted mass selected from the LL,FF fit.

A similar sliding window analysis was performed for the degenerate nucleon and delta baryons, shown for $\kappa_{\text{val}} = 0.13550$ in Figure 4.3. For the nucleon the fitted masses are in agreement from $t_{\text{min}} = 9$. The final fit selected was the double exponential fit to the LL,FF correlators in the range [10-15] as this gave the lowest errors for most cases, excepting the simple fits to the ground state. At later time slices the errors on the fitted nucleon masses became increasingly large as can be seen from Figure 4.3. This was in part due to the increased noise in the nucleon correlator, a problem which was worse for the delta. Hence for the delta, the effect of reducing the maximum time slice to 14 was investigated. No significant improvement in the fits was observed and so the maximum time slice was selected to be $t_{\text{max}} = 15$. The LL,FF fit proved unstable at the heaviest κ_{val} for the delta and the masses obtained from the factorising fit were very susceptible to small changes in the fit interval. The final fit selected was a double exponential fit to the LL,FL correlator combination, which gave consistent results with the single cosh fit to the FL correlator. The deviation of the masses for the baryons was less than 1.7σ between the largest and smallest mass estimate in every case. The percentage difference in the masses increases dramatically at the lightest valence quark mass if the extreme values taken from the FL and LL,FL,FF fits are compared. The other three types of fit give much closer agreement. This highlights the difficulty observed in extracting the mass for the delta.

4.5.2 Fitting the $\beta = 5.2$, $\kappa_{\text{sea}} = 0.13500$ data set.

The data set at $\beta = 5.2$, $\kappa_{\text{sea}} = 0.13500$ had the largest statistics of all the dynamical data sets and hence the jackknife errors calculated for the time sliced correlator data were greatly reduced. One consequence of this was that it became harder to fit the data, particularly for the pseudoscalar which has the smallest errors in any case. This can be seen from the sliding window plot for the pseudoscalar in Figure 4.5 where the χ^2/d.o.f. lies in the range 2-3 for the majority of fits. One noticeable feature of this plot is the large skewed errors for the masses obtained from fits to the LL,FL pair of correlators. In fact the masses from this fit have not been included in the plot for $t_{\text{min}} \geq 8$ as they lie below the range of the graph. The corresponding χ^2/d.o.f. for these fits have been shown and have acceptable values. However this was because the errors on the fitted masses were so large. The results from the LL,FL fit were thus not considered further.

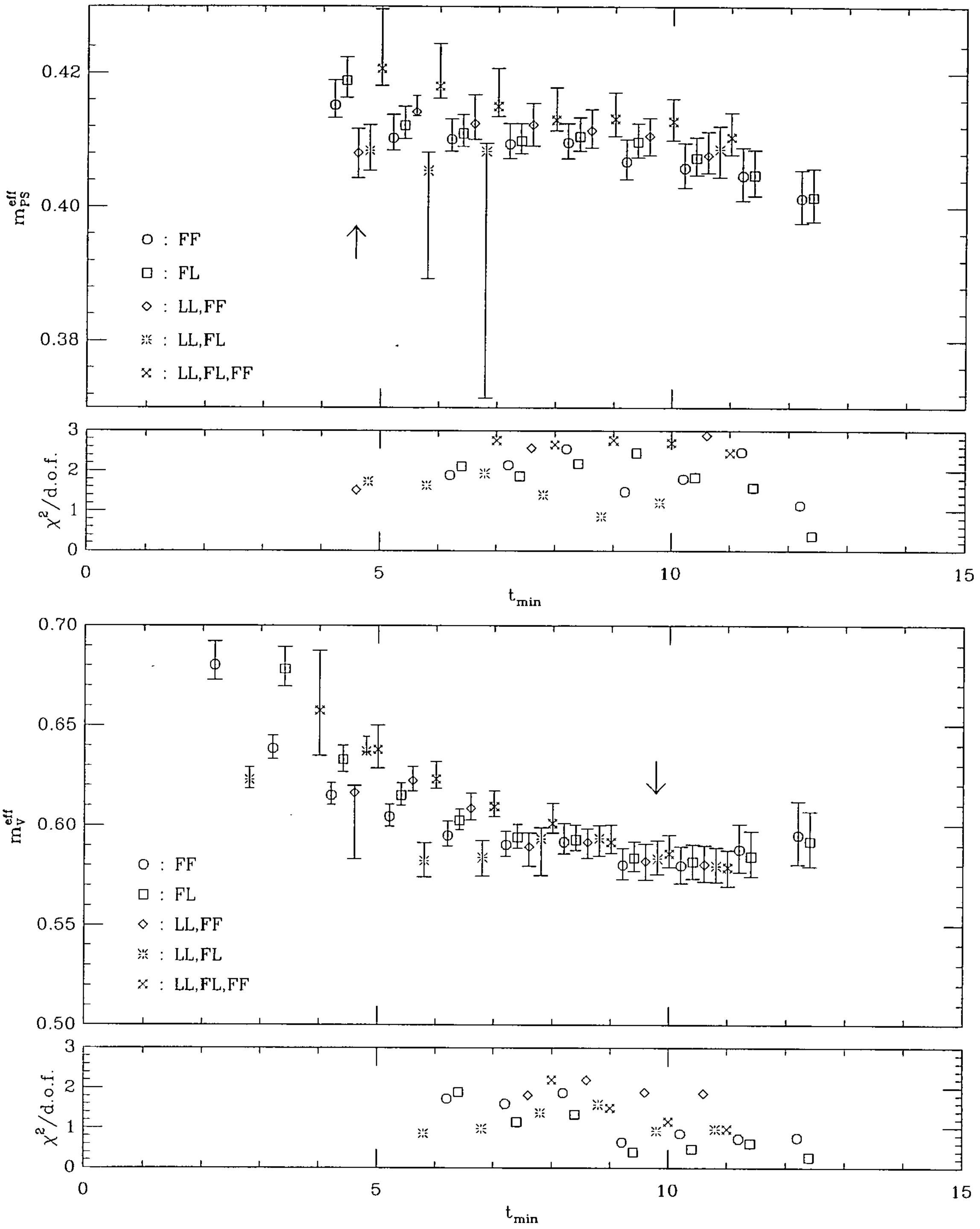

Figure 4.5: As for Figure 4.2 for the pseudoscalar and vector masses for the $\beta = 5.2$, $\kappa_{\rm sea} = 0.13500$ data set at $\kappa_{\rm val} = 0.13500$.

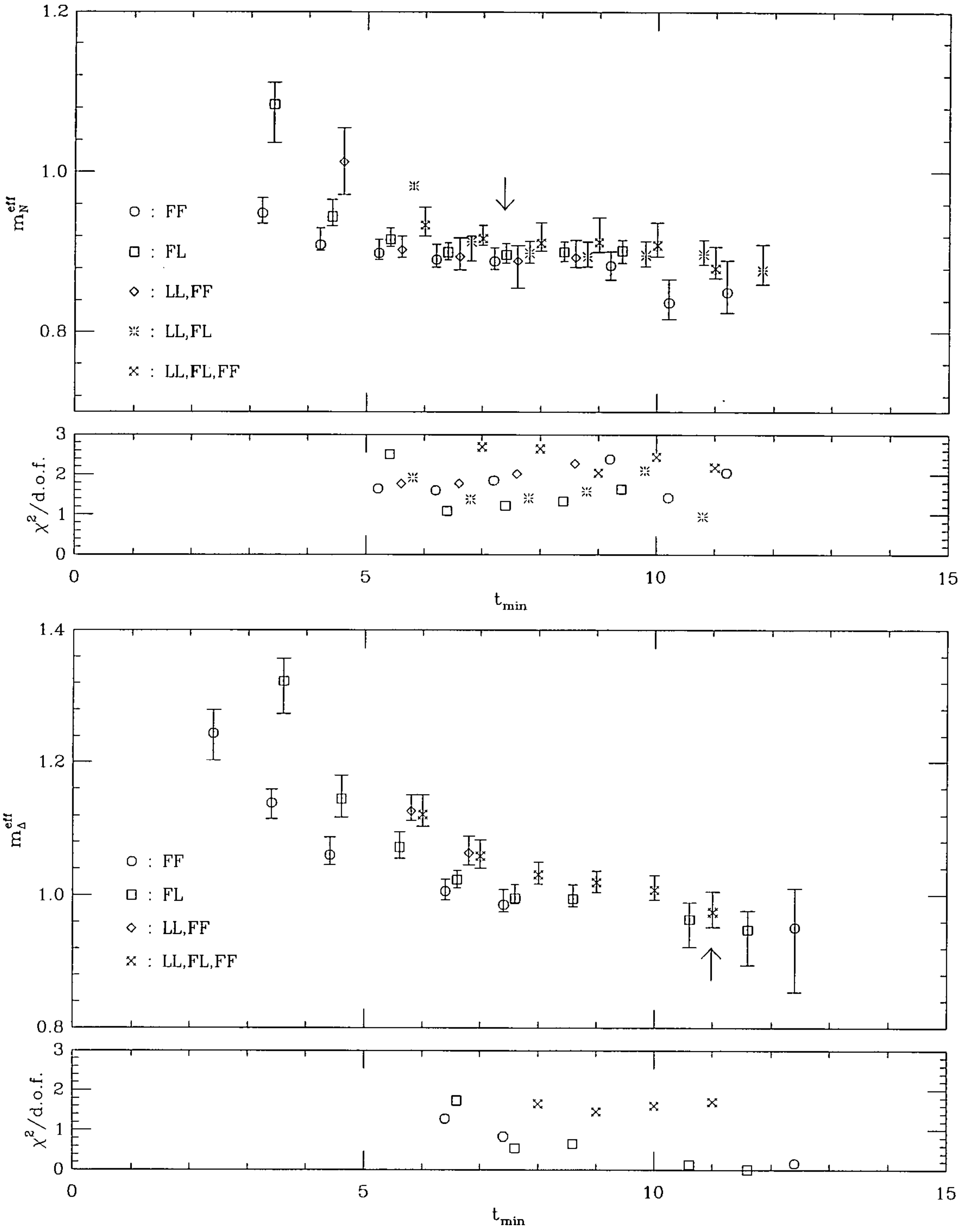

Figure 4.6: As for Figure 4.2 for the nucleon and delta for the $\beta = 5.2$, $\kappa_{sea} = 0.13500$ data set at $\kappa_{val} = 0.13500$.

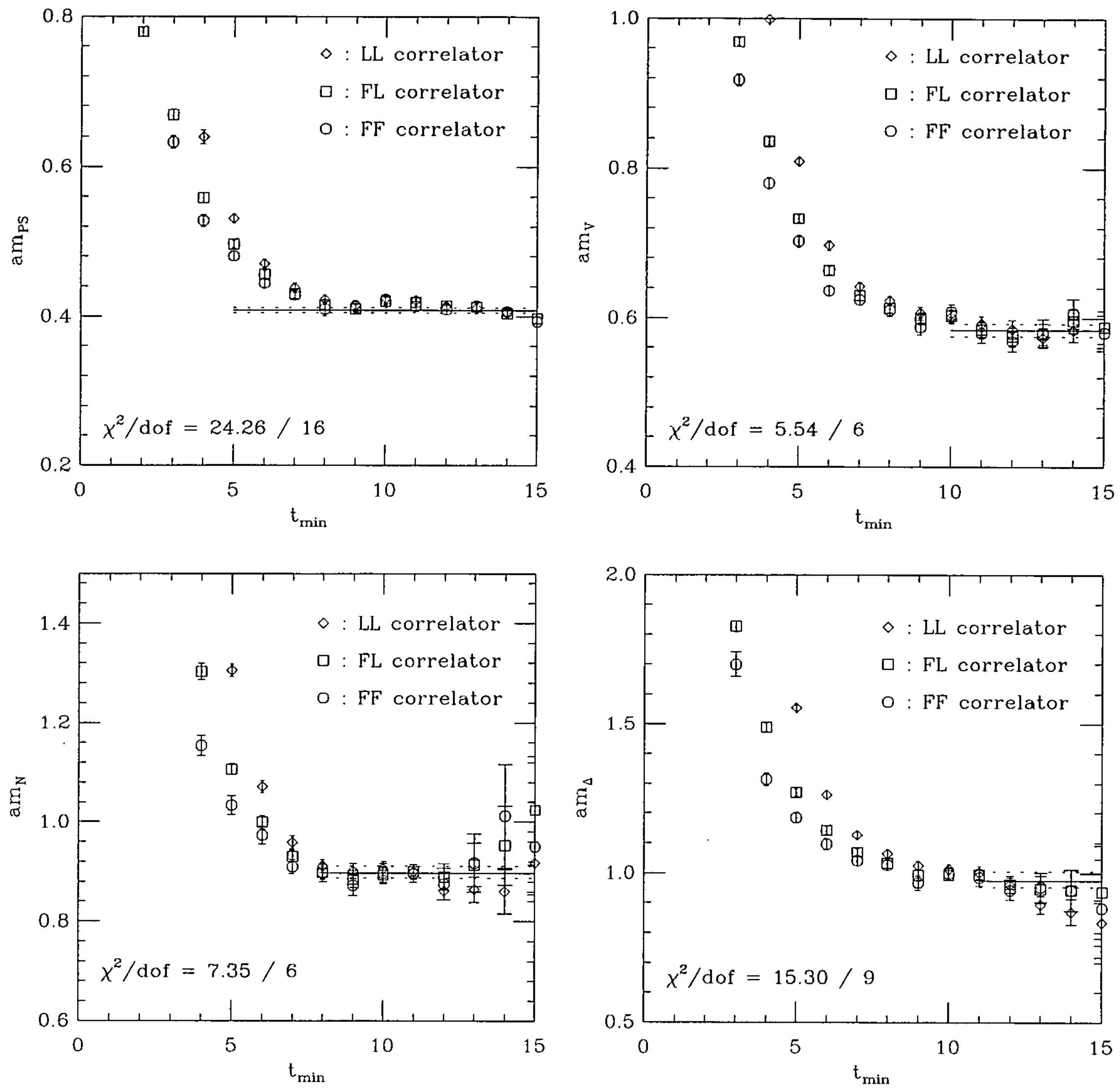

Figure 4.7: As for Figure 4.4 for the $\beta = 5.2$, $\kappa_{\rm sea} = 0.13500$ data set at $\kappa_{\rm val} = 0.13500$. The pseudoscalar has been fitted by a double cosh fit to the LL,FF correlator combination, the vector similarly to the LL,FL combination. The nucleon (delta) was fitted to a single (double) exponential to FL (LL,FL,FF) correlator(s).

Masses from the factorising fit were not selected for the best results as they were slightly larger than the results from the other fits, although still consistent within statistical errors. The χ^2/d.o.f. for the LL,FF fits reached acceptable values at $t_{\rm min} = 11$ or $t_{\rm min} = 5$ except at the heaviest $\kappa_{\rm val}$ where only the $t_{\rm min} = 11$ value was acceptable. These fits were then selected for the final fits. Examining the effective mass plot in Figure 4.7 there is a clear "wiggle" in the plateau which could account for some of the difficulties encountered in fitting the pseudoscalar.

The mass results for the vector for different fit types were in close agreement for fit ranges with $t_{\rm min} \geq 10$. The LL,FF fits were not as stable with respect to small variations in the fit range as the LL,FL fits, which were selected in preference for the final results. Factorising fits gave slightly larger errors than those obtained from the single cosh fits and were not used for the best results. Similar variations in the mass results for the mesons obtained from different fits were observed as for the $\beta = 5.2$, $\kappa_{\rm sea} = 0.13550$ data set.

For the nucleon and delta both simultaneous fits (LL,FF and LL,FL) proved highly unstable, in particular for the LL,FL correlator combination. The LL,FF fits gave mass results with values of χ^2/d.o.f. ≤ 4 for the nucleon and χ^2/d.o.f. ≤ 5 for the delta, with skewed error bars in both cases. Simultaneous fits using both correlator combinations were only possible for the nucleon at the lightest $\kappa_{\rm val}$ as can be seen from Figure 4.6. This could be due to the fact that this correlator has the noisiest signal, reducing the constraints imposed upon the fit. The factorising fits for the nucleon gave similarly high values for the χ^2/d.o.f. and hence the single exponential fits were considered for the final results. From the effective mass plot of the nucleon in Figure 4.7, the onset of the ground state plateau occurs very early around $t = 8$. This meant that single exponential fits were stable for a wide range of fit intervals, the FL fits more stable than the FF fits. A long fit interval of [8-15] was selected for the final fit for the nucleon. For the delta a clear signal of the plateau was not observed in the effective mass plot. In this case the factorising fits, despite larger errors and χ^2/d.o.f. were the most stable as the minimum time slice was varied and thus were selected for the final fits.

4.5.3 Fitting the $\beta = 5.26$, $\kappa_{\rm sea} = 0.13450$ data set.

The sliding window plots for the pseudoscalar and vector for $\kappa_{\rm sea} = \kappa_{\rm val}$ are shown in Figure 4.8. Figure 4.10 shows the corresponding effective mass plots. The final fit for the pseudoscalar was selected to be in the range [9-15] for the LL,FF fit, in preference to the LL,FL fits which gave slightly larger errors. The factorising fit gave consistent results but with a higher χ^2/d.o.f. than the LL,FF fits. The mass difference for the different fit types was less than 0.5%, 0.8σ for the pseudoscalar, indicating that mass is independent of the choice of fit. For the vector the LL,FL fit in the range [9-15] was selected as the final fit. Both the factorising fit and the LL,FF fit, resulted in slightly higher mass values with a correspondingly larger χ^2/d.o.f. and hence were not selected. The early plateau of the ground state at $t = 8$ allowed long fit ranges to be considered even for the single cosh fits. The systematic error in the mass arising from the choice of fit was around 1% for the vector in all cases.

All types of fit were possible for the nucleon. The LL,FF fit was selected as the best fit as this was the most stable fit with low values of the χ^2/d.o.f. in the sliding window analysis. This can be seen in Figure 4.9. Fitted nucleon masses deviate at most by 1.7σ when different fit types are compared. Fitting the delta using the LL,FF type of fit proved difficult, with unacceptable fits over any fit interval for the correlators with $\kappa_{\rm val} = 0.13450$. Factorising fits gave results consistent within statistical errors, however the errors were larger than those obtained from single exponential fits. In addition, the single exponential fits showed the greatest stability as the fit interval was changed slightly. The FF fit was thus selected to be the final fit. As an indication of the uncertainty in the delta mass, the deviation between different mass estimates determined from different fit procedures was at most 2σ.

4.5.4 Fitting the $\beta = 5.29$, $\kappa_{\rm sea} = 0.13400$ data set.

The $\beta = 5.29$, $\kappa_{\rm sea} = 0.13400$ data set was the heaviest sea quark mass considered in the matched ensemble. As can be seen from the sliding window plot for

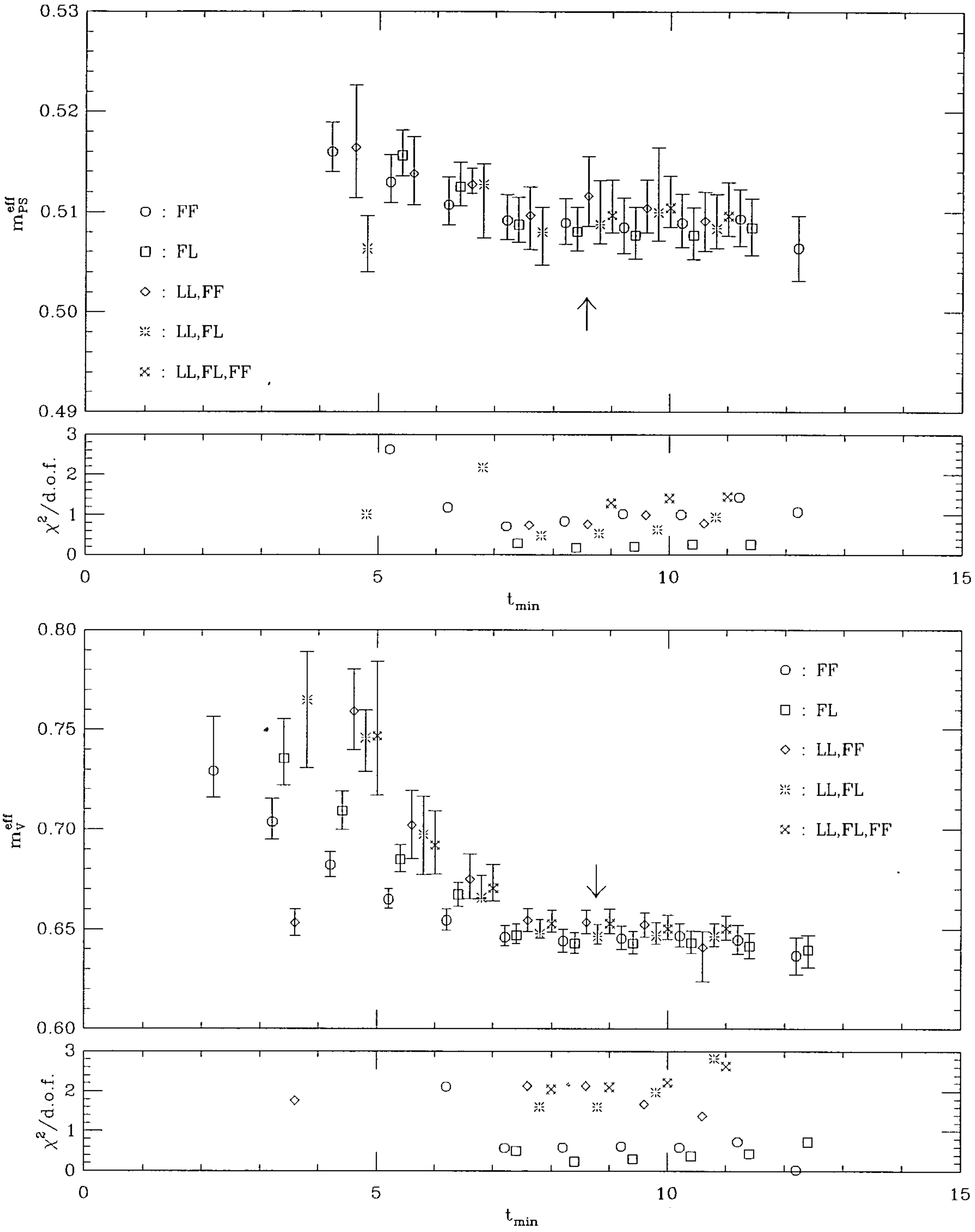

Figure 4.8: As for Figure 4.2 for the pseudoscalar and vector masses for the $\beta = 5.26$, $\kappa_{\rm sea} = 0.13450$ data set at $\kappa_{\rm val} = 0.13450$.

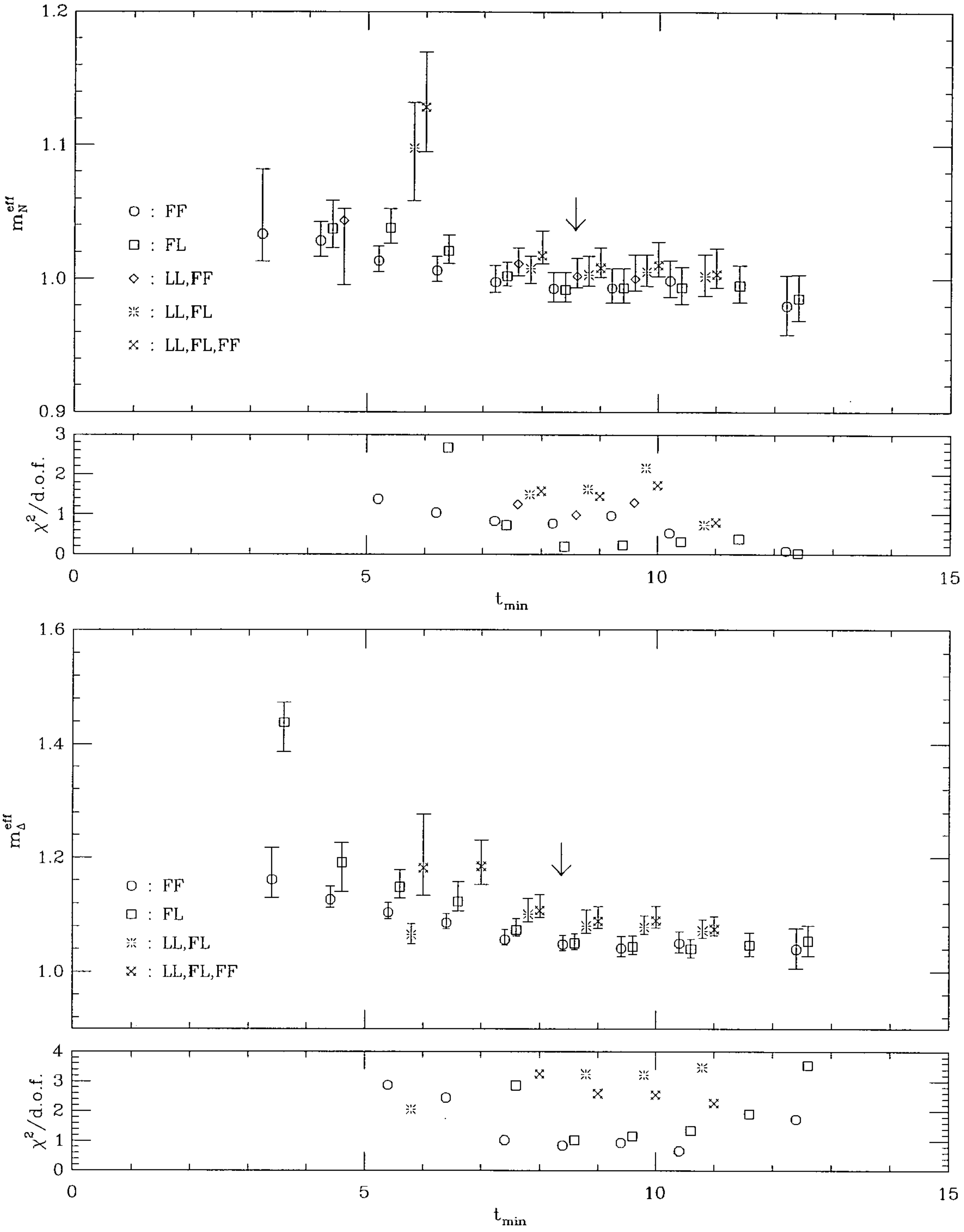

Figure 4.9: As for Figure 4.2 for the nucleon and delta for the $\beta = 5.26$, $\kappa_{\rm sea} = 0.13450$ data set at $\kappa_{\rm val} = 0.13450$.

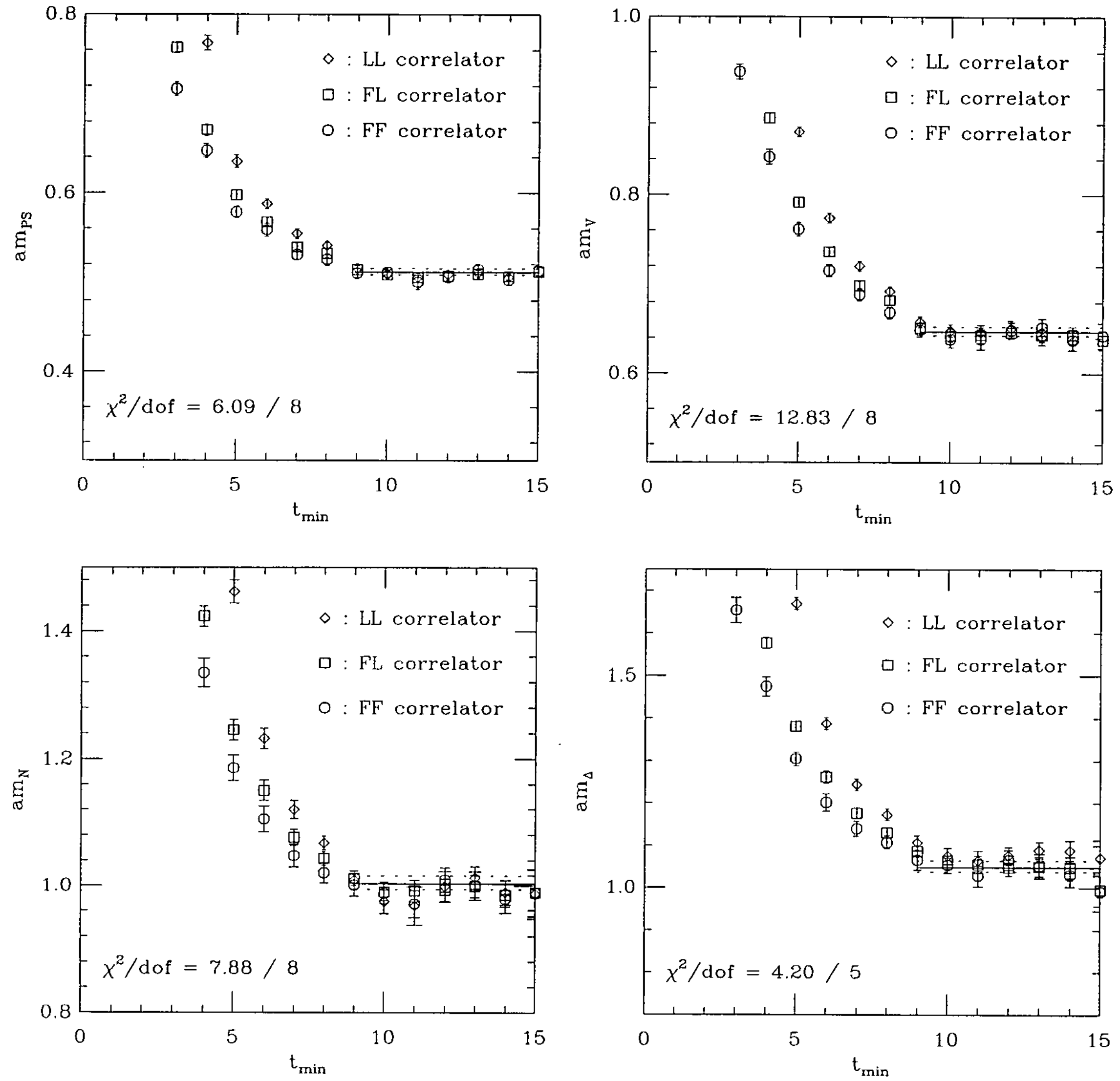

Figure 4.10: As for Figure 4.4 for the $\beta = 5.26$, $\kappa_{\text{sea}} = 0.13450$ data set at $\kappa_{\text{val}} = 0.13450$. The pseudoscalar (vector) have been fitted by a double cosh fit to the LL,FF (LL,FL) correlator combination. The nucleon was fitted by a double exponential to the LL,FF combination and the delta was fitted by a single exponential to the FF correlator.

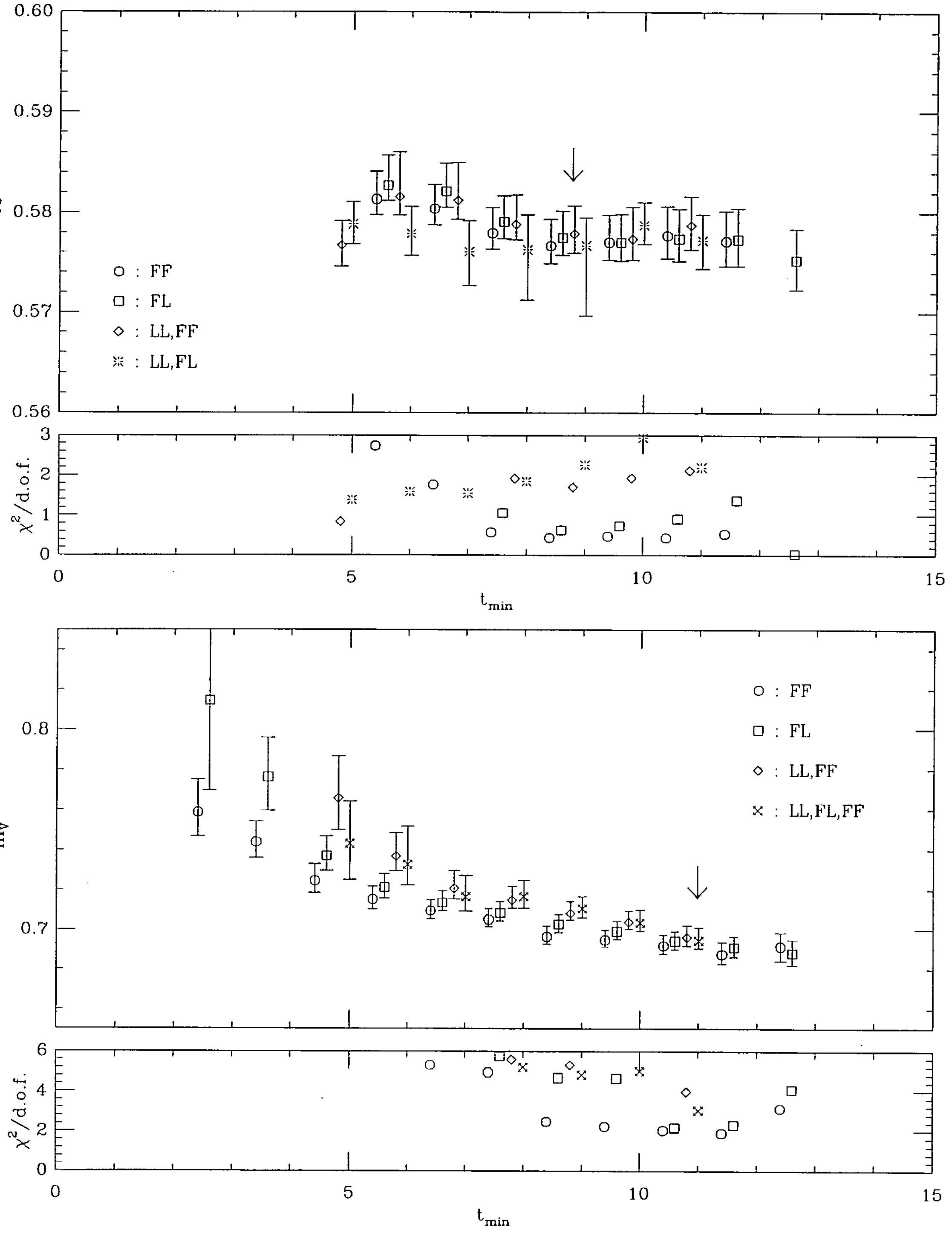

Figure 4.11: As for Figure 4.2 for the pseudoscalar and vector masses for the $\beta = 5.29$, $\kappa_{\rm sea} = 0.13400$ data set at $\kappa_{\rm val} = 0.13400$.

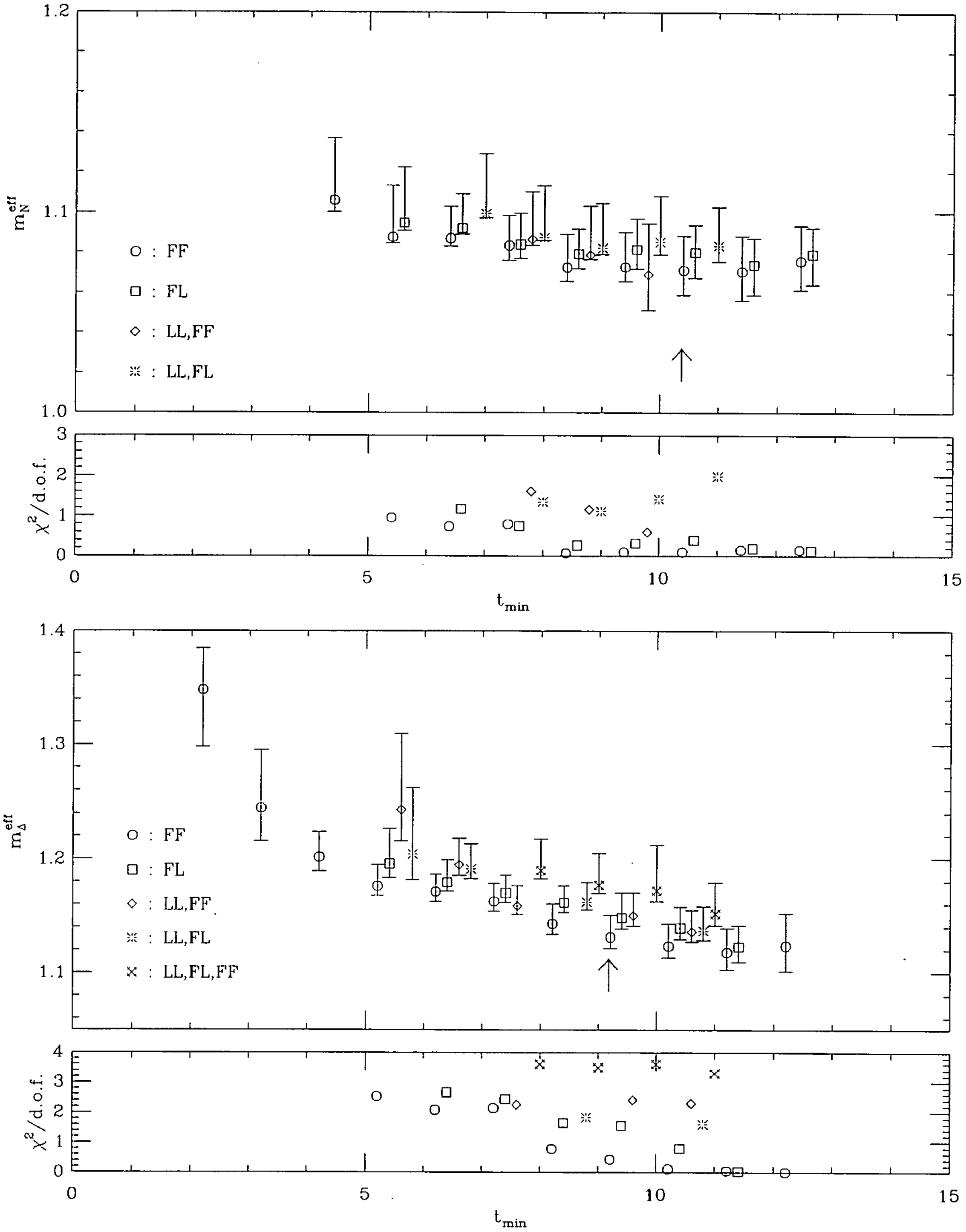

Figure 4.12: As for Figure 4.2 for the nucleon and delta for the $\beta = 5.29$, $\kappa_{\rm sea} = 0.13400$ data set at $\kappa_{\rm val} = 0.13400$.

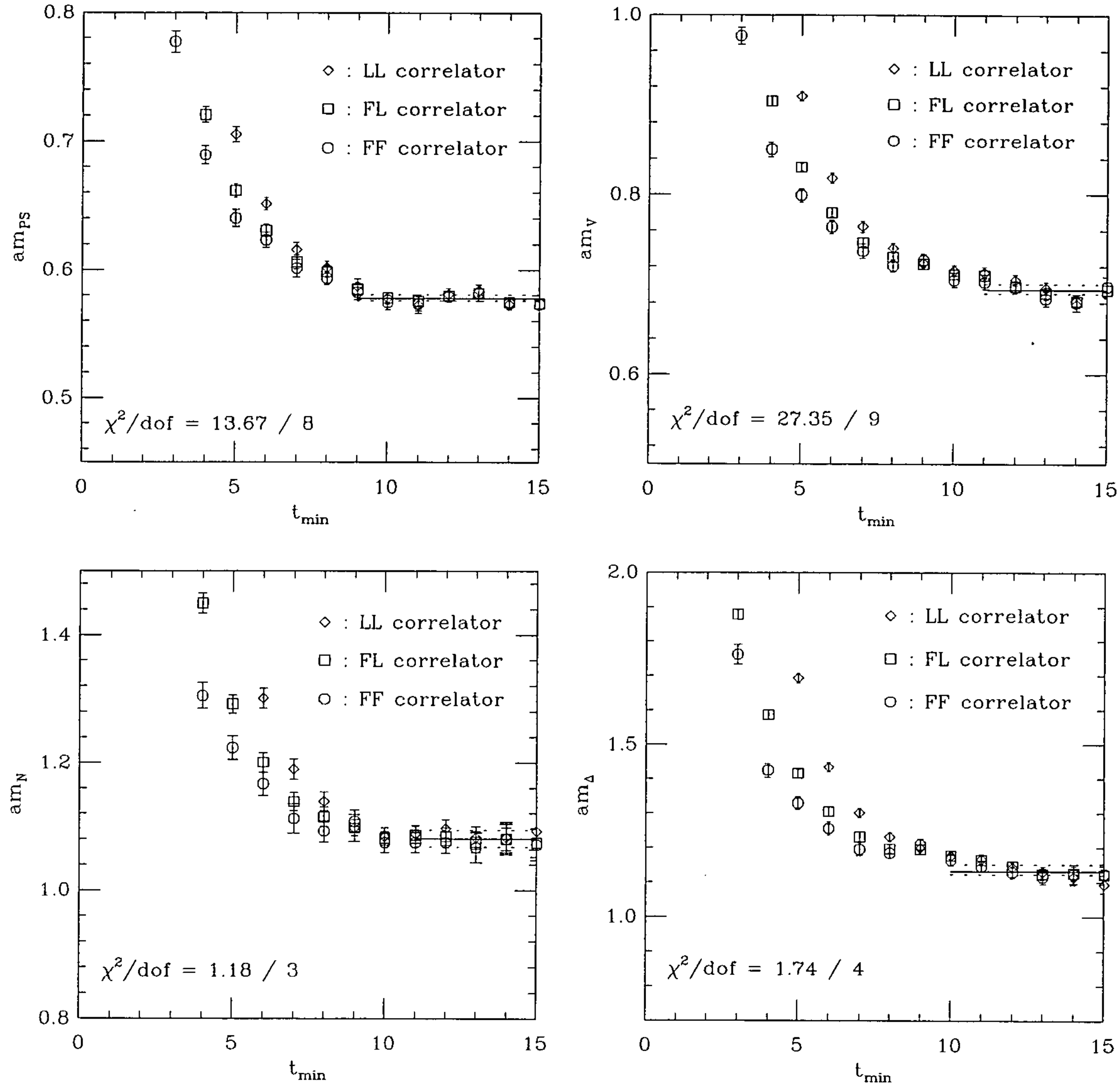

Figure 4.13: As for Figure 4.4 for the $\beta = 5.29$, $\kappa_{\mathrm{sea}} = 0.13400$ data set at $\kappa_{\mathrm{val}} = 0.13400$. The pseudoscalar (vector) have been fitted by a double cosh fit to the LL,FF (LL,FL,FF) correlator combinations. The nucleon and delta were fitted by a single exponential to the FL and FF correlator respectively.

the pseudoscalar in Figure 4.11, the fitted masses are in close agreement for fit intervals with $t_{\text{min}} \geq 9$ for all the fits that were possible. Factorising fits were attempted, however these proved extremely unstable, with values of χ^2/d.o.f. ≥ 6. The factorising fits were then repeated using an uncorrelated fit. This was stable with low χ^2/d.o.f. values and mass results compatible with those obtained from the other types of fit. This indicates that correlations in the data contributed to the instability of the fits. The results from the uncorrelated fits were not considered further as it was clear that the data is correlated. The LL,FF fit was selected as the final fit in preference to the LL,FL fit which had much larger errors. Although the final t_{min} selected in Figure 4.11 for the pseudoscalar may seem a little high, Table C.14 in appendix C shows that the mass results were in extremely good agreement for all fit types.

Figure 4.13 shows that there was not a clear signal of the ground state plateau for the vector. The vector mass was subsequently hard to extract, with the LL,FL fits only possible for two of the κ_{val} values considered. Single cosh fits to the FL correlator gave large χ^2/d.o.f. values which could be the cause of the instability in the LL,FL fits, as can be seen from Figure 4.11. Indeed the range of χ^2/d.o.f. displayed in this plot has been doubled compared with the other plots and all the values lie within the range 2-6. The factorising fit was chosen in preference to the LL,FF fit as this resulted in a more consistent (although high) χ^2/d.o.f. across the full range of valence quark masses.

The simultaneous fits (LL,FF and LL,FL) for the nucleon gave mass results with very skewed error bars, as can be seen from Figure 4.12. In addition, factorising fits were highly unstable and hence no results are reported. The final fits were taken from the single exponential fit to the FL correlator as this fit was the most stable under small variations in the minimum time slice. For the delta all the types of fits considered were possible. Fits to the ground and first excited states were ruled out by the instability of the fitted mass as t_{min} was varied slightly. The final fit was selected to be a single exponential fit to the FF correlator. As can be seen from the graph in Figure 4.13 the effective mass for the delta continues to drop until $t = 13$.

4.5.5 Fitting the matched quenched data set

The analysis of the matched quenched data set at $\beta = 5.93$ is now discussed. A sliding window analysis was undertaken for the pseudoscalar, vector, nucleon and delta. The results of all the fits investigated for the pseudoscalar and vector are displayed in Figure 4.14 for the lightest valence quark mass at $\kappa_{\text{val}} = 0.13390$. The LL,FF fit was selected for the final fit for the pseudoscalar in the range [9-15] as this was the most stable fit with the smallest statistical errors. Final mass results differ by less than 1% between the largest and smallest values. Figure 4.16 shows that the effective mass plots appear very similar to those obtained from the dynamical simulations. For the vector, the best fit was chosen to be the factorising fit. This gave the most stable results with respect to small variations in the fit interval and mass estimates compatible with the single exponential fits.

The onset of the ground state plateau for the nucleon occurs relatively early around $t = 8$. This meant that all the fits had acceptable χ^2/d.o.f. values for long fit intervals. The LL,FF fits to the heaviest valence quark mass proved very unstable and no mass result is quoted for this fit. The final fit was selected to be the LL,FL fit as this gave reasonablely small errors and low χ^2/d.o.f. values. All other fits gave consistent results as can be seen in Figure 4.15. For the delta all fit types were possible. However the factorising fit and the LL,FF fit were the least stable. For this reason the LL,FL fit was chosen as the best fit. This gave the lowest χ^2/d.o.f. and consistent results with the single exponential fits. The deviation between the largest and smallest delta masses estimates was around one σ.

4.6 Summary of fit results

In general the choice of fit procedure to extract the lattice masses did not make a significant impact on the final results for all the data sets considered. Different fit types were selected according to greater stability in the fitted masses and smaller statistical errors. Table C.1 in appendix C contains a summary of the final fit types selected for each data set. The data set with the greatest statistics

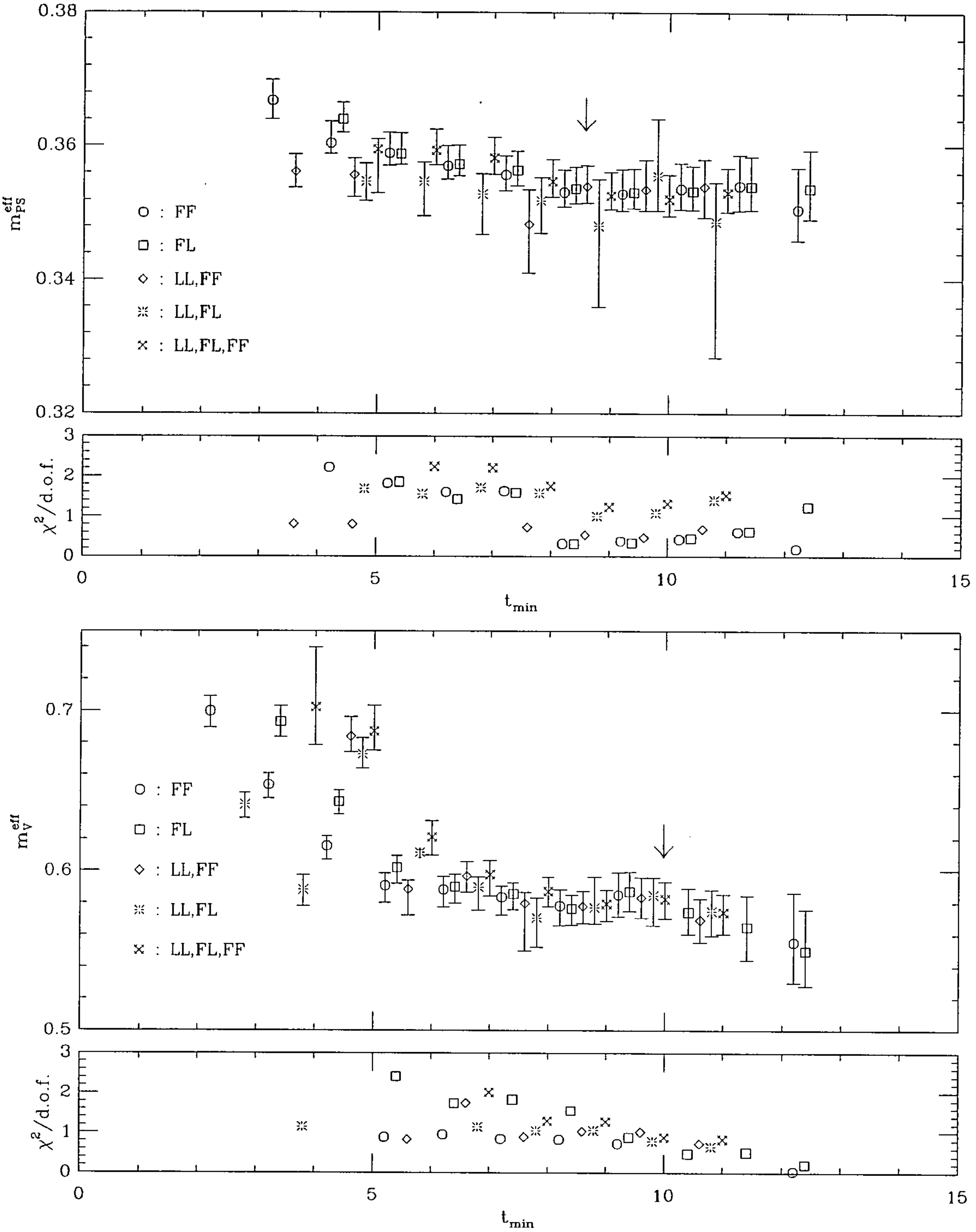

Figure 4.14: As for Figure 4.2 for the pseudoscalar and vector masses for the $\beta = 5.93$ matched quenched data set at $\kappa_{\rm val} = 0.13390$.

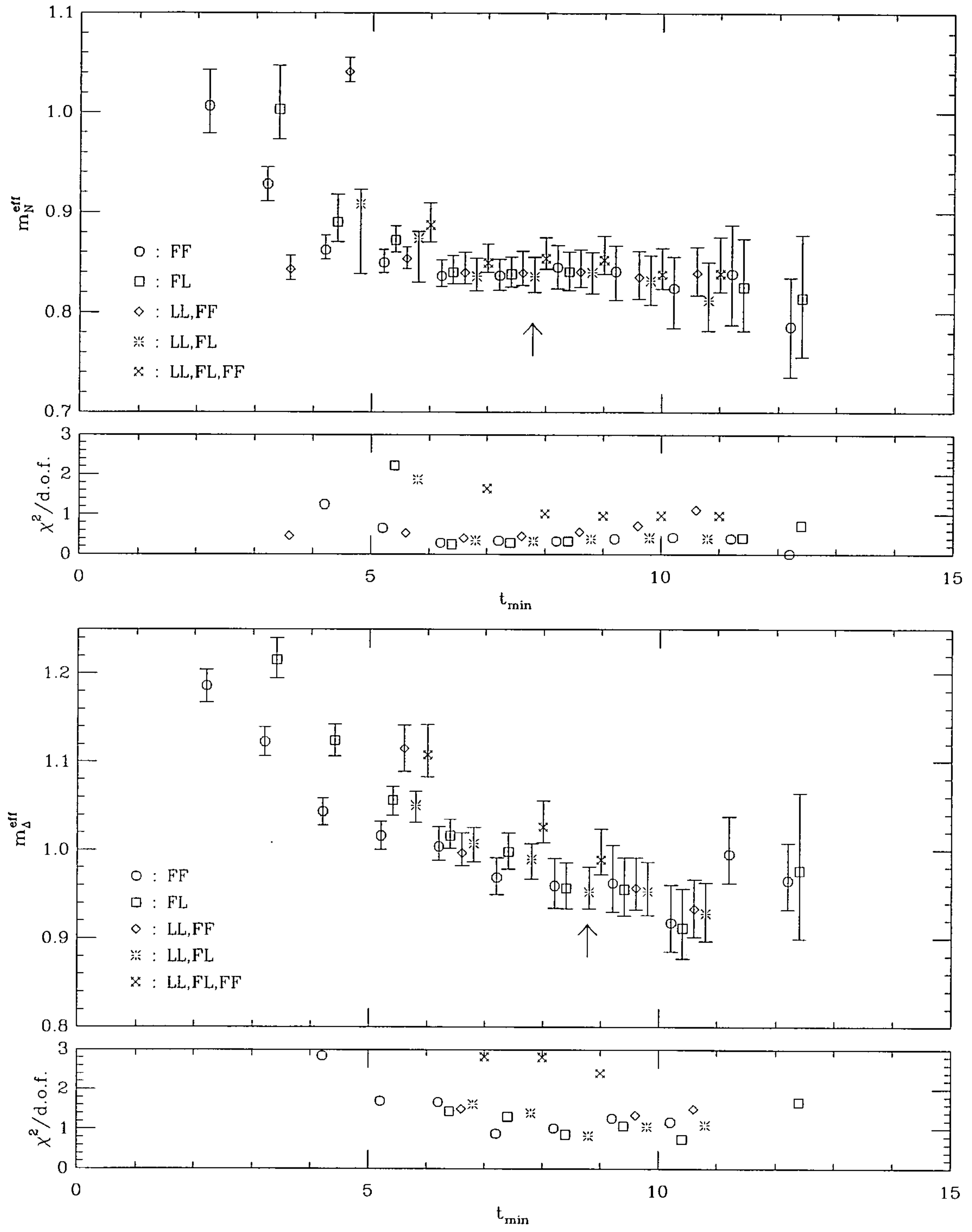

Figure 4.15: As for Figure 4.2 for the nucleon and delta masses for the $\beta = 5.93$ matched quenched data set at $\kappa_{\rm val} = 0.13390$.

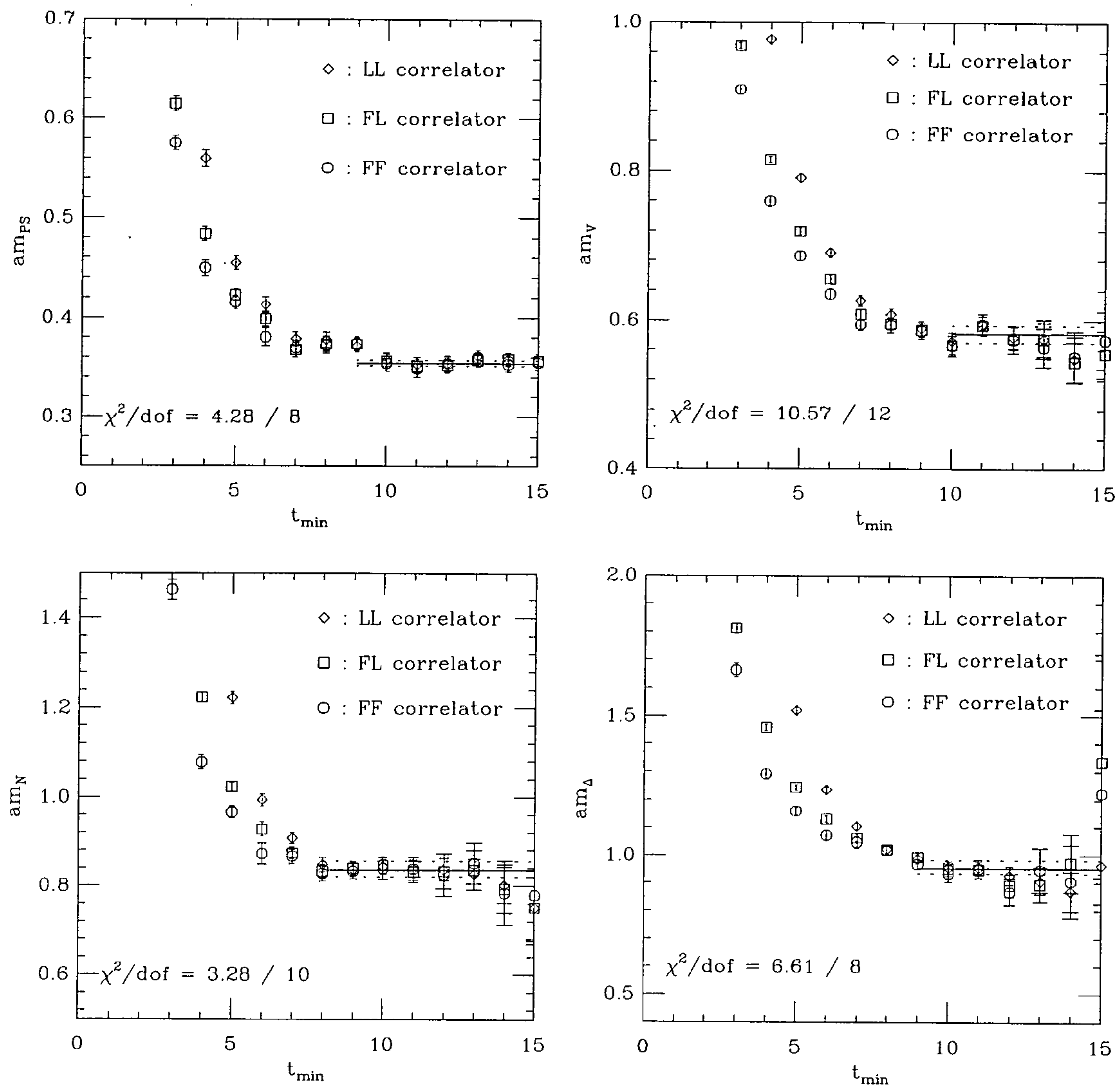

Figure 4.16: As for Figure 4.4 for the $\beta = 5.93$ matched quenched data set at $\kappa_{\mathrm{val}} = 0.13390$. The pseudoscalar (vector) has been fitted by a double cosh fit to the LL,FF (LL,FL,FF) correlator combination. The nucleon and delta were fitted by a double exponential to the LL,FL correlator combination.

($\beta = 5.2$, $\kappa_{\mathrm{sea}} = 0.13500$) proved more difficult to fit due to a reduction in the jackknife errors on the time sliced correlator data and fluctuations in the ground state plateau. Stability of the fits also proved a problem for the data set with the largest $\beta = 5.29$ with difficulties arising from identifying the onset of the plateau. Extracting the masses from correlators generated at the heaviest valence quark mass was usually easier due to a higher signal to noise ratio. Comparing the analysis of the matched quenched data set with the dynamical simulations resulted in no noticeable differences in the relative ease of extracting the mass information.

4.7 The PCAC mass

The partially conserved axial current (PCAC) mass was determined for all the data sets considered in this chapter. The definition of m_{PCAC} and the method of determination has previously been described in section 3.3. For $N_{\mathrm{f}} = 2$ simulations the axial vector improvement coefficient, c_{A} has not yet been determined non-perturbatively. Thus in the analysis of the dynamical data sets the one-loop result for c_{A} from perturbation theory, defined in equation 3.9, was used. The one-loop value of c_{A} was also used for the quenched matched simulation for consistency. In both cases the bare coupling was used to determine c_{A}. Fits were performed to the FL correlator using equation 3.12. The sliding window analysis was very stable with respect to variations in the fit range as was observed in the quenched analysis. Values for the χ^2/d.o.f. were in general around 1, rising to 2 for the lightest sea quark mass simulation. Figure 4.17 shows example effective mass plots obtained for m_{PCAC} for the dynamical data sets at $\kappa_{\mathrm{sea}} = \kappa_{\mathrm{val}}$. The results for m_{PCAC} from all the data sets are collected in appendix C.

4.8 Comparing the lattice results

One way to compare the mass results obtained in the meson sector for each data set is to plot the vector mass against the pseudoscalar mass squared. Figure 4.18 displays this type of plot where the masses are in units of r_0. The experimental points corresponding to the K and K*, and the ϕ and η_s mesons are shown for

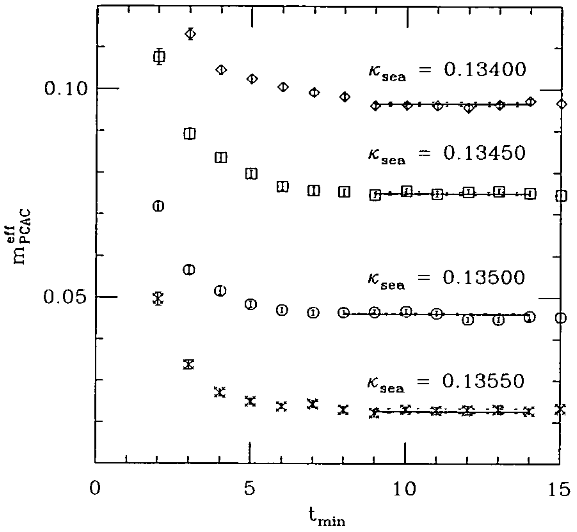

Figure 4.17: The PCAC mass for all the dynamical data sets at $\kappa_{sea} = \kappa_{val}$. The final masses have been superimposed on the effective mass plot.

comparison. (Note that the η_s is not a physical meson). Comparing the dynamical simulation at the lightest sea quark mass with the quenched results, the dynamical data show an improved trend towards the experimental points as can be seen from the upper plot. It is encouraging that the data at the lightest sea quark mass tends to decrease towards the experimental points as the valence quark mass is reduced. Simulations at lighter quark masses are of course needed in order to confirm this behaviour. Indeed the dynamical simulations all show a similar trend towards the experimental values. Within the three matched dynamical data sets themselves however, this trend appears in the opposite direction to what might be expected, the heavier sea quark mass data lying below the lighter quark mass data. This behaviour was also observed for the previous dynamical simulation reported in [92], as can be seen when the results from this paper for the $\beta = 5.2$, $c_{sw} = 1.76$ data set on the $12^3 \cdot 24$ volume are compared with the dynamical matched ensemble data in the lower plot of Figure 4.18. This trend need not be a cause for concern as the effect on the spectrum resulting from changing the lattice spacing towards the continuum limit is as yet unknown. Examining Figure 4.18

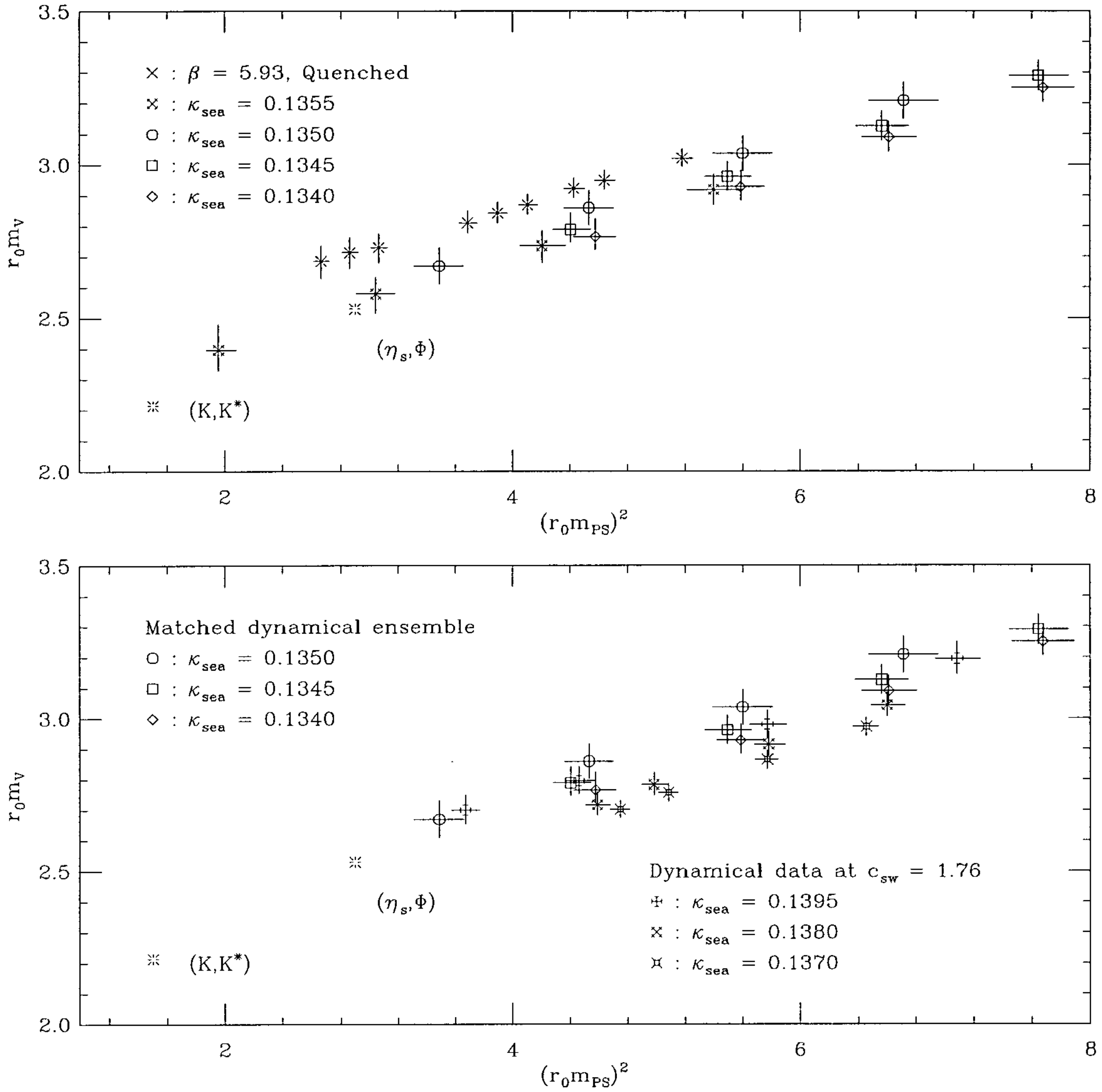

Figure 4.18: Vector mass plotted against the pseudoscalar mass squared in units of r_0. The top plot shows the results for all the data sets. The lower plot compares the matched dynamical ensemble with the previous dynamical simulation reported in [92]. The experimental values are indicated by the burst points.

further, the current dynamical data tend to lie above the data obtained from the previous simulations. This however could be a consequence of small yet significant differences in the determination of the Sommer scale arising from residual lattice artifacts due to the different fit procedures employed for both data sets.

4.9 Hyperfine splitting

In section 3.8, the quenched spectrum failed to reproduce the experimentally observed approximately constant dependence of the hyperfine mass splitting on the quark mass. Setting the scale with r_0, the upper plot in Figure 4.19 shows the vector pseudoscalar hyperfine splitting for all the data sets. Since this plot comprises of the same data illustrated in Figure 4.18 plotted in a different way, the discussion and conclusions of the previous section apply here. The matched quenched data over shoots the experimental results, as expected from the results of the analysis discussed in section 3.8. The dynamical data is lower and although there is still a small slope in the data for the lightest sea quark mass, the matched dynamical data appears much flatter than the quenched data. The lower plot in Figure 4.19 again compares the dynamical matched ensemble data with the previous dynamical simulation data reported in [92]. The recent data at lighter sea quark masses show an improved trend towards the experimental values.

4.10 The J parameter

In the quenched analysis the J parameter, defined in equation 3.15, was found to be more than 17% lower than the experimental value for all quenched data sets under consideration. The reason for this discrepancy has been attributed to errors associated with the quenched approximation. Thus it is expected that the situation will improve with the inclusion of dynamical fermions in the simulations.

Evaluating J in the quenched approximation does not require an extrapolation to the chiral limit. As pointed out in [107], for $N_f = 2$ dynamical fermion simulations this is not necessarily the case. In this type of simulation, the sea quark mass can be identified with the light quarks and the valence quarks are

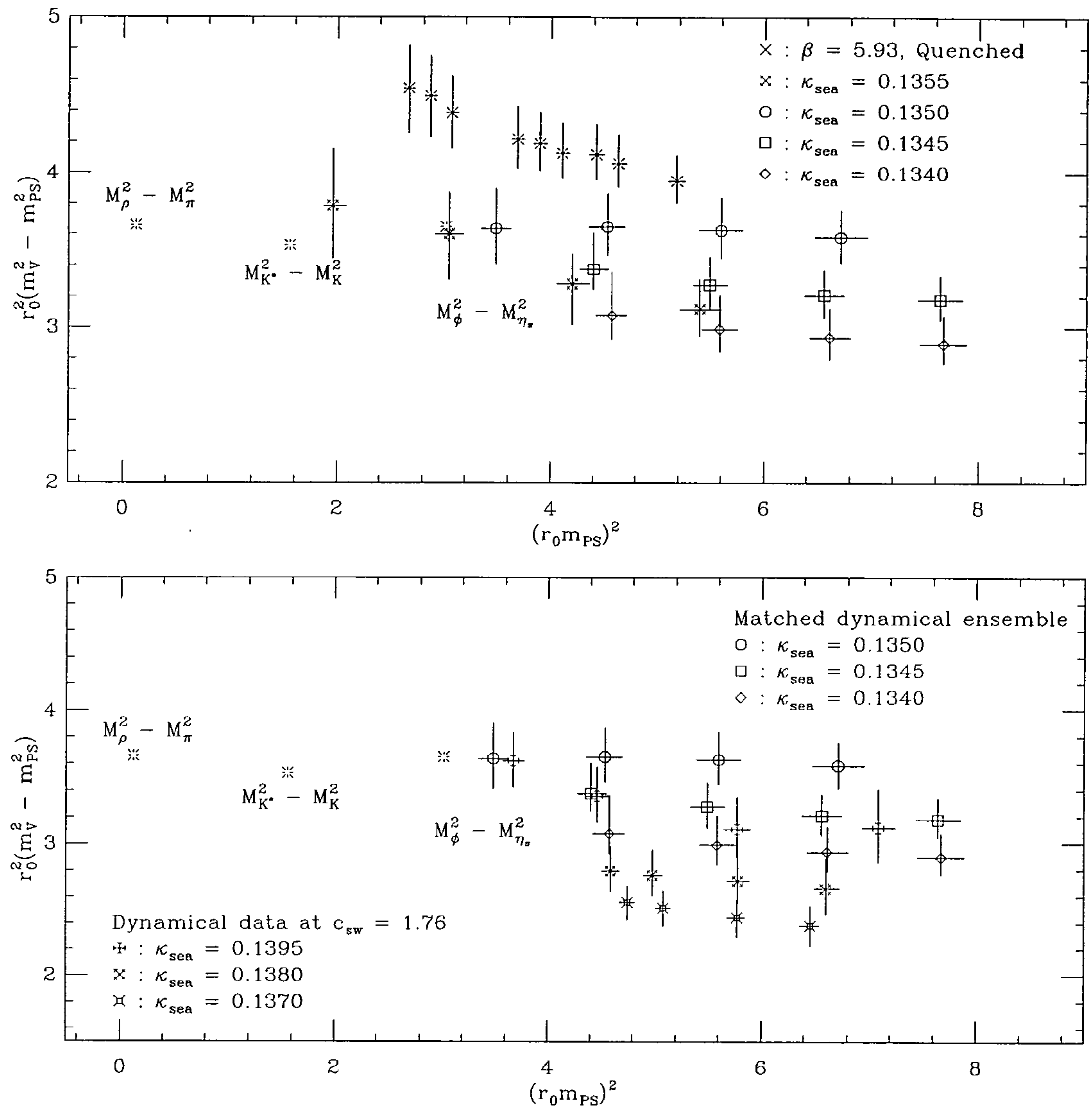

Figure 4.19: Vector-pseudoscalar hyperfine splitting in units of r_0. The top plot shows the results for all data sets. The lower plot compares the matched dynamical ensemble with the previous dynamical simulation reported in [92]. The experimental hyperfine splittings are indicated by the burst points.

then associated with the strange quark. In this scenario the strange quark is still treated within the quenched approximation. Since the light and strange quark masses are treated differently, this means for example, that the vector mass depends not only upon the valence quark mass but also upon the sea quark mass. Thus it may be necessary to perform a chiral extrapolation in the sea quark mass in order to observe an improvement towards the experimental result for J. From the observation that the J parameter determined at fixed κ_{sea} for each data set shows no significant difference from the quenched data result, as can be seen from the left hand plot in Figure 4.20, it appears that an extrapolation may indeed be required to reproduce the experimental value. Note that the J parameter determined from the matched ensemble at $\kappa_{\text{sea}} = \kappa_{\text{val}}$ yields a result of $J = 0.352\ ^{+25}_{-25}$ which is consistent with the other determinations of J.

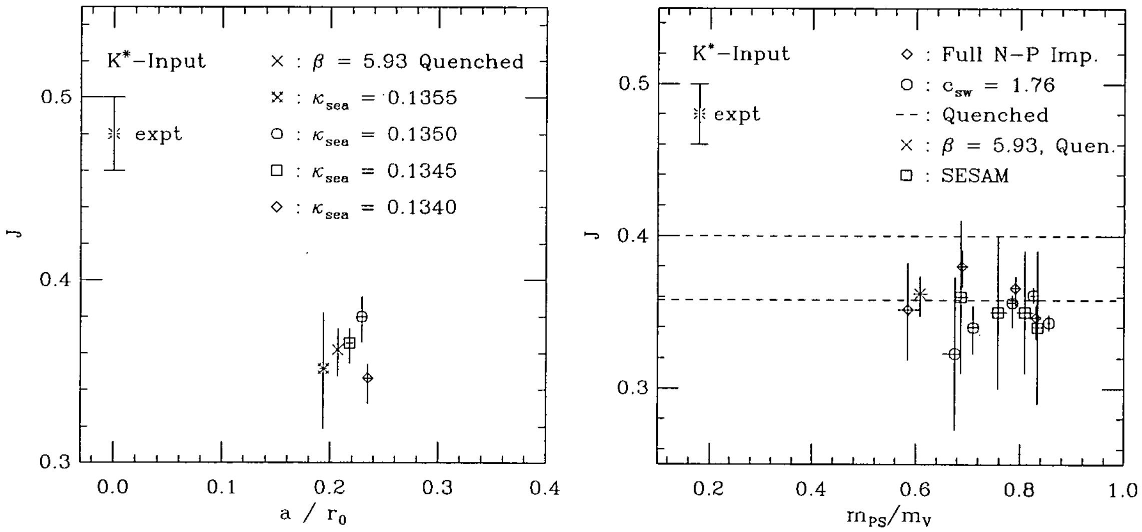

Figure 4.20: The J parameter determined with K* input. The left hand plot shows the results obtained for all the data sets considered in this chapter plotted against the lattice spacing in units of r_0. The points have been offset horizontally for clarity. The right hand plot compares these results with the previous dynamical simulation results at $\beta = 5.2$, $c_{\text{sw}} = 1.76$, $V = 12^3 \cdot 24$ taken from [92]. The results have been plotted against the mass ratio $m_{\text{PS}}/m_{\text{V}}|_{\kappa_{\text{sea}}=\kappa_{\text{val}}}$. The dashed lines represent the limits of the quenched results as determined in section 3.6. Results from the SESAM Collaboration are shown for comparison [107].

Figure 4.20 shows the results for J when the K and K* mesons have been used as input. Using the purely strange mesons as input (ϕ and η_s) gives similar results but slightly larger values, as was observed in the quenched case. The statistical errors on the results are such that there are no significant differences between the quenched and dynamical results. Within the data for the dynamical matched ensemble a slight increase in J is observed as the sea quark mass becomes lighter. However, this trend is not continued by the simulation at the lightest sea quark. Again this need not be too concerning as the situation could well change for simulations at finer lattice spacings.

The right hand plot in Figure 4.20 compares the current results for J with the results obtained for the previous dynamical simulation reported in [92]. The values shown were obtained from the $12^3 \cdot 24$ volume at $\beta = 5.2$, $c_{\mathrm{sw}} = 1.76$, for different sea quark masses. To compare all the results on the same plot, the J parameter has been plotted against the mass ratio $m_{\mathrm{PS}}/m_{\mathrm{V}}$, evaluated at $\kappa_{\mathrm{sea}} = \kappa_{\mathrm{val}}$. For the matched quenched simulation the mass ratio at the lightest valence quark was used. The dashed lines on the graph represent the maximum range of J as determined in the previous chapter for the quenched data sets. This plot shows that the dynamical results discussed here are in agreement with those from the previous simulation. There is some evidence that the recent data are slightly closer to the experimental values, although not significantly. Results from the SESAM Collaboration [107] using data at fixed sea quark mass are included on the plot for comparison. Their results for Wilson fermions are similar to the results reported here with improved Wilson fermions. (For comparison, the parameter values of the SESAM data are: $16^3 \cdot 32$, $\beta = 5.6$, four values of κ_{sea} in the range 0.1560 - 0.1575, corresponding to $1.44 \leq a^{-1}[\mathrm{GeV}] \leq 1.88$ and $0.69 \lesssim m_\pi/m_\rho \lesssim 0.83$). In addition to the linear fit used to determine the slope, SESAM investigated using more complicated fit ansätze including terms with higher powers in the valence quark mass. They find that the J parameter is further reduced in this case. The CP-PACS Collaboration find that the J parameter for relatively large sea quark masses is roughly consistent with their quenched value of $J = 0.346(22)$ [108]. Only at lighter sea quark masses

($m_{\mathrm{PS}}/m_{\mathrm{V}} \approx 0.5$) do they find that J shows an increase ($J < 0.41$) towards the experimental point $J = 0.48(2)$. (For comparison, the parameter values of the CP-PACS data are: $12^3 \cdot 24$, $16^3 \cdot 32$, and $24^3 \cdot 48$ at $\beta = 1.8$, 1.95, 2.1, 2.2 for four values of κ_{sea} at each β value, corresponding to $1.93 \leq a^{-1}[\mathrm{GeV}] \leq 2.58$ and $0.5 \lesssim m_\pi/m_\rho \lesssim 0.8$ using the improved gauge action defined in equation 1.41 and mean field improved Wilson fermions.)

4.11 The Edinburgh plot

Figure 4.21 shows the Edinburgh plot, described in section 3.5, for all the data sets. Data for all the degenerate combinations of κ_{val} for each data set have been included in the plot. At the heaviest valence quark masses the dynamical data lie close to the phenomenological curve. However, as the $m_{\mathrm{PS}}/m_{\mathrm{V}}$ mass ratio decreases the dynamical data points lie significantly higher than the matched quenched data, which are in close agreement with the curve, bearing in mind that the curve only serves as a guide. One explanation of this observation could be the presence of significant finite size effects in the dynamical data, in particular for the nucleon. Finite volume effects are expected to be larger in full QCD simulations [109] than in the quenched approximation. In both quenched and dynamical simulations, one of the constituent valence quarks of a correlator can propagate across the spatial boundary, resulting in possible finite volume effects. However in the quenched approximation, the expectation value of these correlator loops is zero due to the centre $Z(3)$ global symmetry of the pure gauge action. The existence of this exact symmetry means that there is no preferred direction in the complex plane for these loops. In contrast, the inclusion of the mass term in the action in the dynamical simulation breaks the $Z(3)$ symmetry giving rise to a non-zero expectation value for the correlator loops. This enhances the finite size effects in the dynamical case.

The analysis of the previous dynamical fermion simulations reported in [92], included a study of finite volume effects. From these simulations using the preliminary estimate of the clover coefficient, it was concluded that finite sizes effects were practically absent for lattices with a spatial extent of $L \gtrsim 1.6$ fm

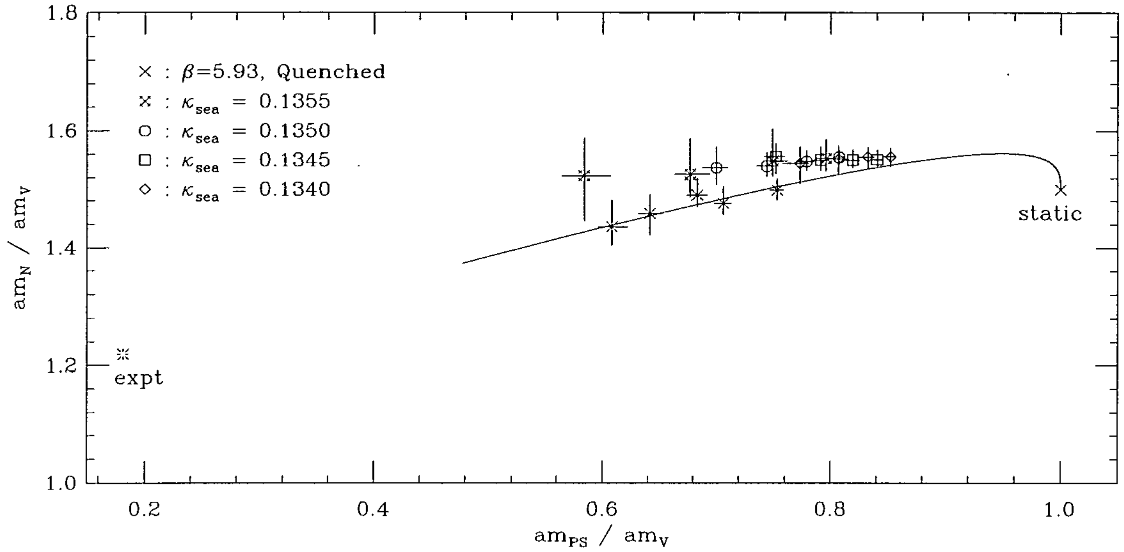

Figure 4.21: The Edinburgh plot for all the data sets. All degenerate κ_{val} correlators have been included. The phenomenological curve derived from [69] has been shown to guide the eye.

and for sea quark masses corresponding to $m_{\mathrm{PS}}/m_{\mathrm{V}} \gtrsim 0.67$. This is the case for the matched ensemble where the spatial extent is greater than 1.71 fm and $m_{\mathrm{PS}}/m_{\mathrm{V}} > 0.69$. However at the lightest sea quark mass simulation, $L = 1.60$ fm and $m_{\mathrm{PS}}/m_{\mathrm{V}} = 0.58$, below this approximate bound. This suggests that finite size effects may well be significant for this data set. Additional simulations at different lattice volumes would be needed in order to fully investigate finite size effects.

4.12 Chiral extrapolations

In the quenched approximation, chiral extrapolations of the unphysically heavy lattice hadron masses were performed to make contact with physically observed hadrons composed from light quarks. Traditionally this is achieved by extrapolating the hadron masses in terms of the valence quark mass to the normal quark mass, m_{n} defined in section 3.10. With dynamical fermion simulations extrapolations can now be performed in the sea quark mass. By associating the sea quark mass with the light quarks, extrapolations were performed using hadron masses determined from correlators with $\kappa_{\text{sea}} = \kappa_{\text{val}}$. This means that light hadrons can be studied in a background sea of light quarks. Hadrons composed from strange quarks must still be considered within the quenched approximation. In order to perform extrapolations at $\kappa_{\text{sea}} = \kappa_{\text{val}}$ an extrapolation of the pseudoscalar mass squared to find κ_{crit} is required to determine the sea quark mass. The previous dynamical fermion simulations at fixed β in [92] determined κ_{crit} from the lightest three pseudoscalar masses, although five data points were available. As noted earlier, the reason for this was the strong dependence of the lattice spacing on the sea quark mass, particularly at the heavier quark masses. The current matched set of dynamical simulations were generated in order to investigate chiral extrapolations at a fixed value of the lattice spacing.

4.12.1 Pseudoscalar extrapolation at $\kappa_{\text{sea}} = \kappa_{\text{val}}$

For the matched ensemble of dynamical data sets, chiral extrapolations of the pseudoscalar mass were investigated using the masses determined at $\kappa_{\text{sea}} = \kappa_{\text{val}}$. The critical value of the hopping parameter associated with the sea quark mass, $\kappa^{\text{sea}}_{\text{crit}}$ can be defined to be the point where the pseudoscalar mass is zero, assuming the PCAC relationship holds. Of course since β varies throughout the extrapolation this is only one possible definition of κ_{crit}. From this, an uncorrelated linear fit in the improved sea quark mass of the form

$$m^2_{\text{PS}} = \alpha + \frac{2}{\kappa_{\text{sea}}}\left(\beta + \frac{\gamma}{\kappa_{\text{sea}}}\right) \tag{4.16}$$

where the coefficients are given by

$$\alpha = \frac{B}{\kappa^{\text{sea}}_{\text{crit}}}\left(-1 + \frac{b_{\text{m}}}{2\kappa^{\text{sea}}_{\text{crit}}}\right), \quad \beta = \frac{B}{2}\left(1 - \frac{b_{\text{m}}}{\kappa^{\text{sea}}_{\text{crit}}}\right), \quad \gamma = \frac{Bb_{\text{m}}}{4} \tag{4.17}$$

was examined. This expression is just the simplified form of equation 3.26 for degenerate values of the hopping parameter. Naturally there is no question of using a correlated fit as each data point is taken from an independently generated simulation. The improvement coefficient b_{m}, used as input, has not yet been determined non-perturbatively and the one-loop perturbative expression in equation 3.24 was thus used as a preliminary estimate. Note that $b_{\rm m}$ depends on β and so was different for each point in the matched extrapolation. This fit was investigated primarily as the simplest choice available which allowed a degree of freedom in the fit and was consistent with $O(a)$ improvement. From this fit

$$\kappa_{\rm crit}^{\rm sea} = 0.135988 \ {}^{+37}_{-40} \tag{4.18}$$

Figure 4.22 shows the pseudoscalar mass squared plotted against the improved sea quark mass defined by

$$\widetilde{m}_{\rm q}^{\rm sea} = m_{\rm q}^{\rm sea}(1 + b_{\rm m} m_{\rm q}^{\rm sea}), \qquad m_{\rm q}^{\rm sea} = \frac{1}{2}\left(\frac{1}{\kappa_{\rm sea}} - \frac{1}{\kappa_{\rm crit}^{\rm sea}}\right) \tag{4.19}$$

both in lattice units and in units of r_0. The resulting χ^2/d.o.f. = 5.55/1 shows that the linear ansatz clearly does not represent the current data, even in the case where the masses have been scaled by r_0. Additional matched data points would be required to refute this. (A similar extrapolation performed with $m_{\rm PCAC}$ gave a value of $\kappa_{\rm crit}^{\rm sea} = 0.135892 \ {}^{+14}_{-13}$ with χ^2/d.o.f. = 59.18/1. The χ^2/d.o.f. was large due to the very small statistical errors in $m_{\rm PCAC}$ and again a linear ansatz was not suitable.) For completeness, fitting the unimproved sea quark mass by setting $b_{\rm m} = 0$ gave a slightly higher χ^2/d.o.f. value. However, assuming that the value obtained for $\kappa_{\rm crit}^{\rm sea}$ is reliable, chiral extrapolations can then be investigated for the other hadrons.

4.12.2 Hadron extrapolations at $\kappa_{\rm sea} = \kappa_{\rm val}$

Taking the result in equation 4.18 for $\kappa_{\rm crit}^{\rm sea}$, uncorrelated linear extrapolations in the improved sea quark mass were investigated for the vector, nucleon and delta using fits of the form

$$m_{\rm H} = A + B\widetilde{m}_{\rm q}^{\rm sea} \tag{4.20}$$

where $m_{\rm H}$ represents the appropriate hadron mass. This is the simplest fit consistent with $O(a)$ improvement which can be considered with the current number of data points. Additional terms in the baryon extrapolations arising from chi-

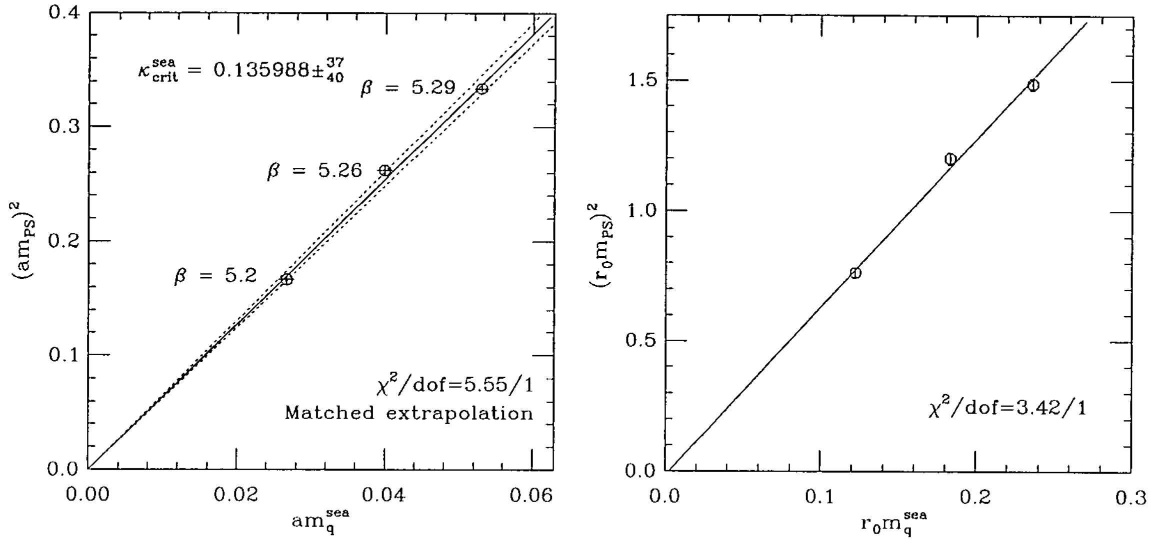

Figure 4.22: Chiral extrapolation of the pseudoscalar for the dynamical matched ensemble at $\kappa_{\rm sea} = \kappa_{\rm val}$ plotted against the improved sea quark mass. The fit is an uncorrelated linear fit to equation 4.16. The masses are in lattice units in the left hand plot and in units of r_0 in the right hand plot.

ral perturbation theory have been investigated by [110] using baryon data taken from UKQCD's previous dynamical fermion simulation, reported in [92]. They find that no firm conclusions can be drawn regarding significant improvements obtained from using this type of fit until the systematic errors are reduced below 10% and data points at lower quark masses are included in the simulation. With only three points at relatively heavy quark masses, the linear fit ansatz was adopted throughout this analysis. Figure 4.23 shows the corresponding extrapolations both in lattice units and in units of r_0. All the fits gave a reasonable χ^2/d.o.f. for the linear fit ansatz. However since only three points are included in the extrapolations and the errors on the data points are quite large, particularly for the baryons, more data points would be required to investigate possible curvature in the data.

To arrive at lattice values of the masses for the hadrons composed of light quarks, the improved normal quark mass must first be determined. Following

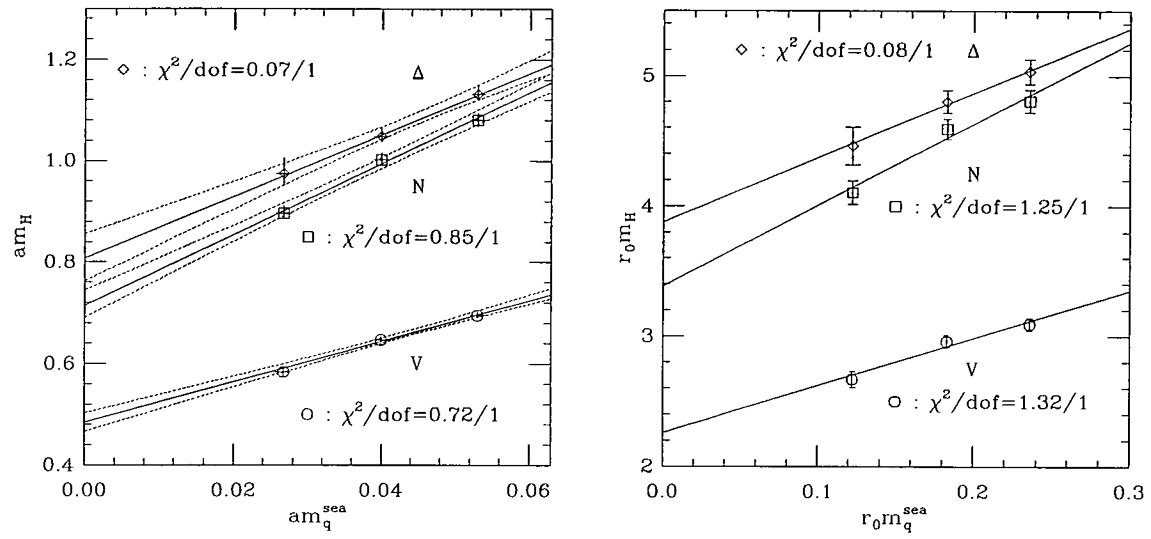

Figure 4.23: Chiral extrapolations of the vector, nucleon and delta for the dynamical matched ensemble at $\kappa_{\text{sea}} = \kappa_{\text{val}}$ plotted against the improved sea quark mass. The fit is an uncorrelated linear fit to equation 4.20. The masses are in lattice units in the left hand plot and in units of r_0 in the right hand plot.

the procedure outlined in section 3.10 the improved normal quark mass was determined from the pseudoscalar extrapolation using equation 3.32. The improvement coefficient b_{m} varies in an undefined way along the course of the extrapolation. Thus it was not possible to determine the unimproved normal quark mass and the corresponding value of κ_{n}. Since the sea quarks are degenerate with the valence quarks in this case, the ρ mass was used to set the scale as opposed to the K* mass. Of course the ρ mass extracted this far from the region of the dynamical data should be viewed with caution. The ρ mass in lattice units was fixed from a linear extrapolation of the vector with the pseudoscalar mass squared to the physical M_π/M_ρ ratio. Figure 4.24 shows this extrapolation including the points corresponding to the physical meson ratios. The $M_{\text{K}}/M_{\text{K}^*}$ mass ratio is shown although these mesons are composed from both strange and light valence quarks. The left hand plot in lattice units shows an extremely good fit with a very low χ^2/d.o.f. When plotted in units of r_0 in the right hand plot, the residual discrepancies in the determination of r_0 are exposed resulting in a higher but still acceptable χ^2/d.o.f.

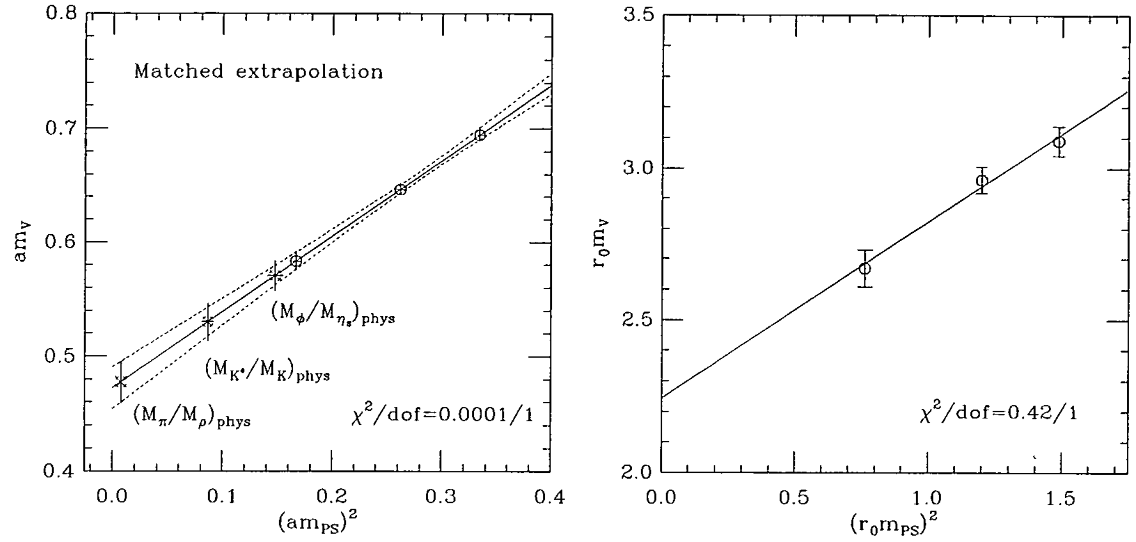

Figure 4.24: The vector mass against the pseudoscalar mass squared fitted by an uncorrelated linear fit. The left hand plot is in lattice units and the right hand plot is in units of r_0. Extrapolated lattice masses determined at the physical meson ratios have been included in the left hand plot.

The improved normal quark mass was then substituted into the baryon extrapolations defined in equation 4.20 to determine the nucleon and Δ masses. Table 4.3 shows the masses of the light hadrons in lattice units together with the improved normal quark mass. The π and ρ meson are fixed to be at the physical mass ratio and hence have only been quoted in lattice units. The nucleon and Δ mass have been converted into physical units using the lattice spacing determined from ρ meson, $1/a_\rho = 1.612\ ^{+64}_{-59}$ GeV. This corresponds to a larger lattice spacing in fm than determined from r_0. The difference is consistent with the variation in a observed in the quenched analysis. This simple analysis results in physical values which are significantly higher than experiment. Data at different values of the lattice spacing would be required in order to perform an extrapolation to the continuum limit to make a more realistic comparison. The SESAM Collaboration [107] have performed chiral extrapolations of hadron masses with

Particle	Value in lattice units	Value in GeV
$\widetilde{m}_{\mathrm{n}}$	$0.00114\ ^{+83}_{-87}$	
m_π	$0.085\ ^{+\ 3}_{-\ 3}$	
m_ρ	$0.478\ ^{+18}_{-18}$	
m_{N}	$0.722\ ^{+30}_{-23}$	$1.165\ ^{+67}_{-57}$
m_Δ	$0.814\ ^{+45}_{-74}$	$1.313\ ^{+90}_{-87}$

Table 4.3: Lattice masses at the normal quark mass. Where physical units have been quoted the scale has been set by the ρ meson.

$\kappa_{\mathrm{sea}} = \kappa_{\mathrm{val}}$ against the sea quark mass at fixed β for four sea quark masses. Since they use unimproved Wilson fermions they do not improve the quark mass. They find that their meson data are well described by both linear and quadratic fits. Comparing the lattice spacing from the ρ mass obtained from both types of fit they see a change of 10% consistent with the difficulties obtained in performing the chiral extrapolation. Their results for the nucleon and Δ failed to reproduce the experimentally observed $\mathrm{N} - \Delta$ mass splitting.

With only three matched data sets with which to perform chiral extrapolations at a constant a, an investigation in the *partially quenched* approximation was carried out on all data sets. The main aim was to compare results with the quenched simulation and with the lightest sea quark mass data set at the smaller lattice spacing.

4.13 Partially quenched analysis

Unlike previous dynamical simulations at fixed β [92, 107, 108, 111] the chiral extrapolations at $\kappa_{\mathrm{sea}} = \kappa_{\mathrm{val}}$ just described depend on both the sea quark mass and β. In this case, it is not clear that the linear behaviour of the pseudoscalar mass squared in equation 4.16 should be expected. Indeed from Figure 4.22, it is possible that a more complicated functional form may be required to extrapolate the data. This highlights the difficulty in defining $\kappa_{\mathrm{crit}}^{\mathrm{sea}}$ for the matched ensemble.

For this reason, it was decided to concentrate on results which can be reached through an analysis of the data in the *partially quenched* approximation. The partially quenched approximation means that extrapolations are performed at fixed $\kappa_{\rm sea}$. In effect, the sea quark mass is held fixed in or above the region of the strange quark mass, rather than extrapolated to the light quark masses. This results in an approximation which is somewhere between the quenched approximation and full QCD. To proceed within the partially quenched scheme, $\kappa_{\rm val}$ must first be extrapolated to the chiral limit for each data set.

4.13.1 Partially quenched chiral extrapolations

Chiral extrapolations to determine the critical value of the valence hopping parameter, $\kappa_{\rm crit}$ were carried out in the same way as described in section 3.9, but this time in the partially quenched approximation. Extrapolations were made using both the pseudoscalar mass squared and the PCAC mass at fixed $\kappa_{\rm sea}$ for each data set. An investigation into the dependence of $\kappa_{\rm crit}$ on the quark mass improvement coefficient $b_{\rm m}$ was performed. The results for all data sets were then compared. The partially quenched bare quark mass, $m_{\rm q}^{\rm PC}$, is defined as

$$m_{\rm q}^{\rm PC} = \frac{1}{2}\left(\frac{1}{\kappa_{\rm val}} - \frac{1}{\kappa_{\rm crit}}\right) \tag{4.21}$$

in analogy with equation 3.21. Assuming this definition of the bare quark mass, the rest of the equations in section 3.9 follow. The critical value of the hopping parameter occurs when the bare quark mass vanishes. The PCAC relation states that the quark mass vanishes when the pseudoscalar mass squared is zero. To lowest order in chiral perturbation theory this is expressed by the functional form

$$m_{\rm PS}^2 = B(\widetilde{m}_{\rm q_1}^{\rm PC} + \widetilde{m}_{\rm q_2}^{\rm PC}) \tag{4.22}$$

where the improved quark masses, $\widetilde{m}_{\rm q_i}^{\rm PC}$ are defined as in section 3.9. For each data set, $\kappa_{\rm crit}$ was determined from an uncorrelated fit to

$$m_{\rm PS}^2 = \alpha + \frac{2}{\kappa_{\rm val}}\left(\beta + \frac{\gamma}{\kappa_{\rm val}}\right) \tag{4.23}$$

where the coefficients α, β and γ are as defined for equation 3.26. In the partially quenched approximation there are expected to be additional terms to be included in the general fit function from chiral logarithms [112, 113] as the valence quark mass becomes small. As with the quenched analysis in the previous chapter, the masses studied here are too heavy for the effect of these terms to be felt and so have not been included in the fits. For extrapolations of the PCAC mass, m_{PS}^2 was replaced by m_{PCAC} in equation 4.23. Variations in the extracted value of κ_{crit} were investigated using different values for b_{m}: no improvement, tree-level improvement and the one-loop value, as defined in equation 3.24. The bare strong coupling constant, g_0^2 was used throughout. The results for κ_{crit} are presented in Table 4.4 for the pseudoscalar extrapolation, and in Table 4.5 for the PCAC mass.

In addition to the fit results included here, correlated fits were performed for all the data sets. The resulting χ^2/d.o.f. was less than 0.5 in all cases for the pseudoscalar extrapolation. Since the κ_{crit} values were in agreement within the statistical errors, the uncorrelated fits were selected in preference in order to be consistent with the procedure adopted for the quenched simulations. For correlated PCAC mass extrapolations, the very small errors on the masses resulted in unacceptably large χ^2/d.o.f. values, and uncorrelated fits were again selected. From Tables 4.4 and 4.5, the results obtained using different values of b_{m} decrease slightly as b_{m} becomes more negative. However, for all values of b_{m} the results were consistent. The one-loop value for b_{m} was selected for both methods of κ_{crit} determination, as this is the current best determination of the quark mass improvement coefficient. Comparing κ_{crit} determined from both methods, the results agree within statistical errors. At this level of accuracy it is hard to quantify the errors of $O(a^2)$ arising between the two methods. Figure 4.25 shows the chiral extrapolations for the lightest sea quark mass simulation. The left hand plot shows an uncorrelated linear fit to equation 4.23 using the one-loop value for b_{m}. The right hand plot shows the same type of fit to the PCAC mass. Clearly the data satisfy the linear ansatz and thus higher order terms were not considered in the analysis.

β	κ_{sea}	Value of b_{m}		κ_{crit}	$\chi^2/\text{d.o.f.}$
5.2	0.13550	b_{m}	$= 0$	0.136363 $^{+67}_{-38}$	0.12 / 2
		$b_{\text{m}}(\text{TL})$	$= -0.5$	0.136334 $^{+64}_{-36}$	0.23 / 2
		$b_{\text{m}}(g_0^2)$	$= -0.611$	**0.136327 $^{+64}_{-35}$**	**0.26 / 2**
5.2	0.13500	b_{m}	$= 0$	0.136652 $^{+58}_{-61}$	0.15 / 2
		$b_{\text{m}}(\text{TL})$	$= -0.5$	0.136575 $^{+54}_{-56}$	0.37 / 2
		$b_{\text{m}}(g_0^2)$	$= -0.611$	**0.136558 $^{+53}_{-55}$**	**0.43 / 2**
5.26	0.13450	b_{m}	$= 0$	0.137100 $^{+73}_{-45}$	0.03 / 2
		$b_{\text{m}}(\text{TL})$	$= -0.5$	0.136989 $^{+67}_{-42}$	0.01 / 2
		$b_{\text{m}}(g_0^2)$	$= -0.6097$	**0.136965 $^{+66}_{-41}$**	**0.02 / 2**
5.29	0.13400	b_{m}	$= 0$	0.137267 $^{+49}_{-68}$	0.08 / 2
		$b_{\text{m}}(\text{TL})$	$= -0.5$	0.137139 $^{+44}_{-62}$	0.26 / 2
		$b_{\text{m}}(g_0^2)$	$= -0.6091$	**0.137112 $^{+44}_{-61}$**	**0.32 / 2**
5.93	Quenched	b_{m}	$= 0$	0.135193 $^{+35}_{-31}$	0.24 / 7
		$b_{\text{m}}(\text{TL})$	$= -0.5$	0.135145 $^{+33}_{-30}$	0.54 / 7
		$b_{\text{m}}(g_0^2)$	$= -0.5973$	**0.135136 $^{+32}_{-29}$**	**0.61 / 7**

Table 4.4: Results for κ_{crit} obtained from an uncorrelated fit to equation 4.23 using different values for b_{m}. The tree-level (TL) and one-loop value of b_{m} from perturbation theory are compared with the unimproved case for all the data sets.

β	κ_{sea}	Value of b_{m}		κ_{crit}	$\chi^2/\text{d.o.f.}$
5.2	0.13550	b_{m}	$= 0$	0.136311 $^{+31}_{-16}$	0.26 / 2
		$b_{\text{m}}(\text{TL})$	$= -0.5$	0.136280 $^{+30}_{-16}$	0.87 / 2
		$b_{\text{m}}(g_0^2)$	$= -0.611$	0.136273 $^{+30}_{-15}$	1.06 / 2
5.2	0.13500	b_{m}	$= 0$	0.136644 $^{+16}_{-14}$	0.05 / 2
		$b_{\text{m}}(\text{TL})$	$= -0.5$	0.136568 $^{+15}_{-13}$	0.95 / 2
		$b_{\text{m}}(g_0^2)$	$= -0.611$	0.136552 $^{+15}_{-13}$	1.34 / 2
5.26	0.13450	b_{m}	$= 0$	0.137090 $^{+16}_{-17}$	0.34 / 2
		$b_{\text{m}}(\text{TL})$	$= -0.5$	0.136982 $^{+15}_{-16}$	1.35 / 2
		$b_{\text{m}}(g_0^2)$	$= -0.6097$	0.136959 $^{+14}_{-16}$	1.69 / 2
5.29	0.13400	b_{m}	$= 0$	0.137313 $^{+17}_{-16}$	0.17 / 2
		$b_{\text{m}}(\text{TL})$	$= -0.5$	0.137188 $^{+16}_{-15}$	0.87 / 2
		$b_{\text{m}}(g_0^2)$	$= -0.6091$	0.137161 $^{+16}_{-15}$	1.12 / 2
5.93	Quenched	b_{m}	$= 0$	0.135147 $^{+16}_{-10}$	0.07 / 7
		$b_{\text{m}}(\text{TL})$	$= -0.5$	0.135101 $^{+15}_{-9}$	0.25 / 7
		$b_{\text{m}}(g_0^2)$	$= -0.5973$	0.135092 $^{+15}_{-9}$	0.39 / 7

Table 4.5: Results for κ_{crit} obtained from an uncorrelated fit to the PCAC mass using equation 4.23, with the pseudoscalar mass replaced by the PCAC mass, using different values for b_{m}. The same values for b_{m} are compared as in Table 4.4.

β	κ_{sea}	B	$\chi^2/\text{d.o.f.}$
5.93	Quenched	3.721 $^{+54}_{-47}$	0.61 / 7
5.29	0.13400	4.172 $^{+65}_{-34}$	0.32 / 2
5.26	0.13450	4.078 $^{+49}_{-69}$	0.02 / 2
5.2	0.13500	4.017 $^{+72}_{-68}$	0.43 / 2
5.2	0.13550	3.635 $^{+62}_{-90}$	0.26 / 2

Table 4.6: Fit results for the pseudoscalar mass squared against the improved quark mass using equation 4.22 in lattice units.

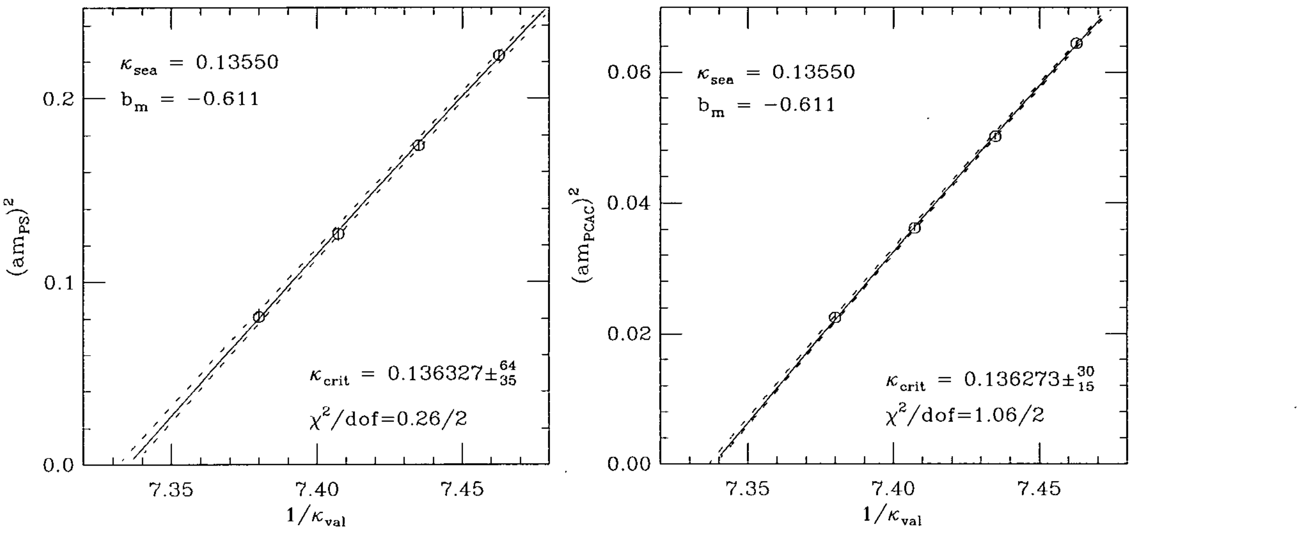

Figure 4.25: Chiral extrapolations in the valence hopping parameter for the pseudoscalar mass and the PCAC mass. Fits are an uncorrelated linear fit to equation 4.23 with the appropriate L.H.S using the one-loop value of $b_m = -0.611$ for the $\beta = 5.2$, $\kappa_{sea} = 0.13550$ dynamical data set.

Using the final selection of κ_{crit} as highlighted in bold in Table 4.4, the chiral extrapolations of the pseudoscalar mass in the improved partially quenched quark mass can be compared for all the data sets. The results are first compared in lattice units in Figure 4.26. The fits to equation 4.22 have not been shown on the graph for clarity, instead the fit parameters are presented in Table 4.6.

The slopes of the matched dynamical extrapolations are in much closer agreement with each other than the matched quenched or the lightest sea quark mass data sets. The fits are uniformly good indicating that the data is well described by the linear fit ansatz. The unmatched dynamical data set clearly has a shallower slope than the matched data which could be due to the difference in the lattice spacing. To eliminate any residual a dependence the fits were repeated after scaling the masses by r_0. The resulting fits are shown in Figure 4.27 for all the data sets. This time the quenched data has the shallowest slope and the lightest sea quark mass data are much closer to the matched dynamical data.

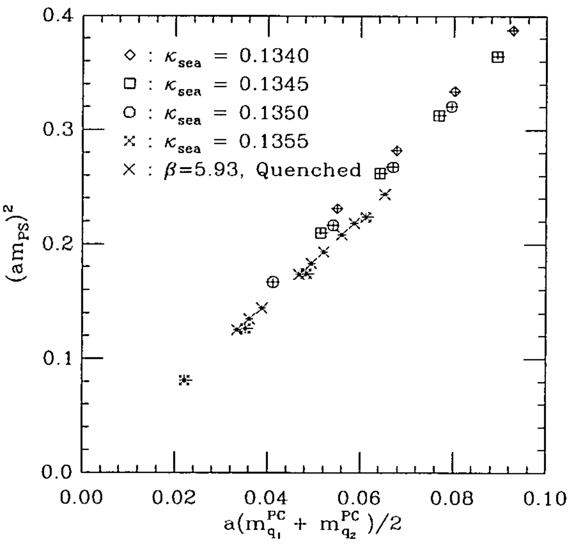

Figure 4.26: Plot of the pseudoscalar mass squared against the average improved partially quenched quark mass, $(\widetilde{m}_{q_1}^{\rm PC} + \widetilde{m}_{q_2}^{\rm PC})/2$ for all data sets.

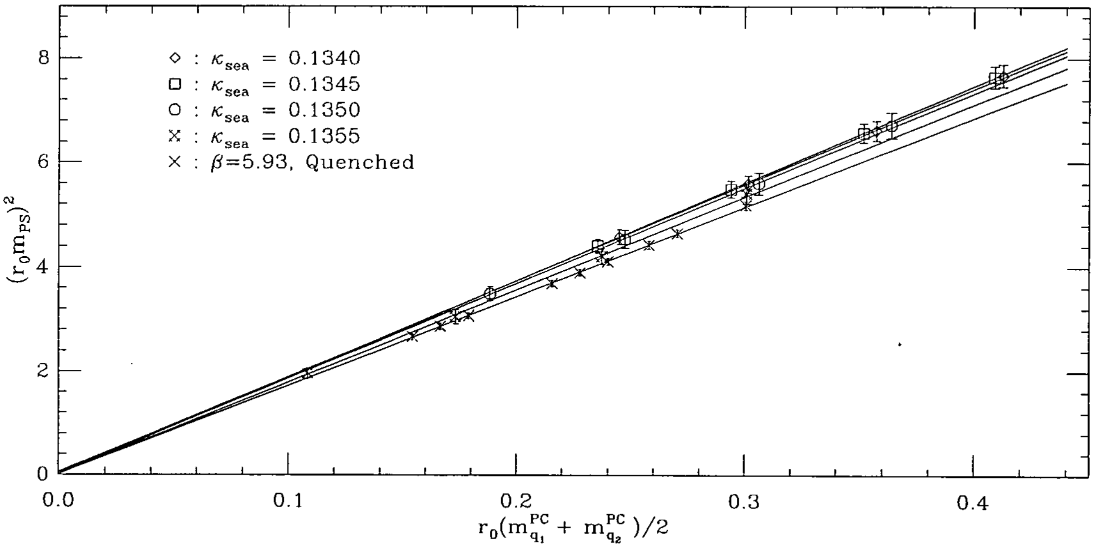

Figure 4.27: As for Figure 4.26 plotted in units of r_0.

The difference between the slopes of the matched dynamical data sets and the quenched slope is a one σ effect, which could be interpreted as a small dynamical effect.

4.13.2 Partially quenched vector extrapolation

Chiral extrapolations in the partially quenched approximation were carried out for the vector. Table 4.7 shows the fit results of an uncorrelated linear fit to the form

$$m_{\rm V} = A + B(\widetilde{m}^{\rm PC}_{q_1} + \widetilde{m}^{\rm PC}_{q_2})/2 \tag{4.24}$$

β	$\kappa_{\rm sea}$	A	B	χ^2/d.o.f.	$1/a_\rho$ [GeV]
5.93	Quenched	$0.501\,^{+17}_{-17}$	$2.35\,^{+25}_{-20}$	0.25 / 7	$1.519\,^{+53}_{-48}$
5.29	0.13400	$0.462\,^{+18}_{-\ 9}$	$2.90\,^{+\ 8}_{-14}$	0.03 / 2	$1.650\,^{+32}_{-61}$
5.26	0.13450	$0.461\,^{+15}_{-\ 8}$	$2.88\,^{+\ 5}_{-15}$	0.01 / 2	$1.652\,^{+28}_{-51}$
5.2	0.13500	$0.461\,^{+13}_{-11}$	$3.02\,^{+12}_{-13}$	0.05 / 2	$1.648\,^{+45}_{-49}$
5.2	0.13550	$0.429\,^{+16}_{-22}$	$2.69\,^{+30}_{-27}$	0.04 / 2	$1.771\,^{+95}_{-73}$

Table 4.7: Fit results for the vector mass against the improved partially quenched quark mass using equation 4.24. The lattice spacing quoted in GeV was determined from the ρ mass as extracted from an uncorrelated linear fit of the vector mass with the pseudoscalar mass squared in the partially quenched approximation.

As can be seen from Table 4.7 and Figure 4.28 the intercepts of the dynamical matched data sets are in close agreement and the slopes are compatible within the statistical errors. This indicates that matching r_0 results in very similar vector masses for the matched ensemble. Table 4.7 includes the lattice spacing as set by the ρ mass from a linear extrapolation of the vector mass with the pseudoscalar mass squared. The lattice spacings of the matched dynamical ensemble are in close agreement which confirms that the vector mass is well matched. These results are 10% larger than the lattice spacings set by r_0, similar to the results observed in the quenched simulations. The quenched data set, although close to the matched data, clearly has a different slope and a different lattice spacing as determined from the ρ. The lightest sea quark data set shows the largest effect, lying lower than the matched data. This difference in the intercept was due to the smaller lattice spacing for the lightest sea quark data set. Figure 4.29 shows the fits repeated when the masses are scaled by r_0 in order to compare all the data on the same footing. From Figure 4.29 the lightest κ_{sea} data set is brought

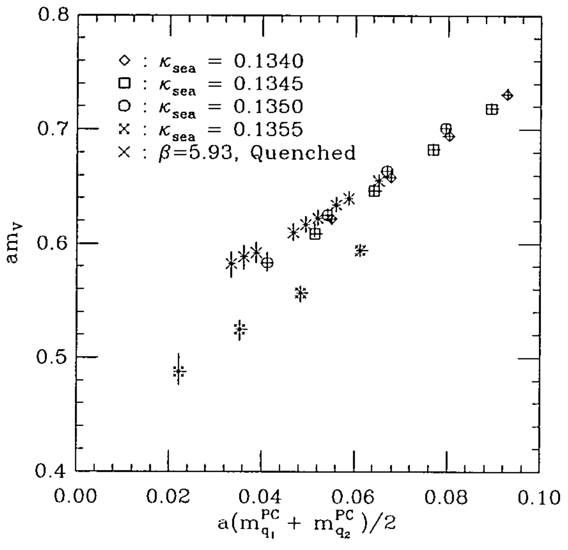

Figure 4.28: Plot of the vector mass against the average improved partially quenched quark mass for all data sets in lattice units.

closer into line with the matched data sets. All the dynamical data sets result in a consistent intercept in the chiral limit. The quenched data was in general higher than the dynamical data and the intercept was over 1.6σ higher than the dynamical results. This can be seen as a small but significant effect resulting from the inclusion of dynamical fermions in the simulation. For all of the data sets the linear fit was a good description of the data at the current level of accuracy.

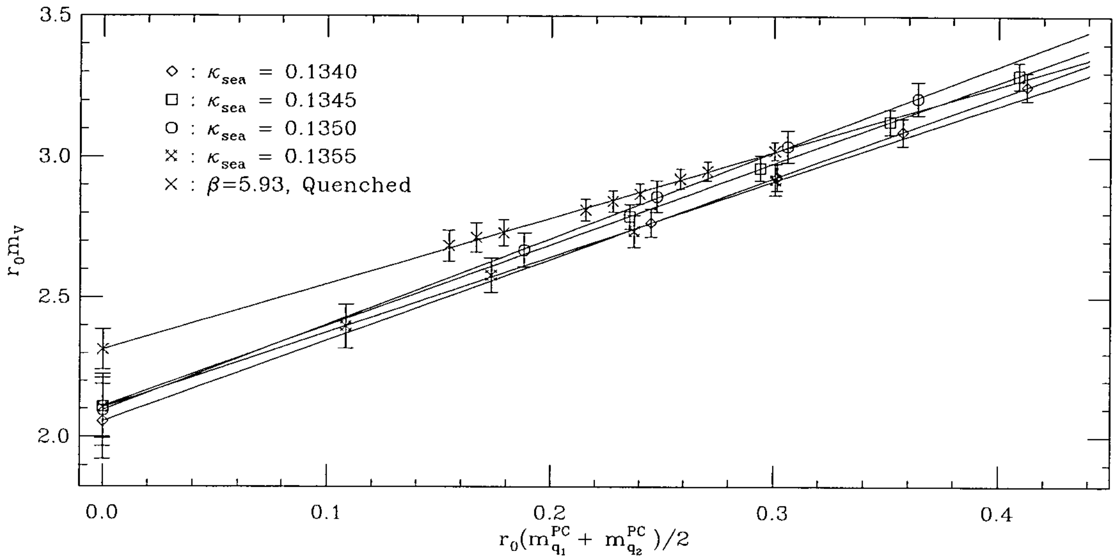

Figure 4.29: Vector mass against the average improved partially quenched quark mass plotted in units of r_0.

4.13.3 Partially quenched baryon chiral extrapolations

Extrapolations of the degenerate nucleon and delta masses were performed using an uncorrelated linear fit of the form

$$m_B = A + B(\widetilde{m}^{PC}_{q_1} + \widetilde{m}^{PC}_{q_2} + \widetilde{m}^{PC}_{q_3})/3 \qquad (4.25)$$

In this case all three constituent quark masses were degenerate. Due to the level of statistical accuracy of the baryon data, particularly for the delta which was significantly more difficult to fit, small dynamical effects were hard to distinguish from the statistical errors. Table 4.8 shows the results of the fit to equation 4.25 for the nucleon and delta. The corresponding data points are plotted in Figure 4.30.

For the nucleon the matched dynamical data points lie close together with the quenched data lying just below. As in the case of the vector, the lightest sea quark mass data set gave the lowest mass results. For the delta this was also the case. In the plot for the delta the matched dynamical points lie slightly below the

Baryon	β	κ_{sea}	A	B	χ^2/d.o.f.
Nucleon	5.93	Quenched	$0.692\ ^{+31}_{-26}$	$4.46\ ^{+42}_{-39}$	0.721 / 3
	5.29	0.13400	$0.704\ ^{+33}_{-26}$	$4.67\ ^{+23}_{-30}$	0.015 / 2
	5.26	0.13450	$0.721\ ^{+27}_{-24}$	$4.40\ ^{+25}_{-24}$	0.012 / 2
	5.2	0.13500	$0.689\ ^{+23}_{-19}$	$5.04\ ^{+20}_{-21}$	0.005 / 2
	5.2	0.13550	$0.638\ ^{+38}_{-43}$	$4.64\ ^{+67}_{-61}$	0.007 / 2
Delta	5.93	Quenched	$0.816\ ^{+42}_{-31}$	$4.11\ ^{+42}_{-50}$	0.004 / 3
	5.29	0.13400	$0.792\ ^{+47}_{-25}$	$4.23\ ^{+25}_{-38}$	0.0004 / 2
	5.26	0.13450	$0.754\ ^{+31}_{-25}$	$4.58\ ^{+24}_{-29}$	0.005 / 2
	5.2	0.13500	$0.799\ ^{+46}_{-40}$	$4.15\ ^{+52}_{-41}$	0.089 / 2
	5.2	0.13550	$0.712\ ^{+44}_{-54}$	$4.72\ ^{+90}_{-69}$	0.265 / 2

Table 4.8: Fit results for the baryon masses fitted in terms of the improved partically quenched quark mass using equation 4.25.

quenched data, however it is hard to say that there is any significant difference between the dynamical and quenched data. This is in part due to the difficulties involved in obtaining reliable estimates for the delta masses. Figure 4.31 shows the linear extrapolations of the baryons in units of r_0.

In the chiral limit the intercepts agree within the statistical errors for all the data sets for both the nucleon and the delta. At the current level of statistics it is impossible to identify effects due to the inclusion of dynamical fermions. More data points and configurations would be needed in the analysis.

4.13.4 Summary of partially quenched analysis

Due to the difficulties in defining a physical interpretation of the mass results for the hadrons in a background sea of strange quarks, the main focus of the chiral extrapolations performed above was to compare the matched dynamical simulations at different sea quark masses with the quenched approximation. It was found that the matched dynamical data were very well matched and produced similar results. No significant differences were observed as the sea quark mass was

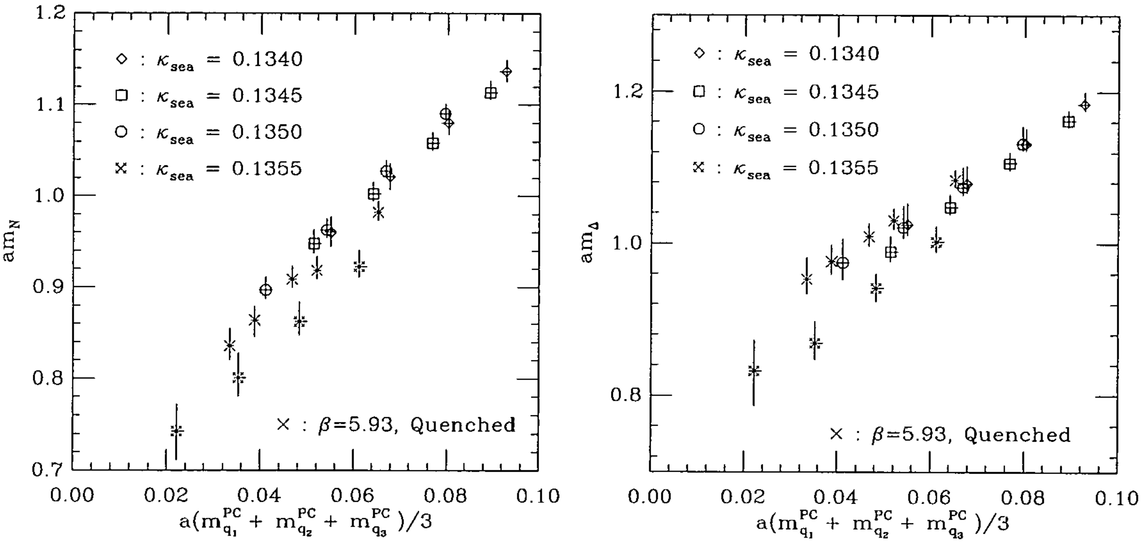

Figure 4.30: Nucleon and delta masses plotted against the average improved partially quenched quark mass.

changed for the matched ensemble. However, comparing the dynamical data with the case of infinitely heavy dynamical quarks in the quenched approximation, small but significant departures from the matched data were observed in the meson sector. The main conclusion is that lighter sea quarks will be needed to observe greater effects of unquenching.

4.14 The continuum limit

The matched ensemble have, by construction, approximately the same fixed value of the lattice spacing, $a \approx 0.11$ fm as defined by r_0. This means that extrapolations to the continuum limit can not be undertaken with the current dynamical data sets. Including the unmatched data set at the lightest sea quark mass, the lattice spacing measured on this data set, $a \approx 0.10$ fm is not sufficiently different to provide a reliable continuum extrapolation. Future simulations at different lattice spacings are required to explore this issue.

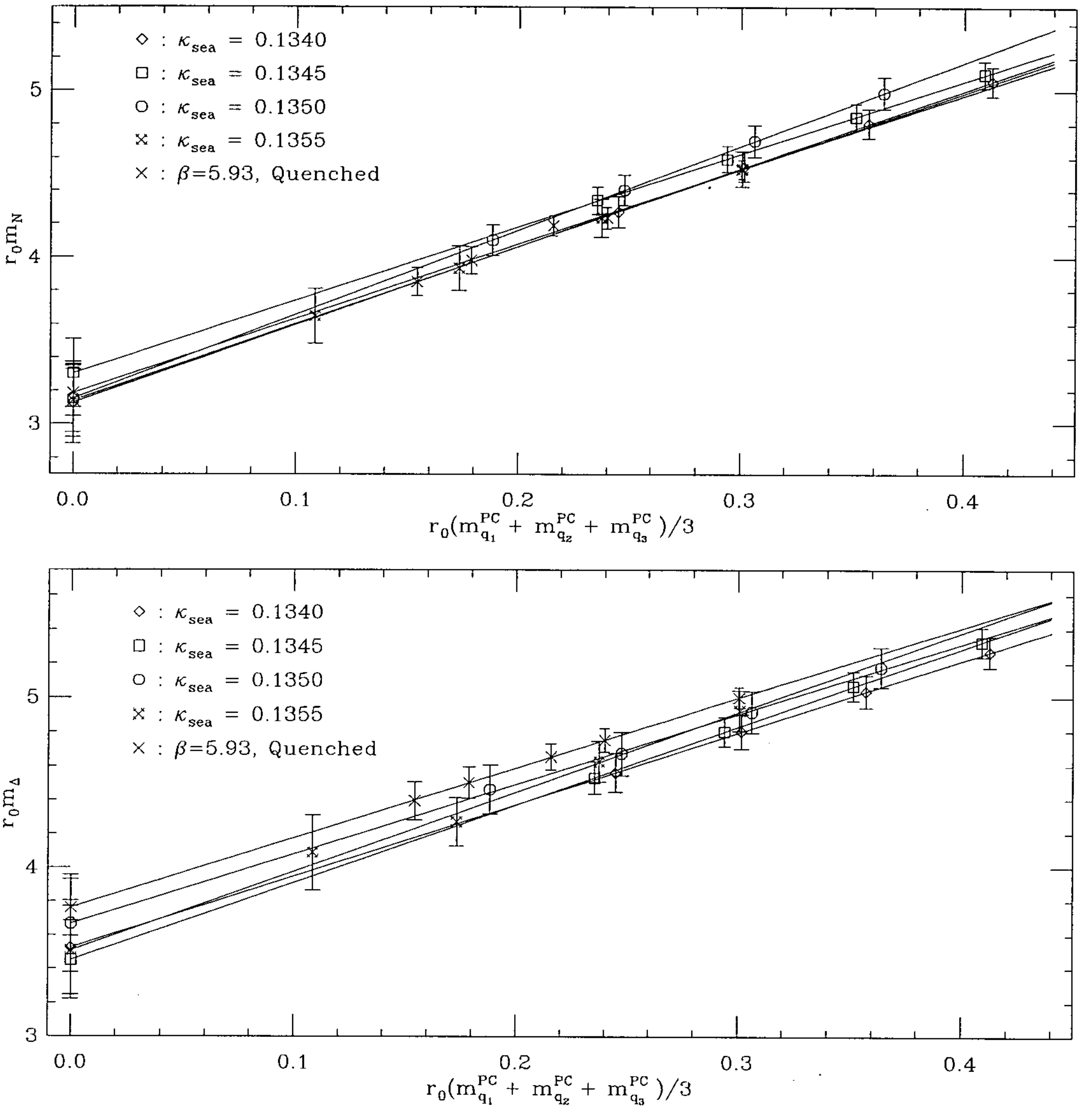

Figure 4.31: As Figure 4.30 plotted in units of r_0. Fits are an uncorrelated linear fit.

4.15 Other evidence for dynamical effects?

The dynamical configurations have been analysed by other members of the UKQCD Collaboration in order to investigate the evidence for dynamical effects in other measurable quantities. The static quark potential was measured by A. C. Irving using the method described in section 4.4, the preliminary results of which were presented in [90]. Full results will appear in [91]. The continuum form for the potential

$$V(r) = V_0 + \sigma r - \frac{e}{r} \tag{4.26}$$

has been rescaled in terms of r_0 as

$$\Big[V(r) - V(r_0)\Big] r_0 = (1.65 - e)\Big(\frac{r}{r_0} - 1\Big) - e\Big(\frac{r_0}{r} - 1\Big) \tag{4.27}$$

in order to compare data from different simulations. This rescaled potential was plotted against the separation scaled by r_0 for all the dynamical data sets in Figure 4.32. The data is compared with the universal string model of the potential, in which the coefficient of the Coulomb term e in equation 4.26 is set to the Lüscher value of $\pi/12$ [114]. Good agreement of the data with the string model is observed. At large separations the string is expected to break, which would be indicted by a flattening of the potential. From the figure there is no sign that this is happening for distances of $r/r_0 \lesssim 2$. Other collaborations [18, 115, 116] also see no indication of string breaking as yet. Reasons for this might be that the sea quark masses are still too heavy to show a significant departure from the string model or that the current maximum separation is not large enough for the creation of a quark anti-quark pair to be energetically favourable. Another explanation may be that the Wilson loop operators used to determine the potential do not have a good overlap with the broken string state [116].

At short distances there is evidence for discretisation errors in the potential. This can be clearly seen by examining the deviation of the potential results from the string model in the lower plot of Figure 4.32. These errors are still present even after lattice artifacts have been taken into account in the fitting procedure,

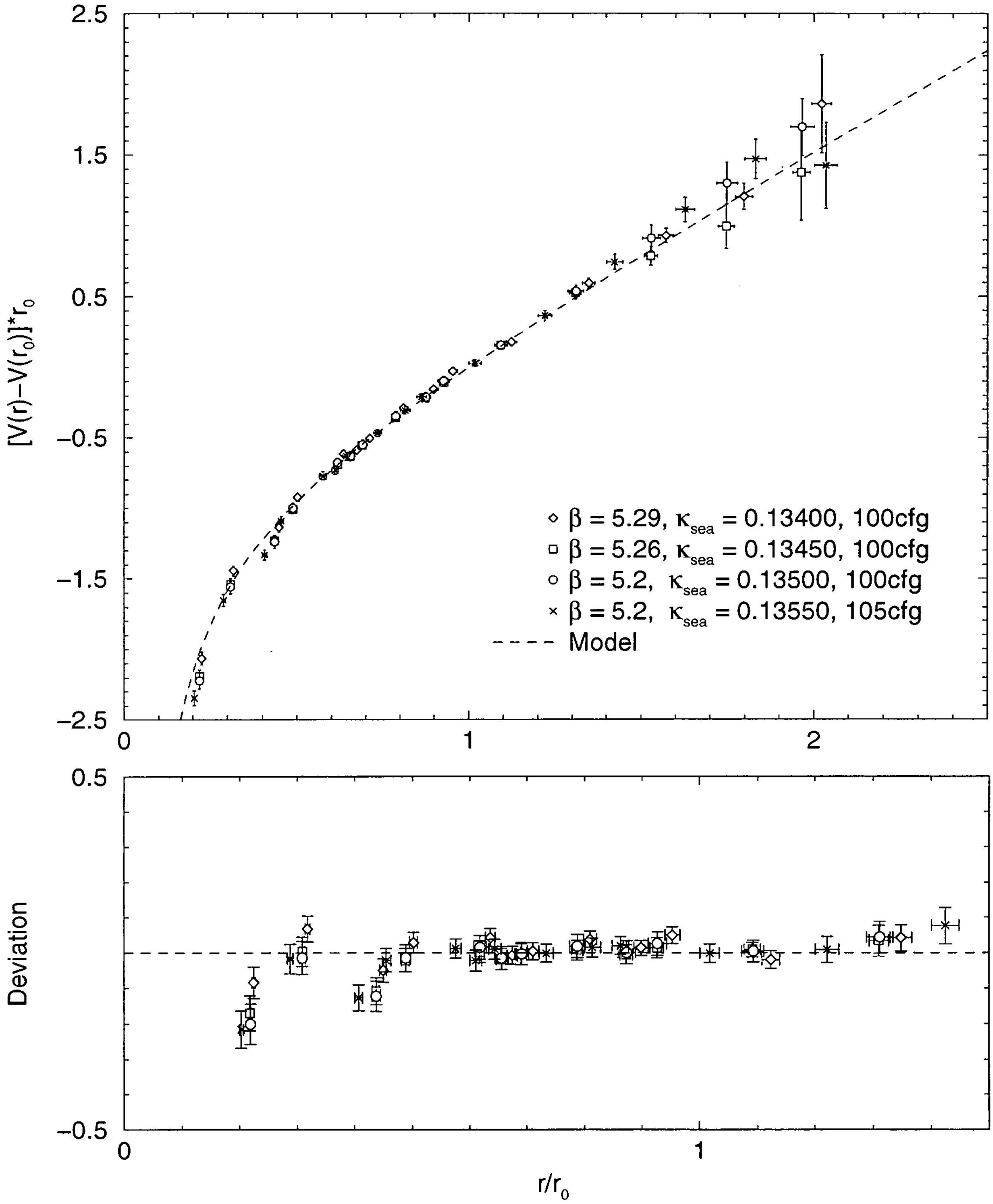

Figure 4.32: Static quark potential measurements for the dynamical data sets. The upper plot shows the data points compared with the universal string model. The lower plot highlights the deviation between the dynamical results and the string model.

as explained in 4.4. In addition, there is some evidence that the lighter sea quark data lie somewhat below the heavier quark data at short distances, indicating the presence of small dynamical fermion effects. This difference at small separations is indicative of a higher value of the Coulomb coefficient e than in the string model. Fits to the data to extract a value for e reveal an increase of 15% ± 4% over previous quenched fits. Figure 4.33 shows the increase in the fitted value of e for the dynamical data sets compared with a previous quenched result. This is consistent with the predicted increase in e from perturbation theory of 14% [117]. The SESAM Collaboration [115] have observed a similar increase of 11% in the value of e when comparing $N_\mathrm{f} = 2$ simulations with the quenched approximation.

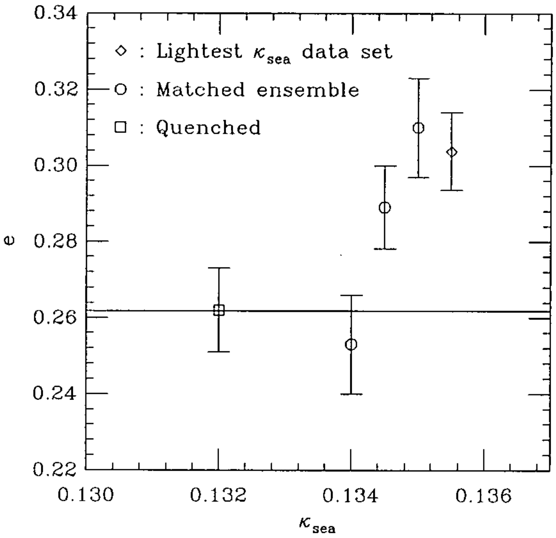

Figure 4.33: Fitted values for the Coulomb coefficient, e, for all the dynamical data sets taken from [90]. The solid line is the Lüscher value, $e = \pi/12$.

Investigations of the topological susceptibility, χ, using the cooling method have been carried out by A. Hart and M. Teper in [118]. The topological susceptibility was fitted to

$$\chi = f_\pi^2 m_\pi^2 / 2N_\mathrm{f} + O(m_\pi^4) \tag{4.28}$$

where the number of quark flavours is $N_\mathrm{f} = 2$ and f_π is the π decay constant. Equation 4.28 indicates that the topological susceptibility is expected to decrease with the sea quark mass. Preliminary studies [118] on the matched dynamical ensemble show that the measured value for χ is indeed lower for the two lightest sea quark mass data sets, providing evidence of dynamical effects. The data for the heaviest sea quark data set is statistically consistent with the quenched result. A more sophisticated analysis of the data is currently ongoing.

Finally, preliminary measurements of the η mass on the $\beta = 5.2$, $c_{\mathrm{sw}} = 1.76$ data sets (where the notation η' is reserved for the $N_{\mathrm{f}} = 3$ case) have been carried out by C. Michael and collaborators in [119]. The η meson is expected to obtain a large contribution to its mass from quark loop effects, as discussed in section 1.5.1. This investigation reported a mass of approximately 800 MeV for η in the chiral limit with an uncontrolled systematic error, which can be compared with the experimental result for η' of 958 MeV [14]. Of course, a quantitative analysis of the systematic errors would be required to corroborate this result.

Chapter 5

Conclusions

This thesis has presented results obtained for the light hadron spectrum from the numerical simulation of lattice QCD. In this chapter, the main conclusions reached in this thesis are summarised and possible extensions of the analysis indicated. First the main results obtained from the quenched simulations are summarised.

5.1 Summary of the quenched analysis

In chapter 3, the results for the light hadron spectrum determined from simulations within the quenched approximation were presented. Data sets at three values of the lattice spacing were analysed in order to explore the continuum limit. A programme of improvement was investigated in order to reduce the discretisation errors which are inherent in any lattice simulation. Three of the quenched data sets implemented the tadpole improvement scheme with the aim of reducing the $O(ag_0^2)$ errors. A further two data sets were simulated using full $O(a)$ non-perturbative improvement in order to examine any improvement in the scaling behaviour over the tadpole improved data sets. At one value of β a comparison of the lattice masses obtained from two data sets with different physical volumes was carried out in order to investigate the error in the analysis due to finite volume effects.

The comparison of the lattice mass results obtained in the finite volume analysis at $\beta = 6.0$ demonstrated that although there were no finite size effects in the lattice values for the vector mass prior to extrapolation a small, yet statistically significant, effect of around 2σ was observed for the pseudoscalar. However, without further investigation it could not be ruled out that this effect has a statistical origin. In the baryon sector, finite size effects were more pronounced, particularly for the decuplet baryons where a 2σ effect was observed. The 1σ effect in the octet baryons was not considered particularly significant given the level of statistical accuracy of the data. There was a noticeable improvement in the scaling behaviour of the non-perturbatively improved data sets over the tadpole data, particularly in the continuum extrapolations where r_0 was chosen to set the scale. Improved scaling was clearly observed in the chiral extrapolations, particularly for the mesons. The value of the J parameter was found to be significantly below the experimental value even in the continuum limit, suggesting that the low value obtained for J is an intrinsic feature of the quenched approximation. The vector-pseudoscalar hyperfine splitting showed a noticeable variation when the scale was set by either the K* mass or r_0, slightly undershooting or overshooting the experimental values respectively. In both cases there was a small negative slope in the data as the quark mass was increased which suggested that the experimentally observed values for the hyperfine splitting in the heavy-light sector would be underestimated.

An investigation of the ratio of the strange quark mass to the normal quark mass at 2 GeV in the modified minimal subtraction ($\overline{\mathrm{MS}}$) renormalisation scheme, yielded a result of $m_{\mathrm{s}}^{\overline{\mathrm{MS}}}/m_{\mathrm{n}}^{\overline{\mathrm{MS}}} \approx 25 \pm 3$. The renormalised quark masses used to determine this ratio were calculated using renormalisation constants from perturbation theory. The results for the quark mass ratio were found to be compatible with the theoretical prediction made in quenched chiral perturbation theory [88], where $M_{\mathrm{s}}/M_{\mathrm{n}} = 24.3 \pm 1.0$.

The continuum values of the non-singlet quenched light hadron spectrum obtained by extrapolating the lattice data in terms of the four different quantities chosen to set the lattice scale, resulted in a 10% uncertainty in the final spectrum results. Assuming that this difference was not due to finite size effects, this uncertainty can then be attributed to the scale ambiguity in the quenched approximation. The results of the continuum extrapolation of the light hadron masses confirmed the evidence previously presented by CP-PACS [4], which showed that the light hadron spectrum in the quenched approximation agrees with experiment to within 10%. The statistical precision of the CP-PACS results is in general better than the results presented here. However the implementation of the improvement programme has shown that extrapolations to the continuum show a milder a dependence. In order to improve the precision of the continuum extrapolations, additional points at different lattice spacings are required. Of course the usual caveats of larger physical volumes, smaller lattice spacings, more statistics and lighter quark masses also apply. The quenched approximation, however, represents an uncontrolled error in the simulation, the effects of which can only be assessed in "full" QCD simulations. The results of chapter 4, which investigated the evidence for the effects of dynamical fermions in the spectrum, are summarised in the next section.

5.2 Summary of the dynamical analysis

In chapter 4, dynamical simulations with two degenerate flavours of $O(a)$ improved Wilson fermions were analysed with the main aim of investigating the effects in the light hadron spectrum arising from the inclusion of fermion loops in the QCD vacuum. Three dynamical simulations with different sea quark masses, forming a matched ensemble, were analysed. The aim of the matching procedure, where each simulation was selected to have approximately the same lattice spacing as defined with respect to the physical value of the Sommer scale, was to facilitate a direct comparison with a quenched simulation at the same lattice spacing. Additionally, choosing the lattice volume to be fixed for each data set meant that chiral extrapolations could be considered separately from continuum extrapolations. The results showed that the matched ensemble displayed a reduced residual dependence upon lattice artifacts, indicated by the similar slopes and intercepts observed in the partially quenched chiral extrapolations. A further simulation with a lighter sea quark mass at a smaller lattice spacing was analysed with the hope of observing a larger effect due to dynamical fermions. Within the dynamical data, no significant effects arising from the small changes in the sea quark mass were observed. Instead the main evidence for sea quark effects came from comparisons with the quenched data. Below is a list describing the evidence for dynamical quark effects in the main observables investigated in chapter 4:

- The *hyperfine splitting* showed an improved trend towards the experimental values for the dynamical data sets. A flattening of the data as the valence quark mass was increased was observed for the matched dynamical ensemble. However this effect was not mirrored by the lightest sea quark mass data.
- There was no significant improvement in the *J parameter* towards the experimental value, particularly at the lightest sea quark mass. This is in line with the results reported by SESAM [107]. However there was some evidence for a slight increase in J as the quark mass was reduced within the matched dynamical ensemble.
- The *Edinburgh plot* showed that the dynamical data was significantly higher than the quenched data, which was in good agreement with the phenomenological curve. This suggested the possibility of larger finite size effects in the dynamical simulations, particularly for the baryons, which should be investigated further.
- Some evidence for dynamical effects was observed in the *partially quenched chiral extrapolations* of the mesons where the scale was set by r_0. The slope of the quenched pseudoscalar extrapolation differed by approximately 1σ from the slopes obtained by extrapolating the dynamical data. A similar effect was observed for the vector, where the intercept of the quenched data was noticeably higher than in the dynamical case. In the baryon sector, dynamical effects were hard to quantify given the statistical accuracy of the data.
- The *static inter-quark potential* showed good agreement with the universal string model with no firm evidence of string breaking. At smaller distances discretisation errors were observed and there was evidence that the lighter sea quark mass data lie below the heavier sea quark data indicating charge

screening. Indeed, fits to the Coulomb term of the potential model indicated a 15%±4% rise in the value of e from the value of the Lüscher coefficient, $e = \pi/12$. This is consistent with the predicted increase in e from perturbation theory of 14% for $N_f = 2$ simulations [117].

- The *topological susceptibility* was observed to decrease as the dynamical sea quark mass became smaller, as anticipated for dynamical fermion simulations.
- Preliminary evidence indicates that the mass of the *singlet η meson* lies somewhere between the experimental masses of the η and η'.

There are a number of directions which could be taken in the analysis of further dynamical fermion simulations. A few of the possible directions are mentioned below. Hadron masses determined from correlators with non-degenerate valence quarks and from additional data sets at different values of the sea quark mass included within the matched ensemble would enable other more complicated fits to be investigated for the chiral extrapolations at $\kappa_{\rm sea} = \kappa_{\rm val}$. The effect of increasing the fuzzing radius, such that a longer plateau for the ground state mass is achieved (at the cost of increased statistical noise), on the extraction of the hadron masses is currently under investigation by other members of UKQCD. Dynamical simulations (perhaps a further matched ensemble) at different lattice spacings should be performed in order to extrapolate to the continuum limit to compare the light hadron spectrum with experiment. Lighter dynamical quark masses could be included in the simulations in an attempt to observe an increased difference from the quenched approximation, and of course, increased statistics, larger volumes and smaller values of the coupling are needed in order to improve the precision of the analysis.

Appendix A

Fitted lattice masses for the quenched simulations

The following tables contain the final results for the fitted hadron masses in lattice units for the quenched simulations considered in chapter 3. The tables are arranged in the following order: pseudoscalar, vector, degenerate delta, nucleon, non-degenerate delta, sigma and lambda, where the data sets have been grouped in terms of their improvement scheme: tadpole or non-perturbative. The unrenormalised PCAC mass results are included at the end of the appendix. A full description of the final fit procedure used to obtain these results can be found in chapter 3. For the octet baryons, κ_2 and κ_3 label the pair of quarks which are flavour symmetric/anti-symmetric under interchange for the sigma/lambda baryons and κ_1 labels the third quark.

β	$L^3 \cdot T$	κ_1	κ_2	am_{PS}	Fit	χ^2/ d.o.f.
5.7	$16^3 \cdot 32$	0.13843	0.13843	$0.7350\ ^{+11}_{-\ 6}$	[6-15]	23.99 / 14
		0.14077	0.13843	$0.6404\ ^{+11}_{-29}$	[5-15]	16.89 / 16
		0.14077	0.14077	$0.5307\ ^{+19}_{-20}$	[5-15]	16.00 / 16
6.0	$16^3 \cdot 48$	0.13700	0.13700	$0.4131\ ^{+13}_{-\ 7}$	[6-23]	22.57 / 30
		0.13810	0.13700	$0.3572\ ^{+16}_{-\ 6}$	[6-23]	21.97 / 30
		0.13856	0.13700	$0.3320\ ^{+21}_{-\ 6}$	[6-23]	27.82 / 30
		0.13810	0.13810	$0.2927\ ^{+21}_{-\ 4}$	[6-23]	26.93 / 30
		0.13856	0.13810	$0.2621\ ^{+23}_{-\ 7}$	[6-23]	29.93 / 30
		0.13856	0.13856	$0.2268\ ^{+25}_{-10}$	[6-23]	30.40 / 30
6.2	$24^3 \cdot 48$	0.13640	0.13640	$0.3033\ ^{+12}_{-10}$	[8-23]	30.03 / 26
		0.13710	0.13640	$0.2643\ ^{+15}_{-11}$	[8-23]	29.29 / 26
		0.13745	0.13640	$0.2436\ ^{+18}_{-13}$	[8-23]	29.02 / 26
		0.13710	0.13710	$0.2206\ ^{+18}_{-12}$	[8-23]	31.97 / 26
		0.13745	0.13710	$0.1959\ ^{+21}_{-16}$	[8-23]	30.92 / 26
		0.13745	0.13745	$0.1680\ ^{+27}_{-18}$	[8-23]	31.13 / 26

Table A.1: Pseudoscalar meson masses for the tadpole improved data sets.

β	$L^3 \cdot T$	κ_1	κ_2	am_{PS}	Fit	χ^2/d.o.f.
6.0	$16^3 \cdot 48$	0.13344	0.13344	$0.3977\ ^{+13}_{-7}$	[6-23]	23.82 / 30
		0.13417	0.13344	$0.3553\ ^{+15}_{-7}$	[6-23]	24.18 / 30
		0.13455	0.13344	$0.3319\ ^{+17}_{-9}$	[6-23]	26.70 / 30
		0.13417	0.13417	$0.3077\ ^{+18}_{-8}$	[6-23]	26.14 / 30
		0.13455	0.13417	$0.2805\ ^{+19}_{-10}$	[6-23]	27.37 / 30
		0.13455	0.13455	$0.2493\ ^{+22}_{-12}$	[6-23]	30.84 / 30
6.0	$32^3 \cdot 64$	0.13344	0.13344	$0.3952\ ^{+16}_{-8}$	[15-31]	14.49 / 15
		0.13417	0.13344	$0.3524\ ^{+15}_{-10}$	[15-31]	14.86 / 15
		0.13455	0.13344	$0.3284\ ^{+15}_{-11}$	[15-31]	13.56 / 15
		0.13417	0.13417	$0.3048\ ^{+13}_{-11}$	[15-31]	13.64 / 15
		0.13455	0.13417	$0.2769\ ^{+13}_{-11}$	[15-31]	12.22 / 15
		0.13455	0.13455	$0.2457\ ^{+14}_{-10}$	[15-31]	13.04 / 15
6.2	$24^3 \cdot 48$	0.13460	0.13460	$0.2803\ ^{+15}_{-10}$	[8-23]	30.99 / 26
		0.13510	0.13460	$0.2492\ ^{+17}_{-12}$	[8-23]	29.08 / 26
		0.13530	0.13460	$0.2361\ ^{+18}_{-14}$	[8-23]	28.42 / 26
		0.13510	0.13510	$0.2149\ ^{+19}_{-14}$	[8-23]	31.54 / 26
		0.13530	0.13510	$0.1998\ ^{+19}_{-17}$	[8-23]	31.18 / 26
		0.13530	0.13530	$0.1836\ ^{+23}_{-18}$	[8-23]	32.04 / 26

Table A.2: Pseudoscalar meson masses for the non-perturbatively improved data sets.

β	$L^3 \cdot T$	κ_1	κ_2	am_V	Fit	χ^2/d.o.f.
5.7	$16^3 \cdot 32$	0.13843	0.13843	$0.9332\ ^{+45}_{-37}$	[7-15]	12.80 / 12
		0.14077	0.13843	$0.8688\ ^{+54}_{-48}$	[7-15]	11.96 / 12
		0.14077	0.14077	$0.8090\ ^{+91}_{-131}$	[7-15]	10.76 / 12
6.0	$16^3 \cdot 48$	0.13700	0.13700	$0.5386\ ^{+32}_{-22}$	[7-23]	23.82 / 28
		0.13810	0.13700	$0.5030\ ^{+40}_{-24}$	[6-23]	27.20 / 30
		0.13856	0.13700	$0.4889\ ^{+45}_{-41}$	[6-23]	27.83 / 30
		0.13810	0.13810	$0.4652\ ^{+52}_{-44}$	[6-23]	26.92 / 30
		0.13856	0.13810	$0.4501\ ^{+66}_{-62}$	[6-23]	29.23 / 30
		0.13856	0.13856	$0.4353\ ^{+88}_{-76}$	[6-23]	25.43 / 30
6.2	$24^3 \cdot 48$	0.13640	0.13640	$0.4005\ ^{+23}_{-26}$	[8-23]	32.65 / 26
		0.13710	0.13640	$0.3761\ ^{+34}_{-29}$	[8-23]	28.79 / 26
		0.13745	0.13640	$0.3648\ ^{+39}_{-44}$	[8-23]	25.39 / 26
		0.13710	0.13710	$0.3522\ ^{+50}_{-44}$	[8-23]	26.83 / 26
		0.13745	0.13710	$0.3412\ ^{+64}_{-63}$	[8-23]	24.85 / 26
		0.13745	0.13745	$0.3306\ ^{+90}_{-95}$	[8-23]	28.83 / 26

Table A.3: Vector meson masses for the tadpole improved data sets.

β	$L^3 \cdot T$	κ_1	κ_2	am_V	Fit	χ^2/d.o.f.
6.0	$16^3 \cdot 48$	0.13344	0.13344	0.5397 $^{+32}_{-30}$	[6-23]	24.02 / 30
		0.13417	0.13344	0.5124 $^{+49}_{-32}$	[6-23]	27.16 / 30
		0.13455	0.13344	0.4997 $^{+51}_{-50}$	[6-23]	29.71 / 30
		0.13417	0.13417	0.4852 $^{+53}_{-53}$	[6-23]	27.92 / 30
		0.13455	0.13417	0.4713 $^{+69}_{-68}$	[6-23]	31.96 / 30
		0.13455	0.13455	0.4577 $^{+85}_{-83}$	[6-23]	30.16 / 30
6.0	$32^3 \cdot 64$	0.13344	0.13344	0.5400 $^{+47}_{-35}$	[10-20]	13.68 / 9
		0.13417	0.13344	0.5143 $^{+53}_{-39}$	[10-20]	14.44 / 9
		0.13455	0.13344	0.5019 $^{+58}_{-46}$	[10-20]	13.75 / 9
		0.13417	0.13417	0.4887 $^{+61}_{-48}$	[10-20]	13.30 / 9
		0.13455	0.13417	0.4762 $^{+74}_{-59}$	[10-20]	10.31 / 9
		0.13455	0.13455	0.4636 $^{+88}_{-76}$	[10-20]	6.69 / 9
6.2	$24^3 \cdot 48$	0.13460	0.13460	0.3887 $^{+32}_{-28}$	[8-23]	33.55 / 26
		0.13510	0.13460	0.3708 $^{+42}_{-36}$	[8-23]	28.99 / 26
		0.13530	0.13460	0.3645 $^{+43}_{-47}$	[8-23]	26.51 / 26
		0.13510	0.13510	0.3531 $^{+55}_{-51}$	[8-23]	29.56 / 26
		0.13530	0.13510	0.3471 $^{+62}_{-61}$	[8-23]	27.91 / 26
		0.13530	0.13530	0.3414 $^{+72}_{-82}$	[8-23]	30.98 / 26

Table A.4: Vector meson masses for the non-perturbatively improved data sets.

β	$L^3 \cdot T$	κ_1	κ_2	κ_3	am_Δ	Fit	χ^2/d.o.f.
5.7	$16^3 \cdot 32$	0.13843	0.13843	0.13843	$1.539\ ^{+21}_{-8}$	[7-15]	23.62 / 12
		0.14077	0.14077	0.14077	$1.334\ ^{+26}_{-17}$	[7-15]	10.59 / 12
6.0	$16^3 \cdot 48$	0.13700	0.13700	0.13700	$0.909\ ^{+7}_{-9}$	[10-23]	23.49 / 22
		0.13810	0.13810	0.13810	$0.810\ ^{+13}_{-13}$	[8-23]	23.95 / 26
		0.13856	0.13856	0.13856	$0.774\ ^{+21}_{-26}$	[8-23]	41.53 / 26
6.2	$16^3 \cdot 48$	0.13640	0.13640	0.13640	$0.691\ ^{+7}_{-7}$	[11-23]	19.42 / 20
		0.13710	0.13710	0.13710	$0.620\ ^{+11}_{-10}$	[11-23]	23.87 / 20
		0.13745	0.13745	0.13745	$0.577\ ^{+19}_{-13}$	[11-23]	20.60 / 20

Table A.5: Degenerate delta masses for the tadpole improved data sets.

β	$L^3 \cdot T$	κ_1	κ_2	κ_3	am_Δ	Fit	χ^2/d.o.f.
6.0	$16^3 \cdot 48$	0.13344	0.13344	0.13344	$0.913\ ^{+9}_{-22}$	[9-23]	21.84 / 24
		0.13417	0.13417	0.13417	$0.852\ ^{+19}_{-23}$	[9-23]	31.33 / 24
		0.13455	0.13455	0.13455	$0.768\ ^{+52}_{-36}$	[10-23]	40.37 / 22
6.0	$32^3 \cdot 64$	0.13344	0.13344	0.13344	$0.899\ ^{+13}_{-14}$	[2-16]	17.56 / 11
		0.13417	0.13417	0.13417	$0.818\ ^{+16}_{-13}$	[2-16]	20.09 / 11
		0.13455	0.13455	0.13455	$0.781\ ^{+18}_{-14}$	[2-16]	21.66 / 11
6.2	$24^3 \cdot 48$	0.13460	0.13460	0.13460	$0.671\ ^{+8}_{-7}$	[11-23]	20.35 / 20
		0.13510	0.13510	0.13510	$0.618\ ^{+14}_{-12}$	[11-23]	21.54 / 20
		0.13530	0.13530	0.13530	$0.596\ ^{+19}_{-13}$	[11-23]	20.31 / 20

Table A.6: Degenerate delta masses for the non-perturbatively improved data sets.

β	$L^3 \cdot T$	κ_1	κ_2	κ_3	am_{N}	Fit	χ^2/d.o.f.
5.7	$16^3 \cdot 32$	0.13843	0.13843	0.13843	$1.423\ ^{+12}_{-\ 4}$	[7-15]	7.37 / 12
		0.14077	0.14077	0.14077	$1.183\ ^{+14}_{-11}$	[6-15]	15.96 / 14
6.0	$16^3 \cdot 48$	0.13700	0.13700	0.13700	$0.817\ ^{+\ 9}_{-\ 4}$	[10-23]	21.26 / 22
		0.13810	0.13810	0.13810	$0.678\ ^{+17}_{-\ 8}$	[10-23]	27.46 / 22
		0.13856	0.13856	0.13856	$0.616\ ^{+26}_{-16}$	[10-23]	26.95 / 22
6.2	$24^3 \cdot 48$	0.13640	0.13640	0.13640	$0.608\ ^{+\ 8}_{-\ 6}$	[11-23]	34.87 / 20
		0.13710	0.13710	0.13710	$0.509\ ^{+12}_{-\ 9}$	[11-23]	38.62 / 20
		0.13745	0.13745	0.13745	$0.467\ ^{+12}_{-20}$	[11-23]	22.68 / 20

Table A.7: Degenerate nucleon masses for the tadpole improved data sets.

β	$L^3 \cdot T$	κ_1	κ_2	κ_3	am_{N}	Fit	χ^2/d.o.f.
6.0	$16^3 \cdot 48$	0.13344	0.13344	0.13344	$0.808\ ^{+10}_{-\ 7}$	[9-23]	25.42 / 24
		0.13417	0.13417	0.13417	$0.711\ ^{+16}_{-13}$	[9-23]	25.74 / 24
		0.13455	0.13455	0.13455	$0.665\ ^{+26}_{-28}$	[9-23]	26.98 / 24
6.0	$32^3 \cdot 64$	0.13344	0.13344	0.13344	$0.799\ ^{+10}_{-10}$	[3-18]	16.82 / 12
		0.13417	0.13417	0.13417	$0.700\ ^{+11}_{-15}$	[3-18]	15.99 / 12
		0.13455	0.13455	0.13455	$0.641\ ^{+16}_{-20}$	[3-18]	14.63 / 12
6.2	$24^3 \cdot 48$	0.13460	0.13460	0.13460	$0.586\ ^{+\ 8}_{-\ 6}$	[10-23]	42.46 / 22
		0.13510	0.13510	0.13510	$0.509\ ^{+10}_{-10}$	[10-23]	41.09 / 22
		0.13530	0.13530	0.13530	$0.487\ ^{+\ 3}_{-14}$	[10-23]	30.35 / 22

Table A.8: Degenerate nucleon masses for the non-perturbatively improved data sets.

β	$L^3 \cdot T$	κ_1	κ_2	κ_3	am_Δ	Fit	χ^2/d.o.f.
6.0	$16^3 \cdot 48$	0.13700	0.13700	0.13810	$0.873 \,^{+8}_{-9}$	[8-23]	24.87 / 26
		0.13700	0.13700	0.13856	$0.882 \,^{+6}_{-15}$	[8-23]	33.70 / 26
		0.13700	0.13810	0.13810	$0.853 \,^{+4}_{-18}$	[8-23]	29.14 / 26
		0.13700	0.13810	0.13856	$0.845 \,^{+9}_{-17}$	[8-23]	34.77 / 26
		0.13700	0.13856	0.13856	$0.832 \,^{+12}_{-17}$	[8-23]	32.84 / 26
		0.13810	0.13810	0.13856	$0.810 \,^{+12}_{-20}$	[8-23]	36.09 / 26
		0.13810	0.13856	0.13856	$0.787 \,^{+19}_{-19}$	[8-23]	33.95 / 26
6.2	$16^3 \cdot 48$	0.13640	0.13640	0.13710	$0.656 \,^{+7}_{-6}$	[11-23]	13.69 / 20
		0.13640	0.13640	0.13745	$0.652 \,^{+8}_{-7}$	[10-23]	31.97 / 22
		0.13640	0.13710	0.13710	$0.642 \,^{+9}_{-7}$	[10-23]	26.04 / 22
		0.13640	0.13710	0.13745	$0.627 \,^{+10}_{-8}$	[10-23]	29.50 / 22
		0.13640	0.13745	0.13745	$0.619 \,^{+11}_{-9}$	[10-23]	29.43 / 22
		0.13710	0.13710	0.13745	$0.602 \,^{+11}_{-10}$	[10-23]	27.46 / 22
		0.13710	0.13745	0.13745	$0.593 \,^{+12}_{-11}$	[10-23]	29.06 / 22

Table A.9: Non-degenerate delta masses for the tadpole improved data sets.

β	$L^3 \cdot T$	κ_1	κ_2	κ_3	am_Δ	Fit	χ^2/d.o.f.
6.0	$16^3 \cdot 48$	0.13344	0.13344	0.13417	0.894^{+11}_{-12}	[9-23]	28.91 / 24
		0.13344	0.13344	0.13455	0.890^{+14}_{-12}	[9-23]	32.61 / 24
		0.13344	0.13417	0.13417	0.872^{+14}_{-13}	[9-23]	25.97 / 24
		0.13344	0.13417	0.13455	0.871^{+15}_{-14}	[9-23]	31.06 / 24
		0.13344	0.13455	0.13455	0.860^{+19}_{-18}	[9-23]	27.57 / 24
		0.13417	0.13417	0.13455	0.845^{+21}_{-20}	[9-23]	29.17 / 24
		0.13417	0.13455	0.13455	0.837^{+25}_{-27}	[9-23]	27.81 / 24
6.0	$32^3 \cdot 64$	0.13344	0.13344	0.13417	0.873^{+14}_{-14}	[2-16]	18.33 / 11
		0.13344	0.13344	0.13455	0.859^{+15}_{-13}	[2-16]	18.62 / 11
		0.13344	0.13417	0.13417	0.845^{+15}_{-14}	[2-16]	19.13 / 11
		0.13344	0.13417	0.13455	0.832^{+16}_{-13}	[2-16]	19.32 / 11
		0.13344	0.13455	0.13455	0.820^{+17}_{-13}	[2-16]	19.42 / 11
		0.13417	0.13417	0.13455	0.805^{+17}_{-13}	[2-16]	20.43 / 11
		0.13417	0.13455	0.13455	0.793^{+18}_{-14}	[2-16]	20.93 / 11
6.2	$24^3 \cdot 48$	0.13460	0.13460	0.13510	0.656^{+7}_{-8}	[10-23]	32.08 / 22
		0.13460	0.13460	0.13530	0.648^{+8}_{-8}	[10-23]	34.17 / 22
		0.13460	0.13510	0.13510	0.638^{+9}_{-8}	[10-23]	29.22 / 22
		0.13460	0.13510	0.13530	0.630^{+10}_{-8}	[10-23]	30.35 / 22
		0.13460	0.13530	0.13530	0.623^{+11}_{-9}	[10-23]	29.17 / 22
		0.13510	0.13510	0.13530	0.611^{+12}_{-10}	[10-23]	28.84 / 22
		0.13510	0.13530	0.13530	0.606^{+13}_{-11}	[10-23]	29.74 / 22

Table A.10: Non-degenerate delta masses for the non-perturbatively improved data sets.

β	$L^3 \cdot T$	κ_1	κ_2	κ_3	am_Σ	Fit	χ^2/d.o.f.
6.0	$16^3 \cdot 48$	0.13700	0.13700	0.13810	$0.777\ ^{+11}_{-5}$	[10-23]	33.07 / 22
		0.13700	0.13700	0.13856	$0.761\ ^{+12}_{-5}$	[10-23]	35.36 / 22
		0.13700	0.13810	0.13810	$0.722\ ^{+14}_{-7}$	[10-23]	34.31 / 22
		0.13700	0.13810	0.13856	$0.713\ ^{+15}_{-8}$	[10-23]	28.68 / 22
		0.13700	0.13856	0.13856	$0.678\ ^{+19}_{-12}$	[10-23]	30.82 / 22
		0.13810	0.13700	0.13700	$0.766\ ^{+11}_{-5}$	[10-23]	24.29 / 22
		0.13810	0.13700	0.13810	$0.733\ ^{+14}_{-7}$	[10-23]	24.95 / 22
		0.13810	0.13700	0.13856	$0.706\ ^{+14}_{-7}$	[10-20]	30.48 / 16
		0.13810	0.13810	0.13856	$0.659\ ^{+18}_{-13}$	[10-23]	32.66 / 22
		0.13810	0.13856	0.13856	$0.634\ ^{+22}_{-19}$	[10-23]	27.15 / 22
		0.13856	0.13700	0.13700	$0.741\ ^{+13}_{-7}$	[10-23]	26.87 / 22
		0.13856	0.13700	0.13810	$0.698\ ^{+17}_{-8}$	[10-23]	27.18 / 22
		0.13856	0.13700	0.13856	$0.697\ ^{+15}_{-8}$	[10-23]	28.44 / 22
		0.13856	0.13810	0.13810	$0.654\ ^{+21}_{-11}$	[10-23]	25.59 / 22
		0.13856	0.13810	0.13856	$0.642\ ^{+21}_{-10}$	[10-23]	27.54 / 22
6.2	$24^3 \cdot 48$	0.13640	0.13640	0.13710	$0.576\ ^{+3}_{-8}$	[11-23]	34.85 / 20
		0.13640	0.13640	0.13745	$0.554\ ^{+6}_{-7}$	[12-23]	28.30 / 18
		0.13640	0.13710	0.13710	$0.539\ ^{+9}_{-8}$	[13-23]	32.50 / 16
		0.13640	0.13710	0.13745	$0.526\ ^{+9}_{-8}$	[13-23]	29.71 / 16
		0.13640	0.13745	0.13745	$0.504\ ^{+9}_{-13}$	[13-23]	34.91 / 16
		0.13710	0.13640	0.13640	$0.563\ ^{+6}_{-5}$	[12-23]	30.13 / 18
		0.13710	0.13640	0.13710	$0.539\ ^{+7}_{-8}$	[12-23]	41.45 / 18
		0.13710	0.13640	0.13745	$0.515\ ^{+10}_{-8}$	[13-23]	31.06 / 18
		0.13710	0.13710	0.13745	$0.494\ ^{+6}_{-11}$	[13-23]	35.07 / 16
		0.13710	0.13745	0.13745	$0.463\ ^{+12}_{-24}$	[14-23]	26.09 / 14
		0.13745	0.13640	0.13640	$0.540\ ^{+6}_{-7}$	[12-23]	31.09 / 18
		0.13745	0.13640	0.13710	$0.510\ ^{+10}_{-8}$	[13-23]	33.24 / 16
		0.13745	0.13640	0.13745	$0.497\ ^{+15}_{-9}$	[13-23]	32.69 / 16
		0.13745	0.13710	0.13710	$0.470\ ^{+8}_{-19}$	[14-23]	36.98 / 16
		0.13745	0.13710	0.13745	$0.455\ ^{+7}_{-22}$	[14-23]	32.15 / 14

Table A.11: Non-degenerate sigma masses for the tadpole improved data sets.

β	$L^3 \cdot T$	κ_1	κ_2	κ_3	am_Σ	Fit	χ^2/d.o.f.
6.0	$16^3 \cdot 48$	0.13344	0.13344	0.13417	$0.780\ ^{+10}_{-\ 6}$	[9-23]	40.18 / 24
		0.13344	0.13344	0.13455	$0.766\ ^{+11}_{-\ 7}$	[9-23]	41.16 / 24
		0.13344	0.13417	0.13417	$0.743\ ^{+12}_{-\ 8}$	[9-23]	41.76 / 24
		0.13344	0.13417	0.13455	$0.735\ ^{+12}_{-10}$	[9-23]	38.36 / 24
		0.13344	0.13455	0.13455	$0.708\ ^{+13}_{-14}$	[9-23]	40.86 / 24
		0.13417	0.13344	0.13344	$0.771\ ^{+11}_{-\ 6}$	[9-23]	31.74 / 24
		0.13417	0.13344	0.13417	$0.745\ ^{+14}_{-\ 7}$	[9-23]	33.32 / 24
		0.13417	0.13344	0.13455	$0.728\ ^{+12}_{-10}$	[9-23]	42.71 / 24
		0.13417	0.13417	0.13455	$0.697\ ^{+13}_{-13}$	[9-23]	40.45 / 24
		0.13417	0.13455	0.13455	$0.677\ ^{+15}_{-17}$	[9-23]	37.07 / 24
		0.13455	0.13344	0.13344	$0.750\ ^{+13}_{-\ 7}$	[9-23]	33.71 / 24
		0.13455	0.13344	0.13417	$0.719\ ^{+15}_{-10}$	[9-23]	35.97 / 24
		0.13455	0.13344	0.13455	$0.717\ ^{+15}_{-12}$	[9-23]	38.68 / 24
		0.13455	0.13417	0.13417	$0.689\ ^{+18}_{-13}$	[9-23]	35.86 / 24
		0.13455	0.13417	0.13455	$0.679\ ^{+18}_{-15}$	[9-23]	39.77 / 24
6.0	$32^3 \cdot 64$	0.13344	0.13344	0.13417	$0.769\ ^{+10}_{-11}$	[3-18]	16.59 / 12
		0.13344	0.13344	0.13455	$0.755\ ^{+10}_{-12}$	[3-18]	16.76 / 12
		0.13344	0.13417	0.13417	$0.732\ ^{+10}_{-13}$	[3-18]	16.71 / 12
		0.13344	0.13417	0.13455	$0.726\ ^{+10}_{-13}$	[3-18]	16.11 / 12
		0.13344	0.13455	0.13455	$0.695\ ^{+12}_{-16}$	[3-18]	17.47 / 12
		0.13417	0.13344	0.13344	$0.764\ ^{+\ 9}_{-11}$	[3-18]	17.12 / 12
		0.13417	0.13344	0.13417	$0.740\ ^{+10}_{-12}$	[3-18]	16.11 / 12
		0.13417	0.13344	0.13455	$0.716\ ^{+10}_{-14}$	[3-18]	16.71 / 12
		0.13417	0.13417	0.13455	$0.684\ ^{+12}_{-16}$	[3-18]	15.62 / 12
		0.13417	0.13455	0.13455	$0.659\ ^{+15}_{-19}$	[3-18]	15.91 / 12
		0.13455	0.13344	0.13344	$0.745\ ^{+10}_{-13}$	[3-18]	18.19 / 12
		0.13455	0.13344	0.13417	$0.712\ ^{+11}_{-14}$	[3-18]	17.62 / 12
		0.13455	0.13344	0.13455	$0.711\ ^{+10}_{-15}$	[3-18]	16.10 / 12
		0.13455	0.13417	0.13417	$0.678\ ^{+13}_{-16}$	[3-18]	16.55 / 12
		0.13455	0.13417	0.13455	$0.666\ ^{+13}_{-18}$	[3-18]	14.94 / 12

Table A.12: Non-degenerate sigma masses for the non-perturbatively improved data sets.

β	$L^3 \cdot T$	κ_1	κ_2	κ_3	am_Σ	Fit	χ^2/d.o.f.
6.2	$24^3 \cdot 48$	0.13460	0.13460	0.13510	$0.555\,^{+\,3}_{-\,9}$	[12-23]	29.96 / 18
		0.13460	0.13460	0.13530	$0.547\,^{+\,1}_{-10}$	[12-23]	30.38 / 18
		0.13460	0.13510	0.13510	$0.528\,^{+\,8}_{-10}$	[13-23]	32.65 / 16
		0.13460	0.13510	0.13530	$0.522\,^{+10}_{-10}$	[13-23]	31.14 / 16
		0.13460	0.13530	0.13530	$0.513\,^{+\,7}_{-12}$	[13-23]	33.49 / 16
		0.13510	0.13460	0.13460	$0.545\,^{+\,9}_{-\,6}$	[13-23]	31.02 / 16
		0.13510	0.13460	0.13510	$0.525\,^{+\,9}_{-\,8}$	[13-23]	35.60 / 16
		0.13510	0.13460	0.13530	$0.514\,^{+\,9}_{-10}$	[13-23]	32.29 / 16
		0.13510	0.13510	0.13530	$0.500\,^{+\,6}_{-11}$	[13-23]	34.46 / 16
		0.13510	0.13530	0.13530	$0.497\,^{+\,7}_{-11}$	[13-23]	33.27 / 16
		0.13530	0.13460	0.13460	$0.530\,^{+\,9}_{-\,7}$	[13-23]	31.30 / 16
		0.13530	0.13460	0.13510	$0.509\,^{+\,7}_{-11}$	[13-23]	34.99 / 16
		0.13530	0.13460	0.13530	$0.503\,^{+\,9}_{-11}$	[13-23]	34.51 / 16
		0.13530	0.13510	0.13510	$0.493\,^{+\,1}_{-12}$	[13-23]	38.57 / 16
		0.13530	0.13510	0.13530	$0.487\,^{+\,1}_{-13}$	[13-23]	35.94 / 16

Table A.13: Non-degenerate sigma masses for the non-perturbatively improved data sets.

β	$L^3 \cdot T$	κ_1	κ_2	κ_3	am_Λ	Fit	χ^2/d.o.f.
6.0	$16^3 \cdot 48$	0.13700	0.13700	0.13810	0.771^{+11}_{-5}	[10-23]	26.43 / 22
		0.13700	0.13700	0.13856	0.749^{+13}_{-6}	[10-23]	29.00 / 22
		0.13700	0.13810	0.13810	0.732^{+13}_{-7}	[10-23]	28.57 / 22
		0.13700	0.13810	0.13856	0.703^{+16}_{-9}	[10-23]	31.14 / 22
		0.13700	0.13856	0.13856	0.697^{+15}_{-9}	[10-23]	30.32 / 22
		0.13810	0.13700	0.13700	0.778^{+12}_{-5}	[10-23]	32.41 / 22
		0.13810	0.13700	0.13810	0.718^{+14}_{-7}	[10-23]	36.92 / 22
		0.13810	0.13700	0.13756	0.707^{+15}_{-8}	[10-23]	28.00 / 22
		0.13810	0.13810	0.13856	0.659^{+20}_{-12}	[10-23]	27.49 / 22
		0.13810	0.13856	0.13856	0.643^{+20}_{-12}	[10-23]	27.63 / 22
		0.13856	0.13700	0.13700	0.763^{+14}_{-5}	[10-23]	35.09 / 22
		0.13856	0.13700	0.13810	0.710^{+16}_{-7}	[10-23]	35.05 / 22
		0.13856	0.13700	0.13856	0.672^{+18}_{-12}	[10-23]	35.56 / 22
		0.13856	0.13810	0.13810	0.655^{+18}_{-12}	[10-23]	31.43 / 22
		0.13856	0.13810	0.13856	0.626^{+23}_{-19}	[10-23]	28.39 / 22
6.2	$24^3 \cdot 48$	0.13640	0.13640	0.13710	0.568^{+7}_{-6}	[13-23]	28.45 / 16
		0.13640	0.13640	0.13745	0.545^{+9}_{-7}	[13-23]	30.52 / 16
		0.13640	0.13710	0.13710	0.535^{+11}_{-7}	[13-23]	34.43 / 16
		0.13640	0.13710	0.13745	0.510^{+9}_{-9}	[13-23]	32.27 / 16
		0.13640	0.13745	0.13745	0.491^{+16}_{-10}	[13-23]	29.70 / 16
		0.13710	0.13640	0.13640	0.571^{+8}_{-7}	[13-23]	25.83 / 16
		0.13710	0.13640	0.13710	0.532^{+11}_{-8}	[13-23]	32.33 / 16
		0.13710	0.13640	0.13745	0.518^{+8}_{-8}	[13-23]	37.35 / 16
		0.13710	0.13710	0.13745	0.491^{+3}_{-11}	[13-23]	40.78 / 16
		0.13710	0.13745	0.13745	0.457^{+5}_{-22}	[14-23]	31.06 / 14
		0.13745	0.13640	0.13640	0.558^{+9}_{-7}	[13-23]	25.76 / 16
		0.13745	0.13640	0.13710	0.522^{+10}_{-9}	[13-23]	29.20 / 16
		0.13745	0.13640	0.13745	0.492^{+8}_{-15}	[13-23]	31.84 / 16
		0.13745	0.13710	0.13710	0.492^{+7}_{-13}	[13-23]	32.65 / 16
		0.13745	0.13710	0.13745	0.451^{+13}_{-25}	[14-23]	22.15 / 14

Table A.14: Non-degenerate lambda masses for the tadpole improved data sets.

β	$L^3 \cdot T$	κ_1	κ_2	κ_3	am_Λ	Fit	χ^2/d.o.f.
6.0	$16^3 \cdot 48$	0.13344	0.13344	0.13417	$0.775\ ^{+11}_{-6}$	[9-23]	34.81 / 24
		0.13344	0.13344	0.13455	$0.757\ ^{+12}_{-7}$	[9-23]	36.88 / 24
		0.13344	0.13417	0.13417	$0.744\ ^{+13}_{-7}$	[9-23]	36.25 / 24
		0.13344	0.13417	0.13455	$0.722\ ^{+15}_{-10}$	[9-23]	38.22 / 24
		0.13344	0.13455	0.13455	$0.713\ ^{+16}_{-11}$	[9-23]	36.58 / 24
		0.13417	0.13344	0.13344	$0.781\ ^{+11}_{-6}$	[9-23]	38.65 / 24
		0.13417	0.13344	0.13417	$0.739\ ^{+12}_{-8}$	[9-23]	42.45 / 24
		0.13417	0.13344	0.13455	$0.727\ ^{+14}_{-9}$	[9-23]	38.60 / 24
		0.13417	0.13417	0.13455	$0.692\ ^{+16}_{-12}$	[9-23]	38.47 / 24
		0.13417	0.13455	0.13455	$0.679\ ^{+17}_{-15}$	[9-23]	38.06 / 24
		0.13455	0.13344	0.13344	$0.769\ ^{+12}_{-8}$	[9-23]	40.67 / 24
		0.13455	0.13344	0.13417	$0.734\ ^{+13}_{-10}$	[9-23]	40.73 / 24
		0.13455	0.13344	0.13455	$0.702\ ^{+14}_{-14}$	[9-23]	40.76 / 24
		0.13455	0.13417	0.13417	$0.698\ ^{+14}_{-13}$	[9-23]	40.07 / 24
		0.13455	0.13417	0.13455	$0.674\ ^{+15}_{-19}$	[9-23]	35.69 / 24
6.0	$32^3 \cdot 64$	0.13344	0.13344	0.13417	$0.765\ ^{+10}_{-11}$	[3-18]	16.96 / 12
		0.13344	0.13344	0.13455	$0.748\ ^{+10}_{-13}$	[3-18]	17.76 / 12
		0.13344	0.13417	0.13417	$0.737\ ^{+10}_{-12}$	[3-18]	16.31 / 12
		0.13344	0.13417	0.13455	$0.711\ ^{+10}_{-15}$	[3-18]	17.61 / 12
		0.13344	0.13455	0.13455	$0.704\ ^{+10}_{-15}$	[3-18]	16.35 / 12
		0.13417	0.13344	0.13344	$0.772\ ^{+10}_{-11}$	[3-18]	16.37 / 12
		0.13417	0.13344	0.13417	$0.730\ ^{+10}_{-13}$	[3-18]	16.92 / 12
		0.13417	0.13344	0.13455	$0.719\ ^{+11}_{-14}$	[3-18]	16.87 / 12
		0.13417	0.13417	0.13455	$0.680\ ^{+12}_{-16}$	[3-18]	16.22 / 12
		0.13417	0.13455	0.13455	$0.664\ ^{+13}_{-18}$	[3-18]	15.21 / 12
		0.13455	0.13344	0.13344	$0.759\ ^{+10}_{-11}$	[3-18]	16.15 / 12
		0.13455	0.13344	0.13417	$0.724\ ^{+10}_{-14}$	[3-18]	15.95 / 12
		0.13455	0.13344	0.13455	$0.691\ ^{+12}_{-16}$	[3-18]	18.26 / 12
		0.13455	0.13417	0.13417	$0.684\ ^{+10}_{-17}$	[4-18]	14.59 / 11
		0.13455	0.13417	0.13455	$0.657\ ^{+16}_{-19}$	[3-18]	16.34 / 12

Table A.15: Non-degenerate lambda masses for the non-perturbatively improved data sets.

β	$L^3 \cdot T$	κ_1	κ_2	κ_3	am_Λ	Fit	χ^2/d.o.f.
6.2	$24^3 \cdot 48$	0.13460	0.13460	0.13510	$0.548\ ^{+8}_{-7}$	[13-23]	31.68 / 16
		0.13460	0.13460	0.13530	$0.534\ ^{+9}_{-8}$	[13-23]	32.28 / 16
		0.13460	0.13510	0.13510	$0.524\ ^{+9}_{-8}$	[13-23]	34.93 / 16
		0.13460	0.13510	0.13530	$0.510\ ^{+7}_{-11}$	[13-23]	34.48 / 16
		0.13460	0.13530	0.13530	$0.502\ ^{+8}_{-12}$	[13-23]	33.53 / 16
		0.13510	0.13460	0.13460	$0.552\ ^{+9}_{-7}$	[13-23]	27.59 / 16
		0.13510	0.13460	0.13510	$0.522\ ^{+9}_{-10}$	[13-23]	31.55 / 16
		0.13510	0.13460	0.13530	$0.516\ ^{+7}_{-10}$	[13-23]	37.31 / 16
		0.13510	0.13510	0.13530	$0.497\ ^{+3}_{-11}$	[13-23]	39.22 / 16
		0.13510	0.13530	0.13530	$0.474\ ^{+4}_{-27}$	[14-23]	34.28 / 14
		0.13530	0.13460	0.13460	$0.543\ ^{+10}_{-7}$	[13-23]	27.91 / 16
		0.13530	0.13460	0.13510	$0.516\ ^{+11}_{-10}$	[13-23]	30.42 / 16
		0.13530	0.13460	0.13530	$0.507\ ^{+6}_{-14}$	[13-23]	31.56 / 16
		0.13530	0.13510	0.13510	$0.497\ ^{+7}_{-13}$	[13-23]	32.42 / 16
		0.13530	0.13510	0.13530	$0.497\ ^{+4}_{-15}$	[13-23]	31.10 / 16

Table A.16: Non-degenerate lambda masses for the non-perturbatively improved data sets.

β	$L^3 \cdot T$	κ_1	κ_2	am_{PCAC}	Fit	χ^2/d.o.f.
5.7	$16^3 \cdot 32$	0.13843	0.13843	0.10935^{+30}_{-28}	[9-14]	1.93 / 5
		0.14077	0.13843	0.08108^{+28}_{-27}	[9-14]	1.46 / 5
		0.14077	0.14077	0.05430^{+29}_{-26}	[9-14]	1.02 / 5
6.0	$16^3 \cdot 48$	0.13700	0.13700	0.05392^{+9}_{-9}	[13-22]	11.12 / 9
		0.13810	0.13700	0.04007^{+10}_{-11}	[13-22]	11.43 / 9
		0.13856	0.13700	0.03421^{+10}_{-13}	[13-22]	10.35 / 9
		0.13810	0.13810	0.02647^{+11}_{-13}	[13-22]	10.89 / 9
		0.13856	0.13810	0.02070^{+12}_{-14}	[13-22]	11.40 / 9
		0.13856	0.13856	0.01498^{+14}_{-16}	[13-22]	12.45 / 9
6.2	$24^3 \cdot 48$	0.13640	0.13640	0.04176^{+6}_{-6}	[9-22]	9.67 / 13
		0.13710	0.13640	0.03201^{+5}_{-6}	[9-22]	8.57 / 13
		0.13745	0.13640	0.02710^{+6}_{-7}	[9-22]	7.89 / 13
		0.13710	0.13710	0.02234^{+6}_{-7}	[9-22]	8.05 / 13
		0.13745	0.13710	0.01747^{+6}_{-7}	[9-22]	7.58 / 13
		0.13745	0.13745	0.01262^{+7}_{-7}	[9-22]	7.25 / 13

Table A.17: The unrenormalised PCAC masses for the tadpole improved data sets.

β	$L^3 \cdot T$	κ_1	κ_2	am_{PCAC}	Fit	χ^2/d.o.f.
6.0	$16^3 \cdot 48$	0.13344	0.13344	$0.04801\ ^{+8}_{-9}$	[12-22]	15.54 / 10
		0.13417	0.13344	$0.03803\ ^{+9}_{-10}$	[12-22]	16.49 / 10
		0.13455	0.13344	$0.03275\ ^{+10}_{-10}$	[12-22]	16.74 / 10
		0.13417	0.13417	$0.02817\ ^{+10}_{-11}$	[12-22]	16.04 / 10
		0.13455	0.13417	$0.02292\ ^{+11}_{-11}$	[12-22]	16.68 / 10
		0.13455	0.13455	$0.01766\ ^{+14}_{-11}$	[12-22]	16.06 / 10
6.0	$32^3 \cdot 64$	0.13344	0.13344	$0.04828\ ^{+10}_{-14}$	[19-30]	10.18 / 11
		0.13417	0.13344	$0.03832\ ^{+9}_{-15}$	[19-30]	11.34 / 11
		0.13455	0.13344	$0.03304\ ^{+9}_{-15}$	[19-30]	13.36 / 11
		0.13417	0.13417	$0.02845\ ^{+9}_{-15}$	[19-30]	12.93 / 11
		0.13455	0.13417	$0.02321\ ^{+10}_{-16}$	[19-30]	14.93 / 11
		0.13455	0.13455	$0.01801\ ^{+12}_{-17}$	[19-30]	17.75 / 11
6.2	$24^3 \cdot 48$	0.13460	0.13460	$0.03526\ ^{+5}_{-6}$	[9-22]	8.35 / 13
		0.13510	0.13460	$0.02798\ ^{+5}_{-6}$	[9-22]	7.47 / 13
		0.13530	0.13460	$0.02505\ ^{+5}_{-6}$	[9-22]	7.28 / 13
		0.13510	0.13510	$0.02075\ ^{+6}_{-6}$	[9-22]	7.96 / 13
		0.13530	0.13510	$0.01783\ ^{+6}_{-7}$	[9-22]	8.05 / 13
		0.13530	0.13530	$0.01491\ ^{+6}_{-7}$	[9-22]	8.34 / 13

Table A.18: The unrenormalised PCAC masses for the non-perturbatively improved data sets.

Appendix B

Light hadron spectrum results for the quenched simulations

This appendix contains the results for the normal and strange quark masses obtained for the quenched simulations discussed in chapter 3. In addition, the lattice values of the light hadron spectrum at the physical quark masses are reported for each data set. The results are quoted in every case for each of the four choices of quantity used to set the scale in the determination of the physical values of the quark masses: the ρ mass, the K* mass, the nucleon mass and r_0^{-1}. The uppermost table on each page refers to the tadpole improved data sets, while the lower tables correspond to the non-perturbatively improved data sets.

β	$L^3 \cdot T$	Q	$\widetilde{m}_{\rm n}$	$\kappa_{\rm n}$	$m_{\rm n}^{\overline{\rm MS}}(1/a)$ MeV
5.7	$16^3 \cdot 32$	m_ρ	0.00297^{+12}_{-13}	0.14306^{+3}_{-4}	4.95^{+23}_{-24}
		$m_{\rm K^*}$	0.00274^{+9}_{-11}	0.14307^{+3}_{-4}	4.75^{+18}_{-21}
		$m_{\rm N}$	0.00387^{+18}_{-19}	0.14302^{+3}_{-4}	5.65^{+30}_{-31}
		r_0^{-1}	0.00288^{+1}_{-2}	0.14306^{+2}_{-4}	4.87^{+2}_{-4}
6.0	$16^3 \cdot 48$	m_ρ	0.00165^{+7}_{-6}	0.13914^{+2}_{-1}	4.36^{+20}_{-18}
		$m_{\rm K^*}$	0.00154^{+5}_{-4}	0.13915^{+2}_{-1}	4.22^{+15}_{-13}
		$m_{\rm N}$	0.00211^{+20}_{-12}	0.13913^{+2}_{-1}	4.94^{+49}_{-37}
		r_0^{-1}	0.00138^{+1}_{-1}	0.13916^{+2}_{-1}	3.99^{+3}_{-3}
6.2	$24^3 \cdot 48$	m_ρ	0.00123^{+8}_{-3}	0.13785^{+2}_{-1}	4.18^{+28}_{-16}
		$m_{\rm K^*}$	0.00114^{+6}_{-3}	0.13785^{+2}_{-1}	4.02^{+22}_{-14}
		$m_{\rm N}$	0.00140^{+6}_{-12}	0.13784^{+2}_{-1}	4.46^{+27}_{-39}
		r_0^{-1}	0.00095^{+1}_{-1}	0.13786^{+2}_{-1}	3.67^{+4}_{-4}

β	$L^3 \cdot T$	Q	$\widetilde{m}_{\rm n}$	$\kappa_{\rm n}$	$m_{\rm n}^{\overline{\rm MS}}(1/a)$ MeV
6.0	$16^3 \cdot 48$	m_ρ	0.00163^{+8}_{-4}	0.13519^{+2}_{-1}	4.27^{+22}_{-15}
		$m_{\rm K^*}$	0.00153^{+6}_{-4}	0.13520^{+2}_{-1}	4.13^{+17}_{-13}
		$m_{\rm N}$	0.00221^{+19}_{-19}	0.13517^{+2}_{-1}	4.97^{+48}_{-47}
		r_0^{-1}	0.00130^{+1}_{-1}	0.13520^{+2}_{-1}	3.97^{+3}_{-3}
6.0	$32^3 \cdot 64$	m_ρ	0.00170^{+8}_{-7}	0.13517^{+1}_{-1}	4.37^{+22}_{-21}
		$m_{\rm K^*}$	0.00159^{+6}_{-6}	0.13518^{+1}_{-1}	4.23^{+17}_{-18}
		$m_{\rm N}$	0.00210^{+15}_{-21}	0.13516^{+1}_{-1}	4.89^{+42}_{-51}
		r_0^{-1}	0.00130^{+1}_{-1}	0.13519^{+1}_{-1}	3.82^{+3}_{-3}
6.2	$24^3 \cdot 48$	m_ρ	0.00121^{+9}_{-4}	0.13577^{+2}_{-1}	4.13^{+32}_{-20}
		$m_{\rm K^*}$	0.00113^{+6}_{-3}	0.13577^{+2}_{-1}	3.99^{+21}_{-11}
		$m_{\rm N}$	0.00153^{+5}_{-14}	0.13576^{+2}_{-1}	4.66^{+27}_{-43}
		r_0^{-1}	0.00093^{+1}_{-1}	0.13578^{+2}_{-1}	3.63^{+4}_{-4}

Table B.1: Lattice values for the improved normal quark mass, with the corresponding $\kappa_{\rm n}$ value, for the quenched data sets. The quark mass has been evaluated in the $\overline{\rm MS}$ renormalisation scheme at $1/a$. The scale is set by the physical quantity Q. The error in r_0 has not been taken into account.

			“K - input”		“ϕ - input”	
β	$L^3 \cdot T$	Q	$\widetilde{m}_s$	κ_s	$\widetilde{m}_s$	κ_s
5.7	$16^3 \cdot 32$	m_ρ	0.0741^{+29}_{-32}	0.14004^{+14}_{-14}	0.0938^{+60}_{-63}	0.13916^{+28}_{-27}
		m_{K^*}	0.0685^{+22}_{-26}	0.14029^{+11}_{-10}	0.0795^{+38}_{-38}	0.13980^{+17}_{-18}
		m_N	0.0966^{+44}_{-48}	0.13904^{+22}_{-21}	0.1468^{+94}_{-117}	0.13670^{+56}_{-46}
		r_0^{-1}	0.0719^{+3}_{-6}	0.14013^{+2}_{-2}	0.0884^{+21}_{-24}	0.13941^{+10}_{-10}
6.0	$16^3 \cdot 48$	m_ρ	0.0413^{+17}_{-14}	0.13758^{+6}_{-6}	0.0510^{+38}_{-32}	0.13719^{+14}_{-14}
		m_{K^*}	0.0385^{+13}_{-10}	0.13769^{+5}_{-5}	0.0441^{+25}_{-17}	0.13747^{+8}_{-9}
		m_N	0.0526^{+51}_{-30}	0.13712^{+13}_{-20}	0.0766^{+105}_{-68}	0.13614^{+29}_{-43}
		r_0^{-1}	0.0345^{+2}_{-2}	0.13785^{+1}_{-0}	0.0338^{+15}_{-17}	0.13788^{+7}_{-5}
6.2	$24^3 \cdot 48$	m_ρ	0.0306^{+19}_{-8}	0.13672^{+4}_{-7}	0.0381^{+42}_{-14}	0.13643^{+6}_{-16}
		m_{K^*}	0.0284^{+14}_{-7}	0.13680^{+3}_{-5}	0.0326^{+26}_{-9}	0.13664^{+4}_{-10}
		m_N	0.0350^{+15}_{-29}	0.13655^{+12}_{-6}	0.0485^{+36}_{-69}	0.13602^{+27}_{-14}
		r_0^{-1}	0.0237^{+3}_{-2}	0.13699^{+1}_{-1}	0.0200^{+18}_{-20}	0.13713^{+8}_{-7}

			“K - input”		“ϕ - input”	
β	$L^3 \cdot T$	Q	$\widetilde{m}_s$	κ_s	$\widetilde{m}_s$	κ_s
6.0	$16^3 \cdot 48$	m_ρ	0.0407^{+21}_{-11}	0.13374^{+5}_{-8}	0.0484^{+46}_{-19}	0.13345^{+7}_{-17}
		m_{K^*}	0.0383^{+15}_{-10}	0.13383^{+4}_{-6}	0.0427^{+28}_{-13}	0.13366^{+5}_{-10}
		m_N	0.0552^{+48}_{-48}	0.13318^{+19}_{-18}	0.0803^{+95}_{-102}	0.13221^{+40}_{-38}
		r_0^{-1}	0.0324^{+2}_{-2}	0.13405^{+1}_{-1}	0.0275^{+20}_{-22}	0.13423^{+9}_{-7}
6.0	$32^3 \cdot 64$	m_ρ	0.0426^{+21}_{-18}	0.13365^{+7}_{-8}	0.0521^{+47}_{-35}	0.13329^{+13}_{-18}
		m_{K^*}	0.0397^{+16}_{-14}	0.13376^{+5}_{-7}	0.0448^{+31}_{-24}	0.13357^{+9}_{-12}
		m_N	0.0525^{+38}_{-52}	0.13327^{+19}_{-14}	0.0754^{+89}_{-119}	0.13239^{+45}_{-35}
		r_0^{-1}	0.0325^{+2}_{-4}	0.13403^{+1}_{-1}	0.0255^{+19}_{-28}	0.13429^{+11}_{-7}
6.2	$24^3 \cdot 48$	m_ρ	0.0303^{+22}_{-11}	0.13468^{+4}_{-8}	0.0371^{+52}_{-23}	0.13443^{+9}_{-19}
		m_{K^*}	0.0283^{+15}_{-9}	0.13476^{+3}_{-5}	0.0320^{+31}_{-14}	0.13462^{+5}_{-11}
		m_N	0.0382^{+11}_{-35}	0.13438^{+13}_{-4}	0.0560^{+31}_{-84}	0.13370^{+33}_{-12}
		r_0^{-1}	0.0233^{+3}_{-3}	0.13495^{+1}_{-1}	0.0180^{+21}_{-23}	0.13515^{+9}_{-7}

Table B.2: Lattice values for the strange quark mass, with the corresponding κ_s value, for the quenched data sets using the “K - input” and “ϕ - input” methods. The scale is set by the physical quantity Q. The error in r_0 has not been taken into account.

			$m_s^{\overline{\rm MS}}(1/a)$ MeV	
β	$L^3 \cdot T$	Q	"K - input"	"ϕ - input"
5.7	$16^3 \cdot 32$	m_ρ	$123\,^{+6}_{-6}$	$156\,^{+11}_{-11}$
		m_{K^*}	$119\,^{+4}_{-5}$	$138\,^{+7}_{-7}$
		m_N	$141\,^{+7}_{-8}$	$214\,^{+15}_{-18}$
		r_0^{-1}	$121\,^{+1}_{-1}$	$149\,^{+4}_{-4}$
6.0	$16^3 \cdot 48$	m_ρ	$109\,^{+5}_{-4}$	$134\,^{+1}_{-9}$
		m_{K^*}	$105\,^{+4}_{-3}$	$121\,^{+7}_{-5}$
		m_N	$123\,^{+12}_{-9}$	$179\,^{+25}_{-18}$
		r_0^{-1}	$100\,^{+1}_{-1}$	$98\,^{+4}_{-5}$
6.2	$24^3 \cdot 48$	m_ρ	$104\,^{+7}_{-4}$	$130\,^{+14}_{-6}$
		m_{K^*}	$100\,^{+5}_{-3}$	$115\,^{+9}_{-4}$
		m_N	$111\,^{+7}_{-10}$	$154\,^{+13}_{-22}$
		r_0^{-1}	$92\,^{+1}_{-1}$	$77\,^{+7}_{-8}$

			$m_s^{\overline{\rm MS}}(1/a)$ MeV	
β	$L^3 \cdot T$	Q	"K - input"	"ϕ - input"
6.0	$16^3 \cdot 48$	m_ρ	$107\,^{+6}_{-5}$	$127\,^{+12}_{-6}$
		m_{K^*}	$103\,^{+4}_{-3}$	$115\,^{+8}_{-4}$
		m_N	$124\,^{+12}_{-12}$	$181\,^{+23}_{-24}$
		r_0^{-1}	$95\,^{+1}_{-1}$	$81\,^{+6}_{-6}$
6.0	$32^3 \cdot 64$	m_ρ	$109\,^{+5}_{-5}$	$134\,^{+12}_{-9}$
		m_{K^*}	$106\,^{+4}_{-4}$	$119\,^{+8}_{-7}$
		m_N	$121\,^{+11}_{-13}$	$174\,^{+22}_{-28}$
		r_0^{-1}	$96\,^{+1}_{-1}$	$75\,^{+6}_{-8}$
6.2	$24^3 \cdot 48$	m_ρ	$104\,^{+8}_{-5}$	$127\,^{+18}_{-9}$
		m_{K^*}	$100\,^{+6}_{-4}$	$113\,^{+11}_{-6}$
		m_N	$116\,^{+7}_{-11}$	$170\,^{+12}_{-26}$
		r_0^{-1}	$91\,^{+1}_{-1}$	$70\,^{+8}_{-9}$

Table B.3: The strange quark mass has been evaluated in the $\overline{\rm MS}$ renormalisation scheme at $1/a$ for the quenched data sets using the "K - input" and "ϕ - input" methods. The scale is set by the physical quantity Q. The error in r_0 has not been taken into account.

β	$L^3 \cdot T$	Q	m_ρ	m_ϕ	m_{K^*}
5.7	$16^3 \cdot 32$	m_ρ	0.676^{+14}_{-15}	0.849^{+13}_{-18}	0.765^{+14}_{-20}
		m_{K^*}	0.676^{+13}_{-19}	0.833^{+12}_{-15}	0.754^{+13}_{-14}
		m_N	0.683^{+15}_{-24}	0.902^{+13}_{-13}	0.792^{+11}_{-17}
		r_0^{-1}	0.676^{+13}_{-18}	0.842^{+6}_{-8}	0.759^{+9}_{-13}
6.0	$16^3 \cdot 48$	m_ρ	0.398^{+8}_{-7}	0.501^{+7}_{-7}	0.448^{+8}_{-8}
		m_{K^*}	0.396^{+9}_{-9}	0.493^{+7}_{-6}	0.446^{+8}_{-6}
		m_N	0.397^{+9}_{-9}	0.531^{+14}_{-8}	0.464^{+9}_{-6}
		r_0^{-1}	0.395^{+9}_{-9}	0.483^{+4}_{-4}	0.439^{+6}_{-6}
6.2	$24^3 \cdot 48$	m_ρ	0.301^{+9}_{-4}	0.379^{+7}_{-5}	0.340^{+8}_{-7}
		m_{K^*}	0.301^{+9}_{-9}	0.373^{+6}_{-5}	0.337^{+8}_{-4}
		m_N	0.302^{+9}_{-9}	0.390^{+5}_{-9}	0.346^{+5}_{-7}
		r_0^{-1}	0.300^{+9}_{-9}	0.361^{+4}_{-4}	0.331^{+6}_{-7}

β	$L^3 \cdot T$	Q	m_ρ	m_ϕ	m_{K^*}
6.0	$16^3 \cdot 48$	m_ρ	0.407^{+11}_{-6}	0.518^{+9}_{-7}	0.463^{+10}_{-8}
		m_{K^*}	0.408^{+11}_{-10}	0.511^{+8}_{-7}	0.459^{+9}_{-6}
		m_N	0.410^{+10}_{-10}	0.558^{+13}_{-14}	0.484^{+9}_{-9}
		r_0^{-1}	0.408^{+10}_{-10}	0.495^{+5}_{-5}	0.451^{+7}_{-8}
6.0	$32^3 \cdot 64$	m_ρ	0.416^{+10}_{-8}	0.525^{+10}_{-7}	0.472^{+10}_{-8}
		m_{K^*}	0.419^{+11}_{-9}	0.518^{+9}_{-7}	0.466^{+10}_{-8}
		m_N	0.420^{+11}_{-9}	0.551^{+11}_{-14}	0.486^{+9}_{-9}
		r_0^{-1}	0.418^{+11}_{-9}	0.499^{+6}_{-5}	0.458^{+8}_{-7}
6.2	$24^3 \cdot 48$	m_ρ	0.303^{+10}_{-5}	0.383^{+8}_{-6}	0.345^{+8}_{-8}
		m_{K^*}	0.307^{+9}_{-11}	0.378^{+7}_{-6}	0.340^{+9}_{-5}
		m_N	0.308^{+9}_{-11}	0.403^{+4}_{-10}	0.356^{+5}_{-8}
		r_0^{-1}	0.306^{+9}_{-11}	0.364^{+4}_{-4}	0.335^{+7}_{-7}

Table B.4: Lattice values of the mesons at the physical quark masses obtained using Q to set the scale for the quenched data sets. The π and K meson can not be determined since they are used to set the quark masses. Note that the ρ and K* mass cannot be predicted in the case where they set the scale.

β	$L^3 \cdot T$	Q	m_Δ	m_{Σ^*}	m_{Ξ^*}	m_Ω
5.7	$16^3 \cdot 32$	m_ρ	1.123^{+41}_{-32}	1.215^{+35}_{-27}	1.307^{+30}_{-23}	1.399^{+29}_{-20}
		m_{K^*}	1.122^{+42}_{-32}	1.207^{+35}_{-28}	1.292^{+30}_{-23}	1.378^{+28}_{-20}
		m_{N}	1.126^{+41}_{-32}	1.247^{+33}_{-25}	1.367^{+30}_{-21}	1.487^{+30}_{-20}
		r_0^{-1}	1.122^{+41}_{-32}	1.212^{+34}_{-25}	1.302^{+27}_{-19}	1.391^{+23}_{-13}
6.0	$16^3 \cdot 48$	m_ρ	0.734^{+20}_{-29}	0.777^{+15}_{-23}	0.820^{+12}_{-17}	0.864^{+9}_{-14}
		m_{K^*}	0.733^{+20}_{-29}	0.774^{+15}_{-23}	0.814^{+12}_{-18}	0.854^{+9}_{-13}
		m_{N}	0.735^{+20}_{-28}	0.790^{+15}_{-21}	0.845^{+14}_{-17}	0.901^{+17}_{-16}
		r_0^{-1}	0.733^{+20}_{-29}	0.769^{+16}_{-24}	0.805^{+12}_{-19}	0.841^{+8}_{-14}
6.2	$24^3 \cdot 48$	m_ρ	0.539^{+14}_{-11}	0.578^{+12}_{-8}	0.616^{+11}_{-6}	0.655^{+10}_{-7}
		m_{K^*}	0.539^{+14}_{-11}	0.574^{+12}_{-9}	0.610^{+10}_{-7}	0.646^{+9}_{-6}
		m_{N}	0.540^{+14}_{-11}	0.584^{+10}_{-9}	0.628^{+8}_{-10}	0.672^{+8}_{-13}
		r_0^{-1}	0.538^{+14}_{-11}	0.568^{+12}_{-9}	0.598^{+9}_{-7}	0.628^{+7}_{-6}

β	$L^3 \cdot T$	Q	m_Δ	m_{Σ^*}	m_{Ξ^*}	m_Ω
6.0	$16^3 \cdot 48$	m_ρ	0.768^{+48}_{-35}	0.809^{+34}_{-26}	0.850^{+22}_{-18}	0.891^{+13}_{-13}
		m_{K^*}	0.767^{+48}_{-35}	0.806^{+34}_{-28}	0.845^{+23}_{-19}	0.884^{+13}_{-14}
		m_{N}	0.769^{+47}_{-35}	0.826^{+29}_{-25}	0.882^{+16}_{-19}	0.938^{+18}_{-26}
		r_0^{-1}	0.767^{+48}_{-35}	0.799^{+36}_{-30}	0.832^{+26}_{-22}	0.865^{+16}_{-17}
6.0	$32^3 \cdot 64$	m_ρ	0.711^{+26}_{-18}	0.766^{+21}_{-15}	0.821^{+18}_{-14}	0.876^{+19}_{-15}
		m_{K^*}	0.711^{+26}_{-18}	0.762^{+21}_{-15}	0.813^{+18}_{-14}	0.864^{+18}_{-15}
		m_{N}	0.713^{+26}_{-18}	0.780^{+22}_{-18}	0.848^{+20}_{-22}	0.916^{+21}_{-29}
		r_0^{-1}	0.709^{+26}_{-18}	0.751^{+22}_{-15}	0.793^{+18}_{-14}	0.835^{+15}_{-13}
6.2	$24^3 \cdot 48$	m_ρ	0.547^{+22}_{-16}	0.586^{+17}_{-12}	0.625^{+13}_{-9}	0.664^{+11}_{-8}
		m_{K^*}	0.547^{+22}_{-16}	0.583^{+17}_{-12}	0.619^{+13}_{-9}	0.656^{+10}_{-8}
		m_{N}	0.548^{+22}_{-16}	0.597^{+13}_{-13}	0.646^{+7}_{-13}	0.695^{+5}_{-17}
		r_0^{-1}	0.546^{+22}_{-16}	0.576^{+18}_{-13}	0.605^{+13}_{-10}	0.635^{+9}_{-8}

Table B.5: Lattice values of the decuplet baryons at the physical quark masses obtained using Q to set the scale for the quenched data sets.

β	$L^3 \cdot T$	Q	m_{N}	m_{Λ}	m_{Σ}	m_{Ξ}
5.7	$16^3 \cdot 32$	m_ρ	$0.936\,^{+21}_{-23}$	$1.044\,^{+19}_{-19}$	$1.044\,^{+19}_{-19}$	$1.152\,^{+19}_{-17}$
		m_{K^*}	$0.935\,^{+21}_{-23}$	$1.035\,^{+19}_{-19}$	$1.035\,^{+19}_{-19}$	$1.134\,^{+17}_{-17}$
		m_{N}	$0.940\,^{+22}_{-24}$	$1.081\,^{+24}_{-23}$	$1.081\,^{+24}_{-23}$	$1.221\,^{+26}_{-24}$
		r_0^{-1}	$0.935\,^{+21}_{-23}$	$1.040\,^{+18}_{-17}$	$1.040\,^{+18}_{-17}$	$1.145\,^{+15}_{-13}$
6.0	$16^3 \cdot 48$	m_ρ	$0.545\,^{+25}_{-16}$	$0.610\,^{+20}_{-13}$	$0.612\,^{+20}_{-12}$	$0.679\,^{+16}_{-10}$
		m_{K^*}	$0.544\,^{+25}_{-16}$	$0.605\,^{+20}_{-13}$	$0.607\,^{+21}_{-12}$	$0.669\,^{+17}_{-\ 9}$
		m_{N}	$0.547\,^{+26}_{-16}$	$0.631\,^{+27}_{-17}$	$0.632\,^{+27}_{-17}$	$0.718\,^{+28}_{-18}$
		r_0^{-1}	$0.543\,^{+25}_{-16}$	$0.597\,^{+21}_{-13}$	$0.599\,^{+21}_{-13}$	$0.655\,^{+16}_{-10}$
6.2	$24^3 \cdot 48$	m_ρ	$0.391\,^{+\ 8}_{-16}$	$0.447\,^{+\ 6}_{-11}$	$0.447\,^{+\ 8}_{-11}$	$0.502\,^{+\ 8}_{-\ 8}$
		m_{K^*}	$0.391\,^{+\ 8}_{-16}$	$0.442\,^{+\ 5}_{-12}$	$0.442\,^{+\ 7}_{-12}$	$0.494\,^{+\ 7}_{-\ 8}$
		m_{N}	$0.392\,^{+\ 8}_{-17}$	$0.456\,^{+\ 7}_{-17}$	$0.456\,^{+\ 9}_{-17}$	$0.519\,^{+\ 9}_{-18}$
		r_0^{-1}	$0.390\,^{+\ 8}_{-16}$	$0.433\,^{+\ 4}_{-13}$	$0.433\,^{+\ 6}_{-13}$	$0.476\,^{+\ 5}_{-\ 9}$

β	$L^3 \cdot T$	Q	m_{N}	m_{Λ}	m_{Σ}	m_{Ξ}
6.0	$16^3 \cdot 48$	m_ρ	$0.576\,^{+23}_{-25}$	$0.638\,^{+19}_{-17}$	$0.640\,^{+20}_{-17}$	$0.704\,^{+17}_{-11}$
		m_{K^*}	$0.575\,^{+23}_{-25}$	$0.633\,^{+19}_{-18}$	$0.636\,^{+19}_{-18}$	$0.696\,^{+16}_{-13}$
		m_{N}	$0.578\,^{+24}_{-25}$	$0.664\,^{+24}_{-25}$	$0.666\,^{+24}_{-24}$	$0.754\,^{+24}_{-24}$
		r_0^{-1}	$0.574\,^{+23}_{-25}$	$0.622\,^{+19}_{-20}$	$0.625\,^{+19}_{-20}$	$0.676\,^{+16}_{-14}$
6.0	$32^3 \cdot 64$	m_ρ	$0.560\,^{+19}_{-27}$	$0.629\,^{+15}_{-20}$	$0.631\,^{+16}_{-20}$	$0.702\,^{+14}_{-15}$
		m_{K^*}	$0.560\,^{+19}_{-27}$	$0.623\,^{+15}_{-21}$	$0.626\,^{+15}_{-21}$	$0.692\,^{+13}_{-16}$
		m_{N}	$0.563\,^{+20}_{-28}$	$0.648\,^{+19}_{-29}$	$0.650\,^{+19}_{-28}$	$0.737\,^{+20}_{-30}$
		r_0^{-1}	$0.558\,^{+19}_{-27}$	$0.609\,^{+15}_{-22}$	$0.612\,^{+15}_{-21}$	$0.666\,^{+12}_{-17}$
6.2	$24^3 \cdot 48$	m_ρ	$0.412\,^{+\ 6}_{-19}$	$0.447\,^{+\ 6}_{-11}$	$0.463\,^{+\ 6}_{-13}$	$0.513\,^{+\ 9}_{-\ 9}$
		m_{K^*}	$0.412\,^{+\ 6}_{-19}$	$0.458\,^{+\ 5}_{-15}$	$0.459\,^{+\ 5}_{-13}$	$0.506\,^{+\ 7}_{-10}$
		m_{N}	$0.414\,^{+\ 6}_{-20}$	$0.476\,^{+\ 6}_{-20}$	$0.478\,^{+\ 6}_{-19}$	$0.541\,^{+\ 6}_{-19}$
		r_0^{-1}	$0.411\,^{+\ 6}_{-19}$	$0.448\,^{+\ 4}_{-17}$	$0.450\,^{+\ 5}_{-15}$	$0.488\,^{+\ 4}_{-11}$

Table B.6: Lattice values of the octet baryons at the physical quark masses obtained using Q to set the scale for the quenched data sets. Note that the nucleon mass cannot be predicted when $Q = m_{\mathrm{N}}$.

Appendix C

Fitted lattice masses for the dynamical simulations

This appendix contains the results for the fitted lattice masses for the dynamical fermion simulations considered in chapter 4. The masses in lattice units and in units of r_0 have been determined by considering different types of fit as described in section 4.5. The notation FF or FL labels a single cosh (exponential) fit to the correspondingly fuzzed meson (baryon) correlator. The label LL,FF or LL,FL corresponds to a simultaneous double cosh (exponential) fit to those pair of correlators for the mesons (baryons). Finally the notation LL,FL,FF corresponds to a factorising fit to the ground and excited states to the three correlator combinations, LL, FL and FF. The final fits selected for the subsequent analysis are listed in Table C.1 and are highlighted in bold in the results tables. Mass results obtained from the matched quenched simulation at $\beta = 5.93$ are included in this appendix for comparison. Where N/A appears in the table, an acceptable fit could not be obtained. Note that where a type of fit was unstable for all κ_{val} values, no results are reported.

β	κ_{sea}	Pseudoscalar	Vector	Nucleon	Delta
5.2	0.13550	LL,FF	LL,FF	LL,FF	LL,FL
5.2	0.13500	LL,FF	LL,FL	FL	LL,FL,FF
5.26	0.13450	LL,FF	LL,FL	LL,FF	FF
5.29	0.13400	LL,FF	LL,FL,FF	FL	FF
5.93	Quenched	LL,FF	LL,FL,FF	LL,FL	LL,FL

Table C.1: The final fits types selected for each data set.

Fuzzing	$\kappa_{\rm val}$	$r_0 m_{\rm PS}$	$am_{\rm PS}$	Fit	χ^2/d.o.f.
FF	0.13400	2.307^{+42}_{-40}	0.470^{+3}_{-2}	[10-15]	2.54 / 4
	0.13450	2.036^{+38}_{-37}	0.414^{+4}_{-3}	[10-15]	2.72 / 4
	0.13500	1.733^{+35}_{-33}	0.353^{+4}_{-3}	[10-15]	3.31 / 4
	0.13550	1.387^{+35}_{-30}	0.282^{+5}_{-4}	[10-15]	4.32 / 4
FL	0.13400	2.309^{+42}_{-41}	0.470^{+3}_{-3}	[10-15]	0.65 / 4
	0.13450	2.036^{+39}_{-37}	0.414^{+4}_{-3}	[10-15]	0.29 / 4
	0.13500	1.731^{+37}_{-33}	0.352^{+5}_{-3}	[10-15]	0.44 / 4
	0.13550	1.379^{+39}_{-31}	0.281^{+6}_{-4}	[10-15]	1.17 / 4
LL,FF	0.13400	2.324^{+42}_{-41}	$\mathbf{0.473}^{+3}_{-3}$	[9-15]	11.86 / 8
	0.13450	2.051^{+39}_{-37}	$\mathbf{0.417}^{+4}_{-3}$	[9-15]	12.21 / 8
	0.13500	1.746^{+37}_{-39}	$\mathbf{0.355}^{+5}_{-5}$	[9-15]	11.60 / 8
	0.13550	1.399^{+44}_{-30}	$\mathbf{0.285}^{+8}_{-4}$	[9-15]	10.30 / 8
LL,FL	0.13400	2.316^{+42}_{-45}	0.471^{+3}_{-5}	[9-15]	6.01 / 8
	0.13450	2.041^{+39}_{-57}	0.415^{+4}_{-9}	[9-15]	6.62 / 8
	0.13500	1.751^{+32}_{-69}	0.356^{+3}_{-13}	[8-15]	10.21 / 10
	0.13550	1.382^{+43}_{-45}	0.281^{+7}_{-8}	[8-15]	5.21 / 10
LL,FL,FF	0.13400	2.316^{+43}_{-40}	0.471^{+4}_{-2}	[10-15]	14.27 / 12
	0.13450	2.047^{+40}_{-37}	0.416^{+4}_{-3}	[10-15]	16.42 / 12
	0.13500	1.747^{+39}_{-33}	0.356^{+5}_{-3}	[10-15]	16.75 / 12
	0.13550	1.398^{+43}_{-29}	0.285^{+7}_{-3}	[10-15]	12.05 / 12

Table C.2: Pseudoscalar masses for $\beta = 5.2$, $\kappa_{\rm sea} = 0.13550$.

Fuzzing	κ_{val}	$r_0 m_{\mathrm{V}}$	$a m_{\mathrm{V}}$	Fit	χ^2/d.o.f.
FF	0.13400	2.908^{+55}_{-54}	0.592^{+5}_{-5}	[10-15]	3.23 / 4
	0.13450	2.720^{+58}_{-55}	0.553^{+7}_{-6}	[10-15]	1.78 / 4
	0.13500	2.548^{+74}_{-66}	0.519^{+12}_{-10}	[10-15]	0.66 / 4
	0.13550	2.425^{+142}_{-102}	0.493^{+28}_{-19}	[10-15]	0.74 / 4
FL	0.13400	2.916^{+55}_{-55}	0.593^{+5}_{-5}	[10-15]	4.58 / 4
	0.13450	2.725^{+56}_{-55}	0.555^{+6}_{-6}	[10-15]	2.29 / 4
	0.13500	2.545^{+65}_{-64}	0.518^{+10}_{-10}	[10-15]	1.00 / 4
	0.13550	2.393^{+116}_{-88}	0.487^{+22}_{-16}	[10-15]	1.55 / 4
LL,FF	0.13400	2.919^{+56}_{-54}	$\mathbf{0.594}^{+\mathbf{5}}_{-\mathbf{5}}$	[10-15]	7.92 / 6
	0.13450	2.736^{+55}_{-60}	$\mathbf{0.557}^{+\mathbf{6}}_{-\mathbf{8}}$	[9-15]	9.48 / 8
	0.13500	2.579^{+57}_{-67}	$\mathbf{0.525}^{+\mathbf{8}}_{-\mathbf{10}}$	[9-15]	7.24 / 8
	0.13550	2.397^{+86}_{-71}	$\mathbf{0.488}^{+\mathbf{16}}_{-\mathbf{12}}$	[9-15]	4.27 / 8
LL,FL	0.13400	2.915^{+54}_{-61}	0.593^{+5}_{-7}	[10-15]	6.09 / 6
	0.13450	2.746^{+60}_{-55}	0.559^{+8}_{-6}	[9-15]	15.10 / 8
	0.13500	2.552^{+63}_{-70}	0.519^{+9}_{-11}	[9-15]	4.13 / 8
	0.13550	2.400^{+144}_{-109}	0.488^{+28}_{-21}	[10-15]	2.26 / 6
LL,FL,FF	0.13400	2.938^{+56}_{-53}	0.598^{+6}_{-4}	[10-15]	12.89 / 12
	0.13450	2.744^{+55}_{-52}	0.558^{+6}_{-5}	[10-15]	7.94 / 12
	0.13500	2.558^{+58}_{-57}	0.521^{+8}_{-8}	[10-15]	5.69 / 12
	0.13550	2.368^{+86}_{-75}	0.482^{+15}_{-13}	[10-15]	7.59 / 12

Table C.3: Vector masses for $\beta = 5.2$, $\kappa_{\mathrm{sea}} = 0.13550$.

Fuzzing	κ_{val}	$r_0 m_{\mathrm{N}}$	am_{N}	Fit	χ^2/d.o.f.
FF	0.13400	4.47^{+11}_{-10}	0.910^{+18}_{-12}	[11-15]	3.02 / 3
	0.13450	4.14^{+14}_{-9}	0.843^{+25}_{-13}	[11-15]	1.33 / 3
	0.13500	3.85^{+16}_{-9}	0.783^{+31}_{-11}	[9-15]	0.10 / 5
	0.13550	3.59^{+16}_{-14}	0.731^{+29}_{-25}	[10-15]	1.91 / 4
FL	0.13400	4.44^{+11}_{-9}	0.903^{+17}_{-10}	[11-15]	1.33 / 3
	0.13450	4.16^{+13}_{-9}	0.847^{+22}_{-12}	[10-15]	1.98 / 4
	0.13500	3.83^{+17}_{-11}	0.779^{+31}_{-18}	[11-15]	1.51 / 3
	0.13550	3.55^{+15}_{-9}	0.723^{+28}_{-15}	[8-15]	2.99 / 6
LL,FF	0.13400	4.53^{+12}_{-10}	$\mathbf{0.923}^{+18}_{-12}$	[10-15]	7.34 / 6
	0.13450	4.24^{+13}_{-10}	$\mathbf{0.862}^{+22}_{-15}$	[10-15]	7.37 / 6
	0.13500	3.93^{+15}_{-12}	$\mathbf{0.801}^{+27}_{-20}$	[10-15]	7.04 / 6
	0.13550	3.65^{+16}_{-17}	$\mathbf{0.743}^{+30}_{-32}$	[10-15]	3.96 / 6
LL,FL	0.13400	4.45^{+11}_{-10}	0.905^{+17}_{-13}	[10-15]	4.81 / 6
	0.13450	4.23^{+16}_{-13}	0.862^{+29}_{-23}	[9-15]	8.06 / 8
	0.13500	3.94^{+16}_{-17}	0.802^{+30}_{-32}	[9-15]	8.02 / 8
	0.13550	3.65^{+18}_{-18}	0.743^{+35}_{-33}	[9-15]	5.76 / 8
LL,FL,FF	0.13400	4.59^{+12}_{-10}	0.935^{+18}_{-14}	[10-15]	15.49 / 12
	0.13450	4.26^{+14}_{-11}	0.867^{+23}_{-18}	[10-15]	17.39 / 12
	0.13500	3.94^{+15}_{-14}	0.803^{+27}_{-24}	[10-15]	13.92 / 12
	0.13550	3.70^{+12}_{-25}	0.754^{+21}_{-50}	[10-15]	6.87 / 12

Table C.4: Nucleon masses for $\beta = 5.2$, $\kappa_{\mathrm{sea}} = 0.13550$.

Fuzzing	κ_{val}	$r_0 m_\Delta$	$a m_\Delta$	Fit	χ^2/d.o.f.
FF	0.13400	4.87^{+12}_{-10}	0.992^{+19}_{-12}	[10-15]	5.70 / 4
	0.13450	4.57^{+12}_{-11}	0.930^{+20}_{-15}	[10-15]	5.25 / 4
	0.13500	4.26^{+13}_{-13}	0.866^{+22}_{-23}	[10-15]	6.09 / 4
	0.13550	4.08^{+18}_{-15}	0.831^{+35}_{-28}	[8-15]	6.64 / 6
FL	0.13400	4.92^{+13}_{-10}	1.001^{+20}_{-13}	[10-15]	5.06 / 4
	0.13450	4.62^{+13}_{-11}	0.939^{+22}_{-15}	[10-15]	5.34 / 4
	0.13500	4.40^{+15}_{-15}	0.895^{+28}_{-27}	[9-15]	7.20 / 5
	0.13550	4.37^{+21}_{-27}	0.890^{+39}_{-53}	[8-15]	7.96 / 6
LL,FF	0.13400	4.89^{+14}_{-10}	0.994^{+23}_{-13}	[11-15]	6.77 / 4
	0.13450	N/A			
	0.13500	4.26^{+15}_{-14}	0.866^{+26}_{-24}	[10-15]	8.39 / 6
	0.13550	4.11^{+16}_{-24}	0.836^{+30}_{-47}	[10-15]	8.45 / 6
LL,FL	0.13400	4.92^{+13}_{-11}	$\mathbf{1.002^{+20}_{-13}}$	[10-15]	7.79 / 6
	0.13450	4.62^{+12}_{-12}	$\mathbf{0.941^{+20}_{-18}}$	[10-15]	8.00 / 6
	0.13500	4.27^{+16}_{-13}	$\mathbf{0.869^{+28}_{-22}}$	[10-15]	9.22 / 6
	0.13550	4.09^{+21}_{-24}	$\mathbf{0.832^{+40}_{-46}}$	[9-15]	15.96 / 8
LL,FL,FF	0.13400	4.98^{+15}_{-10}	1.014^{+26}_{-12}	[10-15]	12.88 / 12
	0.13450	4.68^{+15}_{-12}	0.952^{+25}_{-17}	[10-15]	12.00 / 12
	0.13500	4.26^{+17}_{-15}	0.867^{+31}_{-26}	[11-15]	10.53 / 9
	0.13550	3.95^{+25}_{-29}	0.804^{+49}_{-56}	[11-15]	15.90 / 9

Table C.5: Delta masses for $\beta = 5.2$, $\kappa_{\text{sea}} = 0.13550$.

Fuzzing	κ_{val}	$r_0 m_{\mathrm{PS}}$	$a m_{\mathrm{PS}}$	Fit	χ^2/d.o.f.
FF	0.13350	2.588 $^{+46}_{-46}$	0.566 $^{+2}_{-2}$	[10-15]	5.04 / 4
	0.13400	2.365 $^{+43}_{-43}$	0.517 $^{+2}_{-2}$	[10-15]	5.63 / 4
	0.13450	2.125 $^{+39}_{-39}$	0.464 $^{+3}_{-2}$	[10-15]	6.11 / 4
	0.13500	1.861 $^{+36}_{-35}$	0.407 $^{+3}_{-3}$	[10-15]	5.91 / 4
FL	0.13350	2.593 $^{+46}_{-46}$	0.567 $^{+2}_{-2}$	[11-15]	5.04 / 3
	0.13400	2.369 $^{+42}_{-42}$	0.518 $^{+2}_{-2}$	[11-15]	5.36 / 3
	0.13450	2.129 $^{+39}_{-39}$	0.465 $^{+2}_{-2}$	[11-15]	5.60 / 3
	0.13500	1.864 $^{+36}_{-35}$	0.407 $^{+3}_{-3}$	[11-15]	5.52 / 3
LL,FF	0.13350	2.591 $^{+47}_{-46}$	**0.566** $^{+2}_{-2}$	[11-15]	9.86 / 4
	0.13400	2.366 $^{+43}_{-44}$	**0.517** $^{+3}_{-3}$	[5-15]	23.15 / 16
	0.13450	2.129 $^{+40}_{-41}$	**0.465** $^{+3}_{-4}$	[5-15]	23.94 / 16
	0.13500	1.867 $^{+36}_{-37}$	**0.408** $^{+4}_{-4}$	[5-15]	24.26 / 16
LL,FL	0.13350	2.580 $^{+48}_{-50}$	0.564 $^{+4}_{-5}$	[6-15]	16.17 / 14
	0.13400	2.357 $^{+43}_{-76}$	0.515 $^{+2}_{-14}$	[7-15]	18.36 / 12
	0.13450	2.099 $^{+45}_{-56}$	0.459 $^{+6}_{-9}$	[6-15]	20.51 / 14
	0.13500	1.855 $^{+35}_{-81}$	0.405 $^{+3}_{-16}$	[6-15]	22.93 / 14
LL,FL,FF	0.13350	2.597 $^{+47}_{-46}$	0.568 $^{+2}_{-2}$	[11-15]	17.17 / 9
	0.13400	2.377 $^{+43}_{-43}$	0.519 $^{+3}_{-2}$	[11-15]	19.59 / 9
	0.13450	2.140 $^{+39}_{-39}$	0.468 $^{+3}_{-2}$	[11-15]	21.88 / 9
	0.13500	1.878 $^{+37}_{-35}$	0.410 $^{+4}_{-3}$	[11-15]	22.01 / 9

Table C.6: Pseudoscalar masses for $\beta = 5.2$, $\kappa_{\mathrm{sea}} = 0.13500$.

Fuzzing	κ_{val}	$r_0 m_{\text{V}}$	$a m_{\text{V}}$	Fit	χ^2/d.o.f.
FF	0.13350	$3.191\,^{+59}_{-59}$	$0.697\,^{+4}_{-4}$	[10-15]	3.05 / 4
	0.13400	$3.017\,^{+57}_{-57}$	$0.659\,^{+5}_{-5}$	[10-15]	2.93 / 4
	0.13450	$2.839\,^{+57}_{-56}$	$0.620\,^{+6}_{-5}$	[10-15]	2.82 / 4
	0.13500	$2.655\,^{+60}_{-57}$	$0.580\,^{+8}_{-7}$	[10-15]	2.57 / 4
FL	0.13350	$3.204\,^{+59}_{-59}$	$0.700\,^{+4}_{-4}$	[10-15]	3.46 / 4
	0.13400	$3.029\,^{+58}_{-56}$	$0.662\,^{+5}_{-4}$	[10-15]	2.85 / 4
	0.13450	$2.852\,^{+57}_{-55}$	$0.623\,^{+6}_{-5}$	[10-15]	2.26 / 4
	0.13500	$2.670\,^{+60}_{-55}$	$0.584\,^{+8}_{-6}$	[10-15]	1.56 / 4
LL,FF	0.13350	$3.200\,^{+59}_{-59}$	$0.699\,^{+4}_{-4}$	[11-15]	7.46 / 4
	0.13400	$3.051\,^{+57}_{-58}$	$0.667\,^{+4}_{-5}$	[9-15]	15.04 / 8
	0.13450	$2.880\,^{+56}_{-57}$	$0.629\,^{+5}_{-6}$	[9-15]	15.51 / 8
	0.13500	$2.696\,^{+57}_{-65}$	$0.589\,^{+7}_{-10}$	[8-15]	18.17 / 10
LL,FL	0.13350	$3.209\,^{+59}_{-59}$	$\mathbf{0.701}\,^{+4}_{-4}$	[10-15]	10.37 / 6
	0.13400	$3.037\,^{+58}_{-57}$	$\mathbf{0.664}\,^{+5}_{-4}$	[10-15]	8.35 / 6
	0.13450	$2.860\,^{+56}_{-55}$	$\mathbf{0.625}\,^{+6}_{-5}$	[10-15]	7.14 / 6
	0.13500	$2.669\,^{+62}_{-59}$	$\mathbf{0.583}\,^{+9}_{-8}$	[10-15]	5.54 / 6
LL,FL,FF	0.13350	$3.218\,^{+61}_{-57}$	$0.703\,^{+5}_{-3}$	[9-15]	19.39 / 15
	0.13400	$3.048\,^{+60}_{-55}$	$0.666\,^{+6}_{-3}$	[9-15]	17.84 / 15
	0.13450	$2.878\,^{+59}_{-53}$	$0.629\,^{+7}_{-4}$	[9-15]	18.97 / 15
	0.13500	$2.707\,^{+62}_{-54}$	$0.592\,^{+9}_{-6}$	[9-15]	22.38 / 15

Table C.7: Vector masses for $\beta = 5.2$, $\kappa_{\text{sea}} = 0.13500$.

Fuzzing	$\kappa_{\rm val}$	$r_0 m_{\rm N}$	$a m_{\rm N}$	Fit	χ^2/d.o.f.
FF	0.13350	$5.01\ ^{+11}_{-\ 9}$	$1.094\ ^{+13}_{-\ 7}$	[7-15]	22.48 / 7
	0.13400	$4.73\ ^{+11}_{-\ 9}$	$1.033\ ^{+14}_{-\ 8}$	[7-15]	22.83 / 7
	0.13450	$4.42\ ^{+11}_{-\ 9}$	$0.966\ ^{+16}_{-10}$	[7-15]	19.85 / 7
	0.13500	$4.08\ ^{+11}_{-\ 8}$	$0.891\ ^{+19}_{-\ 9}$	[7-15]	11.25 / 7
FL	0.13350	$4.99\ ^{+10}_{-\ 9}$	$\mathbf{1.090\ ^{+11}_{-\ 7}}$	[8-15]	6.83 / 6
	0.13400	$4.70\ ^{+10}_{-\ 9}$	$\mathbf{1.027\ ^{+12}_{-\ 8}}$	[8-15]	7.50 / 6
	0.13450	$4.40\ ^{+10}_{-\ 9}$	$\mathbf{0.962\ ^{+13}_{-\ 8}}$	[8-15]	7.90 / 6
	0.13500	$4.10\ ^{+10}_{-\ 9}$	$\mathbf{0.897\ ^{+14}_{-10}}$	[8-15]	7.35 / 6
LL,FF	0.13350	$5.03\ ^{+11}_{-\ 9}$	$1.098\ ^{+14}_{-\ 7}$	[8-15]	47.41 / 10
	0.13400	$4.80\ ^{+11}_{-\ 9}$	$1.050\ ^{+14}_{-\ 8}$	[7-15]	47.21 / 12
	0.13450	$4.43\ ^{+12}_{-12}$	$0.969\ ^{+20}_{-19}$	[7-15]	33.24 / 12
	0.13500	$4.09\ ^{+13}_{-11}$	$0.895\ ^{+24}_{-17}$	[7-15]	21.26 / 12
LL,FL	0.13350		N/A		
	0.13400		N/A		
	0.13450		N/A		
	0.13500	$4.11\ ^{+73}_{-73}$	$0.899\ ^{+15}_{-12}$	[7-15]	16.57 / 12
LL,FL,FF	0.13350	$5.03\ ^{+13}_{-11}$	$1.099\ ^{+21}_{-14}$	[10-15]	61.60 / 12
	0.13400	$4.77\ ^{+13}_{-11}$	$1.042\ ^{+21}_{-14}$	[10-15]	54.98 / 12
	0.13450	$4.47\ ^{+14}_{-10}$	$0.980\ ^{+24}_{-14}$	[10-15]	44.15 / 12
	0.13500	$4.16\ ^{+15}_{-10}$	$0.909\ ^{+28}_{-14}$	[10-15]	29.24 / 12

Table C.8: Nucleon masses for $\beta = 5.2$, $\kappa_{\rm sea} = 0.13500$.

Fuzzing	κ_{val}	$r_0 m_\Delta$	am_Δ	Fit	χ^2/d.o.f.
FF	0.13350	5.29^{+13}_{-10}	1.156^{+21}_{-7}	[8-15]	7.69 / 6
	0.13400	5.04^{+14}_{-10}	1.101^{+22}_{-8}	[8-15]	7.61 / 6
	0.13450	4.86^{+12}_{-9}	1.062^{+18}_{-9}	[7-15]	11.71 / 7
	0.13500	4.60^{+11}_{-10}	1.006^{+18}_{-14}	[7-15]	8.99 / 7
FL	0.13350	5.34^{+15}_{-10}	1.167^{+25}_{-6}	[8-15]	6.99 / 6
	0.13400	5.09^{+14}_{-9}	1.112^{+24}_{-6}	[8-15]	7.41 / 6
	0.13450	4.83^{+13}_{-9}	1.055^{+22}_{-7}	[8-15]	5.91 / 6
	0.13500	4.55^{+13}_{-9}	0.995^{+21}_{-8}	[8-15]	3.26 / 6
LL,FF	0.13350	5.18^{+13}_{-11}	1.131^{+19}_{-13}	[11-15]	12.86 / 4
	0.13400	4.82^{+12}_{-12}	1.052^{+18}_{-20}	[11-15]	8.50 / 4
	0.13450	5.13^{+15}_{-12}	1.120^{+25}_{-16}	[7-15]	65.41 / 12
	0.13500	4.87^{+14}_{-12}	1.063^{+25}_{-18}	[7-15]	52.94 / 12
LL,FL,FF	0.13350	5.18^{+14}_{-10}	$\mathbf{1.131^{+23}_{-9}}$	[11,15]	14.61 / 9
	0.13400	4.92^{+15}_{-10}	$\mathbf{1.074^{+27}_{-10}}$	[11,15]	14.95 / 9
	0.13450	4.67^{+16}_{-10}	$\mathbf{1.021^{+29}_{-14}}$	[11,15]	15.28 / 9
	0.13500	4.46^{+16}_{-13}	$\mathbf{0.975^{+31}_{-23}}$	[11,15]	15.30 / 9

Table C.9: Delta masses for $\beta = 5.2$, $\kappa_{\text{sea}} = 0.13500$.

Fuzzing	κ_{val}	$r_0 m_{\mathrm{PS}}$	$a m_{\mathrm{PS}}$	Fit	χ^2/d.o.f.
FF	0.13350	2.763 $^{+37}_{-37}$	0.603 $^{+2}_{-2}$	[9-15]	4.09 / 5
	0.13400	2.553 $^{+34}_{-34}$	0.557 $^{+2}_{-2}$	[9-15]	4.05 / 5
	0.13450	2.331 $^{+32}_{-32}$	0.509 $^{+2}_{-2}$	[9-15]	4.18 / 5
	0.13500	2.095 $^{+30}_{-29}$	0.457 $^{+3}_{-2}$	[9-15]	4.52 / 5
FL	0.13350	2.764 $^{+37}_{-37}$	0.603 $^{+2}_{-2}$	[8-15]	3.26 / 6
	0.13400	2.553 $^{+35}_{-34}$	0.557 $^{+3}_{-2}$	[8-15]	2.40 / 6
	0.13450	2.330 $^{+33}_{-31}$	0.509 $^{+3}_{-2}$	[8-15]	1.71 / 6
	0.13500	2.094 $^{+30}_{-28}$	0.457 $^{+3}_{-2}$	[8-15]	1.33 / 6
LL,FF	0.13350	2.765 $^{+38}_{-37}$	**0.604** $^{+3}_{-2}$	[9-15]	6.69 / 8
	0.13400	2.562 $^{+36}_{-35}$	**0.559** $^{+3}_{-3}$	[9-15]	5.70 / 8
	0.13450	2.344 $^{+35}_{-33}$	**0.512** $^{+4}_{-3}$	[9-15]	6.09 / 8
	0.13500	2.098 $^{+33}_{-28}$	**0.458** $^{+4}_{-2}$	[9-15]	7.93 / 8
LL,FL	0.13350	2.761 $^{+38}_{-37}$	0.603 $^{+3}_{-2}$	[9-15]	5.01 / 8
	0.13400	2.549 $^{+36}_{-35}$	0.556 $^{+3}_{-3}$	[9-15]	3.79 / 8
	0.13450	2.331 $^{+36}_{-31}$	0.509 $^{+4}_{-2}$	[9-15]	4.22 / 8
	0.13500	2.100 $^{+41}_{-34}$	0.458 $^{+7}_{-4}$	[9-15]	5.45 / 8
LL,FL,FF	0.13350	2.766 $^{+38}_{-37}$	0.604 $^{+3}_{-2}$	[9-15]	18.03 / 15
	0.13400	2.556 $^{+36}_{-34}$	0.558 $^{+3}_{-2}$	[9-15]	18.05 / 15
	0.13450	2.335 $^{+34}_{-31}$	0.510 $^{+4}_{-2}$	[9-15]	19.31 / 15
	0.13500	2.105 $^{+31}_{-29}$	0.459 $^{+3}_{-2}$	[10-15]	19.76 / 12

Table C.10: Pseudoscalar masses for $\beta = 5.26$, $\kappa_{\mathrm{sea}} = 0.13450$.

Fuzzing	$\kappa_{\rm val}$	$r_0 m_{\rm V}$	$a m_{\rm V}$	Fit	χ^2/d.o.f.
FF	0.13350	3.281 $^{+47}_{-47}$	0.716 $^{+5}_{-4}$	[9-15]	4.31 / 5
	0.13400	3.116 $^{+47}_{-46}$	0.680 $^{+5}_{-5}$	[9-15]	3.56 / 5
	0.13450	2.950 $^{+47}_{-46}$	0.644 $^{+6}_{-6}$	[9-15]	2.92 / 5
	0.13500	2.786 $^{+48}_{-47}$	0.608 $^{+7}_{-7}$	[9-15]	2.73 / 5
FL	0.13350	3.274 $^{+48}_{-46}$	0.715 $^{+5}_{-4}$	[10-15]	2.35 / 4
	0.13400	3.109 $^{+47}_{-45}$	0.679 $^{+5}_{-5}$	[10-15]	1.72 / 4
	0.13450	2.945 $^{+45}_{-44}$	0.643 $^{+5}_{-5}$	[9-15]	1.18 / 5
	0.13500	2.780 $^{+45}_{-43}$	0.607 $^{+6}_{-5}$	[9-15]	1.06 / 5
LL,FF	0.13350	3.308 $^{+48}_{-48}$	0.722 $^{+5}_{-5}$	[10-15]	12.38 / 6
	0.13400	3.148 $^{+47}_{-47}$	0.687 $^{+5}_{-5}$	[10-15]	11.28 / 6
	0.13450	2.988 $^{+47}_{-47}$	0.652 $^{+6}_{-6}$	[10-15]	10.04 / 6
	0.13500	2.818 $^{+47}_{-48}$	0.615 $^{+6}_{-7}$	[10-15]	7.90 / 6
LL,FL	0.13350	3.290 $^{+48}_{-46}$	**0.718** $^{+5}_{-4}$	[9-15]	18.58 / 8
	0.13400	3.126 $^{+47}_{-44}$	**0.682** $^{+5}_{-4}$	[9-15]	15.54 / 8
	0.13450	2.961 $^{+47}_{-42}$	**0.646** $^{+6}_{-4}$	[9-15]	12.83 / 8
	0.13500	2.789 $^{+53}_{-39}$	**0.609** $^{+9}_{-3}$	[9-15]	10.90 / 8
LL,FL,FF	0.13350	3.314 $^{+50}_{-46}$	0.723 $^{+6}_{-4}$	[9-15]	37.02 / 15
	0.13400	3.158 $^{+50}_{-44}$	0.689 $^{+6}_{-4}$	[8-15]	41.70 / 18
	0.13450	2.990 $^{+49}_{-43}$	0.653 $^{+7}_{-4}$	[8-15]	36.81 / 18
	0.13500	2.819 $^{+50}_{-43}$	0.615 $^{+7}_{-5}$	[8-15]	34.08 / 18

Table C.11: Vector masses for $\beta = 5.26$, $\kappa_{\rm sea} = 0.13450$.

Fuzzing	κ_{val}	$r_0 m_{\text{N}}$	$a m_{\text{N}}$	Fit	χ^2/d.o.f.
FF	0.13350	5.08^{+8}_{-7}	1.108^{+10}_{-8}	[9-15]	5.62 / 5
	0.13400	4.81^{+8}_{-7}	1.051^{+11}_{-8}	[9-15]	4.83 / 5
	0.13450	4.55^{+8}_{-7}	0.993^{+12}_{-10}	[9-15]	3.87 / 5
	0.13500	4.28^{+8}_{-8}	0.934^{+14}_{-12}	[9-15]	2.78 / 5
FL	0.13350	5.05^{+9}_{-8}	1.103^{+13}_{-8}	[10-15]	1.13 / 4
	0.13400	4.80^{+9}_{-8}	1.048^{+13}_{-10}	[10-15]	0.96 / 4
	0.13450	4.55^{+9}_{-8}	0.993^{+15}_{-11}	[10-15]	0.93 / 4
	0.13500	4.31^{+9}_{-9}	0.941^{+15}_{-14}	[10-15]	1.09 / 4
LL,FF	0.13350	5.10^{+9}_{-8}	$\mathbf{1.114}^{\mathbf{+12}}_{\mathbf{-8}}$	[9-15]	8.96 / 8
	0.13400	4.85^{+8}_{-7}	$\mathbf{1.058}^{\mathbf{+12}}_{\mathbf{-8}}$	[9-15]	8.07 / 8
	0.13450	4.59^{+9}_{-7}	$\mathbf{1.002}^{\mathbf{+14}}_{\mathbf{-8}}$	[9-15]	7.88 / 8
	0.13500	4.34^{+9}_{-7}	$\mathbf{0.948}^{\mathbf{+16}}_{\mathbf{-10}}$	[9-15]	8.78 / 8
LL,FL	0.13350	5.10^{+8}_{-8}	1.113^{+10}_{-9}	[9-15]	10.33 / 8
	0.13400	4.84^{+8}_{-7}	1.057^{+11}_{-8}	[9-15]	11.38 / 8
	0.13450	4.60^{+9}_{-7}	1.003^{+14}_{-8}	[9-15]	13.06 / 8
	0.13500	4.37^{+8}_{-8}	0.954^{+11}_{-12}	[8-15]	16.22 / 10
LL,FL,FF	0.13350	5.14^{+8}_{-7}	1.122^{+11}_{-7}	[9-15]	21.19 / 15
	0.13400	4.88^{+9}_{-7}	1.065^{+13}_{-7}	[9-15]	21.46 / 15
	0.13450	4.62^{+9}_{-7}	1.008^{+15}_{-7}	[9-15]	21.82 / 15
	0.13500	4.36^{+10}_{-7}	0.951^{+17}_{-9}	[9-15]	21.54 / 15

Table C.12: Nucleon masses for $\beta = 5.26$, $\kappa_{\text{sea}} = 0.13450$.

Fuzzing	$\kappa_{\rm val}$	$r_0 m_\Delta$	am_Δ	Fit	χ^2/d.o.f.
FF	0.13350	5.32^{+9}_{-8}	$\mathbf{1.162}^{+13}_{-9}$	[9-15]	6.23 / 5
	0.13400	5.07^{+9}_{-8}	$\mathbf{1.106}^{+14}_{-10}$	[9-15]	5.16 / 5
	0.13450	4.80^{+10}_{-8}	$\mathbf{1.048}^{+16}_{-11}$	[9-15]	4.20 / 5
	0.13500	4.53^{+11}_{-8}	$\mathbf{0.989}^{+21}_{-12}$	[9-15]	3.58 / 5
FL	0.13350	5.28^{+9}_{-8}	1.152^{+14}_{-10}	[10-15]	3.19 / 4
	0.13400	5.03^{+10}_{-8}	1.098^{+16}_{-11}	[10-15]	3.97 / 4
	0.13450	4.78^{+11}_{-9}	1.044^{+19}_{-13}	[10-15]	4.65 / 4
	0.13500	4.54^{+13}_{-10}	0.991^{+25}_{-16}	[10-15]	5.03 / 4
LL,FF	0.13350	5.44^{+11}_{-9}	1.188^{+18}_{-11}	[9-15]	20.83 / 8
	0.13400	5.17^{+12}_{-8}	1.129^{+22}_{-9}	[10-15]	16.32 / 6
	0.13450		N/A		
	0.13500	4.57^{+8}_{-7}	0.999^{+12}_{-8}	[9-15]	9.62 / 8
LL,FL	0.13350	5.36^{+11}_{-8}	1.170^{+19}_{-11}	[10-15]	19.82 / 6
	0.13400	5.17^{+20}_{-12}	1.128^{+41}_{-18}	[11-15]	7.98 / 4
	0.13450	4.94^{+11}_{-9}	1.078^{+20}_{-13}	[10-15]	19.24 / 6
	0.13500	4.71^{+12}_{-9}	1.028^{+22}_{-14}	[9-15]	18.43 / 8
LL,FL,FF	0.13350	5.35^{+12}_{-8}	1.168^{+20}_{-9}	[11-15]	18.87 / 9
	0.13400	5.13^{+12}_{-8}	1.120^{+22}_{-9}	[11-15]	19.46 / 9
	0.13450	4.93^{+12}_{-8}	1.075^{+22}_{-11}	[11-15]	20.40 / 9
	0.13500	4.75^{+12}_{-10}	1.037^{+23}_{-17}	[11-15]	21.78 / 9

Table C.13: Delta masses for $\beta = 5.26$, $\kappa_{\rm sea} = 0.13450$.

Fuzzing	$\kappa_{\rm val}$	$r_0 m_{\rm PS}$	$a m_{\rm PS}$	Fit	χ^2/d.o.f.
FF	0.13350	$2.770\ ^{+39}_{-38}$	$0.623\ ^{+\ 2}_{-\ 1}$	[8-15]	3.47 / 6
	0.13400	$2.572\ ^{+37}_{-36}$	$0.578\ ^{+\ 3}_{-\ 2}$	[8-15]	3.41 / 6
	0.13450	$2.363\ ^{+35}_{-33}$	$0.531\ ^{+\ 3}_{-\ 2}$	[8-15]	3.51 / 6
	0.13500	$2.141\ ^{+32}_{-31}$	$0.481\ ^{+\ 3}_{-\ 2}$	[8-15]	3.82 / 6
FL	0.13350	$2.768\ ^{+39}_{-39}$	$0.622\ ^{+\ 2}_{-\ 2}$	[9-15]	3.15 / 5
	0.13400	$2.570\ ^{+37}_{-36}$	$0.578\ ^{+\ 3}_{-\ 2}$	[9-15]	3.11 / 5
	0.13450	$2.362\ ^{+35}_{-33}$	$0.531\ ^{+\ 3}_{-\ 2}$	[9-15]	3.26 / 5
	0.13500	$2.140\ ^{+32}_{-31}$	$0.481\ ^{+\ 3}_{-\ 2}$	[9-15]	3.62 / 5
LL,FF	0.13350	$2.770\ ^{+39}_{-39}$	$\mathbf{0.623}\ ^{+\ \mathbf{2}}_{-\ \mathbf{2}}$	[9-15]	15.50 / 8
	0.13400	$2.571\ ^{+37}_{-36}$	$\mathbf{0.578}\ ^{+\ \mathbf{3}}_{-\ \mathbf{2}}$	[9-15]	13.67 / 8
	0.13450	$2.363\ ^{+35}_{-34}$	$\mathbf{0.531}\ ^{+\ \mathbf{3}}_{-\ \mathbf{2}}$	[9-15]	13.35 / 8
	0.13500	$2.139\ ^{+33}_{-36}$	$\mathbf{0.481}\ ^{+\ \mathbf{3}}_{-\ \mathbf{5}}$	[8-15]	12.57 / 10
LL,FL	0.13350	$2.688\ ^{+38}_{-38}$	$0.621\ ^{+\ 3}_{-\ 3}$	[7-15]	17.19 / 12
	0.13400	$2.496\ ^{+36}_{-37}$	$0.576\ ^{+\ 3}_{-\ 3}$	[7-15]	18.70 / 12
	0.13450	$2.356\ ^{+36}_{-46}$	$0.529\ ^{+\ 4}_{-\ 7}$	[8-15]	20.34 / 10
	0.13500	$2.136\ ^{+33}_{-58}$	$0.480\ ^{+\ 3}_{-11}$	[8-15]	22.62 / 10

Table C.14: Pseudoscalar masses $\beta = 5.29$, $\kappa_{\rm sea} = 0.13400$.

Fuzzing	κ_{val}	$r_0 m_{\mathrm{V}}$	$a m_{\mathrm{V}}$	Fit	χ^2/d.o.f.
FF	0.13350	$3.248\ ^{+49}_{-47}$	$0.730\ ^{+5}_{-3}$	[10-15]	9.83 / 4
	0.13400	$3.091\ ^{+48}_{-45}$	$0.695\ ^{+5}_{-3}$	[10-15]	8.91 / 4
	0.13450	$2.932\ ^{+48}_{-44}$	$0.659\ ^{+6}_{-4}$	[10-15]	7.11 / 4
	0.13500	$2.771\ ^{+51}_{-44}$	$0.623\ ^{+8}_{-5}$	[10-15]	4.71 / 4
FL	0.13350	$3.247\ ^{+49}_{-48}$	$0.730\ ^{+5}_{-4}$	[11-15]	7.90 / 3
	0.13400	$3.088\ ^{+48}_{-46}$	$0.694\ ^{+5}_{-4}$	[11-15]	6.49 / 3
	0.13450	$2.928\ ^{+48}_{-45}$	$0.658\ ^{+6}_{-5}$	[11-15]	4.77 / 3
	0.13500	$2.767\ ^{+52}_{-46}$	$0.622\ ^{+8}_{-6}$	[11-15]	3.00 / 3
LL,FF	0.13350	$3.256\ ^{+51}_{-48}$	$0.732\ ^{+6}_{-4}$	[11-15]	20.42 / 4
	0.13400	$3.097\ ^{+51}_{-46}$	$0.696\ ^{+6}_{-4}$	[11-15]	15.91 / 4
	0.13450	$2.927\ ^{+52}_{-47}$	$0.658\ ^{+7}_{-5}$	[11-15]	9.18 / 4
	0.13500	$2.773\ ^{+56}_{-45}$	$0.623\ ^{+9}_{-5}$	[11-15]	6.51 / 4
LL,FL	0.13350		N/A		
	0.13400		N/A		
	0.13450	$2.925\ ^{+50}_{-54}$	$0.657\ ^{+7}_{-8}$	[11-15]	6.69 / 4
	0.13500	$2.770\ ^{+56}_{-49}$	$0.623\ ^{+9}_{-7}$	[11-15]	5.07 / 4
LL,FL,FF	0.13350	$3.251\ ^{+51}_{-47}$	**0.731** $^{+6}_{-4}$	[11-15]	31.42 / 9
	0.13400	$3.090\ ^{+52}_{-46}$	**0.694** $^{+7}_{-4}$	[11-15]	27.35 / 9
	0.13450	$2.928\ ^{+53}_{-44}$	**0.658** $^{+8}_{-4}$	[11-15]	22.87 / 9
	0.13500	$2.766\ ^{+58}_{-44}$	**0.622** $^{+10}_{-5}$	[11-15]	18.62 / 9

Table C.15: Vector masses for $\beta = 5.29$, $\kappa_{\mathrm{sea}} = 0.13400$.

Fuzzing	κ_{val}	$r_0 m_{\text{N}}$	$a m_{\text{N}}$	Fit	χ^2/d.o.f.
FF	0.13350	$5.02\ ^{+9}_{-9}$	$1.129\ ^{+14}_{-11}$	[11-15]	0.32 / 3
	0.13400	$4.77\ ^{+10}_{-9}$	$1.071\ ^{+17}_{-12}$	[11-15]	0.29 / 3
	0.13450	$4.56\ ^{+10}_{-7}$	$1.025\ ^{+18}_{-7}$	[8-15]	3.62 / 6
	0.13500	$4.25\ ^{+12}_{-11}$	$0.955\ ^{+24}_{-21}$	[12-15]	0.22 / 2
FL	0.13350	$5.06\ ^{+9}_{-9}$	$\mathbf{1.137}\ ^{+13}_{-12}$	[11-15]	1.96 / 3
	0.13400	$4.81\ ^{+9}_{-9}$	$\mathbf{1.080}\ ^{+14}_{-13}$	[11-15]	1.18 / 3
	0.13450	$4.55\ ^{+9}_{-9}$	$\mathbf{1.021}\ ^{+15}_{-14}$	[11-15]	0.54 / 3
	0.13500	$4.27\ ^{+10}_{-9}$	$\mathbf{0.960}\ ^{+17}_{-16}$	[11-15]	0.68 / 3
LL,FF	0.13350	$5.08\ ^{+12}_{-7}$	$1.141\ ^{+21}_{-3}$	[9-15]	11.98 / 8
	0.13400	$4.80\ ^{+13}_{-7}$	$1.079\ ^{+24}_{-2}$	[9-15]	9.25 / 8
	0.13450	$4.52\ ^{+14}_{-6}$	$1.016\ ^{+28}_{-3}$	[9-15]	7.73 / 8
	0.13500	$4.26\ ^{+16}_{-7}$	$0.956\ ^{+33}_{-8}$	[10-15]	5.92 / 6
LL,FL	0.13350	$5.08\ ^{+11}_{-7}$	$1.140\ ^{+18}_{-4}$	[9-15]	12.75 / 8
	0.13400	$4.82\ ^{+12}_{-7}$	$1.082\ ^{+22}_{-3}$	[9-15]	8.87 / 8
	0.13450	$4.54\ ^{+13}_{-6}$	$1.020\ ^{+25}_{-4}$	[9-15]	6.08 / 8
	0.13500	$4.27\ ^{+15}_{-6}$	$0.959\ ^{+30}_{-5}$	[9-15]	4.03 / 8

Table C.16: Nucleon masses for $\beta = 5.29$, $\kappa_{\text{sea}} = 0.13400$.

Fuzzing	κ_{val}	$r_0 m_\Delta$	$a m_\Delta$	Fit	χ^2/d.o.f.
FF	0.13350	$5.27\,^{+10}_{-\ 8}$	$\mathbf{1.184}\,^{+16}_{-\ 9}$	[10-15]	1.94 / 4
	0.13400	$5.03\,^{+11}_{-\ 8}$	$\mathbf{1.131}\,^{+19}_{-10}$	[10-15]	1.74 / 4
	0.13450	$4.80\,^{+12}_{-\ 8}$	$\mathbf{1.079}\,^{+23}_{-11}$	[10-15]	1.68 / 4
	0.13500	$4.56\,^{+14}_{-\ 9}$	$\mathbf{1.024}\,^{+28}_{-14}$	[10-15]	1.60 / 4
FL	0.13350	$5.30\,^{+10}_{-\ 8}$	$1.191\,^{+16}_{-\ 8}$	[11-15]	2.18 / 3
	0.13400	$5.07\,^{+11}_{-\ 8}$	$1.139\,^{+19}_{-10}$	[11-15]	2.37 / 3
	0.13450	$4.84\,^{+12}_{-\ 8}$	$1.087\,^{+22}_{-10}$	[11-15]	2.62 / 3
	0.13500	$4.60\,^{+14}_{-\ 9}$	$1.033\,^{+27}_{-14}$	[11-15]	2.81 / 3
LL,FF	0.13350	$5.29\,^{+11}_{-\ 8}$	$1.189\,^{+18}_{-\ 7}$	[11-15]	9.46 / 4
	0.13400	$5.06\,^{+11}_{-\ 8}$	$1.136\,^{+19}_{-\ 9}$	[11-15]	9.21 / 4
	0.13450	$4.93\,^{+11}_{-\ 8}$	$1.107\,^{+19}_{-\ 7}$	[9-15]	13.49 / 8
	0.13500	$4.70\,^{+11}_{-\ 8}$	$1.056\,^{+21}_{-10}$	[9-15]	11.48 / 8
LL,FL	0.13350	$5.30\,^{+11}_{-\ 8}$	$1.191\,^{+19}_{-\ 7}$	[11-15]	6.03 / 4
	0.13400	$5.06\,^{+12}_{-\ 8}$	$1.137\,^{+21}_{-\ 8}$	[11-15]	6.45 / 4
	0.13450	$4.95\,^{+10}_{-\ 8}$	$1.112\,^{+17}_{-\ 9}$	[9-15]	14.84 / 8
	0.13500	$4.63\,^{+15}_{-16}$	$1.041\,^{+29}_{-33}$	[10-15]	13.48 / 6
LL,FL,FF	0.13350	$5.36\,^{+17}_{-\ 9}$	$1.204\,^{+26}_{-10}$	[11-15]	33.06 / 9
	0.13400	$5.13\,^{+14}_{-\ 8}$	$1.152\,^{+28}_{-10}$	[11-15]	29.71 / 9
	0.13450	$4.89\,^{+16}_{-\ 9}$	$1.097\,^{+32}_{-12}$	[11-15]	26.68 / 9
	0.13500	$4.78\,^{+14}_{-\ 8}$	$1.074\,^{+28}_{-11}$	[9-15]	39.61 / 15

Table C.17: Delta masses for $\beta = 5.29$, $\kappa_{\text{sea}} = 0.13400$.

Fuzzing	κ_1	κ_2	$r_0 m_{\mathrm{PS}}$	$a m_{\mathrm{PS}}$	Fit	χ^2/d.o.f.
FF	0.13270	0.13270	2.275^{+18}_{-17}	0.493^{+2}_{-2}	[9-15]	0.70 / 5
	0.13320	0.13270	2.153^{+18}_{-16}	0.467^{+2}_{-2}	[9-15]	0.68 / 5
	0.13340	0.13270	2.102^{+18}_{-16}	0.456^{+2}_{-2}	[9-15]	0.68 / 5
	0.13320	0.13320	2.025^{+17}_{-15}	0.439^{+2}_{-2}	[9-15]	0.72 / 5
	0.13340	0.13320	1.972^{+17}_{-15}	0.428^{+3}_{-2}	[9-15]	0.74 / 5
	0.13340	0.13340	1.919^{+17}_{-15}	0.416^{+3}_{-2}	[9-15]	0.79 / 5
	0.13370	0.13370	1.749^{+17}_{-15}	0.379^{+3}_{-2}	[9-15]	1.06 / 5
	0.13390	0.13370	1.690^{+18}_{-15}	0.366^{+3}_{-2}	[9-15]	1.26 / 5
	0.13390	0.13390	1.629^{+18}_{-14}	0.353^{+3}_{-2}	[9-15]	1.58 / 5
FL	0.13270	0.13270	2.276^{+18}_{-17}	0.494^{+2}_{-2}	[9-15]	1.75 / 5
	0.13320	0.13270	2.154^{+17}_{-16}	0.467^{+2}_{-2}	[9-15]	1.59 / 5
	0.13340	0.13270	2.103^{+17}_{-16}	0.456^{+2}_{-2}	[9-15]	1.53 / 5
	0.13320	0.13320	2.026^{+17}_{-15}	0.439^{+2}_{-2}	[9-15]	1.50 / 5
	0.13340	0.13320	1.973^{+17}_{-15}	0.428^{+2}_{-2}	[9-15]	1.43 / 5
	0.13340	0.13340	1.920^{+17}_{-15}	0.416^{+2}_{-2}	[9-15]	1.41 / 5
	0.13370	0.13370	1.751^{+18}_{-15}	0.380^{+3}_{-2}	[9-15]	1.40 / 5
	0.13390	0.13370	1.691^{+18}_{-14}	0.367^{+3}_{-2}	[9-15]	1.46 / 5
	0.13390	0.13390	1.631^{+18}_{-15}	0.354^{+3}_{-2}	[9-15]	1.57 / 5
LL,FF	0.13270	0.13270	2.276^{+18}_{-16}	$\mathbf{0.493}^{+\mathbf{2}}_{-\mathbf{1}}$	[9-15]	4.99 / 8
	0.13320	0.13270	2.154^{+18}_{-16}	$\mathbf{0.467}^{+\mathbf{2}}_{-\mathbf{2}}$	[9-15]	5.35 / 8
	0.13340	0.13270	2.103^{+17}_{-16}	$\mathbf{0.456}^{+\mathbf{2}}_{-\mathbf{2}}$	[9-15]	5.35 / 8
	0.13320	0.13320	2.027^{+17}_{-16}	$\mathbf{0.439}^{+\mathbf{2}}_{-\mathbf{2}}$	[9-15]	4.98 / 8
	0.13340	0.13320	1.974^{+17}_{-16}	$\mathbf{0.428}^{+\mathbf{2}}_{-\mathbf{2}}$	[9-15]	5.02 / 8
	0.13340	0.13340	1.920^{+17}_{-15}	$\mathbf{0.416}^{+\mathbf{3}}_{-\mathbf{2}}$	[9-15]	4.80 / 8
	0.13370	0.13370	1.752^{+18}_{-15}	$\mathbf{0.380}^{+\mathbf{3}}_{-\mathbf{2}}$	[9-15]	4.60 / 8
	0.13390	0.13370	1.693^{+17}_{-16}	$\mathbf{0.367}^{+\mathbf{3}}_{-\mathbf{2}}$	[9-15]	4.36 / 8
	0.13390	0.13390	1.633^{+18}_{-16}	$\mathbf{0.354}^{+\mathbf{3}}_{-\mathbf{2}}$	[9-15]	4.28 / 8

Table C.18: Pseudoscalar masses for the $\beta = 5.93$ quenched matched data set.

Fuzzing	κ_1	κ_2	$r_0 m_{\rm PS}$	$a m_{\rm PS}$	Fit	χ^2/d.o.f.
LL,FL	0.13270	0.13270	$2.276\ ^{+21}_{-25}$	$0.494\ ^{+\ 3}_{-\ 4}$	[10-15]	5.71 / 6
	0.13320	0.13270	$2.154\ ^{+23}_{-30}$	$0.467\ ^{+\ 4}_{-\ 6}$	[10-15]	6.20 / 6
	0.13340	0.13270	$2.104\ ^{+25}_{-32}$	$0.456\ ^{+\ 4}_{-\ 6}$	[10-15]	6.38 / 6
	0.13320	0.13320	$2.026\ ^{+27}_{-30}$	$0.439\ ^{+\ 5}_{-\ 6}$	[10-15]	6.65 / 6
	0.13340	0.13320	$1.973\ ^{+30}_{-34}$	$0.428\ ^{+\ 6}_{-\ 7}$	[10-15]	5.70 / 6
	0.13340	0.13340	$1.920\ ^{+31}_{-32}$	$0.416\ ^{+\ 6}_{-\ 6}$	[10-15]	5.96 / 6
	0.13370	0.13370	$1.752\ ^{+34}_{-33}$	$0.380\ ^{+\ 7}_{-\ 7}$	[10-15]	6.39 / 6
	0.13390	0.13370	$1.696\ ^{+36}_{-31}$	$0.368\ ^{+\ 8}_{-\ 6}$	[10-15]	6.46 / 6
	0.13390	0.13390	$1.640\ ^{+41}_{-26}$	$0.356\ ^{+\ 8}_{-\ 5}$	[10-15]	6.53 / 6
LL,FL,FF	0.13270	0.13270	$2.276\ ^{+18}_{-17}$	$0.494\ ^{+\ 2}_{-\ 2}$	[9-15]	17.87 / 15
	0.13320	0.13270	$2.154\ ^{+18}_{-16}$	$0.467\ ^{+\ 2}_{-\ 2}$	[9-15]	18.39 / 15
	0.13340	0.13270	$2.103\ ^{+18}_{-16}$	$0.456\ ^{+\ 2}_{-\ 2}$	[9-15]	18.67 / 15
	0.13320	0.13320	$2.026\ ^{+18}_{-16}$	$0.439\ ^{+\ 3}_{-\ 2}$	[9-15]	18.76 / 15
	0.13340	0.13320	$1.973\ ^{+18}_{-16}$	$0.428\ ^{+\ 3}_{-\ 2}$	[9-15]	18.99 / 15
	0.13340	0.13340	$1.919\ ^{+18}_{-16}$	$0.416\ ^{+\ 3}_{-\ 2}$	[9-15]	19.02 / 15
	0.13370	0.13370	$1.748\ ^{+19}_{-15}$	$0.379\ ^{+\ 3}_{-\ 2}$	[9-15]	19.03 / 15
	0.13390	0.13370	$1.688\ ^{+19}_{-14}$	$0.366\ ^{+\ 3}_{-\ 2}$	[9-15]	19.08 / 15
	0.13390	0.13390	$1.626\ ^{+19}_{-14}$	$0.353\ ^{+\ 4}_{-\ 2}$	[9-15]	18.58 / 15

Table C.19: Pseudoscalar masses for the $\beta = 5.93$ quenched matched data set.

Fuzzing	κ_1	κ_2	$r_0 m_V$	$a m_V$	Fit	χ^2/d.o.f.
FF	0.13270	0.13270	3.008^{+35}_{-31}	0.652^{+6}_{-5}	[10-15]	4.86 / 4
	0.13320	0.13270	2.939^{+36}_{-34}	0.637^{+7}_{-6}	[10-15]	5.12 / 4
	0.13340	0.13270	2.914^{+38}_{-35}	0.632^{+7}_{-6}	[10-15]	5.18 / 4
	0.13320	0.13320	2.862^{+41}_{-37}	0.621^{+8}_{-7}	[10-15]	4.11 / 4
	0.13340	0.13320	2.837^{+42}_{-40}	0.615^{+8}_{-8}	[10-15]	4.16 / 4
	0.13340	0.13340	2.807^{+44}_{-42}	0.609^{+9}_{-8}	[10-15]	3.77 / 4
	0.13370	0.13370	2.734^{+55}_{-51}	0.593^{+11}_{-10}	[10-15]	3.22 / 4
	0.13390	0.13370	2.721^{+60}_{-58}	0.590^{+13}_{-12}	[10-15]	3.17 / 4
	0.13390	0.13390	2.697^{+67}_{-65}	0.585^{+14}_{-14}	[10-15]	2.90 / 4
FL	0.13270	0.13270	3.017^{+33}_{-30}	0.654^{+6}_{-5}	[10-15]	6.57 / 4
	0.13320	0.13270	2.947^{+35}_{-32}	0.639^{+6}_{-6}	[10-15]	6.77 / 4
	0.13340	0.13270	2.922^{+36}_{-34}	0.634^{+7}_{-6}	[10-15]	6.85 / 4
	0.13320	0.13320	2.871^{+39}_{-35}	0.622^{+7}_{-6}	[10-15]	5.39 / 4
	0.13340	0.13320	2.846^{+40}_{-36}	0.617^{+8}_{-7}	[10-15]	5.46 / 4
	0.13340	0.13340	2.817^{+42}_{-38}	0.611^{+8}_{-7}	[10-15]	4.89 / 4
	0.13370	0.13370	2.744^{+51}_{-48}	0.595^{+10}_{-10}	[10-15]	4.10 / 4
	0.13390	0.13370	2.730^{+54}_{-53}	0.592^{+11}_{-11}	[10-15]	4.12 / 4
	0.13390	0.13390	2.707^{+59}_{-58}	0.587^{+12}_{-12}	[10-15]	3.55 / 4
LL,FF	0.13270	0.13270	2.990^{+34}_{-38}	0.648^{+6}_{-7}	[9-15]	7.82 / 8
	0.13320	0.13270	2.921^{+34}_{-28}	0.633^{+6}_{-4}	[9-15]	8.03 / 8
	0.13340	0.13270	2.895^{+42}_{-35}	0.628^{+8}_{-6}	[9-15]	9.25 / 8
	0.13320	0.13320	2.838^{+37}_{-30}	0.615^{+7}_{-5}	[9-15]	7.28 / 8
	0.13340	0.13320	2.812^{+38}_{-31}	0.610^{+7}_{-5}	[9-15]	7.42 / 8
	0.13340	0.13340	2.790^{+42}_{-33}	0.605^{+8}_{-6}	[9-15]	10.11 / 8
	0.13370	0.13370	2.710^{+46}_{-43}	0.588^{+9}_{-9}	[9-15]	9.09 / 8
	0.13390	0.13370	2.688^{+47}_{-46}	0.583^{+10}_{-9}	[9-15]	7.87 / 8
	0.13390	0.13390	2.665^{+47}_{-52}	0.578^{+10}_{-11}	[9-15]	8.25 / 8

Table C.20: Vector masses for the $\beta = 5.93$ quenched matched data set.

Fuzzing	κ_1	κ_2	$r_0 m_V$	am_V	Fit	χ^2/d.o.f.
LL,FL	0.13270	0.13270	3.016^{+33}_{-31}	0.654^{+6}_{-5}	[10-15]	7.12 / 6
	0.13320	0.13270	2.925^{+55}_{-57}	0.639^{+6}_{-7}	[10-15]	7.73 / 6
	0.13340	0.13270	2.920^{+35}_{-41}	0.633^{+6}_{-8}	[10-15]	7.97 / 6
	0.13320	0.13320	2.867^{+39}_{-43}	0.622^{+8}_{-8}	[10-15]	6.17 / 6
	0.13340	0.13320	2.842^{+40}_{-48}	0.616^{+8}_{-10}	[10-15]	6.27 / 6
	0.13340	0.13340	2.811^{+41}_{-47}	0.610^{+8}_{-10}	[10-15]	5.75 / 6
	0.13370	0.13370	2.741^{+76}_{-48}	0.594^{+16}_{-10}	[9-15]	8.36 / 8
	0.13390	0.13370	2.724^{+82}_{-55}	0.591^{+17}_{-11}	[9-15]	8.30 / 8
	0.13390	0.13390	2.661^{+90}_{-50}	0.577^{+19}_{-10}	[9-15]	8.45 / 8
LL,FL,FF	0.13270	0.13270	3.021^{+34}_{-30}	$\mathbf{0.655}^{+6}_{-5}$	[10-15]	12.64 / 12
	0.13320	0.13270	2.950^{+35}_{-31}	$\mathbf{0.640}^{+6}_{-5}$	[10-15]	13.10 / 12
	0.13340	0.13270	2.923^{+36}_{-34}	$\mathbf{0.634}^{+7}_{-6}$	[10-15]	13.26 / 12
	0.13320	0.13320	2.870^{+38}_{-34}	$\mathbf{0.622}^{+7}_{-6}$	[10-15]	10.85 / 12
	0.13340	0.13320	2.843^{+40}_{-35}	$\mathbf{0.616}^{+8}_{-6}$	[10-15]	10.98 / 12
	0.13340	0.13340	2.812^{+41}_{-37}	$\mathbf{0.610}^{+8}_{-7}$	[10-15]	10.45 / 12
	0.13370	0.13370	2.731^{+48}_{-46}	$\mathbf{0.592}^{+10}_{-9}$	[10-15]	10.26 / 12
	0.13390	0.13370	2.713^{+51}_{-53}	$\mathbf{0.588}^{+10}_{-11}$	[10-15]	10.24 / 12
	0.13390	0.13390	2.685^{+52}_{-59}	$\mathbf{0.582}^{+11}_{-12}$	[10-15]	10.57 / 12

Table C.21: Vector masses the $\beta = 5.93$ quenched matched data set.

Fuzzing	κ_{val}	$r_0 m_{\mathrm{N}}$	$a m_{\mathrm{N}}$	Fit	χ^2/d.o.f.
FF	0.13270	4.53^{+8}_{-5}	0.983^{+16}_{-10}	[9-15]	1.16 / 5
	0.13320	4.25^{+8}_{-6}	0.922^{+17}_{-12}	[9-15]	1.29 / 5
	0.13340	4.15^{+7}_{-5}	0.899^{+14}_{-10}	[8-15]	1.50 / 6
	0.13370	3.97^{+8}_{-6}	0.861^{+15}_{-11}	[8-15]	1.86 / 6
	0.13390	3.86^{+8}_{-7}	0.837^{+17}_{-14}	[8-15]	2.03 / 6
FL	0.13270	4.54^{+6}_{-5}	0.984^{+12}_{-8}	[9-15]	1.57 / 5
	0.13320	4.25^{+7}_{-5}	0.922^{+14}_{-10}	[9-15]	1.43 / 5
	0.13340	4.14^{+8}_{-6}	0.898^{+17}_{-11}	[9-15]	1.35 / 5
	0.13370	4.00^{+8}_{-6}	0.867^{+16}_{-11}	[8-15]	1.50 / 6
	0.13390	3.87^{+8}_{-7}	0.838^{+17}_{-13}	[8-15]	1.68 / 6
LL,FF	0.13270		N/A		
	0.13320	4.23^{+8}_{-5}	0.918^{+17}_{-10}	[9-15]	2.89 / 8
	0.13340	4.12^{+9}_{-6}	0.894^{+18}_{-11}	[9-15]	2.74 / 8
	0.13370	3.97^{+9}_{-6}	0.862^{+18}_{-11}	[8-15]	3.39 / 10
	0.13390	3.87^{+10}_{-6}	0.839^{+22}_{-12}	[8-15]	4.49 / 10
LL,FL	0.13270	4.53^{+6}_{-5}	$\mathbf{0.982}^{+12}_{-9}$	[7-15]	8.24 / 12
	0.13320	4.24^{+8}_{-5}	$\mathbf{0.918}^{+15}_{-10}$	[9-15]	2.77 / 8
	0.13340	4.19^{+7}_{-5}	$\mathbf{0.908}^{+15}_{-9}$	[7-15]	5.29 / 12
	0.13370	3.98^{+8}_{-9}	$\mathbf{0.864}^{+15}_{-18}$	[8-15]	2.70 / 10
	0.13390	3.85^{+9}_{-8}	$\mathbf{0.836}^{+20}_{-16}$	[8-15]	3.28 / 10
LL,FL,FF	0.13270	4.54^{+9}_{-4}	0.984^{+18}_{-6}	[10-15]	5.58 / 12
	0.13320	4.25^{+10}_{-5}	0.921^{+21}_{-8}	[10-15]	5.74 / 12
	0.13340	4.14^{+11}_{-5}	0.897^{+23}_{-9}	[10-15]	6.40 / 12
	0.13370	3.97^{+12}_{-6}	0.861^{+25}_{-12}	[10-15]	8.89 / 12
	0.13390	3.86^{+13}_{-7}	0.838^{+27}_{-14}	[10-15]	11.67 / 12

Table C.22: Nucleon masses for the $\beta = 5.93$ matched quenched data set.

Fuzzing	κ_{val}	$r_0 m_\Delta$	$a m_\Delta$	Fit	χ^2/d.o.f.
FF	0.13270	$5.02\ ^{+7}_{-6}$	$1.089\ ^{+12}_{-11}$	[8-15]	2.42 / 6
	0.13320	$4.79\ ^{+7}_{-7}$	$1.039\ ^{+14}_{-13}$	[8-15]	3.18 / 6
	0.13340	$4.70\ ^{+8}_{-7}$	$1.019\ ^{+16}_{-14}$	[8-15]	3.70 / 6
	0.13370	$4.53\ ^{+12}_{-10}$	$0.982\ ^{+26}_{-21}$	[9-15]	4.44 / 5
	0.13390	$4.43\ ^{+15}_{-12}$	$0.960\ ^{+31}_{-25}$	[9-15]	5.09 / 5
FL	0.13270	$5.01\ ^{+7}_{-7}$	$1.087\ ^{+12}_{-13}$	[9-15]	5.28 / 5
	0.13320	$4.77\ ^{+8}_{-8}$	$1.033\ ^{+16}_{-15}$	[9-15]	5.05 / 5
	0.13340	$4.67\ ^{+9}_{-8}$	$1.012\ ^{+18}_{-16}$	[9-15]	4.83 / 5
	0.13370	$4.53\ ^{+13}_{-12}$	$0.981\ ^{+28}_{-25}$	[10-15]	4.38 / 4
	0.13390	$4.41\ ^{+17}_{-14}$	$0.955\ ^{+36}_{-30}$	[10-15]	4.30 / 4
LL,FF	0.13270	$5.02\ ^{+7}_{-5}$	$1.089\ ^{+14}_{-9}$	[9-15]	9.05 / 8
	0.13320	$4.76\ ^{+8}_{-6}$	$1.032\ ^{+17}_{-11}$	[8-15]	7.91 / 10
	0.13340	$4.64\ ^{+10}_{-7}$	$1.007\ ^{+20}_{-13}$	[9-15]	6.33 / 8
	0.13370	$4.53\ ^{+14}_{-10}$	$0.982\ ^{+29}_{-20}$	[10-15]	7.17 / 6
	0.13390	$4.41\ ^{+16}_{-12}$	$0.957\ ^{+35}_{-24}$	[10-15]	8.05 / 6
LL,FL	0.13270	$5.00\ ^{+7}_{-5}$	$\mathbf{1.084}\ ^{\mathbf{+13}}_{\mathbf{-9}}$	[9-15]	8.42 / 8
	0.13320	$4.75\ ^{+8}_{-6}$	$\mathbf{1.030}\ ^{\mathbf{+16}}_{\mathbf{-12}}$	[9-15]	6.97 / 8
	0.13340	$4.65\ ^{+9}_{-7}$	$\mathbf{1.009}\ ^{\mathbf{+18}}_{\mathbf{-13}}$	[9-15]	6.75 / 8
	0.13370	$4.50\ ^{+11}_{-8}$	$\mathbf{0.976}\ ^{\mathbf{+22}}_{\mathbf{-17}}$	[9-15]	6.57 / 8
	0.13390	$4.39\ ^{+13}_{-9}$	$\mathbf{0.952}\ ^{\mathbf{+28}}_{\mathbf{-19}}$	[9-15]	6.61 / 8
LL,FL,FF	0.13270	$5.03\ ^{+10}_{-7}$	$1.090\ ^{+20}_{-12}$	[10-15]	21.81 / 12
	0.13320	$4.79\ ^{+11}_{-8}$	$1.039\ ^{+23}_{-16}$	[10-15]	25.73 / 12
	0.13340	$4.70\ ^{+12}_{-10}$	$1.018\ ^{+26}_{-20}$	[10-15]	27.06 / 12
	0.13370	$4.54\ ^{+15}_{-13}$	$0.984\ ^{+33}_{-26}$	[10-15]	27.97 / 12
	0.13390	$4.56\ ^{+17}_{-8}$	$0.989\ ^{+35}_{-17}$	[9-15]	36.08 / 15

Table C.23: Delta masses for the $\beta = 5.93$ matched quenched data set.

β	κ_{sea}	κ_{val}	$r_0 m_{\mathrm{PCAC}}$	$a m_{\mathrm{PCAC}}$	Fit	χ^2/d.o.f.
5.2	0.13550	0.13400	0.317^{+6}_{-6}	0.0645^{+4}_{-4}	[9-14]	2.19 / 5
		0.13450	0.246^{+5}_{-5}	0.0501^{+5}_{-4}	[9-14]	2.25 / 5
		0.13500	0.178^{+4}_{-4}	0.0361^{+6}_{-4}	[9-14]	2.55 / 5
		0.13550	0.110^{+4}_{-3}	0.0225^{+7}_{-4}	[9-14]	2.60 / 5
5.2	0.13500	0.13350	0.407^{+7}_{-7}	0.0890^{+3}_{-3}	[9-14]	12.86 / 5
		0.13400	0.341^{+6}_{-6}	0.0745^{+3}_{-3}	[8-14]	14.24 / 6
		0.13450	0.275^{+5}_{-5}	0.0602^{+3}_{-3}	[8-14]	12.61 / 6
		0.13500	0.211^{+4}_{-4}	0.0460^{+3}_{-3}	[8-14]	11.37 / 6
5.26	0.13450	0.13350	0.481^{+6}_{-6}	0.1050^{+4}_{-4}	[9-14]	8.07 / 5
		0.13400	0.411^{+6}_{-6}	0.0898^{+4}_{-4}	[9-14]	8.13 / 5
		0.13450	0.343^{+5}_{-5}	0.0750^{+4}_{-4}	[9-14]	7.60 / 5
		0.13500	0.277^{+4}_{-4}	0.0605^{+4}_{-4}	[9-14]	6.35 / 5
5.29	0.13400	0.13350	0.497^{+7}_{-7}	0.1117^{+4}_{-4}	[9-14]	6.09 / 5
		0.13400	0.430^{+6}_{-6}	0.0965^{+4}_{-4}	[9-14]	6.42 / 5
		0.13450	0.363^{+5}_{-5}	0.0816^{+4}_{-4}	[9-14]	6.55 / 5
		0.13500	0.298^{+4}_{-4}	0.0670^{+4}_{-4}	[9-14]	6.35 / 5

β	κ_1	κ_2	$r_0 m_{\mathrm{PCAC}}$	$a m_{\mathrm{PCAC}}$	Fit	χ^2/d.o.f.
5.93	0.13340	0.13340	0.248^{+2}_{-2}	0.0538^{+3}_{-3}	[10-14]	5.36 / 4
	0.13340	0.13320	0.263^{+2}_{-2}	0.0569^{+3}_{-3}	[10-14]	5.50 / 4
	0.13320	0.13320	0.277^{+2}_{-2}	0.0600^{+3}_{-3}	[10-14]	5.36 / 4
	0.13340	0.13270	0.298^{+2}_{-2}	0.0647^{+3}_{-3}	[10-14]	5.69 / 4
	0.13320	0.13270	0.313^{+2}_{-2}	0.0679^{+3}_{-3}	[10-14]	5.47 / 4
	0.13270	0.13270	0.349^{+3}_{-3}	0.0757^{+3}_{-3}	[10-14]	4.94 / 4
	0.13370	0.13370	0.205^{+2}_{-2}	0.0445^{+3}_{-3}	[10-14]	5.05 / 4
	0.13390	0.13370	0.191^{+2}_{-2}	0.0413^{+3}_{-3}	[10-14]	5.03 / 4
	0.13390	0.13390	0.176^{+2}_{-2}	0.0382^{+3}_{-3}	[10-14]	4.75 / 4

Table C.24: The PCAC mass for the dynamical data sets and the matched quenched simulation.

References

[1] K. G. Wilson, Phys. Rev. D **10**, 2445 (1974).

[2] H. Hamber and G. Parisi, Phys. Rev. Lett. **47**, 1782 (1981).

[3] D. Weingarten, Phys. Lett. **109B**, 57 (1982).

[4] (CP-PACS Collaboration), S. Aoki *et al.*, Phys. Rev. Lett. **84**, 238 (2000).

[5] R. D. Mawhinney, hep-lat/0001032 (2000).

[6] H. J. Rothe, *Lattice Gauge Theories - An Introduction* (World Scientific, Singapore, 1992).

[7] I. Montvay and G. Münster, *Quantum Fields on a Lattice* (Cambridge University Press, Cambridge, 1994).

[8] R. Gupta, Introduction to Lattice QCD, Lectures given at the LXVIII Les Houches Summer School, hep-lat/9807028, 1998.

[9] M. Lüscher, Advanced Lattice QCD, Lectures given at the LXVIII Les Houches Summer School, hep-lat/9802029, 1998.

[10] R. P. Feynman and A. R. Hibbs, *Quantum Mechanics and Path Integrals* (McGraw-Hill, New York, 1965).

[11] K. Osterwalder and R. Schrader, Comm. Math. Phys **42**, 281 (1975).

[12] M. Lüscher, Comm. Math. Phys. **54**, 283 (1977).

[13] K. Binder, *Applications of the Monte Carlo Method in Statistical Physics* (Springer-Verlag, Berlin, 1987).

[14] (Particle Data Group), C. Caso *et al.*, The European Physical Journal **C** **3**, 1 (1998).

[15] D. Leinweber and T. Cohen, Phys. Rev. D **49**, 3512 (1994).

[16] S. Güsken, hep-lat/9906034 (1999).

[17] K. Symanzik, Nucl. Phys. B **226**, 187 and 205 (1983).

[18] (CP-PACS Collaboration), S. Aoki *et al.*, Phys. Rev. D **60**, 114508 (1999).

[19] Y. Iwasaki, (1983), university of Tsukuba report UTHEP-118.

[20] K. G. Wilson, in *New Phenomena in Subnuclear Physics*, edited by A. Zichichi (Plenum, New York, 1975).

[21] B. Sheikholeslami and R. Wohlert, Nucl. Phys. B **259**, 572 (1985).

[22] H. B. Nielsen and M. Ninomiya, Nucl. Phys. B **185**, 20 (1981).

[23] P. H. Ginsparg and K. G. Wilson, Phys. Rev. D **25**, 2649 (1982).

[24] P. Hernández, K. Jansen, and M. Lüscher, Nucl. Phys. B **552**, 363 (1999).

[25] M. Lüscher, S. Sint, R. Sommer, and P. Weisz, Nucl. Phys. B **478**, 365 (1996).

[26] G. P. Lepage and P. B. Mackenzie, Phys. Rev. D **48**, 2250 (1992).

[27] M. Alford, T. Klassen, and P. Lepage, Phys. Rev. D **58**, 034503 (1998).

[28] K. Jansen *et al.*, Phys. Lett. B **372**, 275 (1996).

[29] M. Lüscher and P. Weisz, Nucl. Phys. B **479**, 429 (1996).

[30] M. Lüscher *et al.*, Nucl. Phys. B **491**, 323 (1997).

[31] S. Sint and R. Sommer, Nucl. Phys. B **465**, 71 (1996).

[32] S. Sint and R. Sommer, Nucl. Phys. B (Proc. Suppl.) **63**, 856 (1998).

[33] D. J. Gross and F. Wilczek, Phys. Rev. D **8**, 3633 (1973).

[34] H. D. Politzer, Phys. Rev. Lett. **30**, 1346 (1973).

[35] W. E. Caswell, Phys. Rev. Lett. **33**, 244 (1974).

[36] D. R. T. Jones, Nucl. Phys. B **75**, 531 (1974).

[37] A. A. Belavin and A. A. Migdal, JETP Lett. **19**, 181 (1974).

[38] F. Fucito *et al.*, Nucl. Phys. B **210**, 407 (1982).

[39] P. A. Rowland, Ph.D. thesis, University of Edinburgh, 1997.

[40] T. Bhattacharya, R. Gupta, G. Kilcup, and S. Sharpe, Phys. Rev. D **53**, 6486 (1996).

[41] J. N. Labrenz and S. R. Sharpe, Phys. Rev. D **54**, 4095 (1996).

[42] D. B. Leinweber, R. M. Woloshyn, and T. Draper, Phys. Rev. D **43**, 1659 (1991).

[43] D. B. Leinweber, T. Draper, and R. M. Woloshyn, Phys. Rev. D **46**, 3067 (1992).

[44] (UKQCD Collaboration), C. R. Allton *et al.*, Phys. Rev. D **47**, 5128 (1993).

[45] S. Güsken, Nucl. Phys. B (Proc. Suppl.) **17**, 361 (1990).

[46] (UKQCD Collaboration), P. Lacock *et al.*, Phys. Rev. D **51**, 6403 (1995).

[47] R. Gupta, Phys. Rev. D **48**, 3330 (1993).

[48] C. T. H. Davies *et al.*, Phys. Rev. D **50**, 6963 (1994).

[49] W. H. Press, S. A. Teukolsky, W. T. Vetterling, and B. P. Flannery, *Numerical Recipes in C* (Cambridge University Press, Cambridge, 1992).

[50] C. Michael and A. McKerrell, Phys. Rev. D **51**, 3745 (1995).

[51] B.Efron, Soc. for Industrial and Applied mathematics (1982).

[52] (UKQCD Collaboration), C. M. Michael and H. S. Shanahan, Nucl. Phys. B (Proc. Suppl.) **47**, 337 (1996).

[53] (UKQCD Collaboration), H. S. Shanahan *et al.*, Phys. Rev. D **55**, 1584 (1997).

[54] (UKQCD Collaboration), R. D. Kenway, Nucl. Phys. B (Proc. Suppl.) **53**, 206 (1997).

[55] S. M. Ryan, Ph.D. thesis, University of Edinburgh, 1996.

[56] (UKQCD collaboration), K. C. Bowler *et al.*, hep-lat/9910022 (1999).

[57] (UKQCD Collaboration), C. R. Allton *et al.*, Nucl. Phys. B **407**, 331 (1993).

[58] D. A. Smith, Ph.D. thesis, University of Edinburgh, 1997.

[59] (UKQCD Collaboration), H. Simma and D. Smith, Conference Proceedings, 31st International Symposium Ahrenshoop on the Theory of Elementary Particles, Buckow, September 2-6 (1997).

[60] W. Bardeen, A. Duncan, E. Eichten, and H. Thacker, Phys. Rev. D **59**, 014507 (1999).

[61] W. Bardeen *et al.*, Nucl. Phys. B (Proc. Suppl.) **63**, 141 (1998).

[62] W. Bardeen *et al.*, Phys. Rev. D **57**, 1633 (1998).

[63] P. V. Baal and A. S. Kronfeld, Nucl. Phys. B (Proc. Suppl.) **9**, 227 (1989).

[64] D. Hochberg and H. B. Thacker, Nucl. Phys. B **257**, 729 (1985).

[65] M. Fukugita *et al.*, Phys. Lett. B **294**, 380 (1992).

[66] M. Lüscher, Commun. Math. Phys. **104**, 177 (1986).

[67] M. Lüscher, Commun. Math. Phys. **105**, 153 (1986).

[68] K. C. Bowler *et al.*, Phys. Lett. B **162**, 354 (1985).

[69] S. Ono, Phys. Rev. D **17**, 888 (1978).

[70] M. Göckeler *et al.*, Phys. Rev. D **57**, 5562 (1998).

[71] (UKQCD collaboration), P. Lacock and C. Michael, Phys. Rev. D **52**, 5213 (1995).

[72] D. Becirevic *et al.*, hep-lat/9809129 (1998).

[73] R. Sommer, Nucl. Phys. B **411**, 839 (1994).

[74] (ALPHA Collaboration), M. Guagnelli, R. Sommer and H. Wittig, Nucl. Phys. B **535**, 389 (1998).

[75] M. Neubert, Phys. Rept. **245**, 259 (1994).

[76] P. A. Boyle, Ph.D. thesis, University of Edinburgh, 1997.

[77] H. Wittig, Nucl. Phys. B (Proc. Suppl.) **63**, 47 (1998).

[78] S. Sint and P. Weisz, Nucl. Phys. B **502**, 251 (1997).

[79] G. M. de Divitiis and R. Petronzio, Phys. Lett. B **419**, 311 (1998).

[80] S. R. Sharpe, Phys. Rev. D **46**, 3146 (1992).

[81] C. W. Bernard and M. F. L. Golterman, Phys. Rev. D **46**, 853 (1992).

[82] M. Gell-Mann, R. J. Oakes, and B. Renner, Phys. Rev. **175**, 2195 (1968).

[83] H. Wittig, Private Communication, 1999.

[84] M. Göckeler *et al.*, Phys. Lett. B **391**, 388 (1997).

[85] (ALPHA and UKQCD collaborations), J. Garden, J. Heitger, R. Sommer, and H. Wittig, hep-lat/9906013 (1999).

[86] (UKQCD Collaboration), C. R. Allton *et al.*, Phys. Rev. D **49**, 474 (1994).

[87] (ALPHA Collaboration), S. Capitani *et al.*, Nucl. Phys. B **544**, 669 (1999).

[88] H. Leutwyler, Phys. Lett. B **378**, 667 (1996).

[89] A. C. Irving, Private Communication, 1999.

[90] (UKQCD Collaboration), J. Garden, Nucl. Phys. B (Proc. Suppl.) **83-84**, 165 (2000).

[91] (UKQCD Collaboration), C. R. Allton *et al.*, Light hadron spectrum and QCD potential with non-perturbatively improved dynamical fermions, in preparation.

[92] (UKQCD Collaboration), C. R. Allton *et al.*, Phys. Rev. D **60**, 034507 (1999).

[93] Z. Sroczynski, Ph.D. thesis, University of Edinburgh, 1998.

[94] (UKQCD Collaboration), A. C. Irving, Nucl. Phys. B (Proc. Suppl.) **73**, 874 (1999).

[95] (UKQCD Collaboration), A. C. Irving *et al.*, Phys. Rev. D **58**, 114504 (1998).

[96] A. C. Irving and J. C. Sexton, Phys. Rev. D **55**, 5456 (1997).

[97] R. Edwards, U. Heller, and T. Klassen, Nucl. Phys. B **517**, 337 (1998).

[98] S. Duane, A. D. Kennedy, B. J. Pendleton, and D. Roweth, Phys. Lett. B **195**, 216 (1987).

[99] S. M. Pickles, Ph.D. thesis, University of Edinburgh, 1998.

[100] B. Joó, Ph.D. thesis, University of Edinburgh, 2000.

[101] (APLHA Collaboration), Karl Jansen and R. Sommer, Nucl. Phys. B **530**, 185 (1998).

[102] R. G. Edwards, U. M. Heller, and T. R. Klassen, Phys. Rev. Lett. **80**, 3448 (1998).

[103] C. Michael, Phys. Lett. B **283**, 103 (1992).

[104] S. Perantonis and C. Michael, Nucl. Phys. B **347**, 854 (1990).

[105] S. Perantonis, A. Huntley, and C. Michael, Nucl. Phys. B **326**, 544 (1989).

[106] (UKQCD Collaboration), S. P. Booth *et al.*, Nucl. Phys. B **394**, 509 (1993).

[107] (SESAM Collaboration), N. Eicker *et al.*, Phys. Rev. D **59**, 014509 (1999).

[108] (CP-PACS Collaboration), R. Burkhalter, Nucl. Phys. B (Proc. Suppl.) **73**, 3 (1999).

[109] S. Aoki *et al.*, Phys. Rev. D **50**, 486 (1994).

[110] D. B. Leinweber, A. W. Thomas, K. Tsushima, and S. V. Wright, Phys. Rev. D **61**, 074502 (2000).

[111] (SESAM Collaboration), N. Eicker *et al.*, Phys. Lett. B **407**, 290 (1997).

[112] S. R. Sharpe, Phys. Rev. D **56**, 7052 (1997).

[113] C. Bernard and M. Golterman, Phys. Rev. D **49**, 486 (1994).

[114] M. Lüscher, Nucl. Phys. B **180**, 317 (1981).

[115] (SESAM Collaboration), U. Glässner *et al.*, Phys. Lett. B **383**, 98 (1996).

[116] K. Schilling, hep-lat/9909152 (1999).

[117] A. X. El-Khadra, G. Hockney, A. S. Kronfeld, and P. B. Mackenzie, Phys. Rev. Lett. **69**, 729 (1992).

[118] A. Hart and M. Teper, hep-lat/9909072 (1999), and in progress.

[119] (UKQCD Collaboration), C. Michael, M. S. Foster, and C. McNeile, hep-lat/9909036 (1999).